The Osmium Isotopic Composition of Seawater: Past and Present

SPROSON, ADAM,DAVID

SPROSON, ADAM,DAVID (2017) *The Osmium Isotopic Composition of Seawater: Past and Present*, Durham theses, Durham University. Available at Durham E-Theses Online: http://etheses.dur.ac.uk/12262/

The Osmium Isotopic Composition of Seawater: Past and Present

Adam D. Sproson

College of St. Hild & St. Bede

A thesis submitted in partial fulfilment of the requirements for the degree of Doctor of Philosophy at Durham University

Department of Earth Sciences, Durham University

June, 2017

Abstract

The osmium isotopic composition of seawater ($^{187}Os/^{188}Os$) reflects a balance between radiogenic continental sources and unradiogenic mantle and extraterrestrial derived sources. Reconstruction of this value has allowed us to unlock vital information about a series of Earth system processes, both today and in Earth's geological past. This body of work looks to reconstruct the $^{187}Os/^{188}Os$ of seawater for past and present oceans using the $^{187}Os/^{188}Os$ composition of shales and macroalgae (seaweed) respectively.

The $^{187}Os/^{188}Os$ composition of Icelandic (0.16 to 0.99) and Japanese (0.16 to 1.09) macroalgae are highly variable, and reflect the mixing between multiple sources. The $^{187}Os/^{188}Os$ of Icelandic coastal waters is dominated by seawater and local river catchments, and has been utilised to trace the influence of basaltic weathering on the global Os cycle. The $^{187}Os/^{188}Os$ of Japanese coastal waters is dominated by seawater and river catchments draining Miocene-Holocene continental rocks or anthropogenic sources, and has been utilised to trace mankind's impact on the global Os cycle. The $^{187}Os/^{188}Os$ profiles of shales from the Silurian Ireviken, Mulde, Lau and Klonk biovents are similar to those previously recorded for the Hirnantian glaciation. This data suggests the Silurian has been punctuated by several glaciations associated with fluctuations in global temperatures, sea-level and the carbon cycle. When combined with the Li isotopic (δ^7Li) composition of carbonates, this study suggests glacial processes caused large changes in oxidative and silicate weathering.

This study has successfully utilised macroalgae as a proxy for the $^{187}Os/^{188}Os$ of seawater and proven it can become a powerful tracer of Earth system processes and human activity. This study has also redefined the Silurian as an icehouse, and suggests the long term decline in atmospheric CO_2, due to orogeny, land-plant diversification, volcanic-arc degassing and/or paleogeography, was reversed by periodic glaciations which acted to enhance oxidative weathering whilst suppressing silicate weathering.

Declaration

I declare that this thesis, which I submit for the degree of Doctor of Philosophy at Durham University, is my own work and not substantially the same as any which has previously been submitted at this or any other university.

Adam D. Sproson

College of St. Hild & St. Bede, Durham University

June 2017

Acknowledgements

I would like to dedicate this PhD thesis to my parents, Julie and Richard Sproson, for without them, none of this could be possible. They have supported me financially, emotionally and academically throughout my entire life. They have always kept an open mind and have never pressured me to take my life in any particular direction. This has led me to the environmental and paleoclimatic sciences I so much love and treasure and the start of a career in something I feel intensely passionate about. For that I am eternally indebted.

I would like to thank my PhD supervisors, Prof. David Selby, Prof. Kevin Burton and Prof. David Harper for their constant advice and support in this endeavour. In particular, I would like to thank Prof. David Selby for his finantial and academic support. Without him none of this research could have been possible. He always allowed me to develop new ideas and carry further research if the mood struck me, with no sign of financial constrait. This has led to the development of some unique research that has gone above and beyond the original remit of the project. In my opinion he is an exceptional supervisor and the best supervisor I have had (so far).

I would like to thank my friends and colleagues in Durham. In particular I would like to thank Fienke Nanne, Thomas Underwood, Elizabeth Atar, Edward Inglis and Ben Maunder. They have made the last four years some of the best in my life. They have filled the duration of my PhD with truly fun and enjoyable experiences and supported me through the hard times (of which there were many).

I would like to thank Joanna Hesselink for helping me in the lab during the start of my PhD and teaching me the tricks of the trade. I would also like to thank Antonia Hoffman for her help towards the end of my PhD and making things run smoothly. Chris Ottley and Geoff Nowell receive my gratitude for keeping the mass spectrometers in operation thoughout my PhD and for helping with analyses. Thank you to the rest of the Selby Group i.e. Yang Li, Junjie Liu and Zeyang Liu for making the lab a sane place to work and helping interpret my data.

I would like to thank Katsuhiko Suzuki, Ryoko Senda, Maria Luisa Tejeda, Marc-Alban Millet and Dieter Korn for their assistance with fieldwork during my PhD. In particular I would like to thank Director. Katz Suzuki for supervising me during my research in Japan. I would like to thank Jindirch Hladil, Emilia Jarochowska, Jiri Fryda, Ladislav Slavik and David Loydell for their tireless efforts in providing me with enough samples to make my study of the Silurian possible. To that extent I would also like to thank Philip Pogge von Strandmann for his help and expertise in both analysing and interpreting lithium isotope data.

Finally, I would like to thank The Japanese Society for the Promotion of Science, the Geological Society of London, the College of St. Hild & St. Bede (John Simpson Greenwell memorial fund) and Prof. David Selby for helping to fund my research. Without their money, none of this research would have been possible.

Contents

Abstract 2

Declaration 3

Acknowledgements 4

Chapter 1 10

1.1 The ^{187}Os/^{188}Os of contemporary seawater 13

1.1.1 Osmium isotopes in macroalgae 14

1.1.2 Osmium isotopes in Iceland 15

1.1.3 Osmium isotopes in Japan 16

1.2 The ^{187}Os/^{188}Os of seawater during the Silurian 18

1.2.1 Climatic change during the Silurian 18

1.2.2 Application of the Re-Os system to the Silurian 20

1.2.3 Application of the Lithium isotope system to the Silurian 21

1.3 References 22

Chapter 2 28

2.1 Introduction 30

2.2 Field and analytical techniques 33

2.2.1 Sampling and storage 34

2.2.2 Macroalgae species and habitats 35

2.2.3 Re-Os analysis 36

2.2.3.1 Macroalgae 37

2.2.3.2 Bed load 37

2.2.3.3 Seawater 38

2.2.3.4 Mass Spectrometry 38

2.2.4 Statistical tests 39

2.3 Results 40

2.3.1 Macroalgae 40

2.3.2 Bed load 42

2.3.3 Dissolved load 44

2.3.4 Partition coefficient 46

2.4 Discussion 47

2.4.1 Biological and environmental controls on Re and Os uptake in macroalgae 47

2.4.2 Environmental controls on the ^{187}Os/^{188}Os of macroalgae 52

2.4.2.1 Influence of estuarine conditions on the ^{187}Os/^{188}Os of macroalgae 52
2.4.2.2 Influence of basaltic weathering on the ^{187}Os/^{188}Os of macroalgae 54
2.4.3 Biological and environmental controls on ^{187}Re/^{188}Os of macroalgae 57
2.5 Implications and future outlook 60
2.6 References 62
Chapter 3 66
3.1 Introduction 67
3.2 Field and analytical techniques 71
3.2.1 Sampling and storage 71
3.2.2 Macroalgae species and habitats 73
3.2.3 Re-Os analysis 73
3.2.3.1 Macroalgae 73
3.2.3.2 Mass Spectrometry 74
3.3 Results 74
3.3.1 Hokkaido and Northern Honshu 76
3.3.2 Tokyo Bay 78
3.3.3 Osaka Bay 79
3.3.4 Ise and Mikawa Bay 80
3.3.5 Izu Peninsula 82
3.3.6 Noto Peninsula 83
3.4 Discussion 85
3.4.1 Biological and environmental controls on the ^{187}Re/^{188}Os of macroalgae 86
3.4.2 Natural sources of osmium to macroalgae 88
3.4.3 Anthropogenic sources of osmium to macroalgae 92
3.4.4 Anthropogenic influence on the global osmium cycle 99
3.4.4.1 Anthropogenic impact on Japanese coastal waters 99
3.4.4.2 Anthropogenic contributions of osmium from Japan 100
3.4.4.3 Impact of anthropogenic osmium on surface waters 101
3.5 Implications and future outlook 102
3.6 References 104
Chapter 4 111
4.1 Introduction 112
4.2 Materials and methods 116
4.2.1 Geological setting 116

4.2.1.1 Aizpute core 117
4.2.1.2 Lusklint & Lickershamn 117
4.2.1.3 Bartoszyce 118
4.2.1.4 Hunninge core 118
4.2.1.5 Kosov 118
4.2.1.6 Klonk core 119
4.2.2 Sample preparation 119
4.2.3 Osmium isotope analysis of shales 120
4.2.4 Lithium isotope analysis of bulk carbonates 121
4.2.5 Isotope modeling 123
4.2.5.1 Osmium isotope modeling 123
4.2.5.2 Lithium isotope modeling 124
4.3 Results 126
4.3.1 Rhenium-osmium isotope data 126
4.3.1.1 Aizpute-41 Core 129
4.3.1.2 Bartoszyce Core 130
4.3.1.3 Kosov section 131
4.3.1.4 Klonk Core 133
4.3.2 Lithium isotope and trace metal data 134
4.3.2.1 Lusklint section 135
4.3.2.2 Lickershamn section 136
4.3.2.3 Hunninge-1 drillcore 138
4.3.2.4 Kosov section 139
4.4 Discussion 139
4.4.1 Isotopic constraints on Silurian seawater chemistry 141
4.4.1.1 Climatically induced changes in ocean circulation 141
4.4.1.2 Flood Basalt Volcanism 145
4.4.1.3 Temperature-weathering feedbacks 146
4.4.1.4 Hydrothermal activity 147
4.4.1.5 Glaciation 149
4.4.2 Scenarios for triggering Silurian Glaciations 156
4.4.2.1 Orogeny 157
4.4.2.2 Land plant diversification 157
4.4.2.3 Volcanic arc degassing 158

4.4.2.4 Paleogeography 159
4.4.2.5 Orbital forcing 159
4.4.2.6 Why did we not see 'Snowball Earth' conditions during the Silurian? 160
4.4.3 Weathering feedbacks help regulate atmospheric CO_2 161
4.5 Implications and future outlook 164
4.6 References 166
Chapter 5 178
5.1 Re-Os isotope uptake and distribution in macroalgae 179
5.2 Re-Os isotopes in macroalgae as a tracer of Earth system processes 180
5.3 Re-Os isotopes in macroalgae as a tracer of anthropogenic processes 181
5.4 The Os and Li isotopic composition of Silurian seawater 182
5.6 Future outlook 183
5.7 References 185

Chapter 1

Introduction

Temporal and spatial variations in the isotopic composition of seawater reflect the effects of fluctuation in Earth system processes on ocean chemistry. Many radiogenic isotope systems in seawater are sensitive to variations in continental weathering and erosion, making them a powerful archive for reconstructing responses to climatic or tectonic change, with silicate weathering receiving special attention due its perceived control on atmospheric CO_2 over geological timescales (Berner et al., 1983; Walker et al., 1981). Of these radiogenic systems, the rubidium-strontium (^{87}Rb-^{86}Sr) radiogenic isotope system has been the most widely used, with variations in the marine ^{87}Sr/^{86}Sr record reflecting fluctuations in continental inputs caused by orogenesis (Raymo et al., 1988) and glaciations (Armstrong, 1971). However, as a consequence of the long residence time of Sr in the oceans (2 - 4 Myr) short-term fluctuations in inputs are hard to detect (Richter and Turekian, 1993).

The osmium isotopic composition of seawater (^{187}Os/^{188}Os) reflects a balance between radiogenic continental sources and unradiogenic mantle and extraterrestrial derived sources (Peucker-Ehrenbrink and Ravizza, 2000). Therefore, much like Sr isotopes, Os isotopes have been utilised to infer information about past changes in continental weathering (See Peucker-Ehrenbrink and Ravizza, 2012). However, unlike Sr, the residence time of Os in the ocean (1-50 kyr) is sufficiently short to respond to short-periodic fluctuations in input, whilst still being long enough to attain a global signal (Levasseur et al., 1999; Oxburgh, 2001; Rooney et al., 2016). Therefore, the ^{187}Os/^{188}Os composition of seawater offers the ability to distinguish between high-frequency climatic and low frequency tectonic forcing (Peucker-Ehrenbrink and Ravizza, 2000). This has allowed us to unlock vital information about a series of Earth system processes in the Earth's geological past such as: flood basalt volcanism (Cohen and Coe, 2002; Du Vivier et al., 2014; Ravizza and Peucker-Ehrenbrink, 2003; Turgeon and Creaser, 2008); paleoweathering (Finlay et al., 2010; Ravizza et al., 2001; Schmitz et al., 2004) basin connectivity (Poirier and Hillaire-

Marcel, 2009); and, bolide impacts (Paquay et al., 2008). However, despite three decades of work, there still remains a great dearth of data $^{187}Os/^{188}Os$ for pre-Cenozoic time (See Peucker-Ehrenbrink and Ravizza, 2012). In part, this study looks to correct this by determining the $^{187}Os/^{188}Os$ of seawater for the Silurian.

In the modern ocean, the $^{187}Os/^{188}Os$ composition of seawater has been reasonably well constrained through direct analysis using ultra-low blank techniques capable of oxidising all osmium to a common oxidation state (Chen and Sharma, 2009; Gannoun and Burton, 2014; Levasseur et al., 1998; Paul et al., 2009). Nevertheless, direct analysis of seawater remains analytically challenging due to the low concentrations (Peucker-Ehrenbrink et al., 2013), and measurements of rivers, estuaries and coastal waters are therefore sparse (Gannoun et al., 2006; Huh et al., 2004; Sharma et al., 2007; Sharma and Wasserburg, 1997; Turekian et al., 2007). The composition of the global riverine inputs therefore remains poorly constrained, raising the possibility that the osmium input into the ocean could be underestimated by a factor of ~3 (Oxburgh, 2001). This may have led to a discrepancy between oceanic osmium residence times estimated from mass balance calculations (35 - 50 kyr) and those inferred from the evolution (1 - 4 kyr) of the osmium isotope record (Levasseur et al., 1999; Oxburgh, 2001; Rooney et al., 2016; Sharma et al., 1999).

Recent work suggests macroalgae concentrates Os (with abundances that vary from 12.6 to 78.5 ppt), whilst maintaining the $^{187}Os/^{188}Os$ composition of the seawater it inhabits (Racionero-Gómez et al., 2016; Racionero-Gómez et al., 2017). This suggests that macroalgae could act as a proxy for the $^{187}Os/^{188}Os$ composition of local waters whilst removing some of the analytical challenges associated with direct analysis of seawater i.e. ultra-low concentrations and multiple oxidation states. Macroalgae existing in coastal waters, therefore, should record an ^{187}Os/^{188}Os signature that reflects a balance of local inputs, including riverine input, local bedrock, anthropogenic activity and seawater.

In this body of work we will apply the macroalgae-Os-seawater proxy to real world settings to test its ability to record Earth system processes during the present. In Chapter 2 we will utilise macroalgae collected from Icelandic coastal waters to trace fluctuations in the ^{187}Os/^{188}Os of freshwater and seawater around Iceland, and determine the influence of basaltic weathering on the global osmium budget. In Chapter 3 we will utilise macroalgae from Japanese coastal waters to help constrain the anthropogenic influence on the global Os cycle. Finally, in Chapter 4 we will utilise the Re-Os isotope systematics of shales to determine fluctuations in the ^{187}Os/^{188}Os of seawater during the Silurian, and shed light on the mechanisms behind abrupt climatic change during this time.

1.1 The ^{187}Os/^{188}Os of contemporary seawater

Osmium is among the least abundant elements in seawater, therefore early attempts to analyse the concentration and isotopic composition of seawater directly were plagued with difficulties. Koide et al. (1996) used a 25 L sample of seawater spiked with a ^{190}Os tracer, separating Os with anion-exchange chromatography and them purifying it using distillation techniques. Sharma et al. (1997) reduced seawater and tracer Os by bubbling SO_2(g) and then co-precipitating Os with iron oxyhydroxide in 4-10 L samples. The problem with these techniques is that they require handling a large volume of sample. Three subsequent techniques attempted to use smaller volumes of sample (50 g to 1.5 kg), and tried to equilibrate tracer and water Os by oxidising it to a common oxidation state (OsO_4). However, Chen and Sharma (2009) discovered that each of these methods did not yield identical concentrations to those of Woodhouse et al. (1999). They found higher temperatures (300°C) were required to oxidise all species of Os present in seawater. With a reliable chemical separation technique in hand it has become possible to measure Os, although still analytical challenging, with as little as 20g of seawater (Sharma et al., 2012).

Despite this capability, problems still arise from the nature of Os in seawater. Extremely low concentrations of Os in seawater i.e. 90fg in 100ml of seawater, means you get significant interference from procedural blanks of ~3.6fg (Chen and Sharma, 2009). This is compounded by contamination from the use of polyethylene bottles for seawater storage (Sharma et al, 2012). We propose to develop a new proxy for the Os isotopic composition of seawater based on Os measurements of macroalgae, which does not suffer from these problems i.e. Os concentrations in seaweed are >50 pg/g and therefore far higher than the procedural blank (~50 fg), whilst the long term storage of seaweed does not suffer from the storage techniques used.

1.1.1 Osmium isotopes in macroalgae

Work conducted by B. Racionero-Gómez and myself at the University of Durham looked into the biological uptake of Re (Racionero-Gómez et al., 2016) and Os (Racionero Gomez et al., 2017) into macroalgae. These studies utilised a single macroalgae species, *Fucus vesiculosus*, and analysed its Re and Os abundance and uptake, as well as assessing if it could record the Os isotope composition of the seawater in which it lived. It was demonstrated that Os and Re are not located in one specific biological structure, but found throughout the organism. Osmium uptake was determined by culturing *F. vesiculosus* with different concentrations of Os with a known $^{187}Os/^{188}Os$ composition (~0.16). The cultured samples took on the isotopic composition of the culture in which they lived, which is significantly different to the background composition of un-doped seawater (~0.94) (Fig. 1). This suggests macroalgae can attain the isotopic composition of seawater, and therefore could potentially act as a proxy for understanding a variety of Earth system processes.

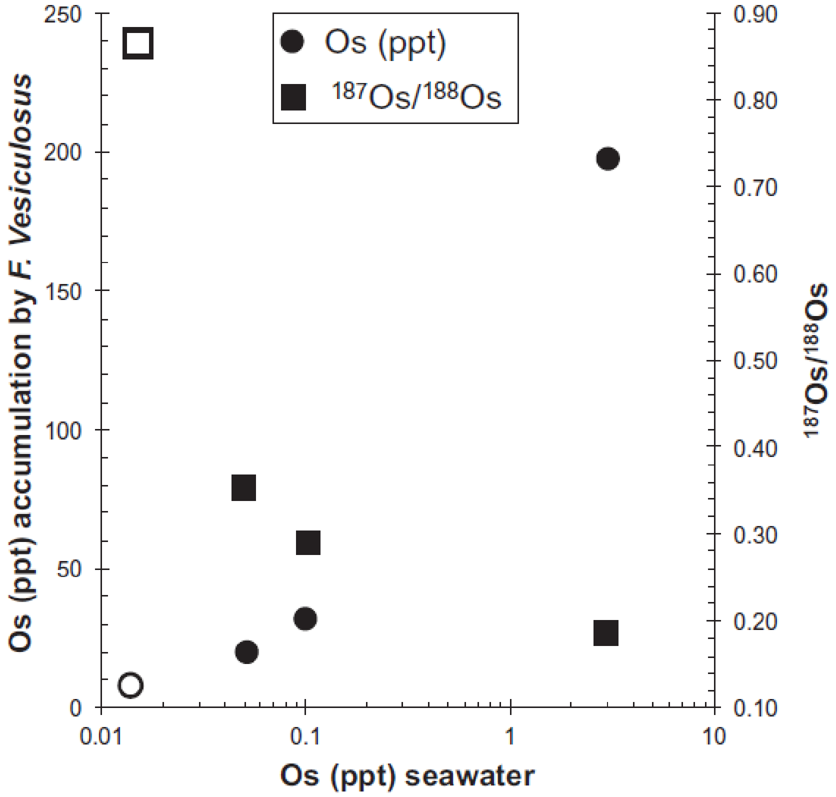

Fig. 1. Osmium (ppt) accumulation (circles) and $^{187}Os/^{188}Os$ compositions (squares) in F. versiculosus under different culture media Os abundances. See Racionero-Gómez et al. (2017) for more details.

1.1.2 Osmium isotopes in Iceland

Iceland consists of an essentially monolithological basaltic terrain of varying ages (historic to 12 Ma), yielding a large range in the $^{187}Os/^{188}Os$ (0.15 to 1.04) of riverine dissolved loads (Gannoun et al., 2006). Unradiogenic $^{187}Os/^{188}Os$ values can be explained by congruent basalt weathering and/or hydrothermal input, with radiogenic $^{187}Os/^{188}Os$ values arising from two distinct processes: the $^{187}Os/^{188}Os$ of glacier-fed rivers can be explained by the entrainment of seawater aerosols into precipitation and subsequent glacial melting; while the $^{187}Os/^{188}Os$ composition of direct-runoff and spring-fed rivers can be explained by the incongruent weathering of certain primary basaltic minerals that possess exceptionally high

^{187}Re/^{188}Os, which over time evolves to radiogenic ^{187}Os/^{188}Os values (Gannoun et al., 2004).

The chemistry of macroalgae from shallow coastal waters is dominated by the brackish conditions in which it lives. Macroalgae therefore come in contact with both fresh water and seawater sources through a single tidal cycle, and in theory, the ^{187}Os/^{188}Os composition of macroalgae should represent a mixing between the ^{187}Os/^{188}Os composition of these two sources. In Iceland, as previously explained, the ^{187}Os/^{188}Os composition of riverine inputs will be highly variable, ranging from unradiogenic values near the central rift zone, through to highly radiogenic values in the outer parts of Iceland. This diverse range of ^{187}Os/^{188}Os compositions makes Iceland a unique environment with which to test the ability of macroalgae to record the ^{187}Os/^{188}Os composition of the seawater it inhabits.

Chapter 2 presents Re-Os abundance and isotope data for macroalgae and dissolved and bed loads from coastal waters and rivers draining basaltic watersheds of Iceland. This represents the first examination of the influence of both seawater and river water osmium on the ^{187}Os/^{188}Os composition of macroalgae and demonstrates the ability of macroalgae to trace fluctuations in the ^{187}Os/^{188}Os of freshwater and seawater around Iceland. Chapter 2 utilises this to determine the influence of basaltic weathering on the global osmium budget.

1.1.3 Osmium isotopes in Japan

The present-day open ocean seawater ^{187}Os/^{188}Os value of ~1.06 reflects the balance between unradiogenic mantle-derived Os and radiogenic continental Os (Peucker-Ehrenbrink, & Ravizza, 2000). Dissolution of background extraterrestrial matter contributes little to the unradiogenic sources of Os. On the other hand, Os released by anthropogenic activities has been detected in coastal sediments, lakes and estuaries from sources such as sewage sludge, catalytic convertors, and use as a staining reagent in biomedical research

(Esser and Turekian, 1993; Rauch et al., 2004; Ravizza and Bothner, 1996; Turekian et al., 2007; Williams et al., 1997). Atmospheric anthropogenic Os attributed to the smelting of various ores and catalytic convertors, has also been detected in rain and snow, which is impacting Os in oceanic surface waters and therefore the global Os budget (Chen et al., 2009). These anthropogenic sources are generally characterized by unradiogenic ^{187}Os/^{188}Os compositions (~0.12) related to the isotopic composition of PGEs refined for human use.

Japan offers a unique place in which to study the influence of anthropogenic processes on regional variations in the marine Os cycle. Large, densely populated, sprawling metropolitan areas often fall in close proximity to coastal waters, inlet seas or bays. Waters in these regions are likely to be dominated by unradiogenic Os produced by sewage treatment plants, hospitals, refineries and vehicle exhaust. Moreover, these metropolitan areas are often juxtaposed to sparsely populated rural and/or mountainous regions, with little human activity and therefore anthropogenic influence. The ^{187}Os/^{188}Os composition of coastal waters in these regions is therefore likely to be dominated by natural sources of Os. In particular, Japanese river catchments are dominated by the weathering of Miocene-Holocene volcanic and sedimentary rocks of radiogenic ^{187}Os/^{188}Os compositions. As previously explained, the ^{187}Os/^{188}Os composition of macroalgae from coastal waters likely represents a mixing between the ^{187}Os/^{188}Os composition of seawater and local freshwaters inputs. Macroalgae from densely populated regions of Japan will therefore likely show a strong influence from highly unradiogenic PGE ^{187}Os/^{188}Os values derived from local human activity. Meanwhile, the ^{187}Os/^{188}Os composition of macroalgae from more sparsely populated regions will show a stronger influence from natural freshwater sources.

Chapter 3 presents Re-Os abundance and isotope data for macroalgae from Tokyo Bay, Osaka Bay, Ise Bay, Mikawa Bay, Izu Peninsula, Noto Peninsula, Hokkaido and northern Honshu. Tokyo Bay, Osaka Bay and Ise/Mikawa Bay lie in close proximity to the densely populated Kanto (Tokyo-Yokohama), Keihanshin (Osaka-Kobe) and Chukyo (Nagoya) metropolitan areas. The ^{187}Os/^{188}Os signature from these regions is much lower than expected for natural river and oceanic systems, but similar to the isotope composition of PGE ores. This suggests that human activity has influenced the Os isotopic composition of macroalgae, and therefore seawater, through the burning of municipal and/or hospital waste, processing of sewage and the extensive use of automobiles in these areas. The Izu Peninsula, Noto Peninsula, Hokkaido and northern Honshu exhibit ^{187}Os/^{188}Os values similar to global river water or Pacific seawater measurements, suggesting little influence from human activity. These results demonstrate the ability of macroalgae to trace fluctuations in the ^{187}Os/^{188}Os of freshwater and seawater around Japan, and utilise this to determine the influence of human activity on the global osmium budget.

1.2 The ^{187}Os/^{188}Os of seawater during the Silurian

1.2.1 Climatic change during the Silurian

In contrast to previous views that the Silurian was an environmentally stable period between the Ordovician icehouse and the Devonian greenhouse (Munnecke et al., 2010), it has more recently become apparent that the Silurian is characterised by a highly dynamic climate attenuated by multiple short-lived events, strong eustatic sea level change and oceanic turnover associated with extinction events after a recovery from the end-Ordovician glaciation (Calner, 2008; Melchin et al., 2012). The carbon isotopic composition of carbonate ($\delta^{13}C_{carb}$) through the Silurian is highly variable, indicating the climate system and carbon cycle were probably more unstable than any other Phanerozoic period and can be regarded as one of the most volatile periods when considering the ocean-atmosphere system (Cramer and Saltzman, 2005).

The Silurian through to the early Devonian is marked by four large-amplitude positive carbon and oxygen isotope excursions, with the $\delta^{13}C_{carb}$ exceeding +5 ‰ during the Ireviken, Mulde, Lau and Klonk bioevents. The Lau carbon isotope excursion (> +8 ‰) is probably the largest post Cambrian $\delta^{13}C_{carb}$ excursion of the entire Phanerozoic. Such excursions are far larger than anything in the Mesozoic or Cenozoic, and therefore any classical interpretations concerning productivity changes are not viable (Bickert et al., 1997). The $\delta^{13}C_{carb}$ isotope excursions are associated with significant positive oxygen isotope ($\delta^{18}O$) excursions of approximately 1 - 3.5 ‰ magnitude (Lehnert et al., 2010; Munnecke et al., 2010; Žigaitė et al., 2010), which are too large to be explained by either temperature, ice volume or salinity alone (Bickert et al., 1997). However, despite these discoveries and over two decades of research, the cause of these climate perturbations is still not understood.

Traditional explanations for these events have invoked a shift between two stable oceanic-climate states, driven by changes in the location of deep-water formation from high to low latitudes (Jeppsson, 1990), or global precipitation rates and continental runoff (Bickert et al., 1997). However, these early attempts to explain Silurian climatic events have received much criticism (Johnson, 2006; Kaljo et al., 2003; Loydell, 1998). More recently it has been postulated that Silurian climatic change could have been driven by glacial expansion over Gondwana, inferred in part from positive oxygen isotope shifts (Trotter et al., 2016) coupled to significant eustatic sea-level change (Díaz-Martínez and Grahn, 2007; Lehnert et al., 2010), much like the Late Ordovician that preceded it (Algeo et al., 2016; Harper et al., 2014). However, the lack of glacial sediments in the stratigraphic record for much of the Silurian (post-Wenlock) has hampered this notion (Caputo, 1998; Díaz-Martínez and Grahn, 2007; Grahn and Caputo, 1992).

1.2.2 Application of the Re-Os system to the Silurian

To shed light on the possible mechanisms behind these abrupt climate perturbations, we have applied the Re-Os isotope system to organic rich shales from geological formations that span the Ireviken, Mulde, Lau and Klonk bioevents. The $^{187}Os/^{188}Os$ of organic rich shales mimics that of seawater at the time of deposition, and reflects a balance between radiogenic continental sources and unradiogenic mantle and extraterrestrial derived sources (Peucker-Ehrenbrink and Ravizza, 2000). Therefore, much like Sr isotopes, Os isotopes have been utilised to infer information about past changes in continental weathering. However, unlike Sr, the residence time of Os in the ocean is sufficiently short to respond to short-periodic fluctuations in input, whilst still being long enough to attain a global signal (Levasseur et al, 1998; Oxburgh, 2001). Therefore, the Os isotope system offers the ability to distinguish between high-frequency climatic and low frequency tectonic forcing (Peucker-Ehrenbrink and Ravizza, 2000).

In Chapter 4 osmium isotope profiles for the Ireviken, Mulde, Lau and Klonk bioevents are presented. These profiles are similar to the Hirnantian glaciation (Finlay et al., 2010), which occurred some 10 Myr prior to the Ireviken Event. The $^{187}Os/^{188}Os$ profiles are related to the weathering of organic-rich sedimentary rocks during the expansion of continental ice over Gondwana, which delivers radiogenic Os to the ocean. This work suggests climatic perturbations during the Silurian are related to glaciations triggered by declining atmospheric CO_2 and temperatures. Once the glaciation was triggered, enhanced oxidative weathering of organic and sulphide rich sedimentary rocks led to a release in CO_2 to the atmosphere which helped reverse global cooling.

1.2.3 Application of the Lithium isotope system to the Silurian

As previously explained, variations in Os isotopes can also be controlled by factors other than continental weathering, such as fluctuations in hydrothermal alteration of juvenile basaltic crust and extra-terrestrial inputs (Peucker-Ehrenbrink and Ravizza, 2000). To test the validity of our Os isotope curves as tracers of continental weathering, we also utilised other continental weathering proxies. The Li isotopic composition of seawater (δ^7Li) reflects a balance between the inputs of Li from rivers (weathering of continental silicate rocks) and mid-ocean ridge spreading centres (weathering of oceanic silicate rocks) and the outputs of Li from the incorporation into marine sediments and altered oceanic crust (Misra and Froelich, 2012). The δ^7Li of carbonates is seen to reflect the δ^7Li of seawater through time, and has been used to reconstruct continental silicate weathering rates in the geological past (Misra and Froelich, 2012). Recently, Pogge von Strandmann et al. (in review) utilised Li isotope measurements in carbonates and shales that span the Hirnantian glaciation. A peak in δ^7Li occurs during the trough in Os isotopes (Finlay et al., 2010) associated with glacial maximum. This shows a strong decline in silicate weathering, reducing the effect of the Earth's primary CO_2 removal mechanism, preventing further cooling and allowing temperatures to build-up, leading to deglaciation.

To test the hypothesis in section 1.2.2 we generated Li isotope records in carbonates from sections spanning the Ireviken, Mulde, Lau and Klonk bioevents (See Chapter 4). Lithium isotope records show a similar profile to the Hirnantian glaciation suggesting suppression in continental silicate weathering under enhanced continental ice sheets. This reduces one of the Earth's major CO_2 withdrawal mechanisms, and when combined with enhanced oxidative weathering, leads to greater levels of atmospheric CO_2. This study suggests that the Earth has a stabilising negative feedback mechanism in which a reduction in atmospheric CO_2 and global temperatures which leads to enhanced continental ice is ultimately reversed by weathering processes which act to increase atmospheric CO_2 and temperatures, preventing a runaway icehouse.

1.3 References

Algeo, T.J., Marenco, P.J., Saltzman, M.R., 2016. Co-evolution of oceans, climate, and the biosphere during the 'Ordovician Revolution': A review. Palaeogeography, Palaeoclimatology, Palaeoecology 458, 1-11.

Armstrong, R.L., 1971. Glacial erosion and the variable isotopic composition of strontium in sea water. Nature 230, 132-133.

Berner, R.A., Lasaga, A.C., Garrels, R.M., 1983. The carbonate-silicate geochemical cycle and its effect on atmospheric carbon dioxide over the past 100 million years. Am J Sci 283, 641-683.

Bickert, T., Pätzold, J., Samtleben, C., Munnecke, A., 1997. Paleoenvironmental changes in the Silurian indicated by stable isotopes in brachiopod shells from Gotland, Sweden. Geochimica et Cosmochimica Acta 61, 2717-2730.

Calner, M., 2008. Silurian global events – at the tipping point of climate change, Mass Extinction. Springer Berlin Heidelberg, pp. 21-57.

Caputo, M.V., 1998. Ordovician–Silurian glaciations and global sea-level changes. Silurian cycles, 15-25.

Chen, C., Sedwick, P.N., Sharma, M., 2009. Anthropogenic osmium in rain and snow reveals global-scale atmospheric contamination. Proceedings of the National Academy of Sciences of the United States of America 106, 7724-7728.

Chen, C., Sharma, M., 2009. High precision and high sensitivity measurements of osmium in seawater. Analytical chemistry 81, 5400-5406.

Cohen, A.S., Coe, A.L., 2002. New geochemical evidence for the onset of volcanism in the Central Atlantic magmatic province and environmental change at the Triassic-Jurassic boundary. Geology 30, 267.

Cramer, B.D., Saltzman, M.R., 2005. Sequestration of 12C in the deep ocean during the early Wenlock (Silurian) positive carbon isotope excursion. Palaeogeography, Palaeoclimatology, Palaeoecology 219, 333-349.

Díaz-Martínez, E., Grahn, Y., 2007. Early Silurian glaciation along the western margin of Gondwana (Peru, Bolivia and northern Argentina): Palaeogeographic and geodynamic setting. Palaeogeography, Palaeoclimatology, Palaeoecology 245, 62-81.

Du Vivier, A.D.C., Selby, D., Sageman, B.B., Jarvis, I., Gröcke, D.R., Voigt, S., 2014. Marine 187Os/188Os isotope stratigraphy reveals the interaction of volcanism and ocean circulation during Oceanic Anoxic Event 2. Earth and Planetary Science Letters 389, 23-33.

Esser, B.K., Turekian, K.K., 1993. Anthropogenic osmium in coastal deposits. Environmental science & technology 27, 2719-2724.

Finlay, A.J., Selby, D., Gröcke, D.R., 2010. Tracking the Hirnantian glaciation using Os isotopes. Earth and Planetary Science Letters 293, 339-348.

Gannoun, A., Burton, K., 2014. High precision osmium elemental and isotope measurements of North Atlantic seawater. JAAS.

Gannoun, A., Burton, K.W., Thomas, L.E., Parkinson, I.J., van Calsteren, P., Schiano, P., 2004. Osmium isotope heterogeneity in the constituent phases of mid-ocean ridge basalts. Science 303, 70-72.

Gannoun, A., Burton, K.W., Vigier, N., Gíslason, S.R., Rogers, N., Mokadem, F., Sigfússon, B., 2006. The influence of weathering process on riverine osmium isotopes in a basaltic terrain. Earth and Planetary Science Letters 243, 732-748.

Grahn, Y., Caputo, M.V., 1992. Early Silurian glaciations in Brazil. Palaeogeography, Palaeoclimatology, Palaeoecology 99, 9-15.

Harper, D.A.T., Hammarlund, E.U., Rasmussen, C.M.Ø., 2014. End Ordovician extinctions: A coincidence of causes. Gondwana Research 25, 1294-1307.

Huh, Y., Birck, J.-L., Allègre, C.J., 2004. Osmium isotope geochemistry in the Mackenzie River basin. Earth and Planetary Science Letters 222, 115-129.

Jeppsson, L., 1990. An oceanic model for lithological and faunal changes tested on the Silurian record. Journal of the Geological Society 147, 663-674.

Johnson, M.E., 2006. Relationship of Silurian sea-level fluctuations to oceanic episodes and events. GFF 128, 115-121.

Kaljo, D., Martma, T., Männik, P., Viira, V., 2003. Implications of Gondwana glaciations in the Baltic late Ordovician and Silurian and a carbon isotopic test of environmental cyclicity. Bulletin de la Société géologique de France 174, 59-66.

Koide, M., Goldberg, E.D., Walker, R., 1996. The analysis of seawater osmium. Deep Sea Research Part II: Topical Studies in Oceanography 43, 53-55.

Lehnert, O., Männik, P., Joachimski, M.M., Calner, M., Frýda, J., 2010. Palaeoclimate perturbations before the Sheinwoodian glaciation: A trigger for extinctions during the 'Ireviken Event'. Palaeogeography, Palaeoclimatology, Palaeoecology 296, 320-331.

Levasseur, S., Birck, J.-L., Allegre, C., 1999. The osmium riverine flux and the oceanic mass balance of osmium. Earth and Planetary Science Letters 174, 7-23.

Levasseur, S., Birck, J.-L., Allègre, C.J., 1998. Direct measurement of femtomoles of osmium and the 187Os/186Os ratio in seawater. Science 282, 272-274.

Loydell, D.K., 1998. Early Silurian sea-level changes. Geological Magazine 135, 447-471.

Melchin, M.J., Sadler, P.M., Cramer, B.D., Cooper, R.A., Gradstein, F.M., Hammer, O., 2012. Chapter 21 - The Silurian Period, in: Gradstein, F.M., Ogg, J.G., Schmitz, M.D., Ogg, G.M. (Eds.), The Geologic Time Scale. Elsevier, Boston, pp. 525-558.

Misra, S., Froelich, P.N., 2012. Lithium isotope history of Cenozoic seawater: changes in silicate weathering and reverse weathering. Science 335, 818-823.

Munnecke, A., Calner, M., Harper, D.A.T., Servais, T., 2010. Ordovician and Silurian sea–water chemistry, sea level, and climate: A synopsis. Palaeogeography, Palaeoclimatology, Palaeoecology 296, 389-413.

Oxburgh, R., 2001. Residence time of osmium in the oceans. Geochemistry, Geophysics, Geosystems 2, 1018.

Paquay, F.S., Ravizza, G.E., Dalai, T.K., Peucker-Ehrenbrink, B., 2008. Determining chondritic impactor size from the marine osmium isotope record. Science 320, 214-218.

Paul, M., Reisberg, L., Vigier, N., 2009. A new method for analysis of osmium isotopes and concentrations in surface and subsurface water samples. Chemical Geology 258, 136-144.

Peucker-Ehrenbrink, B., Ravizza, G., 2000. The marine osmium isotope record. Terra Nova 12, 205-219.

Peucker-Ehrenbrink, B., Ravizza, G., 2012. Osmium Isotope Stratigraphy. 145-166.

Peucker-Ehrenbrink, B., Sharma, M., Reisberg, L., 2013. Recommendations for analysis of dissolved osmium in seawater. Eos, Transactions American Geophysical Union 94, 73-73.

Pogge von Strandmann, P.A.E., Desrochers, A., Murphy, M.J., Finlay, A.J., Selby, D., Lenton, T.M., in review. Global climate stabilisation by chemical weathering during the Hirnantian glaciation. Geochemical Perspectives Letters.

Poirier, A., Hillaire-Marcel, C., 2009. Os-isotope insights into major environmental changes of the Arctic Ocean during the Cenozoic. Geophysical Research Letters 36.

Racionero-Gómez, B., Sproson, A., Selby, D., Gröcke, D., Redden, H., Greenwell, H., 2016. Rhenium uptake and distribution in phaeophyceae macroalgae, Fucus vesiculosus. Royal Society Open Science 3, 160161.

Racionero-Gómez, B., Sproson, A.D., Selby, D., Gannoun, A., Gröcke, D.R., Greenwell, H.C., Burton, K.W., 2017. Osmium uptake, distribution, and 187Os/188Os and 187Re/188Os compositions in Phaeophyceae macroalgae, Fucus vesiculosus: Implications for determining the 187Os/188Os composition of seawater. Geochimica et Cosmochimica Acta 199, 48-57.

Rauch, S., Hemond, H.F., Peucker-Ehrenbrink, B., 2004. Recent changes in platinum group element concentrations and osmium isotopic composition in sediments from an urban lake. Environmental science & technology 38, 396-402.

Ravizza, G., Bothner, M.H., 1996. Osmium isotopes and silver as tracers of anthropogenic metals in sediments from Massachusetts and Cape Cod bays. Geochimica et Cosmochimica Acta 60, 2753-2763.

Ravizza, G., Norris, R.N., Blusztajn, J., Aubry, M.P., 2001. An osmium isotope excursion associated with the Late Paleocene thermal maximum: Evidence of intensified chemical weathering. Paleoceanography 16, 155-163.

Ravizza, G., Peucker-Ehrenbrink, B., 2003. Chemostratigraphic evidence of Deccan volcanism from the marine osmium isotope record. Science 302, 1392-1395.

Raymo, M.E., Ruddiman, W.F., Froelich, P.N., 1988. Influence of late Cenozoic mountain building on ocean geochemical cycles. Geology 16, 649-653.

Richter, F.M., Turekian, K.K., 1993. Simple models for the geochemical response of the ocean to climatic and tectonic forcing. Earth and Planetary Science Letters 119, 121-131.

Rooney, A.D., Selby, D., Lloyd, J.M., Roberts, D.H., Lückge, A., Sageman, B.B., Prouty, N.G., 2016. Tracking millennial-scale Holocene glacial advance and retreat using osmium isotopes: Insights from the Greenland ice sheet. Quaternary Science Reviews 138, 49-61.

Schmitz, B., Peucker-Ehrenbrink, B., Heilmann-Clausen, C., Åberg, G., Asaro, F., Lee, C.-T.A., 2004. Basaltic explosive volcanism, but no comet impact, at the Paleocene–Eocene boundary: high-resolution chemical and isotopic records from Egypt, Spain and Denmark. Earth and Planetary Science Letters 225, 1-17.

Sharma, M., Balakrishna, K., Hofmann, A.W., Shankar, R., 2007. The transport of Osmium and Strontium isotopes through a tropical estuary. Geochimica et Cosmochimica Acta 71, 4856-4867.

Sharma, M., Chen, C., Blazina, T., 2012. Osmium contamination of seawater samples stored in polyethylene bottles. Limnology and Oceanography: Methods 10, 618-630.

Sharma, M., Papanastassiou, D., Wasserburg, G., 1997. The concentration and isotopic composition of osmium in the oceans. Geochimica et Cosmochimica Acta 61, 3287-3299.

Sharma, M., Wasserburg, G., 1997. Osmium in the rivers. Geochimica et cosmochimica acta 61, 5411-5416.

Sharma, M., Wasserburg, G., Hofmann, A., Chakrapani, G., 1999. Himalayan uplift and osmium isotopes in oceans and rivers. Geochimica et Cosmochimica Acta 63, 4005-4012.

Trotter, J.A., Williams, I.S., Barnes, C.R., Männik, P., Simpson, A., 2016. New conodont δ18O records of Silurian climate change: Implications for environmental and biological events. Palaeogeography, Palaeoclimatology, Palaeoecology 443, 34-48.

Turekian, K.K., Sharma, M., Gordon, G.W., 2007. The behavior of natural and anthropogenic osmium in the Hudson River–Long Island Sound estuarine system. Geochimica et Cosmochimica Acta 71, 4135-4140.

Turgeon, S.C., Creaser, R.A., 2008. Cretaceous oceanic anoxic event 2 triggered by a massive magmatic episode. Nature 454, 323-326.

Walker, J.C.G., Hays, P.B., Kasting, J.F., 1981. A negative feedback mechanism for the long-term stabilization of Earth's surface temperature. Journal of Geophysical Research 86, 9776.

Williams, G., Marcantonio, F., Turekian, K.K., 1997. The behavior of natural and anthropogenic osmium in Long Island Sound, an urban estuary in the eastern US. Earth and planetary science letters 148, 341-347.

Woodhouse, O., Ravizza, G., Falkner, K.K., Statham, P., Peucker-Ehrenbrink, B., 1999. Osmium in seawater: vertical profiles of concentration and isotopic composition in the eastern Pacific Ocean. Earth and Planetary Science Letters 173, 223-233.

Žigaitė, Ž., Joachimski, M.M., Lehnert, O., Brazauskas, A., 2010. δ18O composition of conodont apatite indicates climatic cooling during the Middle Pridoli. Palaeogeography, Palaeoclimatology, Palaeoecology 294, 242-247.

Chapter 2

Tracing the influence of weathering processes on coastal waters surrounding a basaltic terrain using osmium isotopes in macroalgae*

*A version of this chapter will be submitted to Global Biogeochemical Cycles, co-authored with David Selby, Abdelmouchine Gannoun, Kevin W. Burton and Jeremy M. Lloyd.

This study presents rhenium (Re) and osmium (Os) abundance and isotope data for macroalgae, dissolved load and bedload from the Icelandic coastal waters, an environment adjacent to predominantly basaltic terrains, ranging in age from historic to ca. 12 Ma. Both the Re and Os abundance in macroalgae are shown to be primarily controlled by uptake from the dissolved load of local seawater. In a habitat with varying salinity through the tidal cycle, macroalgae Re and Os abundances vary, depending on the relative influence of local freshwater inputs. Incorporation of Re and Os into macroalgae is complicated by additional Re uptake from suspended particulates and/or bedload, which is not observed for Os, suggesting different uptake pathways for both Re and Os. The ^{187}Os/^{188}Os (0.16 to 0.99) and ^{187}Re/^{188}Os (~65 to 40,320) compositions of macroalgae are highly variable, and can be explained in terms of an unradiogenic ^{187}Os/^{188}Os contribution with low ^{187}Re/^{188}Os from rivers draining younger catchments that have undergone congruent basalt weathering (and/or hydrothermal input), and a radiogenic ^{187}Os/^{188}Os contribution from two distinct sources: rivers draining older catchments that have undergone incongruent weathering of primary basaltic minerals that possess exceptionally high ^{187}Re/^{188}Os ratios that have evolved to radiogenic ^{187}Os/^{188}Os ratios; and, North Atlantic seawater. Macroalgae can attain a ^{187}Re/^{188}Os far higher than that recorded for the Icelandic geochemical reservoirs due to the preferential uptake of Re over Os at high Re concentrations in the dissolved load, therefore macroalgae cannot be used to determine the ^{187}Re/^{188}Os of seawater. This study confirms the utility of macroalgae as a proxy for the Os isotopic composition of seawater, which holds the potential to elucidate a range of Earth system processes. However, it is not yet possible to directly relate the macroalgae Os concentration to that of the water in which they live. Finally, these results suggest that macroalgae is not a substantial sink for either Re or Os. Therefore, global macroalgae biomass, today or during the Earth's geological past, does not play a significant role in the marine Os and Re cycles.

2.1 Introduction

Temperature and atmospheric carbon dioxide (CO_2) have fluctuated widely throughout the Phanerozoic, from warm greenhouse to cold icehouse conditions. Nevertheless, throughout this time, temperature and CO_2 have always remained within the narrow limits that allow life to exist and evolve through the interaction between the atmosphere, hydrosphere, biosphere and lithosphere (Berner et al., 1983). Over geological timescales (Myr) temperature has partly been controlled by interactions between atmospheric CO_2 and continental weathering. Rising temperatures stimulate increased chemical weathering of silicate rocks drawing down CO_2 from the atmosphere, leading to a decline in temperature (Berner et al., 1983; Walker et al., 1981). Many radiogenic isotope systems in seawater are sensitive to variations in continental weathering and erosion, making ocean chemistry a powerful archive for reconstructing responses to climatic or tectonic change.

Of these, the rubidium-strontium (^{87}Rb-^{86}Sr) radiogenic isotope system has been the most widely used, with variations in the marine ^{87}Sr/^{86}Sr record reflecting fluctuations in continental inputs caused by orogenesis (Raymo et al., 1988) and glaciations (Armstrong, 1971). However, as a consequence of the long residence time of Sr in the oceans (2 - 4 Myr) short-term fluctuations in inputs are hard to detect (Richter and Turekian, 1993). The osmium isotopic composition of seawater (^{187}Os/^{188}Os) reflects a balance between radiogenic continental sources and unradiogenic mantle and extraterrestrial derived sources (Peucker-Ehrenbrink and Ravizza, 2000). Therefore, much like Sr isotopes, Os isotopes have been utilised to infer information about past changes in continental weathering (See Peucker-Ehrenbrink and Ravizza, 2012 and references therein). However, unlike Sr, the residence time of Os in the ocean (1-50 kyr) is sufficiently short to respond to short-periodic fluctuations in input, whilst still being long enough to attain a global signal (Levasseur et al., 1998; Oxburgh, 2001; Rooney et al., 2016). Therefore, the ^{187}Os/^{188}Os composition offers the ability to distinguish between high-frequency climatic and low frequency tectonic forcing (Peucker-Ehrenbrink and Ravizza, 2000).

In the modern ocean, the ^{187}Os/^{188}Os composition of seawater has been reasonably well constrained through direct analysis using ultra-low blank techniques capable of oxidising all osmium to a common oxidation state (Chen and Sharma, 2009; Gannoun and Burton, 2014; Levasseur et al., 1998; Paul et al., 2009). Nevertheless, direct analysis of seawater remains analytically challenging because of the low concentrations and multiple oxidation states (Peucker-Ehrenbrink et al., 2013), and measurements of rivers, estuaries and coastal waters are therefore sparse (Gannoun et al., 2006; Huh et al., 2004; Sharma et al., 2007; Sharma and Wasserburg, 1997; Turekian et al., 2007). Therefore the composition of the global riverine input remains poorly constrained, raising the possibility that the osmium input to the ocean is underestimated, thereby accounting for the discrepancy between oceanic osmium residence times estimated from mass balance calculations (35 - 50 kyr) and those inferred from the evolution of the osmium isotope record (1 - 4 kyr) (Levasseur et al., 1999; Oxburgh, 2001; Rooney et al., 2016; Sharma et al., 1999). Although it is also proposed that the difference in residence time estimates relates to the local removal of Os (Sharma et al., 2007).

Recent work indicates that macroalgae (seaweed) concentrates Os (with abundances that vary from 12.6 to 78.5 ppt), whilst maintaining the ^{187}Os/^{188}Os composition of the seawater it inhabits (Racionero-Gómez et al., 2017; Rooney et al., 2016). This suggests that macroalgae could act as a proxy for the ^{187}Os/^{188}Os composition of local waters whilst removing some of the analytical challenges associated with direct analysis of seawater i.e. ultra-low concentrations and multiple oxidation states. Macroalgae existing in coastal waters, therefore, should record an ^{187}Os/^{188}Os signature that reflects a balance of local inputs, including riverine input, local bedrock and seawater.

Iceland consists of an essentially monolithological basaltic terrain of varying ages (historic to 12 Ma), yielding a large range in the ^{187}Os/^{188}Os (0.15 to 1.04) of riverine dissolved loads (Gannoun et al., 2006). Unradiogenic ^{187}Os/^{188}Os values can be explained by congruent basalt weathering and/or hydrothermal input, with radiogenic ^{187}Os/^{188}Os values arising from two distinct processes. The ^{187}Os/^{188}Os of glacier-fed rivers can be explained by the entrainment of seawater aerosols into precipitation and subsequent glacial melting. The ^{187}Os/^{188}Os composition of direct-runoff and spring-fed rivers can be explained by the incongruent weathering of certain primary basaltic minerals that possess exceptionally high ^{187}Re/^{188}Os, which over time evolves to radiogenic ^{187}Os/^{188}Os values (Gannoun et al., 2004). Iceland therefore provides a unique environment with respect to ^{187}Os/^{188}Os in which to test the ability of macroalgae to record the ^{187}Os/^{188}Os composition of the seawater it inhabits.

This study presents Re-Os abundance and isotope data for macroalgae and dissolved and bed loads from coastal waters and rivers draining basaltic watersheds of Iceland. Given that watersheds of Iceland are essentially monolithological, their ^{187}Os/^{188}Os composition is determined by the age of basalt, the preferential weathering of constituent basalt minerals and the entrainment of rain, sea and hydrothermal waters (Gannoun et al., 2006). This study represents the first examination of the influence of both seawater and river water osmium on the ^{187}Os/^{188}Os composition of macroalgae. These results demonstrate the ability of macroalgae to trace fluctuations in the ^{187}Os/^{188}Os of freshwater and seawater around Iceland, and utilise this to determine the influence of basaltic weathering on the global osmium budget.

2.2 Field and analytical techniques

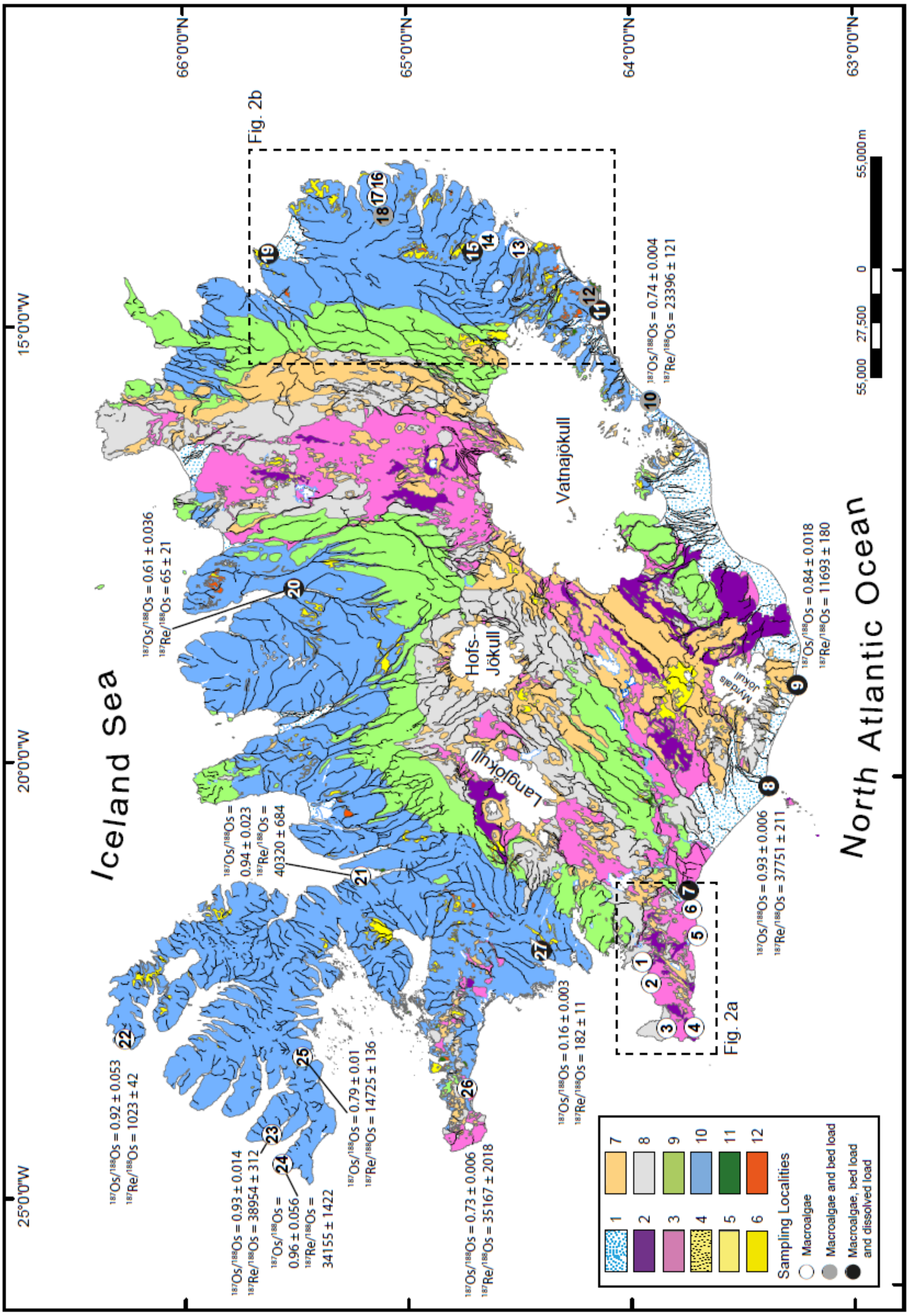

Fig. 1. Geological map of Iceland modified after Jóhannesson (2014): 1 = Holocene sediments; 2 = basic and intermediate lavas (postglacial, historic, younger than AD 871); 3 = basic and intermediate lavas (postglacial, prehistoric, older than AD 871); 4 = acid lavas (postglacial, historic, younger than AD 871); 5 = acid lavas (postglacial, prehistoric, older than AD 871); 6 = acid extrusives (Miocene, Pliocene and Pleistocene, older than 11,000 yrs); 7 = basic and intermediate hyaloclastite, pillow lava and associated sediments (Upper Pleistocene, younger than 0.8 myr); 8 = basic and intermediate interglacial and supraglacial lavas with intercalated sediments (Upper Pleistocene, younger than 0.8 myr); 9 = basic and intermediate extrusive rocks with intercalated sediments (Upper Pliocene and Lower Pleistocene, 0.8 - 3.3 myr); 10 = basic and intermediate extrusive rocks with intercalated sediments (Miocene and Lower Pliocene, older than 3.3 myr); 11 = basic and intermediate intrusions, gabbro, dolerite and diorite; 12 = acid intrusions, rhyolite, granophyre and granite. Sample type and localities are indicated in the legend. Dashed lines represent an outline of areas shown in Figures 2a and 2b.

2.2.1 Sampling and storage

Macroalgae, bedload sands and waters from the Icelandic coastline were sampled at eighteen locations during late August of 2014 (Fig. 1; samples 7-23 and 27). A further nine locations were sampled between late July and early August of 2015 (Fig. 1; samples 1-6 and 24-26). In total twenty-seven macroalgae, eleven bed load and eight water samples were collected (Fig. 1; Table 1 - 2). Macroalgae and bedload were washed using deionised (Milli-Q™) water to remove any attached sediment and salt. They were then dried for 12 h at 60 °C and stored in plastic zip-lock bags. Macroalgae and bed load were later crushed using an agate pestle and mortar prior to analysis. Water samples were filtered through 0.2 µm cellulose acetate filters using a pressurized Sartorius® Teflon unit. Filtrate aliquots were stored in pre-cleaned Savillex® Teflon bottles to prevent Os contamination (Sharma et al., 2012). Salinity was measured using a Hanna® HI 98192 conductivity meter.

2.2.2 Macroalgae species and habitats

Specific macroalgae species were not targeted during this study, and samples were selected based on their availability at sample sites. There was however a preference to brown macroalgae over green and red macroalgae due to their relatively high abundance in Re (Mas et al., 2005; Prouty et al., 2014; Racionero-Gómez et al., 2016; Yang, 1991) and Os (Racionero-Gómez et al., 2017; Rooney et al., 2016). Four species of brown macroalgae (*Fucus vesiculosus, Fucus spiralis, Fucus distichus* and *Ascophyllum nodosum*) were analysed.

Fig. 2. Geological maps of the Reykjanes Peninsula (**a**) and Eastern Fjords (**b**). Key is the same as in Figure 1.

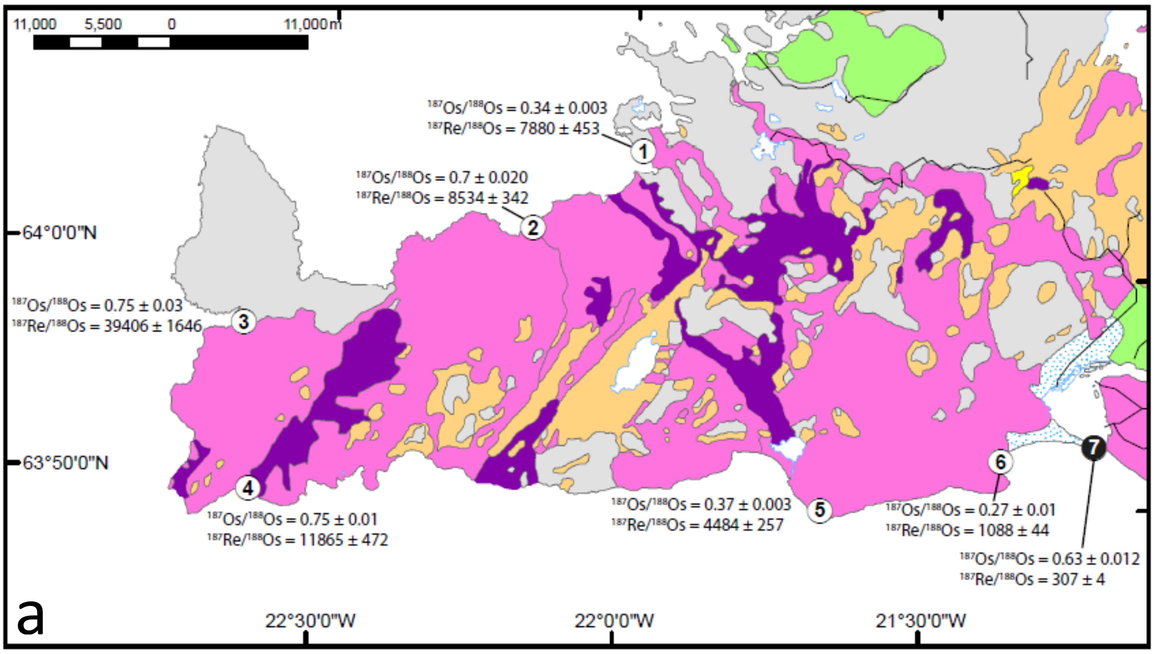

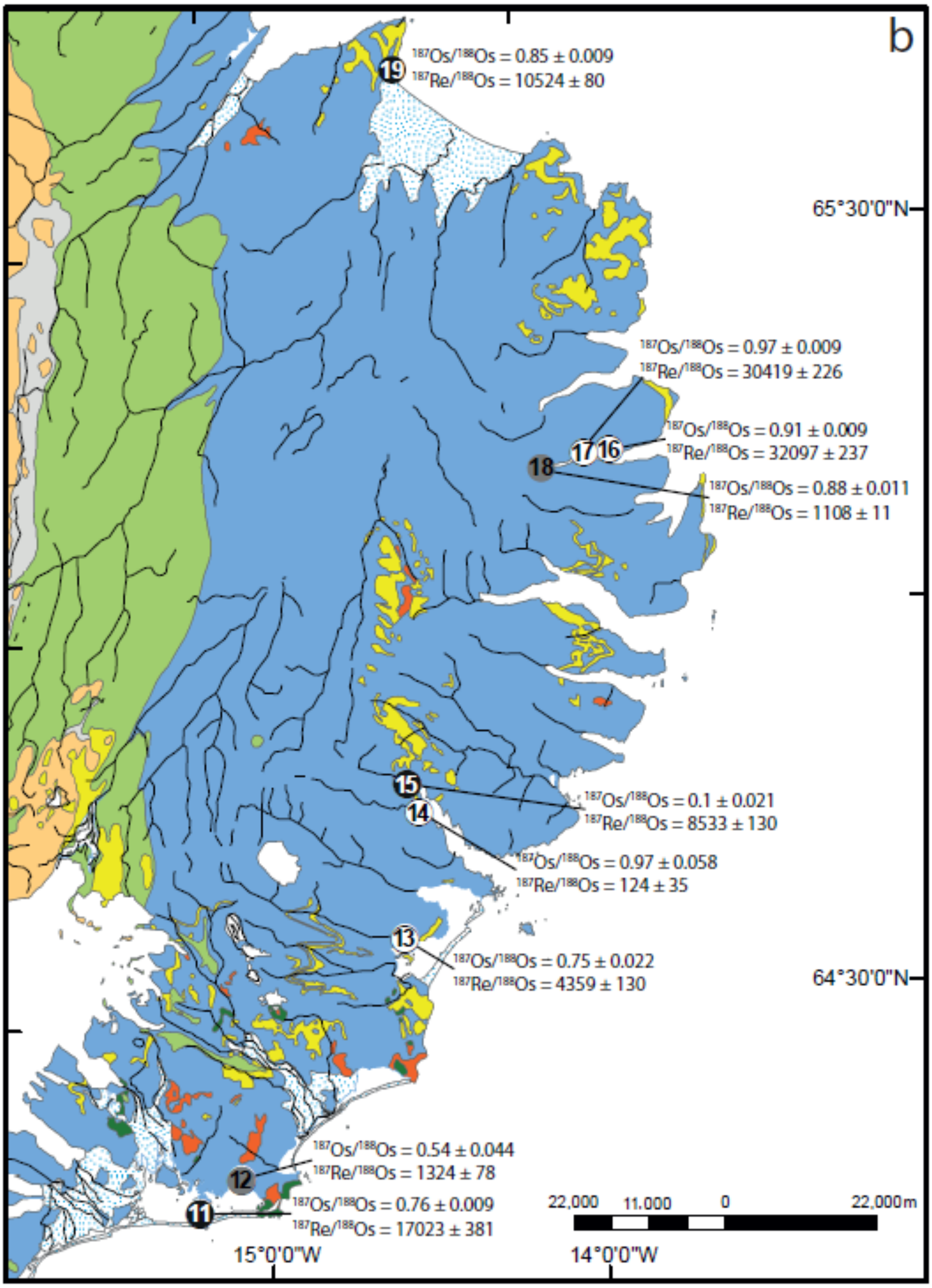

2.2.3 Re-Os analysis

The Re-Os analysis for macroalgae and bedload were carried out in the Durham Geochemistry Centre (Laboratory for Sulfide and Source Rock Geochronology and Geochemistry). The seawater Os analyses were conducted at Laboratoire Magmas et

Volcans at the Campus Universitaire des Cézeaux, with the Re fraction processed at the Durham Geochemistry Centre.

2.2.3.1 Macroalgae

The technique for chemical separation of Re and Os from macroalgae is reported by Racionero-Gómez et al. (2017). In brief, approximately 200 mg of powdered macroalgae was introduced into a Carius tube together with 11 N HCl (3 mL), 15.5 N HNO_3 (6 mL) and a known amount of ^{185}Re + ^{190}Os tracer solution and heated to 220°C in an oven for 24 h. The Os was isolated from the acid medium using $CHCl_3$ solvent extraction and then back extracted into HBr. The Os was further purified using a CrO_3-H_2SO_4 – HBr micro-distillation (Birck et al., 1997; Cohen and Waters, 1996). The remaining Re-bearing acid medium was evaporated to dryness at 80°C, with the Re isolated and purified using both NaOH-acetone solvent extraction and HNO_3-HCl anion chromatography (Cumming et al., 2013).

2.2.3.2 Bed load

The detailed analytical procedure for silicates has been adapted from Ishikawa et al. (2014). Approximately 1 g of bed load was crushed using an agate mortar. The powder is dissolved with HCl + HF (4 mL: 2 mL) in a 22 ml-savillex® vial at 100°C. The acid-sample medium was evaporated to dryness at 80°C before 11N HCl (1 mL) was added and subsequently evaporated twice to remove remaining HF. The resulting acid medium was introduced into a Carius tube together with 11 N HCl (3 mL), 15.5 N HNO_3 (6 mL) and a known amount of the ^{185}Re + ^{190}Os tracer solution and heated at 220°C for 48 h. The extraction and purification of the Os and Re fractions follows the same analytical protocol outlined in section 2.3.1.

2.2.3.3 Seawater

The technique for chemical separation of Re and Os from seawater is reported by Racionero-Gómez et al. (2017). Briefly, ~60 g of water sample, plus a known amount of mixed (^{190}Os + ^{185}Re) tracer solution, together with 2 mL of Br_2, 2 mL of CrO_3-H_2SO_4 solution and 1.5 mL of 98% H_2SO_4 were sealed into a 120 mL savillex vial and heated to 100˚C in an oven for 72 h to equilibrate sample and spike (Gannoun and Burton, 2014). The Os was extracted from the sample into liquid Br_2 followed by a second extraction of Os using 1 mL of Br_2. The 1 mL of liquid Br_2 was added to the sample solution, reacted for 1 h, and then removed. The extracted Br_2 is mixed with 1 mL of 9N HBr and evaporated to dryness, and further purified using a CrO_3-H_2SO_4 – HBr micro-distillation. The Re was purified as outlined for the macroalgae samples (Cumming et al., 2013).

2.2.3.4 Mass Spectrometry

The purified Re and Os fractions were loaded onto Ni and Pt filaments respectively, and measured using NTIMS (Creaser et al., 1991; Völkening et al., 1991) on a Thermo Scientific TRITON mass spectrometer using Faraday collectors in static mode, and an electron multiplier in dynamic mode respectively. The Re and Os abundances and isotope compositions are presented with 2 s.e. (standard error) absolute uncertainties which include full error propagation of uncertainties in the mass spectrometer measurements, blank, spike calibrations, and sample and spike weights. Full analytical blank values for the macroalgae analysis are 10.9 ± 5.9 pg for Re, 0.13 ± 0.13 pg for Os, with a ^{187}Os/^{188}Os composition of 0.61 ± 0.34 (1 SD, n = 4). For the bed load analysis the full analytical blank values are 15.9 ± 0.23 pg for Re, 2.12 ± 0.01 pg for Os, with a ^{187}Os/^{188}Os composition of 0.27 ± 0.001 (2 s.e., n = 1). For the seawater analysis the full analytical blank values are 10 ±

1.3 pg for Re, 0.043 ± 0.002 pg for Os, with a ^{187}Os/^{188}Os composition of 0.72 ± 0.02 (1 SD, n = 4).

To monitor the long-term reproducibility of mass spectrometer measurements Re and Os (DROsS, DTM) reference solutions were analysed. The 125 pg Re solution yields an average ^{185}Re/^{187}Re ratio of 0.5987 ± 0.0023 (2 SD., n = 8), which is in agreement with published values (e.g., Cumming et al., 2013 and references therein). A 50 pg DROsS solution gave an ^{187}Os/^{188}Os ratio of 0.16111 ± 0.0008 (2 SD., n = 8), which is in agreement with reported value for the DROsS reference solution (Nowell et al., 2008). For the seawater Os analysis at the Laboratoire Magmas et Volcans monitor instrument reproducibility using a 1 pg DTM Os solution, which yields a ^{187}Os/^{188}Os value of 0.1740 ± 0.0002 (2 SD, n = 4), which is in agreement with published values (Chen and Sharma, 2009; Gannoun and Burton, 2014).

2.2.4 Statistical tests

Statistical tests were carried out using MATLAB® R2017a (MATLAB 9.2, The MathWorks Inc., Natick, MA, 2017). A one-way analysis of variance (ANOVA) was utilised to determine whether several groups of a factor have a common mean. ANOVA tests for differences between group means by partitioning variation in the data into two components: variation of individual observations from their group mean; and, variation of the group means from the overall mean (Wu and Hamada, 2000; Neter et al, 1996). If during the ANOVA test, the *p*-value of the *F*-statistic (ratio of the mean squares) is smaller than the significance level (0.05), the test rejects the null hypothesis, that all group means are equal, and one of the group means is therefore different from the others. Where the ANOVA test is used the means of each group (avg), the *F*-statistic (F) and the *p*-value will be cited. In the event the null hypothesis is rejected a multiple comparison test is carried out. This will determine which pairs of means are significantly different from each other.

2.3 Results

2.3.1 Macroalgae

Table 1

Rhenium and osmium abundance and isotope data for Icelandic macroalgae samples

Sample Location	Macroalgae Species	[Re] (ppb)	2 s.e.	[Os] (ppt)	2 s.e.	$^{187}Re/^{188}Os$	2 s.e.	$^{187}Os/^{188}Os$	2 s.e.
1	*Fucus vesiculosus*	44.32	2.53	27.85	0.10	7879.7	452.6	0.337	0.003
2	*Fucus spiralis*	14.52	0.57	8.81	0.07	8534.2	342.4	0.700	0.020
3	*Fucus vesiculosus*	38.04	1.50	5.03	0.04	39405.6	1646.4	0.750	0.030
4	*Fucus vesiculosus*	53.37	2.10	23.42	0.10	11864.8	471.8	0.750	0.010
5	*Fucus vesiculosus*	40.52	2.32	44.92	0.16	4483.7	257.4	0.368	0.003
6	*Fucus vesiculosus*	23.56	0.93	106.42	0.42	1087.5	43.5	0.270	0.010
7	*Ascophyllum nodosum*	3.17	0.01	53.04	0.41	307.1	4.3	0.634	0.012
8	*Fucus vesiculosus*	71.92	0.23	10.14	0.04	37751.4	211.2	0.926	0.006
9	*Fucus vesiculosus*	15.39	0.05	6.93	0.06	11692.8	180.0	0.835	0.018
10	*Fucus vesiculosus*	61.68	0.20	13.71	0.05	23395.3	120.6	0.736	0.004
11	*Fucus vesiculosus*	25.66	0.54	7.87	0.05	17023.4	381.1	0.765	0.009
12	*Fucus vesiculosus*	3.58	0.01	13.73	0.36	1323.9	77.5	0.535	0.044
13	*Fucus vesiculosus*	8.86	0.19	10.59	0.12	4358.6	130.2	0.750	0.022
14	*Fucus distichus*	0.11	0.03	4.69	0.10	123.5	34.6	0.970	0.058
15	*Fucus vesiculosus*	14.65	0.05	9.21	0.09	8533.3	130.4	0.995	0.021
16	*Fucus vesiculosus*	50.36	0.13	8.34	0.04	32096.9	237.1	0.913	0.009
17	*Fucus vesiculosus*	43.93	0.11	7.72	0.04	30419.2	226.2	0.967	0.009
18	*Fucus distichus*	1.55	0.01	7.41	0.05	1107.6	10.8	0.879	0.011
19	*Fucus spiralis*	28.83	0.08	14.45	0.08	10523.5	80.0	0.854	0.009
20	*Fucus distichus*	0.10	0.03	7.56	0.15	64.6	20.5	0.612	0.036
21	*Fucus spiralis*	24.96	0.08	3.30	0.03	40320.4	683.7	0.938	0.023
22	*Ascophyllum nodosum*	4.23	0.01	21.98	0.44	1022.7	41.8	0.925	0.053
23	*Fucus vesiculosus*	60.27	0.15	8.24	0.06	38953.6	311.5	0.930	0.014
24	*Ascophyllum nodosum*	88.43	0.29	13.83	0.28	34155.5	1422.1	0.962	0.056
25	*Fucus spiralis*	18.15	0.06	6.45	0.04	14725.3	135.5	0.787	0.010
26	*Ascophyllum nodosum*	63.96	3.65	9.45	0.04	35167.1	2017.9	0.727	0.006
27	*Fucus vesiculosus*	9.58	0.55	254.47	1.69	182.3	10.7	0.161	0.003

The Re and Os abundance and isotope data for macroalgae are given in Table 1. Rhenium and Os abundances show a large range from 0.1 to 88.4 ppb and from 3.3 to 254.5 ppt respectively. Individual species, such as *Fucus vesiculosus, Fucus spiralis, Fucus distichus* and *Ascophyllum nodosum* show variable Re abundances from 3.6 to 71.9 ppb, 14.5 to 28.8 ppb, 0.10 to 1.6 ppb and 3.2 to 88.4 ppb, respectively (Fig. 3a). Individual species, such as *Fucus vesiculosus, Fucus spiralis, Fucus distichus* and *Ascophyllum nodosum* also show a large range in Os abundances from 5.0 to 254.5 ppt, 3.3 to 14.5 ppt, 4.7 to 7.6 ppt and 9.5 to 53.0 ppt, respectively (Fig. 3a). The $^{187}Os/^{188}Os$ compositions of the macroalgae range from 0.16 to 0.99 (Fig. 3b). The reason(s) for the variability is discussed below. The $^{187}Re/^{188}Os$ ratios of the macroalgae are highly variable (~65 to 40,320; Fig. 3b).

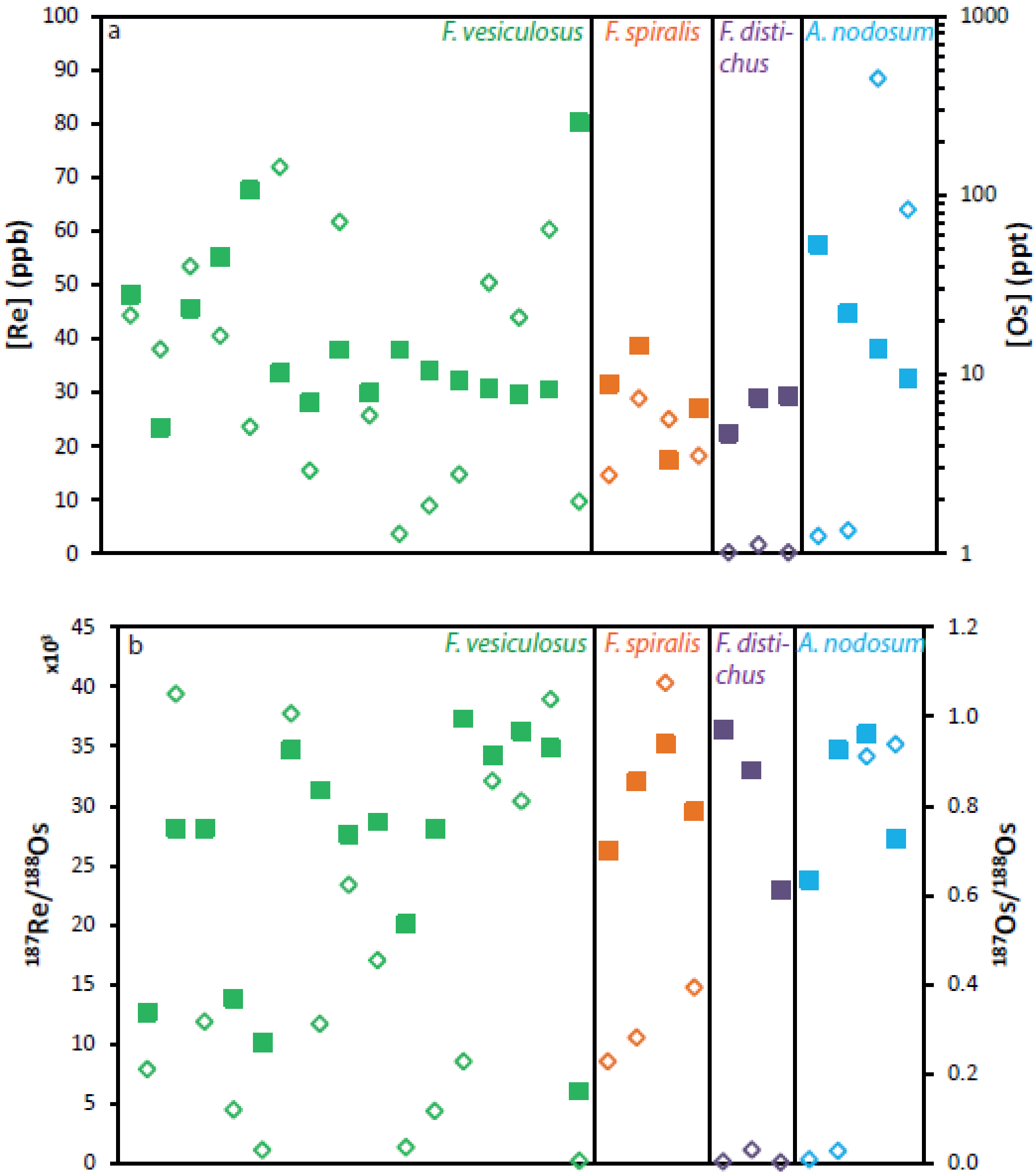

Fig. 3. Rhenium (open diamonds) and osmium (filled squares) abundance (**a**) and isotopic composition (**b**) for *F. vesiculosus* (green), *F. spiralis* (orange), *F. distichus* (purple) and *A. nodosum* (blue).

A one-way ANOVA test was conducted to determine if there was any statistically significant variation in Re abundance, Os abundance, $^{187}Re/^{188}Os$ and $^{187}Os/^{188}Os$ between each macroalgae species. When comparing *Fucus vesiculosus, Fucus spiralis, Fucus distichus* and *Ascophyllum nodosum,* the ANOVA tests for Re abundance (avg = 35.4, 21.6, 0.6, 39.9;

F = 2.29; p-value = 0.1054), Os abundance (avg = 34.9, 8.3, 6.5, 24.6; F = 0.45; p-value = 0.7178), $^{187}Re/^{188}Os$ (avg = 16904, 18525, 431, 17663; F = 1.18; p-value = 0.3385) and $^{187}Os/^{188}Os$ (avg = 0.68, 0.82, 0.82, 0.82; F = 0.68; p-value = 0.5744) all have a p-values which fall above the significance level (p-value = 0.05). We can therefore accept the null hypothesis that each species has a common mean for each parameter studied.

2.3.2 Bed load

Table 2

Rhenium and osmium abundance and isotope data for Icelandic bed loads

Sample Loacation	[Re] (ppb)	2 s.e.	[Os] (ppt)	2 s.e.	$^{187}Re/^{188}Os$	2 s.e.	$^{187}Os/^{188}Os$	2 s.e.
7	0.73	0.02	41.21	0.18	85.6	2.1	0.157	0.002
8	0.91	0.03	7.23	0.04	646.3	23.0	0.591	0.007
9	0.89	0.02	15.60	0.07	277.8	6.6	0.231	0.003
10	1.11	0.04	9.13	0.04	593.03	20.98	0.228	0.003
11	0.89	0.03	8.81	0.04	494.3	17.6	0.250	0.003
12	0.55	0.02	24.99	0.12	108.02	3.97	0.337	0.004
15	0.69	0.02	23.71	0.11	143.2	5.2	0.292	0.004
18	0.51	0.02	10.42	0.05	238.6	8.8	0.224	0.003
19	1.03	0.04	12.52	0.06	405.5	14.4	0.271	0.003
20	0.61	0.02	11.41	0.05	259.96	9.45	0.220	0.003
27	0.63	0.02	69.05	0.31	44.2	1.6	0.204	0.003

The Re and Os abundance and isotopic data of bed loads are presented in Table 2. Rhenium and Os abundances range from 0.5 to 1.1 ppb and 7.3 to 69.1 ppt respectively. This compares well to Re and Os abundances previously recorded in Icelandic basalts, which range from 0.05 to 1.8 ppb and 3.7 to 1954.9 ppt respectively (Debaille et al., 2009; Gannoun et al., 2006). Macroalgae and bed load retain similar levels of Os with the exception of the macroalgae sample from location 27 (Fig. 1), which is heavily enriched in Os (~254 ppt; Fig. 4a). Macroalgae is enriched in Re by several orders of magnitude when compared to bed load. A significant correlation ($R^2 = 0.6061$) in Re abundance is observed between macroalgae and the corresponding bed load (Fig. 4b). The ^{187}Os/^{188}Os composition of the bed load ranges from 0.16 to 0.59, with an average of 0.27, which is closer to the unradiogenic end-member. The bed load ^{187}Os/^{188}Os values are more radiogenic than those previously recorded for Icelandic basalts (Gannoun et al., 2006), although data in this study is from the older extremities of Iceland (Figs. 1 - 2), where more radiogenic ingrowth of ^{187}Os will have occurred. In almost all cases, the ^{187}Os/^{188}Os ratios of macroalgae are significantly more radiogenic than the corresponding bed load (Fig. 5a). The ^{187}Re/^{188}Os ratio of the bedload ranges from 44.2 to 646.3, which fall close to the lower end of the range reported for Icelandic basalts (45 - 1698; Gannoun et al., 2006). Although the macroalgae possess much greater ^{187}Re/^{188}Os than the corresponding bed load, a strong correlation (R^2 = 0.7962) between the macroalgae and bed load ^{187}Re/^{188}Os is observed (Fig. 5b).

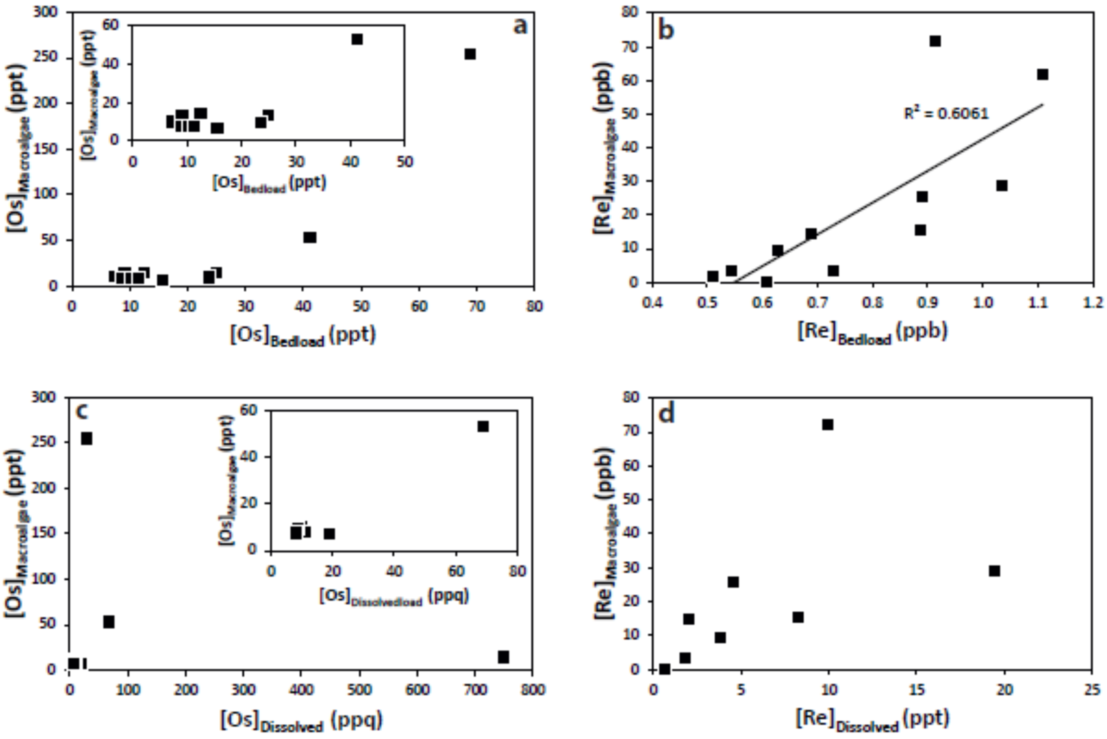

Fig. 4. Bedload osmium (**a**) and rhenium (**b**) abundance and dissolved load osmium (**c**) and rhenium (**d**) abundance versus the corresponding abundance in macroalgae. See text for discussion.

2.3.3 Dissolved load

Table 3

Rhenium and osmium abundance and isotope data for Icelandic dissolved loads

Sample Loacation	[Re] (ppt)	2 s.e.	[Os] (ppq)	2 s.e.	^{187}Re/^{188}Os	2 s.e.	^{187}Os/^{188}Os	2 s.e.	Salinity (ppt)	±
7	1.9	0.2	69.2	0.3	130.99	11.07	0.160	0.002	0.140	0.001
8	10.0	0.7	9.7	0.1	5467.3	375.4	0.876	0.023	33.580	0.336
9	8.3	0.6	18.9	0.2	2229.6	152.8	0.569	0.017	29.680	0.297
11	4.5	0.3	11.2	0.1	2097.98	147.97	0.693	0.014	30.080	0.301
15	2.1	0.2	8.5	0.1	1184.03	105.84	0.230	0.009	0.220	0.002
19	19.4	1.3	750.7	3.0	125.4	8.4	0.168	0.002	23.780	0.238
20	0.6	0.1	8.1	0.1	365.7	60.8	0.198	0.007	0.000	0.001
27	3.8	0.3	30.1	0.2	613.3	43.9	0.237	0.006	9.170	0.092

The Re and Os abundance and isotopic data of filtered water samples are reported in Table 3. Rhenium and Os abundances range from 0.6 to 19.4 ppt and 8.1 to 750.7 ppq respectively. These values are highly variable when compared to oceanic Re (~8.2 ppt) (Anbar et al., 1992; Colodner et al., 1995; Colodner et al., 1993b) and Os (~10 ppq) (Gannoun and Burton, 2014; Levasseur et al., 1998; Sharma et al., 1997; Woodhouse et al., 1999) concentration. However, they compare well with Re and Os concentrations found in global river estimates which range from 24 ppq to 2.3 ppb and 4.6 to 52.1 ppq respectively (Colodner et al., 1993a; Levasseur et al., 1999; Miller et al., 2011; Sharma and Wasserburg, 1997), with the exception of sample 19 (750.7 ppq), which has an Os concentration several orders of magnitude higher than for any water ever recorded. With the exception of sample 19, Os concentrations are similar to previously recorded Icelandic rivers (1.0 - 20.5 ppq; Gannoun et al., 2006). Macroalgae are highly enriched in Re and Os when compared to the dissolved load of the rivers measured here (Figs. 4c, d), in keeping with previous observations whereby macroalgae is seen to take up and concentrate these elements from seawater (Racionero-Gómez et al., 2016; Racionero-Gómez et al., 2017).

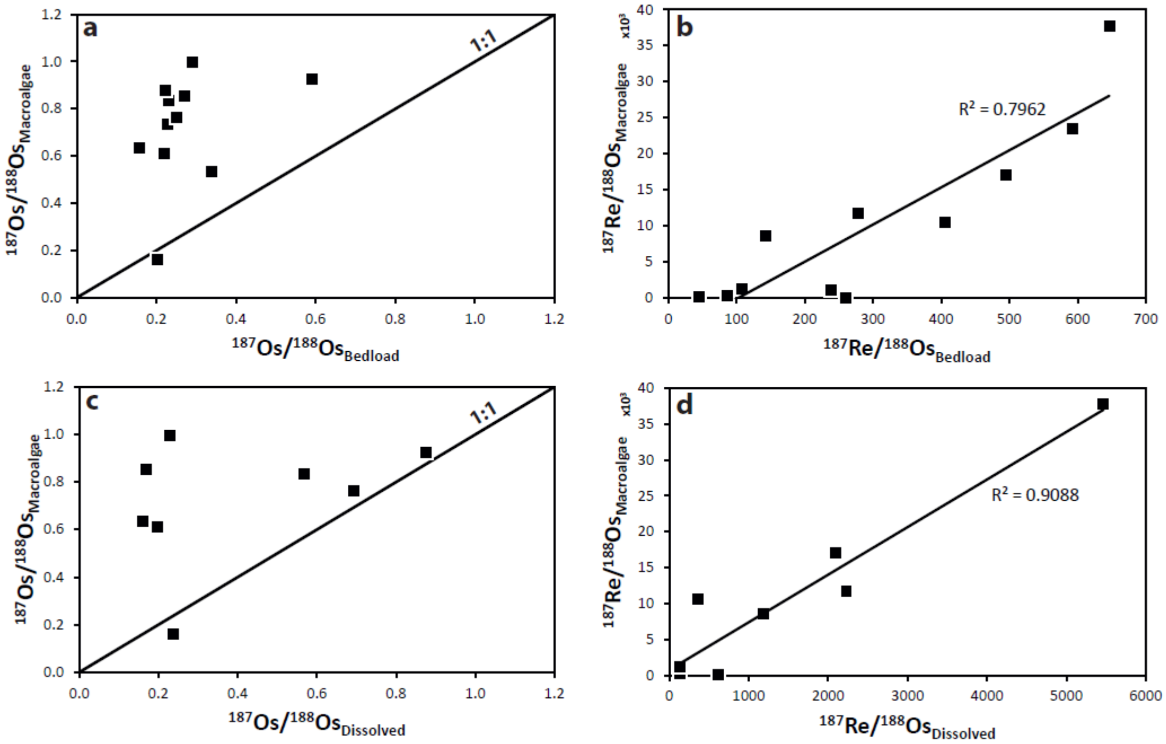

Fig. 5. Bedload ^{187}Os/^{188}Os (**a**) and ^{187}Re/^{188}Os (**b**) and dissolved load ^{187}Os/^{188}Os (**c**) and ^{187}Re/^{188}Os (**d**) versus the corresponding ratio in macroalgae. See text for discussion.

The ^{187}Os/^{188}Os ratio of the dissolved load ranges from 0.16 to 0.88. These values are less radiogenic than open ocean ^{187}Os/^{188}Os values (~1.06) (Gannoun and Burton, 2014; Levasseur et al., 1998; Sharma et al., 1997; Woodhouse et al., 1999) falling close to the range of Icelandic rivers (0.15 - 1.04) (Gannoun et al., 2006). In almost all cases the ^{187}Os/^{188}Os ratios of macroalgae are significantly more radiogenic than the corresponding dissolved load (Fig. 5c). The most radiogenic values were obtained for macroalgae close to the oldest basalt in the eastern and north-western parts of Iceland, while the most unradiogenic isotope ratios were found either close to the central active zone or the rivers draining it (Table 1; Fig. 1). The ^{187}Re/^{188}Os ratio of the dissolved load ranges from 125.4 to 5467.3. The lower and upper values of this range are similar to average global riverine (227) and seawater (4270) ^{187}Re/^{188}Os ratios, respectively (Peucker-Ehrenbrink and Ravizza, 2000) suggesting the influence of both river water and seawater at these sampling locations. This is confirmed by salinity data, which shows a weak correlation ($R^2 = 0.469$) with $^{187}Re/^{188}Os$ and generally higher ratios at higher salinity and vice versa (Table 3). The macroalgae $^{187}Re/^{188}Os$ are generally several times greater than the corresponding dissolved load (Fig. 5d). A strong correlation ($R^2 = 0.9088$) in $^{187}Re/^{188}Os$ values is observed between macroalgae and the dissolved load (Fig. 5d).

2.3.4 Partition coefficient

The partition coefficient (K_d) for Os and Re is:

$$K_d = \frac{[X]_s}{[X]_l}$$

where $[X]_s$ is the total elemental abundance for macroalgae, $[X]_l$ is the elemental abundance in the dissolved load of seawater, and X refers to the element in question. The K_d values for sample locations where both macroalgae and seawater measurements are recorded in table 4.

Table 4

Partition coefficients between macroalgae and seawater for Re and Os abundance.

Sample Location	Re K_d	Os K_d
7	1693	767
8	7200	1049
9	1860	366
11	5644	702
15	7113	1084
19	1484	19
20	156	932
27	2536	8448

2.4 Discussion

2.4.1 Biological and environmental controls on Re and Os uptake in macroalgae

Rhenium and Os abundance in macroalgae are consistent with previous studies, showing variations both between species and within each species itself (Fig. 3). Rhenium abundances in *Fucus vesiculosus* from sample location 3, 8, 10 and 24 (Fig. 1) compare well with values of 51.0 to 103.4 ppb in the UK (Racionero-Gómez et al., 2016) and 60.8 to 84.9 ppb in Norway (Mas et al., 2005). However, most *Fucus vesiculosus* in this study have lower concentrations than those from the literature, ranging from 3.6 to 50.4 ppb. Likewise, *Fucus disichus* and *Ascophyllum nodosum* show a lower abundance of Re than recorded values for California (Yang, 1991) and Greenland (Rooney et al., 2016), with the exception of sample 21. Previous Os abundance determinations for *Fucus vesiculosus* from the UK (33.8 ppt; Racionero-Gómez et al., 2017) and *Ascophyllum nodosum* from Greenland (12.6 ppt; Rooney et al., 2016) fall within the ranges found in this study. However, Os abundance for *Fucus distichus* recorded in Greenland (14.0 ppt; Rooney et al., 2016) is far higher than the range for Icelandic *Fucus distichus* of this study.

It has previously been suggested that the age of the macroalgae - due to its rapid accumulation rates (Yang, 1991) - and geographical distribution - due to relatively ubiquitous oceanic Re concentrations (Mas et al., 2005) - do not play a part in controlling the Re concentration in macroalgae. However, seasonal variations, the chemical species of the Re perrhenate compound, fertility and growth-media Re concentration have all been suggested as possible causes of Re variation in macroalgae (Mas et al., 2005; Racionero-Gómez et al., 2016). Likewise, due to fast Os uptake (Racionero-Gómez et al., 2017) and relatively ubiquitous oceanic Os concentrations (Peucker-Ehrenbrink and Ravizza, 2000), it is conceivable that seasonal variations and growth-media Os concentration could cause the variations in Os seen in macroalgae (Racionero-Gómez et al., 2017).

All samples were collected during the same season (July-August) suggesting seasonality does play an important role in the variations in Re and Os abundance observed in this study. At high concentrations it has been found that the species of Re salt does not greatly affect the levels of Re incorporated into macroalgae and by homogenising the sample, as was done in this study, the influence of high Re non-fertile tips can be mitigated (Racionero-Gómez et al., 2016). However, culturing of macroalgae under increasing seawater Re and Os concentrations has been shown to cause an increase in uptake in Re (Racionero-Gómez et al., 2016) and Os (Racionero-Gómez et al., 2017) in macroalgae. Although oceanic Re (8.2 ppt) and Os (~10 ppq) concentration is seen to be fairly ubiquitous (Anbar et al., 1992; Colodner et al., 1993b; Levasseur et al., 1998; Sharma et al., 1997; Woodhouse et al., 1999), riverine Re (3.1 ppt) and Os (9.1 ppq) abundance is generally much lower, but also highly variable (Colodner et al., 1993a; Levasseur et al., 1999; Miller et al., 2011; Sharma and Wasserburg, 1997). Therefore, the geographical distribution could play an important role if macroalgae living on the continental shelf in an estuarine habitat are in close proximity to a freshwater source. Under estuarine conditions, a mixture of freshwater and seawater could cause highly variable Re and Os abundances through a tidal cycle, leading to variable abundances in macroalgae.

Macroalgae in this study were collected from coastal waters surrounding Iceland, generally close to the mouths of major rivers (Figs. 1 - 2). Previously, it has been shown that Re concentration acts conservatively in the Amazon estuary with low concentrations (0.21 ppt) at low salinity and high concentrations (8.6 ppt) at high salinity (Colodner et al., 1993a). Osmium on the other hand, has been shown to behave non-conservatively in estuaries, experiencing removal from the water column at low salinities in temperate and arctic estuaries (Levasseur et al., 2000; Turekian et al., 2007) and at high salinities in tropical estuaries (Martin et al., 2001; Sharma et al., 2007), suggesting potential Os removal at low salinities in Iceland. Given that the macroalgae studied here tends to live in brackish water, it will interact with seawater of varying salinity through a tidal cycle. Samples located closer to a freshwater source could therefore receive less Re and Os than a deeper water sample, which can be seen in samples 16, 17 and 18 (Table 1; Fig. 2b), which show progressively higher Re and Os abundances as you move seaward. This could explain some of the Re variability in *F. vesiculosus*, whereas samples (7, 9, 11, 12, 13, 14, 15, 18, 20 and 27; Table 1; Fig. 1) close to riverine inputs generally have lower Re abundances (8.1 ppb) than those that are not spatially near riverine inputs (43 ppb). However, Os does not follow this trend suggesting that some other mechanisms control macroalgae Os uptake and concentration.

The Os abundance of the dissolved load of water measured in this study (8.1 to 750.7 ppq) compares well with global river estimates (4.6 - 52.1 ppq) (Levasseur et al., 1999; Sharma and Wasserburg, 1997) with the exception of sample 19 (750.7 ppq), which has an Os abundance several orders of magnitude higher than any recorded water. This high variation in Os abundance can be attributed to the influence of Icelandic freshwater sources (1.0 - 20.5 ppq), with lower concentrations found in rivers draining older, more radiogenic ^{187}Os/^{188}Os bearing basaltic catchments (1.9 ppq) when compared to younger, less radiogenic ^{187}Os/^{188}Os basaltic catchments (10.5 ppq) (Gannoun et al., 2006). This could also explain some of the variation seen in the macroalgae Os abundance, whereby samples (13, 14, 15, 16, 17, 18 and 20; Table 1; Fig. 1) found close to the mouths of rivers draining older catchments have lower concentrations (8.0 ppt) than those draining younger catchments (153.8 ppt; Sample: 7 and 27; Table 1; Fig. 1). However, this is further complicated by the potential influence of geothermal waters that possess relatively high Os concentrations (19.7 ppq; Gannoun et al., 2006), which could explain the higher Os concentration (36.1 ppt) found in macroalgae around the Reykjanes peninsula (Samples 1 - 6; Table 1; Fig. 2a). This is supported by experimental studies, which shown increasing Re and Os abundances in cultured *F. vesiculosus* with increasing Re and Os abundances in the cultures media (Racionero-Gómez et al., 2016; Racionero-Gómez et al., 2017).

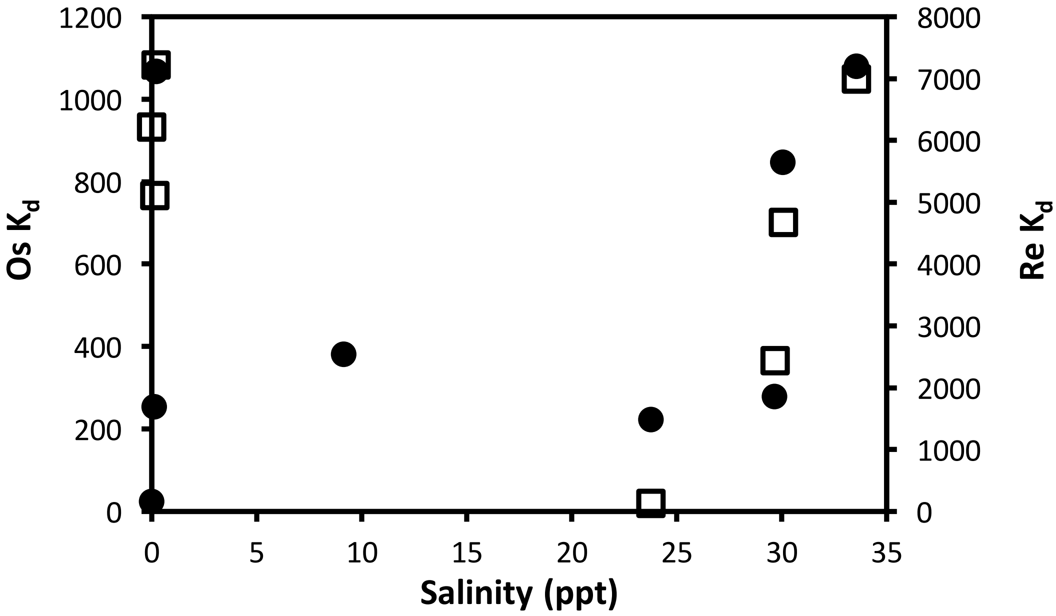

Fig. 6. Partitions coefficients (K_d) for Os (open squares) and Re (closed circles) for varying salinities.

Rhenium and Os partition coefficients between macroalgae and local seawater (Table 4) show a large variation with salinity (Fig. 6). Osmium K_d remains relatively high at both high and low salinities, but decreases towards intermediate salinities (Fig. 6). Rhenium shows variable K_d at low salinities and high Kd at high salinity, but decreases towards intermediate salinities (Fig. 6). This suggests salinity controls on Re and Os uptake into macroalgae with greater uptake at freshwater (low) and seawater (high) salinity. Uptake of both elements is reduced at intertidal zone (intermediate) salinities. This could arise for several reasons in macroalgae such as: growth rates; salinity stress or the conservative/unconservative behaviour of Re and Os in an estuarine habitat. Growth rates are known to increase at intermediate salinities (15 to 20 psu) in some macroalgae species (Martins et al., 1999). However, if Re and Os uptake is linked to metabolic activity, we would expect higher abundances in macroalgae at intermediate salinities as more Re and Os are confused for elements of a similar ionic radius (Racionero-Gómez et al., 2016;

Racionero-Gómez et al., 2017). Salinity stress can be caused by fluctuating salinity in the fluid medium whereby the macroalgae transports salts, and therefore potentially Re and Os, to maintain their cellular osmolality. In marine and fresh water systems, salinity will remain relatively constant and therefore macroalgae will not undergo salinity stress. However, in the intertidal zone, salinity will vary through a tidal cycle and macroalgae will therefore be affected by salinity stress. This could potentially prevent macroalgae from maintaining constant Re and Os uptake and therefore Re and Os abundance (Fig. 6). As will be discussed further in section 2.4.2.1, Re has been seen to behave conservatively in an estuarine habitat while Os has been observed to behave both conservatively or unconservatively in estuarine habitats (Levasseur et al., 2000; Martin et al., 2001; Sharma et al., 2007; Turekian et al., 2007; Miller et al., 2011). This could lead to higher Re uptake high Re, high salinity, seawater (Fig. 6). Rhenium uptake decreases as you move landwards as mixing with freshwater drives the concentration of Re down towards freshwater values (Fig. 6). Osmium on the other hand has been seen to act unconservatively in estuaries with Os removal at intermediate salinities as sediment dispersal during mixing causes scavenging onto particulate material (Martin et al., 2001). This would act to lower Os abundance in intertidal waters and therefore lower Os uptake in macroalgae (Fig. 6). However, Os abundance in seawater measured in this study is not seen to vary with salinity (Table 3).

Previous studies have identified that Re accumulation in *F. vesiculosus* is variable across structural components, indicating some cells are more specialised for Re uptake (Racionero-Gómez et al., 2016), which is not the case for Os (Racionero-Gómez et al., 2017). Although the biological mechanism by which macroalgae extract Re and Os from their media is not known, culturing studies have shown that macroalgae directly take up both Re and Os from the dissolved load of seawater through syn-life bioadsorption/bioaccumulation (Racionero-Gómez et al., 2016; Racionero-Gómez et al., 2017). However, these studies did not look into Re and Os uptake in macroalgae from the particulate or bed load of seawater. A strong correlation between macroalgae and dissolved load Os abundance is clear from previous studies (Racionero-Gómez et al., 2017), but the absence of any correlation between macroalgae and bed load Os abundance found in this study (Fig. 4a) suggests that Os uptake is purely from the dissolved load with little uptake directly from the bed load. However, macroalgae Re shows a correlation with both the dissolved (Racionero-Gómez et al., 2016) and bed load (Fig 4b). This suggests a potential additional source of Re to macroalgae from the bed load. However, it has been shown that the Re abundance of the holdfast in *F. vesiculosus* is relatively low when compared to the other biological structures and therefore Re is probably not taken up from the bed load via this pathway (Racionero-Gómez et al., 2016).

Although not measured in this study, it has been shown that Re abundance in the particulate load of Icelandic rivers is well correlated with the respective bed load (Gannoun et al., 2006). The similarity of the bed load Re abundance measured in this study (0.5 - 1.1 ppb) to Icelandic rivers (0.3 - 1.8 ppb; Gannoun et al., 2006) could suggest a possible correlation with Re in the particulate load at the sampled locations. Macroalgae Re abundance could potentially be correlated with the particulate load suggesting different biological pathways for the uptake of Os and Re in macroalgae.

2.4.2 Environmental controls on the ^{187}Os/^{188}Os of macroalgae

2.4.2.1 Influence of estuarine conditions on the ^{187}Os/^{188}Os of macroalgae

It has been shown that the ^{187}Os/^{188}Os of floating macroalgae (*Sargassum fluitans* and *S. natans*) from the Gulf of Mexico (Rooney et al., 2016) are indistinguishable from that of the present day oceanic ^{187}Os/^{188}Os value of 1.06 (Peucker-Ehrenbrink and Ravizza, 2000). In contrast, macroalgae from waters off the west coast of Greenland deviate from this value

(0.9 - 1.9), instead recording local continental Os flux into the coastal region (Rooney et al., 2016). Moreover, *Fucus vesiculosus* from an estuary on the east coast of the UK records the ^{187}Os/^{188}Os of the seawater in which it lives (0.94) and when cultured in seawater doped with Os of a known ^{187}Os/^{188}Os composition (0.16), takes on the composition of the new source (Racionero-Gómez et al., 2017). It has therefore been postulated that the ^{187}Os/^{188}Os of macroalgae can act as a proxy for the ^{187}Os/^{188}Os of the seawater in which it lives.

The ^{187}Os/^{188}Os of macroalgae from this study (0.16 - 1.0; Fig. 3b) shows a similar range to the ^{187}Os/^{188}Os of dissolved Os in Icelandic rivers (0.15 - 1.04; Gannoun et al., 2006). However, when we compare the ^{187}Os/^{188}Os of macroalgae with that of the dissolved load from the same location we see no relationship (Fig. 5c). This is probably due to the entrainment of seawater in an estuarine habitat from which these macroalgae and water samples were taken. Under estuarine conditions macroalgae will come into contact with varying amounts of freshwater and seawater through a tidal cycle. Its composition will therefore represent a mixing between the ^{187}Os/^{188}Os of a local freshwater source and the ^{187}Os/^{188}Os of North Atlantic seawater (1.02; Gannoun and Burton, 2014). Macroalgae from deeper waters, with little freshwater influence, are more likely to take on an ^{187}Os/^{188}Os composition similar to seawater (Rooney et al., 2016; this study), unlike their shallow water counterparts (Racionero-Gómez et al., 2017; this study).

This is apparent when the ^{187}Os/^{188}Os of the dissolved load from this study (0.16 - 0.88) is plotted against salinity (Fig. 7). At low salinity, the ^{187}Os/^{188}Os of the freshwater source is dominant and values are closer to that expected for Icelandic rivers (Avg. = 0.4; Gannoun et al, 2006), while at high salinity the ^{187}Os/^{188}Os is closer to a North Atlantic source (Avg. = 1.02; Gannoun and Burton, 2014; Green square in Fig. 7). For each location, macroalgae inhabit waters with an intermediate salinity between these two end-members (black squares in Fig. 7), and therefore the ^{187}Os/^{188}Os represents a mixture of both freshwater and seawater sources. This is supported by arctic, temperate and tropical estuaries, which show an increasing seawater ^{187}Os/^{188}Os influence as you move oceanward to higher salinities (Levasseur et al., 2000; Martin et al., 2001; Sharma et al., 2007; Turekian et al., 2007).

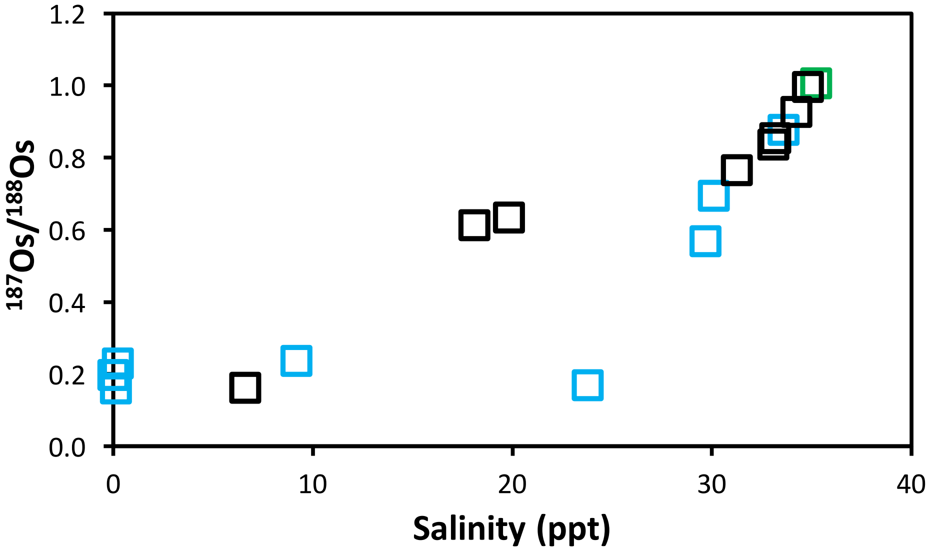

Fig. 7. Osmium isotopic (^{187}Os/^{188}Os) composition versus salinity. Blue and green open squares represent values for the dissolved load (this study) and North Atlantic seawater (Gannoun and Burton, 2014) respectively. Salinity has been interpolated based on ^{187}Os/^{188}Os measurements for macroalgae (open black squares). Macroalgae generally plots at intermediate salinities along a mixing line between the corresponding dissolved load for each location and estimates for the North Atlantic. See text for discussion.

2.4.2.2 Influence of basaltic weathering on the ^{187}Os/^{188}Os of macroalgae

During mantle melting and basalt genesis, both Re and Os become fractionated. Osmium behaves as a compatible element during melting and is retained in the mantle, unlike Re, which is moderately incompatible and enters the melt. Mantle derived basalts thus have very high Re/Os values and their primary mineral phases crystallise in a high Re/Os environment (Burton et al., 2002; Gannoun et al., 2004). Primary minerals such as olivine, pyroxene and plagioclase possess higher $^{187}Re/^{188}Os$ than bulk-rock or glass, and over short-timescales (<10^6 yrs) can produce measurable shifts in radiogenic osmium ($^{187}Os^r$) (See Fig. 9 in Gannoun et al., 2006).

In Iceland, rivers draining older catchments (>10^6 yrs) are undersaturated with respect to these high $^{187}Re/^{188}Os$ bearing minerals (olivine, pyroxene and plagioclase) and preferential weathering of these phases from the host basalt, combined with their age, which allows for radiogenic ingrowth of ^{187}Os from the decay of ^{187}Re, causes elevated radiogenic $^{187}Os/^{188}Os$ in the dissolved load (Gannoun et al., 2006). In contrast, rivers draining younger catchments (<10^6 yrs) are approaching saturation with respect to these same minerals, which in this instance have not had time to attain significant radiogenic ingrowth of ^{187}Os, and weathering tends towards congruency causing the dissolved load to approach that of bulk-rock (Gannoun et al., 2006).

Macroalgae $^{187}Os/^{188}Os$ values in this study (0.16 – 0.99) are generally much lower than the $^{187}Os/^{188}Os$ ratios of 0.81 to 1.89 previously recorded (Rooney et al., 2016; Racionero-Gómez et al., 2017). However, macroalgae in this study reach similar values to cultures doped with the Os standard solution, DROsS (Racionero-Gómez et al., 2017), suggesting that an unradiogenic $^{187}Os/^{188}Os$ source of the Os taken up by the macroalgae. When the $^{187}Os/^{188}Os$ of macroalgae is plotted against the reciprocal of the concentration, all the data fall within a field delimited by three potential end-members (Fig. 8a): Seawater (radiogenic $^{187}Os/^{188}Os$, intermediate [Os]); river water draining an old basaltic catchment (less radiogenic $^{187}Os/^{188}Os$, low [Os]); and, geothermal water and river water draining a young basaltic catchment (unradiogenic $^{187}Os/^{188}Os$, high [Os]). Variations in the $^{187}Os/^{188}Os$ of macroalgae can therefore be explained by the mixing between radiogenic seawater and: relatively less-radiogenic $^{187}Os/^{188}Os$ bearing rivers (Blue squares in Fig. 8a) draining an older catchment which has undergone incongruent weathering of high $^{187}Re/^{188}Os$, and therefore radiogenic $^{187}Os/^{188}Os$, minerals; or unradiogenic $^{187}Os/^{188}Os$ bearing rivers (Pink circles in Fig. 8a) draining younger catchments which have undergone congruent weathering of minerals with unradiogenic $^{187}Os/^{188}Os$. Samples close to glacially fed rivers (Samples 9 and 10; Fig. 1) are likely to attain a radiogenic $^{187}Os/^{188}Os$ signal (Orange diamonds in Fig. 8a) due to the entrainment of seawater into glacial ice (Gannoun et al., 2006).

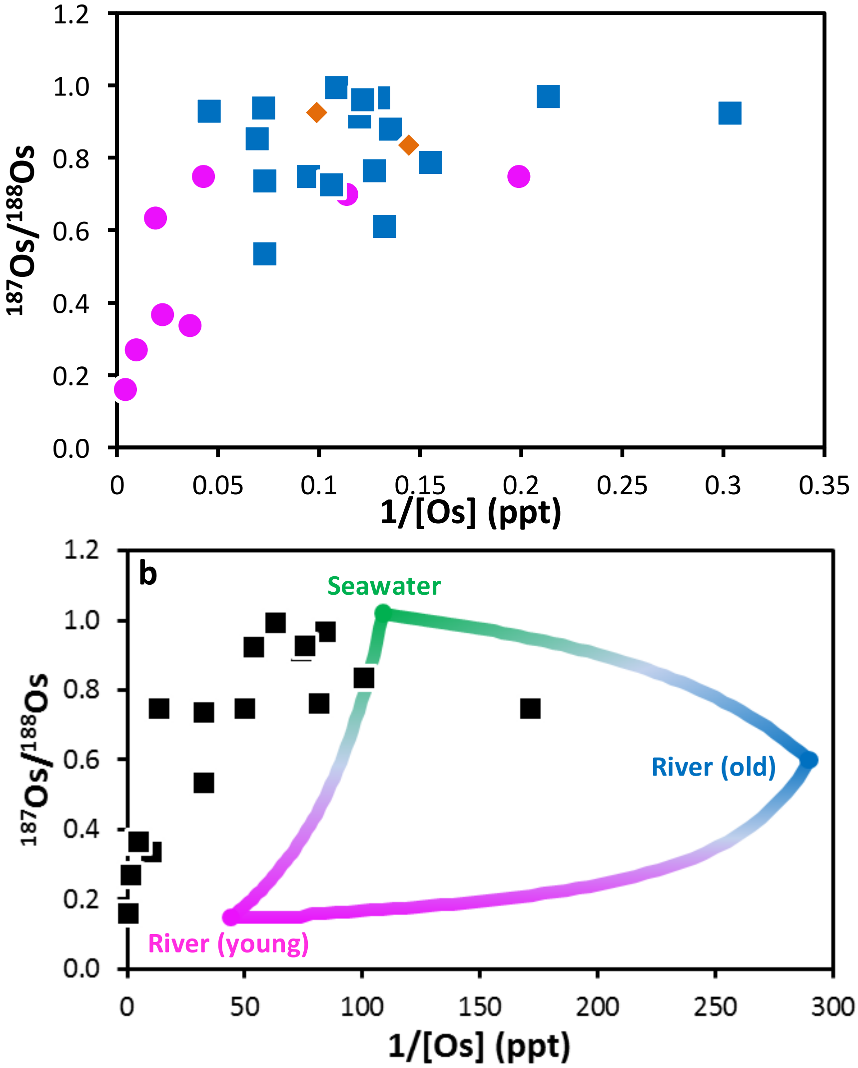

Fig. 8. Osmium isotopic ($^{187}Os/^{188}Os$) composition against the reciprocal of the Os abundance for (**a**) macroalgae sampled close to: rivers draining a young basaltic terrain or geothermal waters (pink circles); rivers draining an old basaltic terrain (blue squares); and, Holocene sediments (orange diamonds) and (**b**) *F. vesiculosus* where the Os abundance is converted to that of seawater (black squares) using the relationship found in Racionero-

Gómez et al. (2017). A three-point end-member mixing diagram based on extreme North Atlantic seawater (Green; Gannoun and Burton, 2014) and rivers draining a young basaltic catchment (pink; Gannoun et al, 2006) and old basaltic catchments (blue, Gannoun et al, 2006). See text for discussion.

This relationship becomes more apparent when the Os abundance in *F. vesiculosus* is converted to the Os abundance in seawater using the relationship found in Racionero-Gómez et al. (2017; $y = 0.0004x^{1.6607}$, $R^2 = 0.9898$), with its reciprocal plotted against the ^{187}Os/^{188}Os of *F. vesiculosus,* and then compared to an idealised 3-point end-member mixing model (Fig. 8b). Data fall upon either: a mixing line between seawater (^{187}Os/^{188}Os = 1.02, [Os] = 10 ppq) and direct-runoff rivers draining old catchments (^{187}Os/^{188}Os = 0.6, [Os] = 3.65 ppq); a mixing line between seawater and direct-runoff rivers draining young rivers or geothermal waters (^{187}Os/^{188}Os = 0.14, [Os] = 22.7 ppq); or, close to the value for seawater itself (Fig. 8b). However, the data is offset in concentration space from an idealised mixing model. This is most likely caused by the conversion rate used, which was developed by doping macroalgae under exceptionally high seawater Os concentrations (Racionero-Gómez et al., 2017). More work is needed to ascertain how macroalgae cultures behave at lower Os concentrations, more akin to those found in nature, for *F. vesiculosus* and other common macroalgae species.

2.4.3 Biological and environmental controls on ^{187}Re/^{188}Os of macroalgae

The ^{187}Re/^{188}Os ratios of macroalgae show a wide range from ~64 to 40,320 (Fig. 3b) similar to previous studies (6.8 to 31,983; Rooney et al., 2016, Racionero-Gómez et al., 2017), but far exceeding that found in global seawater (avg. ^{187}Re/^{188}Os = 4270; Peucker-Ehrenbrink and Ravizza, 2000), global river water (avg. ^{187}Re/^{188}Os = 227; Peucker-Ehrenbrink and Ravizza, 2000) and the dissolved load of waters measured in this study (125- 5467). As previously discussed this may be due to the different sources of Re and Os in macroalgae. Samples located close to a young basaltic terrain (Pink circles in Fig. 9a) are characterised by relatively unradiogenic ^{187}Os/^{188}Os and low ^{187}Re/^{188}Os compositions, as their isotopic signature is controlled by geothermal and river waters dominated by congruent weathering of basaltic bed-rock with relatively unradiogenic ^{187}Os/^{188}Os (0.12 - 0.18) and low ^{187}Re/^{188}Os (23.8 - 1310) compositions. Samples located close to the older basaltic terrains (Blue squares in Fig. 8a) exhibit radiogenic ^{187}Os/^{188}Os and high ^{187}Re/^{188}Os ratios, as their isotopic signature is dominated by river waters that have been influenced by the preferential weathering of old primary basaltic minerals such as olivine, clinopyroxene and plagioclase, which have relatively radiogenic ^{187}Os/^{188}Os (0.13 - 0.25 which has undergone radiogenic ingrowth) and high ^{187}Re/^{188}Os (288 - 7164) ratios (Burton et al., 2002; Gannoun et al., 2004; Gannoun et al., 2006). The influence of seawater, with a relatively radiogenic ^{187}Os/^{188}Os (1.02) and intermediate ^{187}Re/^{188}Os (4270; Peucker-Ehrenbrink and Ravizza, 2000), will pull the macroalgae values towards a seawater end-member (See Fig. 9). Macroalgae therefore hold the potential to not only record the ^{187}Os/^{188}Os of the seawater in which they live, but also the relative ^{187}Re/^{188}Os ratio of the seawater sources. This is confirmed by the strong relationship between the ^{187}Re/^{188}Os of macroalgae and the dissolved load measured in this study (Fig 5d).

Despite this relationship, macroalgae can still exhibit ^{187}Re/^{188}Os ratios greater than expected for Icelandic geochemical reservoirs. It has been proposed that macroalgae uptake Re and Os through the same mechanism leading to competition between these elements and therefore lower Re concentration in macroalgae under higher Os seawater concentration and vice versa (Racionero-Gómez et al., 2017). This is illustrated when the ^{187}Re/^{188}Os ratio of macroalgae is plotted against the reciprocal of the Re concentration (Fig. 9b). At low macroalgae Re concentration (<10 ppb), there is no competition between Re and Os for uptake into macroalgae, and ^{187}Re/^{188}Os ratios remain consistently low

(<5,000). As the Re concentration rises above ~10 ppb, Re is favoured over Os as the two elements begin to compete for uptake into macroalgae leading to an increase in $^{187}Re/^{188}Os$ ratios (5,000-15,000). At exceptionally high Re concentration (>25 ppb), Re continues to be taken up and the macroalgae becomes enriched in Re, leading to exceptionally high $^{187}Re/^{188}Os$ ratios (15,000-40,000).

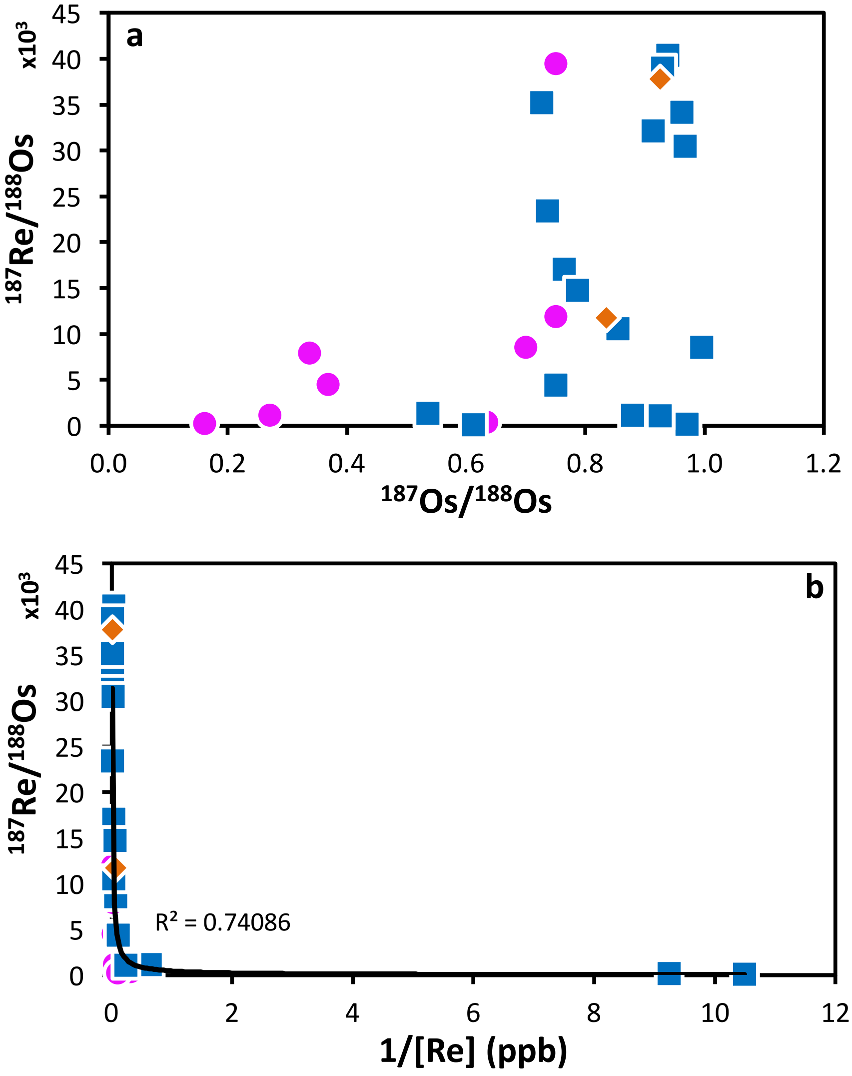

Fig. 9. (**a**) $^{187}Re/^{188}Os$ versus $^{187}Os/^{188}Os$ and (**b**) $^{187}Re/^{188}Os$ against the reciprocal of Re abundance for macroalgae sampled close to: rivers draining a young basaltic terrain or geothermal waters (pink circles); rivers draining an old basaltic terrain (blue squares); and, Holocene sediments (orange diamonds). See text for discussion.

This could be further exacerbated by additional uptake of Re from the bed load and/or particulate load leading to even higher Re concentration relative to Os in macroalgae (Fig. 4b), or the addition of another ^{187}Re/^{188}Os signal imparted from the bedload (Fig. 5b). These biological controls on Re and Os uptake could possibly be the cause of the ^{187}Re/^{188}Os ratios in macroalgae close to the outflow of older river catchments being far higher than those observed for recorded primary basaltic minerals (Fig. 9a).

2.5 Implications and future outlook

The Re-Os data for macroalgae presented here have been successfully used to trace the influence of basaltic weathering on the ^{187}Os/^{188}Os and ^{187}Re/^{188}Os of Icelandic coastal waters and subsequent mixing with more radiogenic seawater. Geothermal water and rivers draining young basaltic catchments impart an unradiogenic ^{187}Os/^{188}Os composition and also a relatively low ^{187}Re/^{188}Os signal to coastal waters. Rivers draining older basaltic catchments, where preferential weathering of primary basaltic minerals high in Re/Os ratios, and which have had sufficient time for the decay of ^{187}Re to form ^{187}Os^{r}, imparts a more radiogenic ^{187}Os/^{188}Os composition and relatively high ^{187}Re/^{188}Os signal to coastal waters. This provides further evidence to support the use of the ^{187}Os/^{188}Os of macroalgae as a proxy for the ^{187}Os/^{188}Os of seawater, overcoming the difficulties associated with direct seawater analysis and potentially becoming a useful tool for tracing a variety of Earth system processes.

If samples obtained at the mouth of a river represents the entire drainage area (Miller et al., 2011), then it is possible to calculate the entire quantity and isotopic composition of dissolved Os that is supplied to the North Atlantic from Icelandic rivers using macroalgae. The rivers containing *F. vesiculosus* studied have an annual discharge of 2.3 km^3/yr, accounting for 1.3% of the total discharge of Icelandic rivers (175 km^3/yr). Given the Os abundance of *F. vesiculosus*, which has been converted to that of seawater and then offset to be more representative of Icelandic geochemical reservoirs (See Fig. 8b), we estimate a dissolved Os flux of 2.35 kg/yr. These values are far higher than previously recorded estimates for Icelandic rivers of 0.98 kg/yr (Gannoun et al., 2006). Some of the discrepancy between these two values is likely due to the underrepresentation of Icelandic rivers in this study (1.3%) when compared to previous studies (21%) (Gannoun et al., 2006), but also suggests that although this newly developed proxy offers the potential to better constrain the ^{187}Os/^{188}Os composition of global riverine inputs, more work is needed to understand the uptake rate of Os by macroalgae at natural levels in order to a better estimate the global riverine abundance. If this can be done, macroalgae could hold the potential to yield a better understanding of the global Os cycle and oceanic residence times.

It is also possible to estimate the entire quantity of Re and Os taken up by macroalgae from Iceland. The four macroalgae species studied here account for 46% of the total biomass of common macroalgae species found around Iceland (Munda, 1987). Given the average Re and Os abundance for each species, we calculate 4.3 to 14.1 kg of Re and 3.3 to 11.8 g of Os are absorbed by these macroalgae over their lifetime. This is rather insignificant when compared to the Icelandic river input of Os to the ocean as described previously. However, it has been shown that upon death macroalgae does not appreciably loose Re (Racionero-Gómez et al., 2016). If this is the same for Os, and 6 to 14% of global macroalgae (6084 Tg/yr) (Krause-Jensen and Duarte, 2016) survives decomposition and is sequestered to sediment, then macroalgae could act as a sink of 0.03 to 89 kg/yr of Re and 0.001 to 0.2 kg/yr for Os, when based on the range of compositions of all macroalgae species studied to date (Mas et al., 2005; Racionero-Gómez et al., 2016; Racionero-Gómez et al., 2017; Rooney et al., 2016; Yang, 1991). This is insignificant when compared to estimates for global sediment sinks of 18 to 29 x10^{3} kg/yr and 260 to 1350 kg/yr for Re and

Os, respectively (Morford and Emerson, 1999; Oxburgh, 2001), suggesting macroalgae alone does not have a significant control in the global marine Re and Os cycle, both today and in Earth's geological past.

2.6 References

Anbar, A.D., Creaser, R.A., Papanastassiou, D.A., Wasserburg, G.J., 1992. Rhenium in seawater: Confirmation of generally conservative behavior. Geochimica et Cosmochimica Acta 56, 4099-4103.

Armstrong, R.L., 1971. Glacial erosion and the variable isotopic composition of strontium in sea water. Nature 230, 132-133.

Berner, R.A., Lasaga, A.C., Garrels, R.M., 1983. The carbonate-silicate geochemical cycle and its effect on atmospheric carbon dioxide over the past 100 million years. Am J Sci 283, 641-683.

Birck, J.L., Barman, M.R., Capmas, F., 1997. Re-Os isotopic measurements at the femtomole level in natural samples. Geostandards newsletter 21, 19-27.

Burton, K.W., Gannoun, A., Birck, J.-L., Allègre, C.J., Schiano, P., Clocchiatti, R., Alard, O., 2002. The compatibility of rhenium and osmium in natural olivine and their behaviour during mantle melting and basalt genesis. Earth and Planetary Science Letters 198, 63-76.

Chen, C., Sharma, M., 2009. High precision and high sensitivity measurements of osmium in seawater. Analytical chemistry 81, 5400-5406.

Cohen, A.S., Waters, F.G., 1996. Separation of osmium from geological materials by solvent extraction for analysis by thermal ionisation mass spectrometry. Analytica Chimica Acta 332, 269-275.

Colodner, D., Edmond, J., Boyle, E., 1995. Rhenium in the Black Sea: comparison with molybdenum and uranium. Earth and Planetary Science Letters 131, 1-15.

Colodner, D., Sachs, J., Ravizza, G., Turekian, K., Edmond, J., Boyle, E., 1993a. The geochemical cycle of rhenium: a reconnaissance. Earth and Planetary Science Letters 117, 205-221.

Colodner, D.C., Boyle, E.A., Edmond, J.M., 1993b. Determination of rhenium and platinum in natural waters and sediments, and iridium in sediments by flow injection isotope dilution inductively coupled plasma mass spectrometry. Analytical Chemistry 65, 1419-1425.

Creaser, R.A., Papanastassiou, D.A., Wasserburg, G.J., 1991. Negative thermal ion mass spectrometry of osmium, rhenium and iridium. Geochimica et Cosmochimica Acta 55, 397-401.

Cumming, V.M., Poulton, S.W., Rooney, A.D., Selby, D., 2013. Anoxia in the terrestrial environment during the late Mesoproterozoic. Geology 41, 583-586.

Debaille, V., Trønnes, R.G., Brandon, A.D., Waight, T.E., Graham, D.W., Lee, C.-T.A., 2009. Primitive off-rift basalts from Iceland and Jan Mayen: Os-isotopic evidence for a mantle source containing enriched subcontinental lithosphere. Geochimica et Cosmochimica Acta 73, 3423-3449.

Gannoun, A., Burton, K., 2014. High precision osmium elemental and isotope measurements of North Atlantic seawater. JAAS.

Gannoun, A., Burton, K.W., Thomas, L.E., Parkinson, I.J., van Calsteren, P., Schiano, P., 2004. Osmium isotope heterogeneity in the constituent phases of mid-ocean ridge basalts. Science 303, 70-72.

Gannoun, A., Burton, K.W., Vigier, N., Gíslason, S.R., Rogers, N., Mokadem, F., Sigfússon, B., 2006. The influence of weathering process on riverine osmium isotopes in a basaltic terrain. Earth and Planetary Science Letters 243, 732-748.

Huh, Y., Birck, J.-L., Allègre, C.J., 2004. Osmium isotope geochemistry in the Mackenzie River basin. Earth and Planetary Science Letters 222, 115-129.

Ishikawa, A., Senda, R., Suzuki, K., Dale, C.W., Meisel, T., 2014. Re-evaluating digestion methods for highly siderophile element and 187Os isotope analysis: Evidence from geological reference materials. Chemical Geology 384, 27-46.

Jóhannesson, H., 2014. Geological Map of Iceland. 1:600 000. Bedrock Geology. Icelandic Institute of Natural History, Reykjavík (2nd edition).

Krause-Jensen, D., Duarte, C.M., 2016. Substantial role of macroalgae in marine carbon sequestration. Nature Geosci 9, 737-742.

Levasseur, S., Birck, J.-L., Allegre, C., 1999. The osmium riverine flux and the oceanic mass balance of osmium. Earth and Planetary Science Letters 174, 7-23.

Levasseur, S., Birck, J.-L., Allègre, C.J., 1998. Direct measurement of femtomoles of osmium and the 187Os/186Os ratio in seawater. Science 282, 272-274.

Levasseur, S., Rachold, V., Birck, J.-L., Allegre, C., 2000. Osmium behavior in estuaries: the Lena River example. Earth and Planetary Science Letters 177, 227-235.

Martin, C.E., Peucker-Ehrenbrink, B., Brunskill, G., Szymczak, R., 2001. Osmium isotope geochemistry of a tropical estuary. Geochimica et Cosmochimica Acta 65, 3193-3200.

Mas, J., Tagami, K., Uchida, S., 2005. Rhenium measurements on North Atlantic seaweed samples by ID-ICP-MS: an observation on the Re concentration factors. Journal of Radioanalytical and Nuclear Chemistry 265, 361-365.

Miller, C.A., Peucker-Ehrenbrink, B., Walker, B.D., Marcantonio, F., 2011. Re-assessing the surface cycling of molybdenum and rhenium. Geochimica et Cosmochimica Acta 75, 7146-7179.

Morford, J.L., Emerson, S., 1999. The geochemistry of redox sensitive trace metals in sediments. Geochimica et Cosmochimica Acta 63, 1735-1750.

Munda, I.M., 1987. Distribution and use of some economically important seaweeds in Iceland, Twelfth International Seaweed Symposium. Springer, pp. 257-260.

Nowell, G., Luguet, A., Pearson, D., Horstwood, M., 2008. Precise and accurate 186 Os/188 Os and 187 Os/188 Os measurements by multi-collector plasma ionisation mass spectrometry (MC-ICP-MS) part I: Solution analyses. Chemical Geology 248, 363-393.

Oxburgh, R., 2001. Residence time of osmium in the oceans. Geochemistry, Geophysics, Geosystems 2, 1018.

Paul, M., Reisberg, L., Vigier, N., 2009. A new method for analysis of osmium isotopes and concentrations in surface and subsurface water samples. Chemical Geology 258, 136-144.

Peucker-Ehrenbrink, B., Ravizza, G., 2000. The marine osmium isotope record. Terra Nova 12, 205-219.

Peucker-Ehrenbrink, B., Ravizza, G., 2012. Osmium isotope stratigraphy. The Geologic Time Scale 2012, 145-166.

Peucker-Ehrenbrink, B., Sharma, M., Reisberg, L., 2013. Recommendations for analysis of dissolved osmium in seawater. Eos, Transactions American Geophysical Union 94, 73-73.

Prouty, N.G., Roark, E.B., Koenig, A.E., Demopoulos, A.W., Batista, F.C., Kocar, B.D., Selby, D., McCarthy, M.D., Mienis, F., Ross, S.W., 2014. Deep-sea coral record of human impact on watershed quality in the Mississippi River Basin. Global Biogeochemical Cycles 28, 29-43.

Racionero-Gómez, B., Sproson, A., Selby, D., Gröcke, D., Redden, H., Greenwell, H., 2016. Rhenium uptake and distribution in phaeophyceae macroalgae, Fucus vesiculosus. Royal Society Open Science 3, 160161.

Racionero-Gómez, B., Sproson, A.D., Selby, D., Gannoun, A., Gröcke, D.R., Greenwell, H.C., Burton, K.W., 2017. Osmium uptake, distribution, and 187Os/188Os and 187Re/188Os compositions in Phaeophyceae macroalgae, Fucus vesiculosus: Implications for determining the 187Os/188Os composition of seawater. Geochimica et Cosmochimica Acta 199, 48-57.

Raymo, M.E., Ruddiman, W.F., Froelich, P.N., 1988. Influence of late Cenozoic mountain building on ocean geochemical cycles. Geology 16, 649-653.

Richter, F.M., Turekian, K.K., 1993. Simple models for the geochemical response of the ocean to climatic and tectonic forcing. Earth and Planetary Science Letters 119, 121-131.

Rooney, A.D., Selby, D., Lloyd, J.M., Roberts, D.H., Lückge, A., Sageman, B.B., Prouty, N.G., 2016. Tracking millennial-scale Holocene glacial advance and retreat using osmium isotopes: Insights from the Greenland ice sheet. Quaternary Science Reviews 138, 49-61.

Sharma, M., Balakrishna, K., Hofmann, A.W., Shankar, R., 2007. The transport of Osmium and Strontium isotopes through a tropical estuary. Geochimica et Cosmochimica Acta 71, 4856-4867.

Sharma, M., Chen, C., Blazina, T., 2012. Osmium contamination of seawater samples stored in polyethylene bottles. Limnology and Oceanography: Methods 10, 618-630.

Sharma, M., Papanastassiou, D., Wasserburg, G., 1997. The concentration and isotopic composition of osmium in the oceans. Geochimica et Cosmochimica Acta 61, 3287-3299.

Sharma, M., Wasserburg, G., 1997. Osmium in the rivers. Geochimica et cosmochimica acta 61, 5411-5416.

Sharma, M., Wasserburg, G., Hofmann, A., Chakrapani, G., 1999. Himalayan uplift and osmium isotopes in oceans and rivers. Geochimica et Cosmochimica Acta 63, 4005-4012.

Turekian, K.K., Sharma, M., Gordon, G.W., 2007. The behavior of natural and anthropogenic osmium in the Hudson River–Long Island Sound estuarine system. Geochimica et Cosmochimica Acta 71, 4135-4140.

Völkening, J., Walczyk, T., Heumann, K.G., 1991. Osmium isotope ratio determinations by negative thermal ionization mass spectrometry. International Journal of Mass Spectrometry and Ion Processes 105, 147-159.

Walker, J.C.G., Hays, P.B., Kasting, J.F., 1981. A negative feedback mechanism for the long-term stabilization of Earth's surface temperature. Journal of Geophysical Research 86, 9776.

Woodhouse, O., Ravizza, G., Falkner, K.K., Statham, P., Peucker-Ehrenbrink, B., 1999. Osmium in seawater: vertical profiles of concentration and isotopic composition in the eastern Pacific Ocean. Earth and Planetary Science Letters 173, 223-233.

Yang, J.S., 1991. High rhenium enrichment in brown algae: a biological sink of rhenium in the sea? Hydrobiologia 211, 165-170.

Chapter 3

Tracing anthropogenic osmium around Japan using the osmium isotopic composition of macroalgae*

*A version of this chapter will be submitted to Environmental Science and Technology, co-authored with David Selby and Katsuhiko Suzuki.

This study presents rhenium (Re) and osmium (Os) abundance and isotope data for macroalgae from Japanese coastal waters adjacent to densely populated megacities (Tokyo, Osaka and Nagoya) and sparsely populated regions of Japan (The Izu peninsula, The Noto peninsula, northern Honshu and Hokkaido). The ^{187}Os/^{188}Os composition of macroalgae is highly variable (0.16 to 1.09) and can be explained in terms of mixing between seawater and: rivers draining Miocene-Holocene continental rocks with a radiogenic ^{187}Os/^{188}Os composition; and/or, anthropogenic sources of Os with an unradiogenic ^{187}Os/^{188}Os composition. The Os emitted from catalytic convertor use in vehicles predominantly controls the Os isotope budget of coastal waters in densely populated regions of Japan. However, Os derived from medical research, municipal solid waste incinerators and sewage outflow can generate localised point sources of anthropogenic Os. Anthropogenic Os attributed to coastal cities, which is transferred via surface waters to world's oceans, represents a substantial source of unradiogenic Os which is driving surface seawater to lower ^{187}Os/^{188}Os ratios (~0.95) than deeper waters (~1.05). This suggests the demand in PGEs, their refining and eventual use in catalytic convertors is impacting the global Os cycle. Finally, this study suggests that osmium isotopes in macroalgae could become a powerful environmental indicator and tracer of continental inputs to the marine Os cycle.

3.1 Introduction

The osmium isotopic composition (^{187}Os/^{188}Os) of seawater reflects a balance between radiogenic continental sources and unradiogenic mantle and extraterrestrial derived sources, and has traditionally been used to trace a wide range of Earth system processes, both today and in the Earth's geological past (Peucker-Ehrenbrink and Ravizza, 2000, 2012). However, human activity is perturbing the marine Os cycle (Chen et al., 2009) and anthropogenic Os contamination has been detected in estuaries (Turekian et al., 2007;

Williams et al., 1997), coastal sediments (Esser and Turekian, 1993; Ravizza and Bothner, 1996), lakes (Rauch et al., 2004) and precipitation (Chen et al., 2009) (See Table 1). Potential sources of anthropogenic Os to the atmosphere and the marine environment include: (i) the combustion of fossil fuels; (ii) smelting of platinum group element (PGE: Os, Ir, Pt, Pd, Ru, Rh) sulphide ores; (iii) smelting of base-metal (Pb, Ni, Cu, and Zn) sulphide ores; (iv) smelting of aluminium ore (v) smelting of chromium ore; (vi) exhaust from automobile catalytic convertors; (vii) emissions from incinerators; and, (viii) sewage outflow (See Table 1).

Table 1

Comparison of natural and anthropogenic sources of Os and Re. Data references are: seawater (Peucker-Ehrenbrink and Ravizza, 2000); river water (Peucker-Ehrenbrink and Ravizza, 2000); precipitation (Chen et al., 2009); loess (Peucker-Ehrenbrink and Jahn, 2001); cosmic dust (Peucker-Ehrenbrink and Ravizza, 2000); HT hydrothermal (Peucker-Ehrenbrink and Ravizza, 2000); LT hydrothermal (Peucker-Ehrenbrink and Ravizza, 2000); fossil fuels (Selby and Creaser, 2005; Selby et al., 2007); base-metal sulphide ores (Lambert et al., 1998; Morgan et al., 2002; Walker et al., 1994); PGE ores (McCandless and Ruiz, 1991); chromites (Walker et al., 2002); aluminium smelter (Gogot et al., 2015); airborne particles (Rauch et al., 2005); urban sediments (Rauch et al., 2004); car catalysts (Poirier and Gariépy, 2005); sewage sludge (Esser and Turekian, 1993); MSWI ashes (Funari et al., 2016).

	[Os] (fg/g)	^{187}Os/^{188}Os	[Re] (pg/g)	^{187}Re/^{188}Os
Natural				
Seawater	10	1.06	8.2	4270
River Water	9.1	1.4	428	227
Precipitation	0.3 - 16.9	0.16 - 0.98		
Loess	3.1 x 10^{4}	1.05	3 x 10^{5}	50
Cosmic Dust	5 x 10^{8}	0.13	3.7 x 10^{7}	0.4
HT hydrothermal	2.8 - 38	0.13 - 0.39		
LT hydrothermal	98	0.11		
Anthropogenic				
Fossil Fuels	0.01 - 295 x 10^{3}	0.9 - 6	0.3 - 40.7 x 10^{3}	400 - 1300
Base-metal Sulphide Ore	0.02 - 89 x 10^{6}	0.13 - 24	0.6 - 286 x 10^{3}	0.8 - 5232
PGE Ore		0.15 - 0.19		

Chromites	2 - 1320 x 10^6	0.12	0.01 - 9.3 x 10^3	0.01 - 2.2
Aluminium Smelter	30 x 10^3	2.5		
Airborne Particles	0.001 - 0.82 pg/m^3	0.3 - 2.8		
Urban Sediments	56 - 395 x 10^3	0.36 - 2.2		
Car Catalysts	6 - 228 x10^3	0.16 - 0.19		
Sewage Sludge	10 - 100 x 10^3	0.6 - 1.7		
MSWI Ashes	26 - 1650 x 10^3	0.24 - 0.7		

Highly radiogenic anthropogenic ^{187}Os/^{188}Os sources include the smelting of bauxite ore (~2.5) and fossil fuels (1.1 to 13.7) (Finlay et al., 2011; Gogot et al., 2015; Selby and Creaser, 2005; Selby et al., 2007). In contrast, the ^{187}Os/^{188}Os values of PGE sulphide ores from the Bushveld Complex, South Africa (0.15 to 0.2), chromites (0.12 to 0.14), municipal solid waste incinerator (MSWI) ash (0.24 to 0.7) and sewage sludge are generally unradiogenic (Esser and Turekian, 1993; Funari et al., 2016; McCandless and Ruiz, 1991; Ravizza and Bothner, 1996; Turekian et al., 2007; Walker et al., 1994; Williams et al., 1997). The ^{187}Os/^{188}Os of base-metal sulphide ores are highly variable, and in some cases can be relatively radiogenic (e.g. Sudbury, Canada) due to contamination from continental sources, whilst in other cases they can record unradiogenic ^{187}Os/^{188}Os values similar to mantle derived sources (e.g. Noril'sk, Russia and Yilgarn craton, Australia) (Lambert et al., 1998; Morgan et al., 2002; Walker et al., 2002). Roughly 95% (Jones, 1999) of all PGEs are derived from unradiogenic sources (0.15 - 0.2), which is reflected in the ^{187}Os/^{188}Os measurements of the catalytic convertors from which they are made (0.1 - 0.2) (Poirier and Gariépy, 2005), suggesting the ^{187}Os/^{188}Os of automobile exhaust will be of similar values (Chen et al., 2009).

Smelters (Gogot et al., 2015; Rodushkin et al., 2007b), incinerators (Funari et al., 2016; Turekian et al., 2007; Williams and Turekian, 2002) and sewage outflow (Esser and Turekian, 1993; Ravizza and Bothner, 1996; Turekian et al., 2007; Williams et al., 1997) represent point sources in anthropogenic Os, whereas catalytic convertors represent a regional influence in densely populated areas (Poirier and Gariépy, 2005). On a global scale, the refining of PGE ores, and to a lesser extent automobile exhaust, has driven global precipitation towards the isotopic composition of ores (~0.2) (Chen et al., 2009). Moreover, present-day surface waters have lower $^{187}Os/^{188}Os$ values (~0.95) than deep waters (~1.05), suggesting humans have impacted the global Os cycle and the world's oceans (Chen et al., 2009). Osmium isotopes therefore hold the potential to become a powerful tracer of hydrologic, oceanographic and anthropogenic processes 'similar to Pb from leaded gasoline usage before 1978 or tritium from atmospheric atomic bomb testing in the early 1960s' (Chen et al., 2009).

Despite this potential, and the establishment of ultra-low blank analytical techniques capable of oxidising all osmium to a common oxidation state (Chen and Sharma, 2009; Gannoun and Burton, 2014; Levasseur et al., 1998; Paul et al., 2009), the direct analysis of Os in seawater still remains analytically challenging due to ultra-low Os concentrations (Peucker-Ehrenbrink et al., 2013). Therefore, the measurements of anthropogenic Os in rivers, estuaries and coastal and oceanic waters remain sparse. Recent work indicates that macroalgae (seaweed) concentrates Os (with abundances that vary from 3.3 to 254.5 ppt), whilst maintaining the $^{187}Os/^{188}Os$ composition of the seawater it inhabits (Racionero-Gómez et al., 2017; Rooney et al., 2016; Chapter 2). This suggests that macroalgae could act as a proxy for the $^{187}Os/^{188}Os$ composition of local waters whilst removing some of the analytical challenges associated with direct analysis of seawater i.e. ultra-low concentrations and multiple oxidation states. Macroalgae existing in coastal waters, therefore, should record an $^{187}Os/^{188}Os$ signature that reflects a balance of local inputs, including riverine input, local bedrock and seawater and has been utilised to understand natural processes in Greenland (Rooney et al., 2016) and Iceland (Chapter 2).

Japan offers a unique place in which to study the influence of anthropogenic processes on regional variations in the marine Os cycle. Large, densely populated, sprawling metropolitan areas often fall in close proximity to coastal waters, inlet seas or bays. These metropolitan areas are often juxtaposed to sparsely populated rural and/or mountainous regions, with little human activity and therefore anthropogenic influence. This study presents Re-Os abundance and isotope data for macroalgae from Tokyo Bay, Osaka Bay, Ise Bay, Mikawa Bay, Izu Peninsula, Noto Peninsula, Hokkaido and northern Honshu.

Tokyo Bay, Osaka Bay and Ise/Mikawa Bay lie in close proximity to the Kanto (Tokyo-Yokohama), Keihanshin (Osaka-Kobe) and Chukyo (Nagoya) metropolitan areas. The ^{187}Os/^{188}Os signature from these regions is much lower than expected for natural river and oceanic systems, but similar to the isotope composition of PGE ores. This suggests that human activity has influenced the ^{187}Os/^{188}Os of macroalgae, and therefore seawater, through the burning of municipal and/or hospital waste, processing of sewage and the extensive use of automobiles in these areas. The Izu Peninsula, the Noto Peninsula, Hokkaido and northern Honshu exhibit ^{187}Os/^{188}Os values similar to global river water or Pacific seawater measurements, suggesting little influence from human activity. These results demonstrate the ability of macroalgae to trace fluctuations in the ^{187}Os/^{188}Os compositions of freshwater and seawater around Japan, and utilise this to determine the influence of human activity on the global osmium budget.

3.2 Field and analytical techniques

3.2.1 Sampling and storage

Macroalgae from Osaka Bay (Sample Location 16-22) were sampled at 7 locations during September 2014. Macroalgae from Tokyo Bay (Sample Location 1-15), the Izu peninsula (Sample Location 31-36) and the Noto peninsula (Samples Location 37-43) were sampled at 28 locations between July and September 2015. A further 8 locations in the Ise (Sample

Location 23-24) and Mikawa (Sample Location 25-30) Bays were sampled during December 2015. Macroalgae from northern Honshu (Sample Location 44-48) were sampled at 5 locations during September 2016. Samples from Hokkaido were purchased at tsukiji fish market in Tokyo. In total sixty-four macroalgae samples were collected (Fig. 1; Table 1). Macroalgae were washed using deionised (Milli-Q™) water to remove any attached sediment and salt. They were then dried for 12 h at 60 °C and stored in plastic zip-lock bags. Macroalgae were later crushed using an agate pestle and mortar prior to analysis.

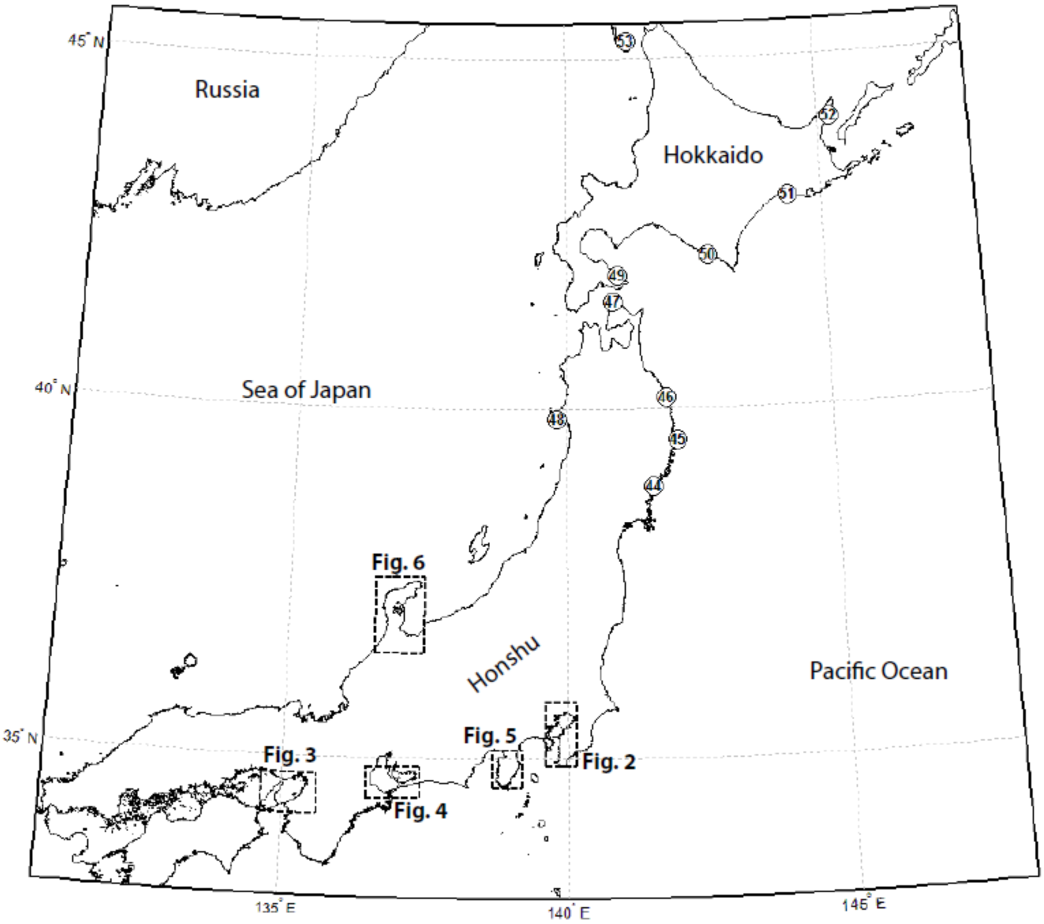

Fig. 1. Map of Japan. Macroalgae sample locations for northern Honshu and Hokkaido are displayed (Circles; Table 2). Dashed lines represent an outline of areas shown in Figures 2 (Tokyo Bay), 3 (Osaka Bay), 4 (Ise and Mikawa Bay), 5 (The Izu peninsula) and 6 (Kanazawa and the Noto peninsula).

3.2.2 Macroalgae species and habitats

Specific macroalgae species were not targeted during this study, and samples were selected based on their availability at sample sites. There was however a preference to brown macroalgae over green and red macroalgae due to their relatively high abundance in Re (Mas et al., 2005; Prouty et al., 2014; Racionero-Gómez et al., 2016; Yang, 1991) and Os (Racionero-Gómez et al., 2017; Chapter 2; Rooney et al., 2016). Twenty species of macroalgae were analysed: *Monostroma nitidum; Urospora penicilliformis; Hizikia fusiformis; Undaria pinnatifidia; Dictyopteris undulata Holmes; Gloiopeltis complanata; Spatoglossum crissum; Gloiopeltis furcate; Sargassum fusiforme; Sargassum muticum; Gelidum elegans Kutzing; Gracilaria vermiculophylla (Ohmi) Papenfuss; Sargassum horneri; Grateloupia carnosa; Schizymenia dubyi; Grateloupia lanceolate; Porphyra tenera Kjellman; Pachydictyon coriaceum (Holmes) Okamura; Gracilaria bursa-pastoris;* and*, Laminaria japonica.*

3.2.3 Re-Os analysis

The Re-Os analysis of macroalgae was carried out in the Durham Geochemistry Centre (Laboratory for Sulfide and Source Rock Geochronology and Geochemistry).

3.2.3.1 Macroalgae

The technique for chemical separation of Re and Os from macroalgae is reported by Racionero-Gómez et al. (2017). In brief, approximately 200 mg of powdered macroalgae was introduced into a Carius tube together with 11 N HCl (3 mL), 15.5 N HNO_3 (6 mL) and a known amount of ^{185}Re + ^{190}Os tracer solution and heated to 220°C in an oven for 24 h. The Os was isolated from the acid medium using $CHCl_3$ solvent extraction and then back extracted into HBr. The Os was further purified using a CrO_3-H_2SO_4 – HBr micro-distillation

(Birck et al., 1997; Cohen and Waters, 1996). The remaining Re-bearing acid medium was evaporated to dryness at 80°C, with the Re isolated and purified using both NaOH-acetone solvent extraction and HNO_3-HCl anion chromatography (Cumming et al., 2013).

3.2.3.2 Mass Spectrometry

The purified Re and Os fractions were loaded onto Ni and Pt filaments respectively, and measured using NTIMS (Creaser et al., 1991; Völkening et al., 1991) on a Thermo Scientific TRITON mass spectrometer using Faraday collectors in static mode, and an electron multiplier in dynamic mode respectively. The Re and Os abundances and isotope compositions are presented with 2 s.e. (standard error) absolute uncertainties which include full error propagation of uncertainties in the mass spectrometer measurements, blank, spike calibrations, and sample and spike weights. Full analytical blank values for the macroalgae analysis are 10.9 ± 5.9 pg for Re, 0.13 ± 0.13 pg for Os, with a $^{187}Os/^{188}Os$ composition of 0.61 ± 0.34 (1 SD, n = 4).

To monitor the long-term reproducibility of mass spectrometer measurements Re and Os (DROsS, DTM) reference solutions were analysed. The 125 pg Re solution yields an average $^{185}Re/^{187}Re$ ratio of 0.5987 ± 0.0023 (2 SD., n = 8), which is in agreement with published values (e.g., Cumming et al., 2013 and references therein). A 50 pg DROsS solution gave an $^{187}Os/^{188}Os$ ratio of 0.16111 ± 0.0008 (2 SD., n = 8), which is in agreement with reported value for the DROsS reference solution (Nowell et al., 2008).

3.3 Results

The Re and Os abundance and isotope data for macroalgae are presented in Table 2. The Re and Os abundance show a large range from 0.02 to 21.43 ppb and 1.96 to 122.76 ppt respectively. The $^{187}Os/^{188}Os$ and $^{187}Re/^{188}Os$ compositions are highly variable and range from 0.16 to 1.09 and 8.7 to 11234.5 respectively. The reason(s) for the variation is discussed is section 4. In section 3.3.2 to 3.3.6, the position of sample locations are compared to several indicators of human activity. Population density data (ESRI, 2014), Os pollution sources (Google Earth, 2016) and CO_2 emission data from EAGrid2010 (Kannari et al., 2007) can be found in panel b, c and d (Figs. 2 to 6) respectively.

Table 2

Rhenium and osmium abundance and isotope data for Japanese macroalgae samples

Sample Location	Macroalgae Species	[Re] (ppb)	2 s.e.	[Os] (ppt)	2 s.e.	$^{187}Re/^{188}Os$	2 s.e.	$^{187}Os/^{188}Os$	2 s.e.
Tokyo Bay									
1	*Monostroma nitidum*	0.02	0.03	3.90	0.08	28.7	38.9	0.519	0.032
2	*Monostroma nitidum*	3.56	0.20	11.27	0.22	1603.9	113.4	0.541	0.031
3	*Monostroma nitidum*	2.88	0.05	3.33	0.07	4462.4	215.1	0.674	0.041
4	*Monostroma nitidum*	0.07	0.03	7.67	0.08	42.2	19.4	0.363	0.011
5	*Urospora penicilliformis*	3.72	0.04	24.03	0.11	789.5	9.3	0.582	0.006
5	*Monostroma nitidum*	0.305	0.001	12.18	0.05	124.7	1.0	0.397	0.004
6	*Monostroma nitidum*	3.65	0.04	29.19	0.56	639.5	26.7	0.592	0.034
7	*Urospora penicilliformis*	0.52	0.03	29.86	0.31	87.9	5.4	0.463	0.014
7	*Urospora penicilliformis*	0.938	0.009	30.06	0.31	156.3	3.6	0.428	0.012
8	*Urospora penicilliformis*	0.233	0.003	26.57	0.50	43.9	1.9	0.436	0.025
rpt	*Urospora penicilliformis*	0.37	0.03	18.14	0.34	101.6	9.3	0.455	0.026
9	*Monostroma nitidum*	0.127	0.001	17.21	0.13	37.0	0.6	0.418	0.009
9	*Monostroma nitidum*	0.269	0.001	17.60	0.08	76.7	0.6	0.450	0.005
10	*Monostroma nitidum*	0.05	0.03	3.77	0.08	71.0	40.5	0.551	0.034
11	*Monostroma nitidum*	0.06	0.03	3.44	0.07	85.7	45.2	0.669	0.041
12	*Hizikia fusiformis*	1.63	0.09	10.00	0.07	861.6	50.3	0.867	0.012
13	*Undaria pinnatifidia*	2.14	0.02	5.85	0.04	1948.2	27.2	0.950	0.015
14	*Dictyopteris undulata Holmes*	0.10	0.03	7.40	0.15	68.5	21.7	0.910	0.053
15	*Gloiopeltis complanata*	7.65	0.14	17.10	0.20	2362.2	66.3	0.857	0.026
Osaka Bay									
16	*Spatoglossum crassum*	1.33	0.07	13.25	0.08	502.6	26.7	0.445	0.007
16	*Gloiopeltis furcata*	0.58	0.03	21.31	0.22	137.3	8.5	0.497	0.014
17	*Sargassum fusiforme*	3.64	0.17	122.76	0.54	143.6	6.9	0.165	0.002
17	*Undaria pinnatifidia*	4.21	0.15	23.91	0.45	876.0	47.7	0.380	0.022
rpt	*Undaria pinnatifidia*	3.49	0.17	24.87	0.39	697.4	40.6	0.364	0.017
18	*Undaria pinnatifidia*	7.05	0.25	22.78	0.25	1589.2	65.5	0.628	0.018
18	*Undaria pinnatifidia*	4.72	0.22	14.34	0.20	1683.0	91.7	0.597	0.023
19	*Undaria pinnatifidia*	4.21	0.15	18.81	0.36	1144.2	62.5	0.591	0.034
19	*Gloiopeltis furcata*	0.55	0.04	11.36	0.12	246.6	18.5	0.521	0.015
20	*Sargassum fusiforme*	2.58	0.10	25.89	0.16	518.8	20.0	0.758	0.010
21	*Sargassum muticum*	0.38	0.03	16.59	0.18	114.5	10.3	0.508	0.015
22	*Undaria pinnatifidia*	3.18	0.12	19.34	0.37	830.8	45.6	0.497	0.029
Ise Bay									
23	*Gelidum elegans*	0.16	0.03	88.80	0.84	8.7	1.7	0.158	0.005

	Kutzing								
23	*Gracilaria vermiculophylla (Ohmi) Papenfuss*	0.08	0.03	27.06	0.49	15.0	5.4	0.185	0.011
24	*Undaria pinnatifida*	1.37	0.07	22.01	0.13	318.5	16.7	0.602	0.008
Mikawa Bay									
25	*Sargassum horneri*	0.36	0.03	10.62	0.21	176.3	18.5	0.742	0.043
26	*Sargassum muticum*	0.24	0.03	7.31	0.15	167.3	23.8	0.689	0.041
27	*Grateloupia carnosa*	3.82	0.18	5.30	0.09	3661.5	217.3	0.544	0.027
28	*Sargassum muticum*	21.43	1.00	14.78	0.08	7523.2	354.7	0.716	0.008
29	*Schizymenia dubyi*	0.19	0.03	3.00	0.06	327.6	55.1	0.513	0.032
30	*Grateloupia lanceolata*	0.27	0.03	3.51	0.04	390.0	48.1	0.537	0.017
Izu Peninsula									
31	*Hizikia fusiformis*	4.83	0.17	16.92	0.19	1504.3	62.5	0.842	0.025
32	*Porphyra tenera Kjellman*	0.61	0.04	7.78	0.09	407.4	26.4	0.704	0.022
33	*Pachydictyon coriaceum (Holmes) Okamura*	4.22	0.15	10.25	0.14	2129.3	97.2	0.692	0.027
34	*Dictyopteris undulata Holmes*	4.79	0.17	15.21	0.14	1628.8	64.8	0.697	0.017
35	*Hizikia fusiformis*	0.65	0.04	28.10	0.32	122.0	7.6	0.905	0.026
36	*Undaria pinnatifidia*	0.89	0.04	8.69	0.06	537.4	26.9	0.776	0.010
Kanazawa and the Noto Peninsula									
37	*Monostroma nitidum*	0.16	0.03	5.18	0.10	158.6	30.7	0.459	0.028
38	*Gracilaria bursa-pastoris*	0.12	0.03	6.13	0.12	100.8	25.5	0.476	0.028
38	*Monostroma nitidum*	0.03	0.03	2.29	0.05	70.2	66.1	0.483	0.031
39	*Gracilaria bursa-pastoris*	0.61	0.04	19.24	0.38	166.0	13.2	0.848	0.049
40	*Dictyopteris undulata Holmes*	3.18	0.15	27.16	0.54	623.1	39.0	0.937	0.054
41	*Sargassum muticum*	1.73	0.09	32.80	0.21	279.1	14.1	0.888	0.011
42	*Dictyopteris undulata Holmes*	2.56	0.11	12.20	0.07	1101.0	49.0	0.822	0.009
43	*Sargassum muticum*	1.60	0.07	25.26	0.17	341.0	16.1	1.017	0.013
Northern Honshu									
44	*Laminaria japonica*	0.82	0.04	3.98	0.05	1078.3	54.7	0.763	0.024
45	*Laminaria japonica*	2.12	0.06	6.40	0.04	1727.7	54.1	0.765	0.008
46	*Laminaria japonica*	1.44	0.05	16.16	0.14	470.1	17.3	0.884	0.018
47	*Laminaria japonica*	0.60	0.03	12.10	0.14	263.2	16.0	0.921	0.027
48	*Laminaria japonica*	3.92	0.11	11.10	0.19	1877.8	83.3	0.923	0.045
Hokkaido									
49	*Laminaria japonica*	7.71	0.02	3.69	0.05	11234.5	257.2	1.016	0.031
50	*Laminaria japonica*	2.637	0.009	4.02	0.08	3517.9	154.1	0.984	0.059
51	*Laminaria japonica*	1.27	0.07	1.96	0.05	3485.2	269.9	1.015	0.068
52	*Laminaria japonica*	2.878	0.009	5.06	0.11	3078.9	132.4	1.075	0.064
53	*Laminaria japonica*	11.87	0.04	11.32	0.10	5689.1	82.2	1.093	0.022

3.3.1 Hokkaido and Northern Honshu

The Re and Os abundance in macroalgae from Northern Honshu and Hokkaido (Fig. 1) varies from 0.6 to 11.87 ppb and 1.96 to 16.16 ppt respectively. The $^{187}Os/^{188}Os$ and $^{187}Re/^{188}Os$ compositions range from 0.76 to 1.09 and 263.2 to 11234.52 respectively. No discernible pattern can be found between Re and Os abundance and geographical position.

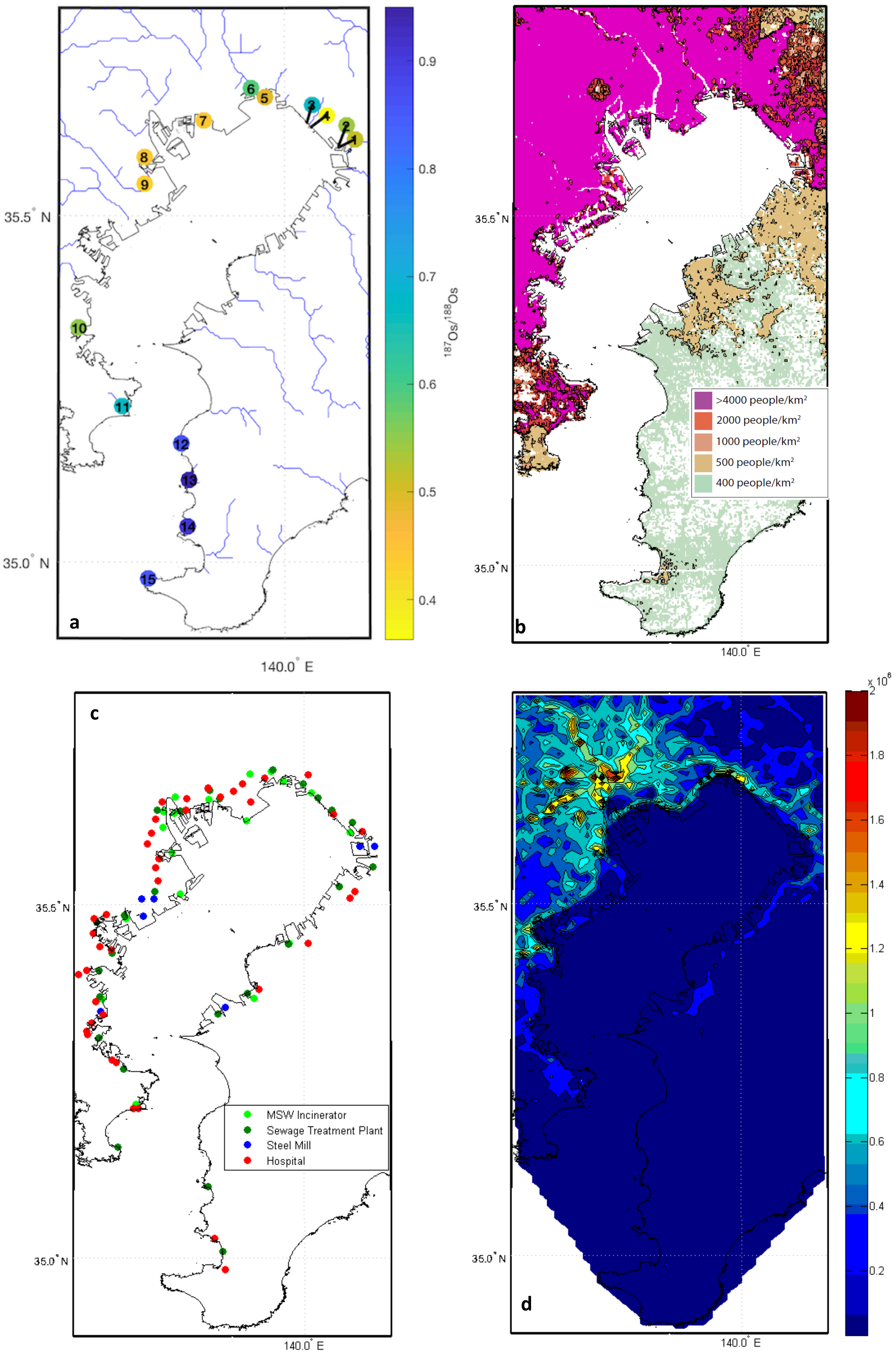
a
1
2
3
4
5
6
7
8
9
10
11
12
13
14
15
35.5° N
35.0° N
140.0° E
0.9
0.8
0.7
0.6
0.5
0.4
$^{187}Os/^{188}Os$
b
35.5° N
35.0° N
140.0° E
>4000 people/km²
2000 people/km²
1000 people/km²
500 people/km²
400 people/km²
c
35.5° N
35.0° N
140.0° E
MSW Incinerator
Sewage Treatment Plant
Steel Mill
Hospital
d
35.5° N
35.0° N
140.0° E
x 10^6
2
1.8
1.6
1.4
1.2
1
0.8
0.6
0.4
0.2

Fig. 2. Sample locations and $^{187}Os/^{188}Os$ macroalgae values (**a**), population density (**b**), potential Os point source locations (**c**) and annual vehicle CO_2 emissions in t-CO_2 km^{-2} yr^{-1} (**d**) for the Tokyo Bay area.

The $^{187}Os/^{188}Os$ and $^{187}Re/^{188}Os$ composition of macroalgae is generally higher in macroalgae from Hokkaido (avg. $^{187}Os/^{188}Os$ = ~1.03; avg. $^{187}Re/^{188}Os$ = ~5401) than northern Honshu (avg. $^{187}Os/^{188}Os$ = ~0.85; avg. $^{187}Re/^{188}Os$ = ~1083).

3.3.2 Tokyo Bay

The Re and Os abundance in macroalgae from Tokyo Bay (Fig. 2a) varies from 0.02 to 7.65 ppb and 3.33 to 30.06 ppt respectively. The $^{187}Os/^{188}Os$ and $^{187}Re/^{188}Os$ compositions range from 0.36 to 0.95 and 28.7 to 4462.4 respectively. No discernible pattern can be found between Re abundance and $^{187}Re/^{188}Os$ composition and geographical position. Osmium abundance is generally higher in macroalgae with proximity to central Tokyo (Samples 5 to 9). The $^{187}Os/^{188}Os$ composition of macroalgae from Tokyo Bay are highly variable. Relatively unradiogenic values (~0.36 to 0.67) are found in macroalgae from the northern and north-eastern parts of the bay, with consistently low (~0.4) $^{187}Os/^{188}Os$ values near central Tokyo (Samples 7 to 9). Macroalgae more proximal to the Pacific Ocean, possess $^{187}Os/^{188}Os$ values that become progressively more radiogenic (~0.7 to 0.95).

The densely populated cities of Yokohama, Tokyo and Chiba occupy western, northern and north-eastern parts of Tokyo Bay respectively (Fig. 2b). A large number of hospitals occupy the western and northern parts of the bay, while municipal solid waste incinerators (MSWIs) and sewage treatment plants dominate parts of the bay close to central Tokyo and Chiba (Fig. 2c). Major highways connecting the cities of Yokohama, Tokyo and Chiba, generate high annual vehicle CO_2 emissions along the edge of the northern part of the Bay (Fig. 2d). Major highways and traffic congestion lead to exceptionally high vehicle emissions in central Tokyo (Fig. 2d).

3.3.3 Osaka Bay

The Re and Os abundance in macroalgae from Osaka Bay (Fig. 3a) varies from 0.38 to 7.05 ppb and 11.36 to 122.76 ppt respectively. The ^{187}Os/^{188}Os and ^{187}Re/^{188}Os compositions range from 0.17 to 0.76 and 114.5 to 1683 respectively. No discernible pattern can be found between Re abundance, Os abundance and ^{187}Re/^{188}Os compositions and geographical position. The ^{187}Os/^{188}Os composition of macroalgae from Osaka Bay is highly variable. Samples along the eastern coast of Awaji Island vary from relatively unradiogenic ^{187}Os/^{188}Os values (0.16 to 0.45) towards the south (Sample site 18) and the centre (Sample site 17) to relatively radiogenic ^{187}Os/^{188}Os values (0.52 to 0.63) in the north (Sample site 18 and 19). The most radiogenic ^{187}Os/^{188}Os values (~0.76) can be found close to central Osaka (Sample site 20), with relatively homogenous ^{187}Os/^{188}Os values of ~0.5 occurring south of Osaka (Sample site 21 and 22).

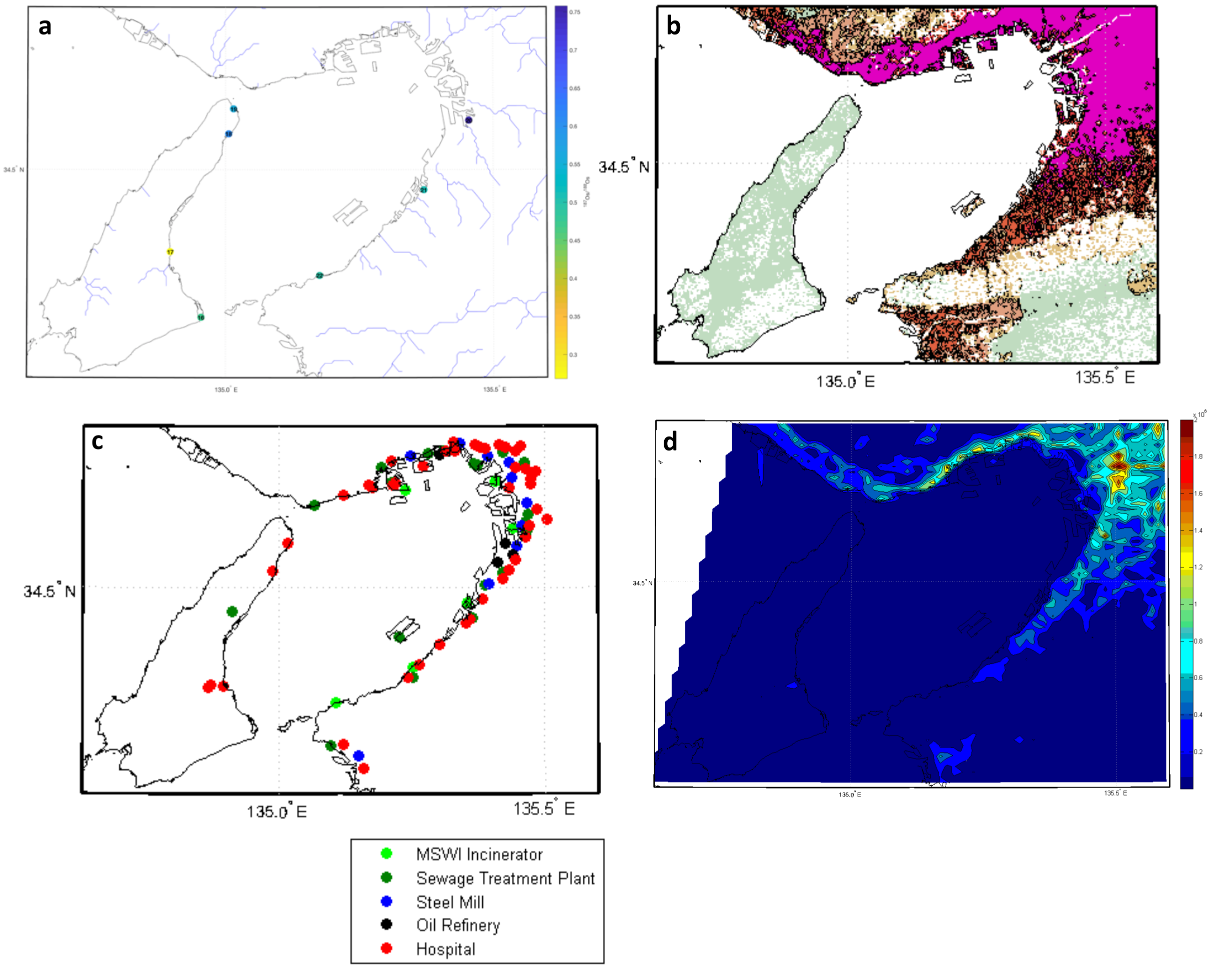

Fig. 3. Sample locations and ^{187}Os/^{188}Os macroalgae values (**a**), population density (**b**), potential Os point source locations (**c**) and annual vehicle CO_2 emissions in t-CO_2 km^{-2} yr^{-1} (**d**) for the Osaka Bay area. See Fig. 2 for population density information.

The densely populated megacity of Osaka lies to the north-east of the bay and the large city of Kobe occupies the northern coast (Fig 3b). These cities generally represent more than 4000 people per square km, while Awaji Island to the south-west has a population lower than 400 people per square km (Fig. 3b). A large number of hospitals, MSWI, sewage treatment plants and steel mills occupy the eastern coastline of Osaka Bay (Fig. 3c). A small section of the eastern bay is occupied by several large oil refineries (Black circles in Fig. 3c). Three hospitals are clustered near central Awaji Island with a further two at the northern tip of the island (Fig. 3c). Major highways running to Osaka and Kobe generate high annual vehicle CO_2 emissions along the northern edge of the Bay (Fig. 3d). Exceptionally high vehicle emissions can be found in central Osaka (Fig. 3d).

3.3.4 Ise and Mikawa Bay

The Re and Os abundance in macroalgae from Ise and Mikawa Bay (Fig. 4a) vary from 0.16 to 21.43 ppb and 3 to 88.8 ppt respectively. The ^{187}Os/^{188}Os and ^{187}Re/^{188}Os compositions range from 0.16 to 0.74 and 8.7 to 7521.2 respectively. No discernible pattern can be found between Re abundance, Os abundance, and ^{187}Re/^{188}Os and geographical position. The ^{187}Os/^{188}Os composition of macroalgae from Ise and Mikawa Bay are highly variable. Moderately radiogenic ^{187}Os/^{188}Os values (~0.51 to 0.54) are found along the northern coastline of Mikawa Bay close to the cities of Gamagori (Sample 29) and Nishio (Sample 30). The ^{187}Os/^{188}Os values along the southern coastline of Mikawa Bay are generally more radiogenic (~0.69 to 0.74) with the exception of sample 27 (~0.54). In the Ise Bay, ^{187}Os/^{188}Os values are relatively unradiogenic (~0.16) close to the city of Matsusaka (Sample

23), with more radiogenic $^{187}Os/^{188}Os$ values (~0.6) close to the mouth of the bay and the Philippine Sea (Sample 24).

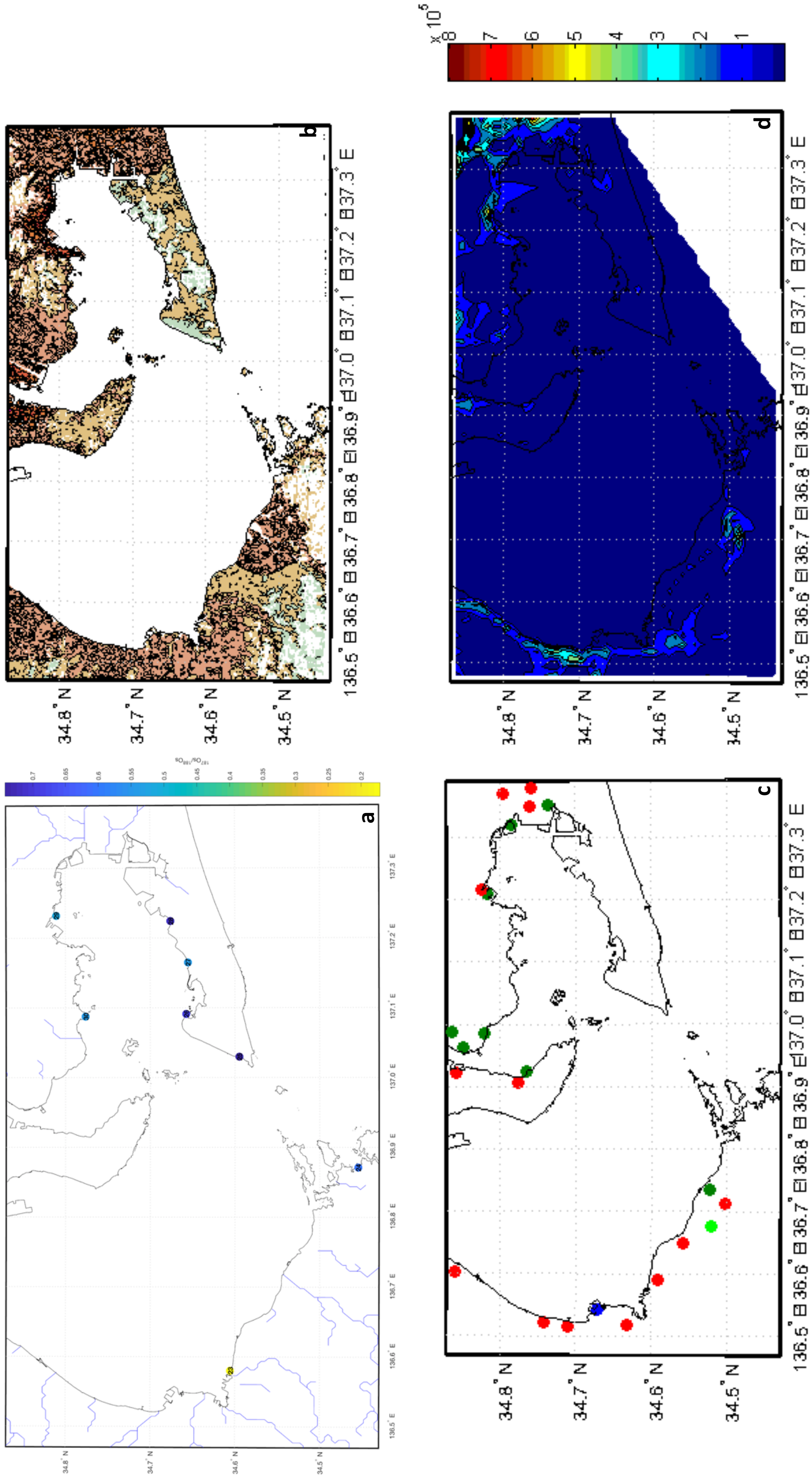

Fig. 4. Sample locations and $^{187}Os/^{188}Os$ macroalgae values (**a**), population density (**b**), potential Os point source locations (**c**) and annual vehicle CO_2 emissions in t-CO_2 km^{-2} yr^{-1} (**d**) for the Ise and Mikawa Bay areas. See Fig. 2 for population density and point source information.

The densely populated cities of Gamagori and Nishio occupy the northern coast of Mikawa Bay, with Toyohashi to the east (Fig. 4b). The densely populated city of Matsuaka occupies the western section of Ise Bay (Fig. 4b), with the megacity, Nagoya, to the north of the map. Several hospitals are spread across the western coastline of Ise Bay with a more densely grouping in Toyohashi (Fig. 4c). Several sewage treatment plants occupy the eastern and northwest regions of Mikawa Bay (Fig. 4c). Vehicle CO_2 emissions are relatively high in Toyohashi and along the western coastline of the Ise Bay (Fig. 4d).

3.3.5 Izu Peninsula

The Re and Os abundance in macroalgae from the Izu Peninsula (Fig. 5a) vary from 0.61 to 4.83 ppb and 7.78 to 28.1 ppt respectively. The $^{187}Os/^{188}Os$ and $^{187}Re/^{188}Os$ compositions range from 0.69 to 0.91 and 122 to 2129.3 respectively. No discernible pattern is observed between Re abundance, Os abundance, and $^{187}Re/^{188}Os$ and geographical position. The $^{187}Os/^{188}Os$ composition of macroalgae from the Izu Peninsula are variable, but all relatively radiogenic (~0.7 to 0.91). Along the southern tip of the peninsula (Sample Location 32 to 34) the $^{187}Os/^{188}Os$ values are ~0.7, with slightly more radiogenic values being found further north on the western coast ($^{187}Os/^{188}Os$ = ~0.84) and eastern coast ($^{187}Os/^{188}Os$ = 0.78 to 0.91). The Izu Peninsula is generally sparsely populated, with the largest city (Numazu) to the northwest of the peninsula (Fig. 5b). Several hospitals and MSWIs line the eastern coast of the peninsula (Fig. 5c). Vehicle CO_2 emissions are low across the entire peninsula, with the exception of the city of Numazu to the north (Fig. 5d).

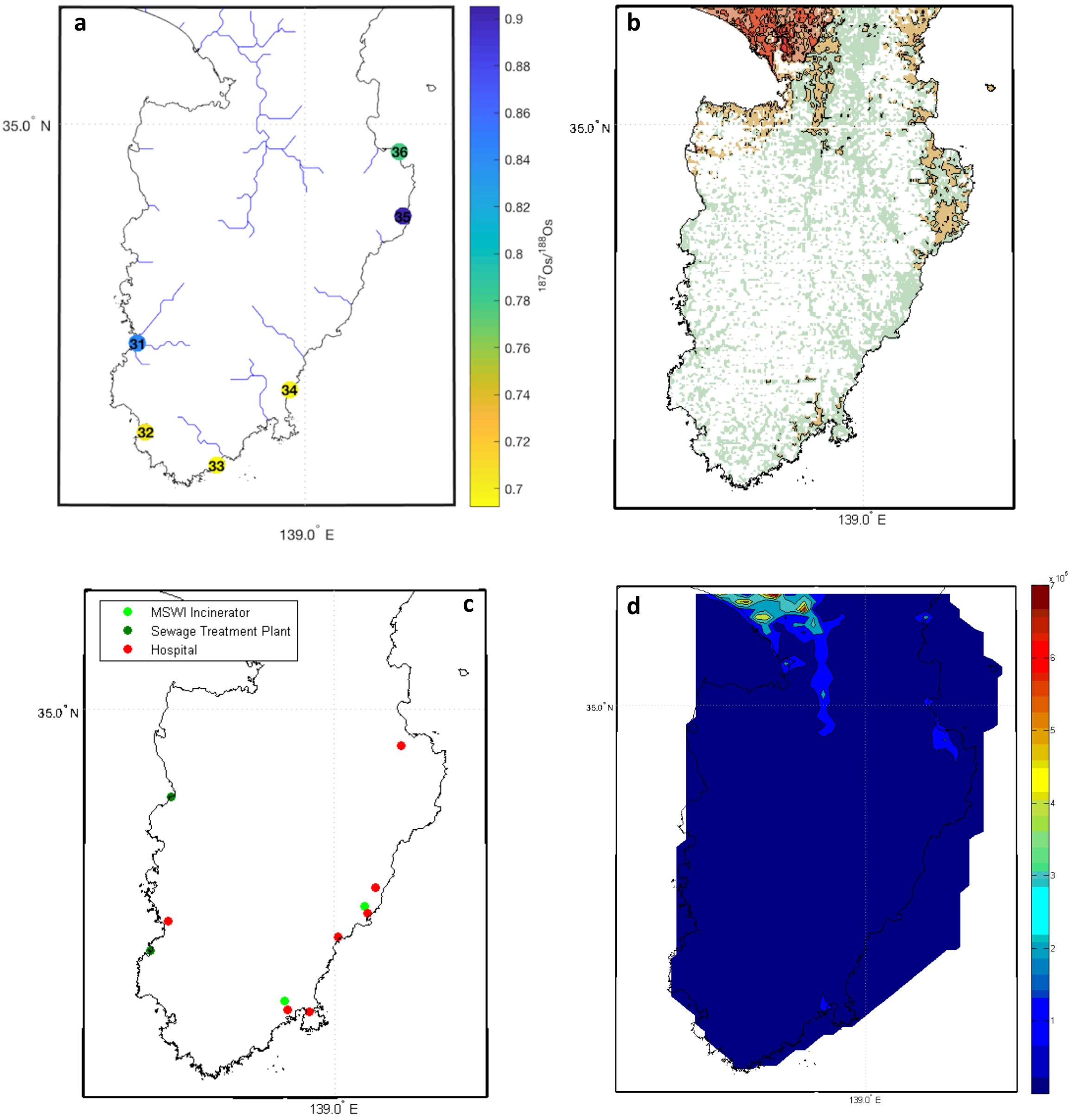

Fig. 5. Sample locations and $^{187}Os/^{188}Os$ macroalgae values (**a**), population density (**b**), potential Os point source locations (**c**) and annual vehicle CO_2 emissions in t-CO_2 km^{-2} yr^{-1} (**d**) for the Izu Peninsula. See Fig. 2 for population density information.

3.3.6 Noto Peninsula

The Re and Os abundance in macroalgae from the Noto Peninsula (Fig. 6a) vary from 0.03 to 3.18 ppb and 2.29 to 32.8 ppt respectively. The $^{187}Os/^{188}Os$ and $^{187}Re/^{188}Os$ compositions range from 0.46 to 1.02 and 70.3 to 1101 respectively. The Re abundance of macroalgae from Kanazawa and the western coast of the Noto Peninsula (Sample Location 37 to 39) is

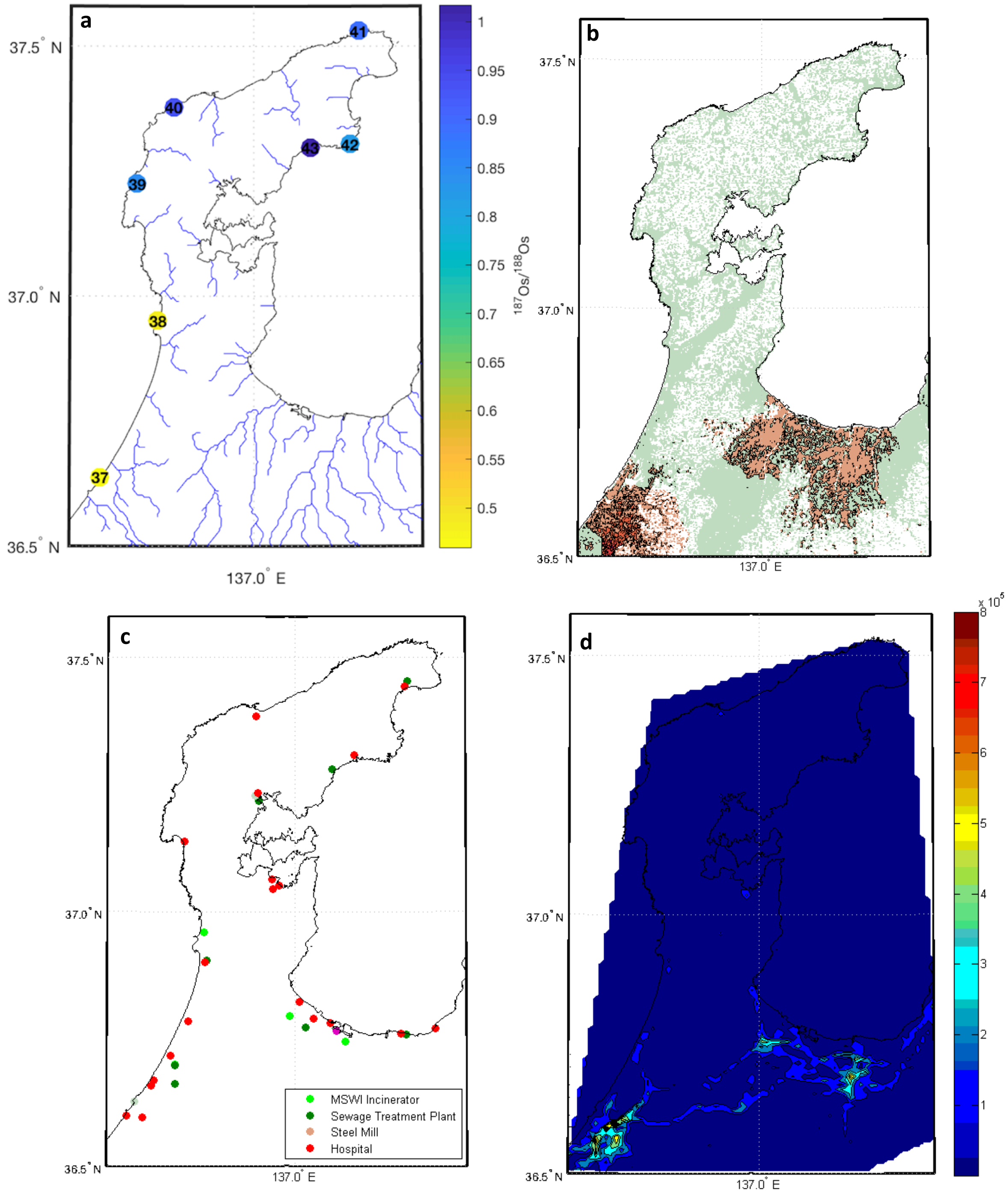

Fig. 6. Sample locations and $^{187}Os/^{188}Os$ macroalgae values (**a**), population density (**b**), potential Os point source locations (**c**) and annual vehicle CO_2 emissions in t-CO_2 km^{-2} yr^{-1} (**d**) for the Noto Peninsula. See Fig. 2 for population density information

lower (0.03 to 0.61 ppb) than for macroalgae of the northern and eastern coast of the Noto Peninsula (1.6 to 3.18 ppb). The Os abundance in macroalgae is lower (2.29 to 6.13 ppt) near the city of Kanazawa (Sample Location 37 and 38) than for macroalgae of the Noto Peninsula (12.2 to 32.8 ppt). The $^{187}Re/^{188}Os$ composition of macroalgae from the western coast of the Noto Peninsula (Sample Location 37 to 39) are lower (70.2 to 166) than for the northern and eastern coast of the Noto Peninsula (279.1 to 1101). The $^{187}Os/^{188}Os$ composition of macroalgae from the Izu Peninsula is highly variable. Relatively unradiogenic values (0.46 to 0.48) are found close to the major city of Kanazawa (Sample Location 37 and 38), whereas samples surrounding the Noto Peninsula are relatively radiogenic (0.82 to 1.02).

The Noto Peninsula is generally sparsely populated, with the largest city (Kanazawa) to the southwest, and the cities of Takaoka, Imizu and Toyama to the south east of the peninsula (Fig. 6b). Hospitals, MSWIs and sewage treatment plants are generally clustered in major cities, with several hospitals spread around the Noto Peninsula (Fig. 6c). Vehicle CO_2 emissions are low across the entire peninsula, with the exception of Kanazawa to the southwest and Takaoka and Toyama to the southeast (Fig. 6d).

3.4 Discussion

The large range in the $^{187}Os/^{188}Os$ composition of macroalgae (0.16 to 1.09) implies that both highly radiogenic and highly unradiogenic sources of Os contribute to the bulk Os in macroalgae. Natural sources of radiogenic Os include seawater, chemical weathering of radiogenic continental crust and the deposition of Aeolian dust, while anthropogenic sources include the smelting of radiogenic base-metal sulphide ores and contamination from fossil fuels. Natural sources of unradiogenic Os include hydrothermal alteration of oceanic crust, volcanism, cosmic dust and the chemical weathering of juvenile basaltic crust, whereas anthropogenic sources involve exhaust from automobiles and the processing of PGE ores, chromites and unradiogenic base-metal sulphide ores. In the following sections we will first discuss the environmental and biological influence on Re and

Os uptake in macroalgae before discussing each of the sources presented above to infer that the Os produced by human activity dominates the isotopic composition of coastal waters in proximity to major Japanese cities.

3.4.1 Biological and environmental controls on the $^{187}Re/^{188}Os$ of macroalgae

The ^{187}Re/^{188}Os of macroalgae show a wide range 8.7 to 11234.5 (Table 2) similar to previous studies (6.8 to 40,320) (Racionero-Gómez et al., 2017; Chapter 2; Rooney et al., 2016). This may be due to the different sources of Re and Os to macroalgae. When the ^{187}Re/^{188}Os of macroalgae is plotted against the ^{187}Os/^{188}Os of macroalgae (Fig. 7a), most Japanese seaweeds show a large variation in ^{187}Os/^{188}Os for a small range in ^{187}Re/^{188}Os when compared to Icelandic macroalgae (grey circles in Fig. 7a). This may suggest that Japan lacks a source high in Re and therefore high ^{187}Re/^{188}Os values, such as old primary basaltic minerals (See Chapter 2; Gannoun et al., 2006). Instead the macroalgae appear to be dominated by sources low in Re such as river water (avg. ^{187}Re/^{188}Os = 227; Peucker-Ehrenbrink and Ravizza, 2000). The ^{187}Re/^{188}Os ratios increase as riverine sources mix with seawater with higher ^{187}Re/^{188}Os (avg. ^{187}Re/^{188}Os = 4270; Peucker-Ehrenbrink and Ravizza, 2000). This is particularly dominant in Hokkaido (black squares in Fig. 7a) where macroalgae from deeper waters have a stronger influence from Pacific Ocean seawater, and thus higher ^{187}Re/^{188}Os values (Fig. 7a).

When the ^{187}Re/^{188}Os of macroalgae is plotted against the reciprocal of the Re concentration (Fig. 7b) we see a similar relationship to Icelandic macroalgae from Chapter 2 (grey circles in Fig. 7b). This suggests similar mechanisms could control Re and Os uptake in Japanese macroalgae. If Re and Os are taken up via the same pathway it will lead to competition between these elements and therefore lower Re concentration in macroalgae under higher Os seawater concentration and vice versa (Chapter 2; Racionero-Gómez et al., 2017). At low Re concentration, there is no competition between Re and Os for uptake into macroalgae, and the ^{187}Re/^{188}Os ratios remain consistently low. As the Re concentration rises, Re is favoured over Os as the two elements begin to compete for uptake into macroalgae, leading to an increase in the ^{187}Re/^{188}Os ratios. At exceptionally high Re concentrations, Re continues to be taken up and the macroalgae becomes enriched in Re,

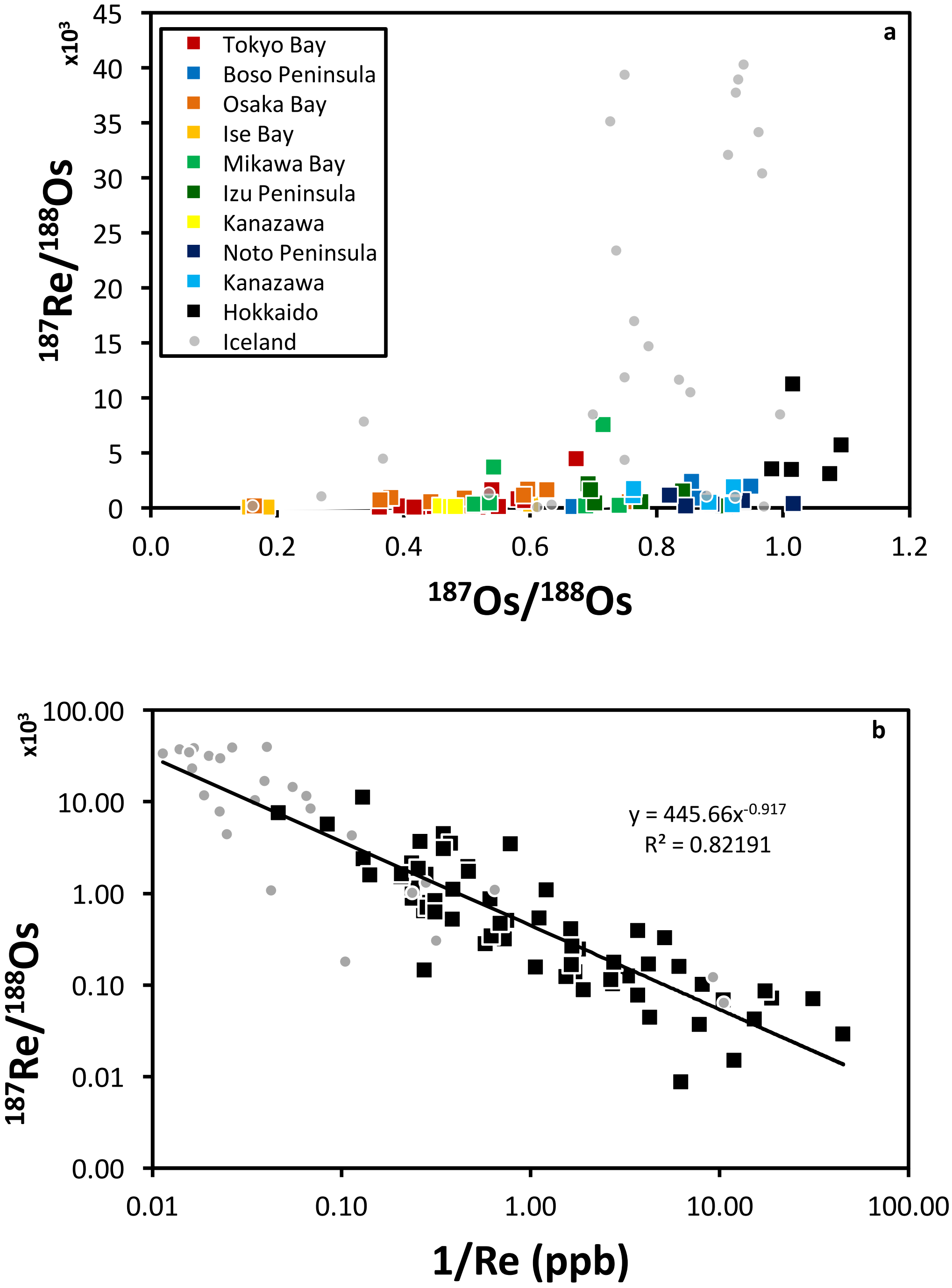

leading to exceptionally high ^{187}Re/^{188}Os ratios in macroalgae (Fig. 7b).

Fig. 7. a) The ^{187}Re/^{188}Os against the ^{187}Os/^{188}Os of macroalgae from Iceland (Chapter 2) and Japan (Chapter 3). **b**) ^{187}Re/^{188}Os ratios against the reciprocal of the Re concentration for Japanese (black squares) and Icelandic (grey circles) macroalgae.

3.4.2 Natural sources of osmium to macroalgae

A large number of macroalgae inhabit brackish waters, and their ^{187}Re/^{188}Os and ^{187}Os/^{188}Os composition will therefore represent a mixing between freshwater riverine inputs and seawater (See Chapter 2). The ^{187}Os/^{188}Os composition and Os abundance of a depth profile from the East Pacific Ocean has been constrained at ~1.04 and 10 ppq respectively (Chen and Sharma, 2009; Gannoun and Burton, 2014; Woodhouse et al., 1999). Further, the hydrogenous ^{187}Os/^{188}Os composition of present day marine sediments suggest that the Sea of Japan has a similar ^{187}Os/^{188}Os composition of ~1.03 (Dalai et al., 2005).

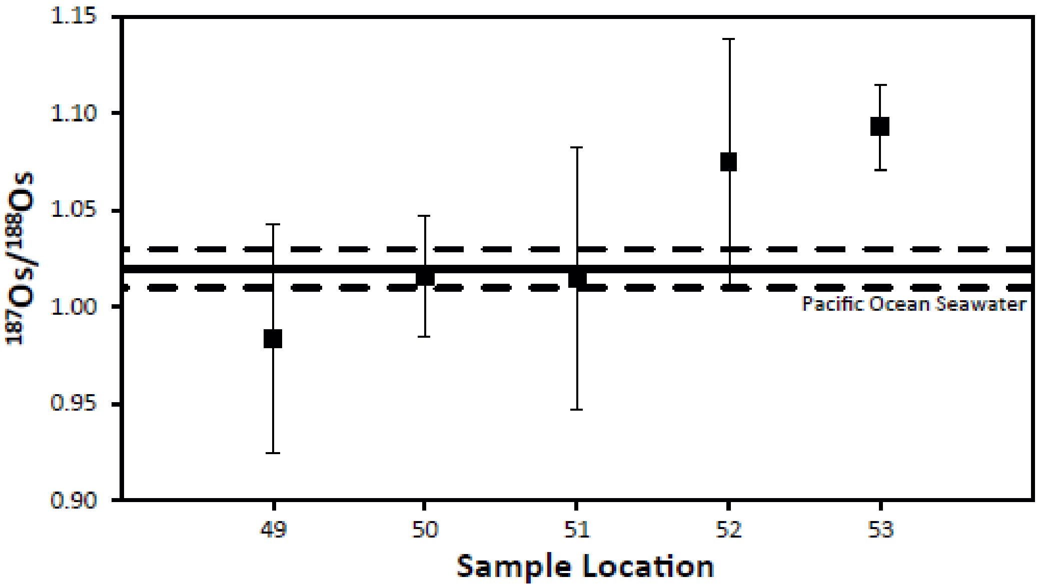

Fig. 8. Osmium isotope composition (^{187}Os/^{188}Os) of macroalgae from Hokkaido sample locations (See Fig. 1). Black line shows data from direct Pacific Ocean seawater measurements (See Gannoun and Burton, 2014).

These ^{187}Os/^{188}Os values are reflected in the ^{187}Os/^{188}Os compositions (Table 2) of macroalgae farmed from deeper pristine waters > 2 miles off the east coast of Hokkaido

(~1.02), which is indistinguishable, within uncertainty, from Os isotope measurements obtained directly from seawater (Fig. 8). The ^{187}Os/^{188}Os composition of macroalgae from shallower coastal waters around Japan will represent the mixing between Pacific seawater values (~1.04) and local continental riverine inputs with a diverse range of ^{187}Os/^{188}Os compositions and Os abundances dependent on the underlying lithology being weathered.

The long chain of Japanese islands along the northwest margin of the Pacific Ocean consists of two trench-arc systems: the East Japan Island Arc which marks the boundary between the Eurasian, Pacific and Philippine Sea plates; and the West Japan Island Arc which represents the boundary between the Eurasian and Philippine Sea plates (Hashimoto, 1991). These features generate a complex geology that can be broken down into five major elements: poorly lithified Neogene-Quaternary sediments and Paleogene sedimentary rocks (~40 %); accretionary complexes consisting mainly of melange, mudstone and sandstone (~17 %); non-alkaline Neogene-Quaternary volcanic rocks (23 %); granitic rocks intruded during the Cretaceous (~10 %); and, metamorphic rocks (~4 %). The underlying in geology of Japan therefore represents a large range of ages and sources i.e. mantle to upper crust.

Parent-daughter fractionation of the Re-Os system during mantle melting leads to Re becoming preferentially partitioned into the melt over Os. As a product of mantle differentiation, continental crust is characterised by higher Re/Os ratios relative to the mantle. With an average continental crust age of ~2.2 Gyr, in situ decay of ^{187}Re has led to the accumulation of appreciable ^{187}Os and a radiogenic ^{187}Os/^{188}Os composition of ~1.4 (Peucker-Ehrenbrink and Jahn, 2001). The erosion and subsequent weathering of complex underlying lithologies has led to highly variable ^{187}Os/^{188}Os values (0.64 to 2.94) and Os abundances (4.6 to 52.1 ppq) in global rivers (Levasseur et al., 1999a). The major cities studied here, and more than 70% of the Japanese population, reside on the Japanese ‘plains’ which are largely underlined by Quaternary sediments (Hashimoto, 1991). It is therefore expected that the ^{187}Os/^{188}Os composition of rivers draining these regions to be similar to the global riverine average of ~1.54 (Levasseur et al., 1999a).

Pleistocene-Holocene sediments and sedimentary rocks occupy the entire drainage basin of the Kanto plains (Ohta et al., 2011), Osaka plains (Ohta et al., 2005; Ohta et al., 2007), Kanazawa plains (Ohta et al., 2004) and Ise plains (Ohta et al., 2005; Ohta et al., 2007), and therefore represent the dominant control on the chemical composition of rivers draining the relevant watershed (Ohta et al., 2005). We would therefore expect the ^{187}Os/^{188}Os of waters in Tokyo Bay (Fig. 2) to represent a mixture between radiogenic rivers (~1.54) draining the coastal plains and Pacific seawater (~1.04) entrained into the bay from the Pacific Ocean via estuarine gravitational circulation. However, the ^{187}Os/^{188}Os of macroalgae from Tokyo Bay (Fig. 2a), Osaka Bay (Fig. 3a), Kanazawa (Fig. 6a) and Ise Bay (Fig. 4a) are relatively unradiogenic and range from 0.36 to 0.95, 0.17 to 0.76, 0.16 to 0.6 and 0.46 to 0.48 (Table 2). This suggests that Os from natural sources has very little influence on the isotopic composition of Tokyo Bay.

Although most regions studied are underlain by sedimentary plains, exceptions to this include the Ryoke belt, Izu peninsula and Noto Peninula. The Ryoke belt is characterised by low P/T type metamorphism and extensive felsic igneous activity that covers a ~800km stretch of inner Southwest Japan (Nakajima, 1994). Granitic rocks are dominant over metamorphic rocks throughout the Ryoke belt, and were derived from magmas produced in the lower crust and/or upper mantle; with potential assimilation of metamorphic rocks or Precambrian crust (Yuhara et al., 2000). Weathering of granitic material dominates central Awaji Island, Kobe city along the north coast of Osaka Bay and the Yahagi River, which flows into northern Mikawa Bay (Ohta et al., 2005; Ohta et al., 2007). The weathering of high pressure metamorphic rocks dominates the Toyo River which flows into the eastern Mikawa Bay (Ohta et al., 2005; Ohta et al., 2007). Most studies suggest the weathering of old (Precambrian) granitic terrain delivers highly radiogenic Os

($^{187}Os/^{188}Os$ = ≥ 2.5) to rivers draining these catchments (Chen et al., 2006; Ehrenbrink and Ravizza, 1996; Huh et al., 2004). However, the Ryoke Belt is made up of more recent (Cretaceous) I-type granites with some sedimentary components of the Mino Terrain (Ishihara and Wu, 2001). Although hard to estimate without direct measurements, the low Os concentration combined with high Re/Os ratios in granites (Johnson et al., 1996), combined with possible crustal contamination of radiogenic Os would lead to high $^{187}Os/^{188}Os$ values in silicic material since the Cretaceous (Alves et al., 1999; Alves et al., 2002; Hart et al., 2003; Hart et al., 2002). We therefore suggest that relatively unradiogenic $^{187}Os/^{188}Os$ values of macroalgae from Osaka Bay (0.17 to 0.76) and Mikawa Bay (0.51 to 0.74) are not related to the weathering of local granites.

The $^{187}Os/^{188}Os$ composition of macroalgae from the south and east coast of the Izu Peninsula (Sample Location 31 to 36; Fig. 5a) and the coast of the Noto Peninsula (Sample Location 39 to 43; Fig. 6a) range from 0.69 to 0.91 and from 0.82 to 1.02 respectively. These values are consistently lower than the $^{187}Os/^{188}Os$ composition of seawater (~1.04), suggesting the influence of an unradiogenic endmember. Low human activity (Fig. 5b and Fig. 6b) and the absence of substantial anthropogenic sources of Os in the regions studied (Fig. 5c, d and Fig. 6c, d) suggests that the dominant source of unradiogenic Os is likely to be natural. Formations exposed on the Izu Peninsula are almost entirely composed of submarine and terrestrial volcanics erupted since the early Miocene, and their reworked deposits (Koyama and Umino, 1991). The north-east tip of the peninsula is dominated by recent (0-0.6 Ma) Higashiizu and Shiofuki basaltic to andesitic lavas and pyroclastics. This contrasts with the southern Izu Peninsula, which is dominated by older (Middle Miocene to Early Pleistocene) basaltic and andesitic volcanics from the Yugashima and Shirahama group. Miocene andesitic lava and sedimentary rocks from the Iwaine and Kurosendai dominate the lithology of the Noto peninsula (Japan, 1992).

Weathering of these volcanic systems dominates stream and coastal sediments emanating from them (Ohta et al., 2005; Ohta et al., 2004; Ohta et al., 2007). We would therefore expect the ^{187}Os/^{188}Os composition of rivers in these regions to have a more mantle signature (~0.12) due to the weathering of basaltic material dominating local catchment areas (Gannoun et al., 2006). However, the decay of abundant ^{187}Re in the older Yugashima and Shirahama groups and the Noto Peninsula may lead to radiogenic ingrowth of ^{187}Os and therefore higher ^{187}Os/^{188}Os compositions in these regions (Gannoun et al., 2004; Gannoun et al., 2006). The ^{187}Os/^{188}Os compositions of macroalgae from the Izu coastal waters therefore constitutes a mixing between radiogenic Pacific seawater (~1.04) and unradiogenic rivers draining a basaltic terrain (>0.12). This is supported by the ^{187}Os/^{188}Os composition of marine sediments from the Yasaka estuary in northern Kyushu, which range from 0.67 to 0.73, and represent a mixture of locally weathered Miocene volcanics and seawater (Zheng et al., 2014).

3.4.3 Anthropogenic sources of osmium to macroalgae

Anthropogenic Os has been detected in estuaries (Turekian et al., 2007; Williams et al., 1997), lakes (Rauch et al., 2004), coastal sediments (Esser and Turekian, 1993; Ravizza and Bothner, 1996), biological organisms (Rodushkin et al., 2007a, b), airborne particles (Rauch et al., 2005) and precipitation (Chen et al., 2009). Sources of anthropogenic Os include hospitals (Esser and Turekian, 1993; Turekian et al., 2007; Williams et al., 1997), MSWIs (Funari et al., 2016), vehicle exhaust (Poirier and Gariépy, 2005) and smelters (Chen et al., 2009; Rodushkin et al., 2007b), and can be either directly introduced into rivers and coastal waters via sewage outflow (Esser and Turekian, 1993; Ravizza and Bothner, 1996; Turekian et al., 2007; Williams et al., 1997) or directly to the atmosphere as volatile OsO_4 during high-temperature processes (Smith, 1974). The ^{187}Os/^{188}Os composition of Os from these sources depends on the original material used in their creation. The ^{187}Os/^{188}Os composition of fossil fuels are highly radiogenic, ranging from 1 to 13.7 (Finlay et al., 2011; Selby and Creaser, 2005). The PGE sulphide ores and chromites have unradiogenic ^{187}Os/^{188}Os values of 0.15 to 0.2 (McCandless and Ruiz, 1991) and 0.12 to 0.14 (Walker et al., 2002) respectively. The ^{187}Os/^{188}Os composition of base-metal sulphide deposits are highly variable: ranging from values similar to PGE ores (Lambert et al., 1998; Walker et al., 1994), through to highly radiogenic values caused by contamination from continental crust during their creation (Morgan et al., 2002).

Osmium has major uses – as a tissue stain for electron microscopy and as a catalyst in steroid synthesis – in medical research (Smith, 1974). Anthropogenic Os from biological and medical research laboratories has been detected in the Hudson River- Long Island Sound estuarine system and Chesapeake Bay with an estimated ^{187}Os/^{188}Os composition of ~0.13 (Esser and Turekian, 1993; Helz et al., 2000; Turekian et al., 2007; Williams et al., 1997). The dominant mode of transport is believed to be sewer outflow from nearby hospitals and atmospheric transport from hospital incinerators, the influence of which can be detected up to 70 km from the source (Esser and Turekian, 1993; Ravizza and Bothner, 1996; Williams et al., 1997). Although not measured here, sewage from outflows in New Haven (Esser and Turekian, 1993), New York City (Williams et al., 1997) and Boston (Ravizza and Bothner, 1996) have ^{187}Os/^{188}Os compositions and Os abundances of between 0.15 to 0.3 and 0.57 to 4.01 ppb respectively.

Densely populated regions of Japan (See panel b in Figs. 2 to 6) are generally served by a large number of major hospitals (See red circles in panel c of Figs. 2 to 6). We would therefore expect a significant influx of unradiogenic Os from hospitals situated in central Tokyo and Yokohama (Fig. 2c), central Osaka (Fig. 3c), western Ise Bay and eastern Mikawa Bay (Fig. 4c) and Kanazawa (Fig. 6c). The ^{187}Os/^{188}Os composition of macroalgae from these regions are generally highly unradiogenic ranging from 0.39 to 0.55 near central Tokyo and Yokohama, 0.5 to 0.76 near Osaka, 0.16 to 0.19 in western Ise Bay, 0.51 to 0.54

in northern Mikawa Bay and 0.46 to 4.48 near Kanazawa (Table 2). Additionally, macroalgae samples from central Awaji Island (Sample Location 17) show highly unradiogenic $^{187}Os/^{188}Os$ values of 0.17 to 0.38, close to the previously recorded $^{187}Os/^{188}Os$ of sewage (0.15 to 0.3). This is most likely due the high number of hospitals in the nearby city of Sumoto to the south or the sewage treatment plant to the north (Fig. 3c). This suggests that the macroalgae have incorporated Os related to medical research from point sources such as hospitals and sewage treatment plants either via sewage outflow or incineration of medical waste (Fig. 9). However, despite the ubiquitous nature of hospitals in major cities e.g. Tokyo and Osaka, the $^{187}Os/^{188}Os$ composition of macroalgae from these regions are not uniformly low. For example, macroalgae in Tokyo Bay show an increase to more radiogenic values westwards from central Tokyo, despite the ubiquity of hospitals in this region. Meanwhile, the macroalgae closest to central Osaka (Sample Location 20) has the highest $^{187}Os/^{188}Os$ values (0.76) for Osaka Bay. This suggests that although medical facilities can offer a point source for anthropogenic Os e.g. Awaji Island, other anthropogenic sources can dominate in other regions.

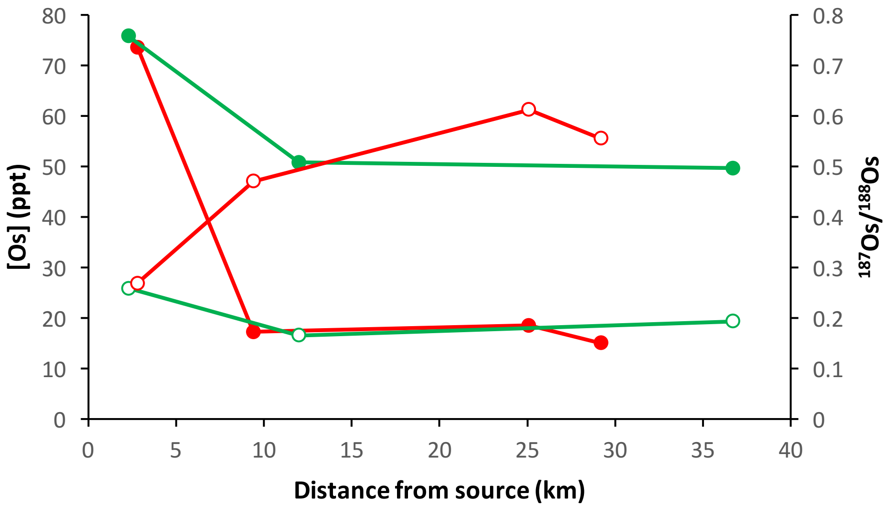

Fig. 9. Macroalgae Os concentration (filled circles) and isotopic composition (open circles) with distance from hospitals in central Awaji Island (red circles) or an oil refinery in central Osaka (green).

MSWIs are considered one of the best options for municipal solid waste management in industrialised countries (Chandler et al., 1997) and are widely used in major Japanese cities. Analysis of bottom and fly ash from Italian MSWIs show a wide range of ^{187}Os/^{188}Os compositions (0.24 to 0.7) and concentrations (0.026 to 1.65 ppb), and it has been predicted that the Os released from MSWI smokestacks will range from 16 to 38 ng Os/m^2/yr (Funari et al., 2016). This is therefore an important source of Os near central Tokyo and Osaka (See light green circles in Fig. 2c and 3c). These additional inputs of potentially unradiogenic Os could cause the relatively unradiogenic ^{187}Os/^{188}Os values in regions with relatively low vehicle emissions i.e. Yokosuka (Sample Location 10), Chiba (Sample Location 1,2 and 5), Kanazawa (Sample Location 38) and the south coast of Osaka Bay (Sample Location 21 and 22).

Automobile catalytic convertors could potentially provide a larger, regionally dispersed, source of anthropogenic Os. Direct measurements of catalytic convertors yield unradiogenic ^{187}Os/^{188}Os values and Os abundances of 0.1 to 0.2 and 6 to 228 ppt respectively (Poirier and Gariépy, 2005). Moreover, new catalytic convertors could be responsible for as much as 120 pg Os/m^2 in the first year of their life (Poirier and Gariépy, 2005), and anthropogenic Os sourced from vehicle exhaust has been detected in airborne particles (Rauch et al., 2005) and global precipitation (Chen et al., 2009). As the majority of PGEs are sourced from the Bushveld Complex (South Africa) and Noril'sk (Russia), we expect catalytic convertors in Japan to have unradiogenic values of 0.15 to 0.2 (Jones, 1999). Here we have utilised total vehicle CO_2 emissions for 2015 from the East Asian Air Pollutant Emission Grid (EAGrid2011) database (Kannari et al., 2007) to try and determine the influence of catalytic convertors on regional variations in anthropogenic Os (See panel d in Figs. 2 to 6).

We can generally see that in regions of high vehicle emissions, we get the most unradiogenic ^{187}Os/^{188}Os values in macroalgae. The ^{187}Os/^{188}Os composition of macroalgae in central Tokyo range from 0.42 to 0.46. These values are indistinguishable from the hydrogenous load of previously recorded marine sediments from the Tama River (~0.3 to 0.4) (Zheng et al., 2014), coincident to where the highest vehicle emissions in Japan are found (Fig. 2d). The ^{187}Os/^{188}Os composition of macroalgae becomes more radiogenic (0.55 to 0.67) in regions of intermediate vehicle emissions such as Yokosuka and Chiba, with the exception of Sample Location 4 which is highly unradiogenic (0.36). The ^{187}Os/^{188}Os composition of macroalgae begins to reach more radiogenic ^{187}Os/^{188}Os values (0.85 to 0.95), close to Pacific Ocean estimates (~1.04), in regions of low vehicle emissions on the Boso Peninsula (Fig. 2d). In Osaka Bay, macroalgae ^{187}Os/^{188}Os values are relatively unradiogenic (0.5 to 0.59) in regions of intermediate vehicle emissions (Fig. 3d). However, macroalgae from Sample Location 20 and 17 where vehicle emissions are highest and lowest respectively, record the most radiogenic ^{187}Os/^{188}Os values (0.76) and unradiogenic values (0.17 to 0.38) respectively. In the case of sample location 17, as previously explained, local influence from hospital and sewage outflow will contribute Os with an unradiogenic ^{187}Os/^{188}Os composition to this region. Meanwhile, sample location 20 is close to an oil refinery (Fig. 3c), which could act as a point source of anthropogenic Os. Osmium in oil is generally highly radiogenic (^{187}Os/^{188}Os = 1 to 13.7) (Finlay et al., 2011; Selby and Creaser, 2005; Selby et al., 2007) and any oil spills or atmospheric emission will therefore carry similar compositions. This is therefore the most likely cause of radiogenic ^{187}Os/^{188}Os values (0.76) in this area (Fig. 9). Mikawa and Ise Bay show similar trends with relatively unradiogenic values close to the regions of highest vehicle emissions (Fig. 4d).

Finally, other potential point sources of anthropogenic Os include the processing of chromites, PGE ores and base-metal sulphide ores. Although PGE ore and chromite smelters are not known to exist in the regions studied here, a wide number of steel mills are located in the Japanese industrial centres such as Tokyo and Osaka (Fig. 2c and 3c). The ^{187}Os/^{188}Os composition of base-metal sulphide deposits are highly variable: ranging from unradiogenic mantle values less than 0.3 (Lambert et al., 1998; Walker et al., 1994), through to highly radiogenic values greater than 0.9 (Morgan et al., 2002). Not knowing the source of ore used at Japanese steel mills, and due to the lack of studies of emissions, it is hard to estimate the influence of these sources on regional fluctuations atmospheric Os. However, it should be noted that steel mills could potentially act as a significant source of anthropogenic Os with potentially highly variable isotopic composition.

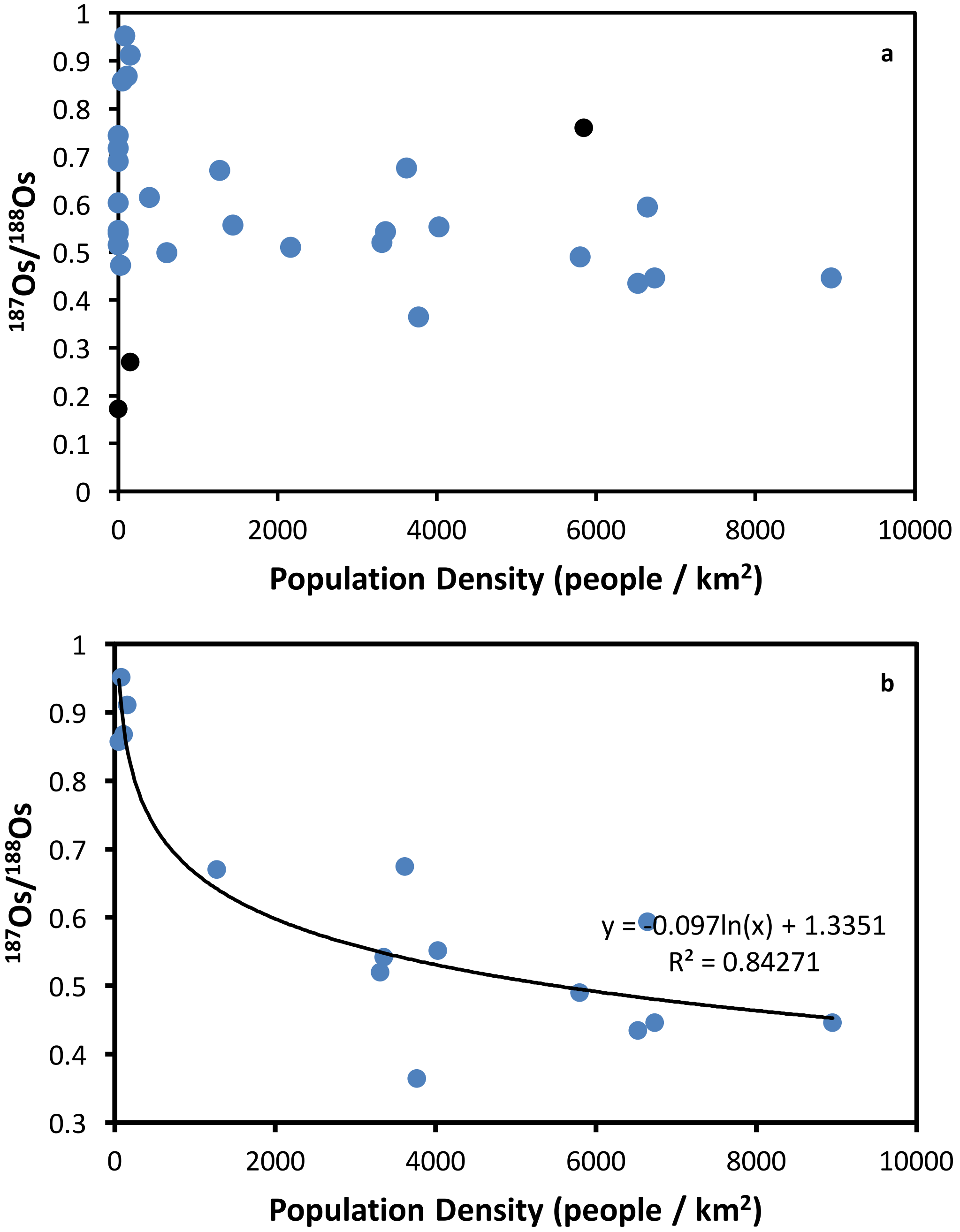

Fig. 10. 187Os/188Os against population density for a 400 km2 area surrounding each sample for (**a**) populated bays studies here (Mikawa, Ise, Osaka and Tokyo Bay) and (**b**) Tokyo Bay. Black symbols represent macroalgae affected by point sources such as hospitals and oil refineries (See Fig. 9).

In conclusion, during this study we have found a wide range of natural and anthropogenic sources to Japanese waters. In regions such as Hokkaido, northern Honshu, the Izu Peninsula, and Noto Peninsula where human activity is low, the osmium isotope budget of coastal waters is dominated by natural Os from Pacific Ocean seawater and riverine sources dominated by the weathering of local rock types such as volcanic, granitic and sedimentary rocks. In densely populated regions such as Tokyo, Yokohama, Chiba, Osaka, Kanazawa, Matsuaka and Toyohashi, anthropogenic sources of Os dominate. Osmium from catalytic convertors dominates the Os isotope budget in coastal water in these regions. However, point sources can become more influential in samples located near hospitals, sewage treatment plants and MSWIs. This is best shown when the ^{187}Os/^{188}Os composition of macroalgae is plotted against population density (Fig. 10). In areas of low population density, the ^{187}Os/^{188}Os of macroalgae ranges from 0.6 to 1 (Fig. 10a). However, as population density increases, the isotopic composition of macroalgae becomes more unradiogenic (0.6 to 0.4). Point sources such as hospitals and oil refineries pull the isotopic composition of macroalgae towards their respective source compositions away from this trend (Black circles in Fig. 10a). This relationship becomes more apparent when the ^{187}Os/^{188}Os of macroalgae is plotted against population density for Tokyo Bay (Fig. 10b). Macroalgae in the less populated region of the Boso Peninsula have an isotopic composition of ~0.9. However, as you move into the bay, and towards the more populated regions to the North of the Bay, the isotopic composition becomes more unradiogenic (0.4).

3.4.4 Anthropogenic influence on the global osmium cycle

3.4.4.1 Anthropogenic impact on Japanese coastal waters

This study has shown that the ^{187}Os/^{188}Os composition of macroalgae can successfully trace the fluctuations in natural and anthropogenic processes around Japan. When the ^{187}Os/^{188}Os composition of macroalgae is plotted against the reciprocal of the concentration, all of the data fall within field delimited by four potential end-members (Fig. 9): seawater (radiogenic ^{187}Os/^{188}Os, intermediate [Os]); river water draining Quaternary sedimentary material (radiogenic ^{187}Os/^{188}Os, low [Os]); river water draining Miocene volcanic rocks (intermediate ^{187}Os/^{188}Os, low [Os]); and, anthropogenic Os with a PGE source (unradiogenic ^{187}Os/^{188}Os, high [Os]). Variations in the ^{187}Os/^{188}Os of macroalgae can therefore be explained by the mixing between these distinct sources.

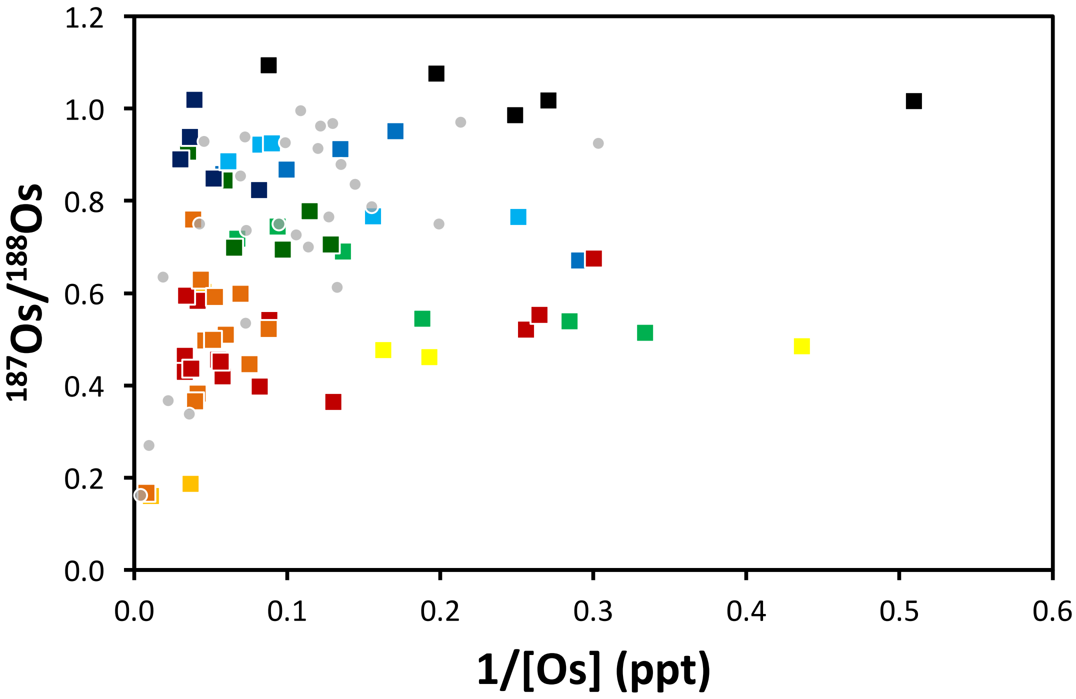

Fig. 11. ^{187}Os/^{188}Os ratios against the reciprocal of the Os concentration for Japanese (Chapter 3) and Icelandic (Chapter 2) macroalgae. See Fig. 7b for key.

Highly populated regions such as Tokyo Bay (red squares), Osaka Bay (dark orange squares), Ise Bay (light orange squares) and Kanazawa (yellow squares) fall on a mixing line between radiogenic seawater and/or river water and anthropogenic sources (Fig. 11). Meanwhile, sparsely populated regions such as Hokkaido (black squares), the Boso Peninsula (light blue squares), the Izu Peninsula (dark green squares) and northern Honshu (light blue squares) fall on a mixing line between radiogenic seawater and radiogenic or relatively unradiogenic river water (Fig. 11). This suggests that human activity has added an additional source of Os to the Japanese marine Os budget and is driving the system towards unradiogenic values. This has caused the ^{187}Os/^{188}Os profile of a relatively old island arc like Japan, to take on the ^{187}Os/^{188}Os profile of a young mid-ocean rift system like Iceland (grey circles in Fig. 11).

3.4.4.2 Anthropogenic contributions of osmium from Japan

Osmium oxide becomes volatile at a catalytic convertors operating temperature (>400°C), releasing 75 - 95% of its Os to the atmosphere within the first year of use (Poirier and Gariépy, 2005). It has been estimated that a 1 kg monolithic catalyst contains between 6 and 228 ppt Os which will be released during its lifetime (Poirier and Gariépy, 2005). Given a population of 127 million people in Japan, and roughly 5.5 million new vehicles on the road in Japan in 2015, we estimate roughly 23 people per car. Given a population of ~15.5 M, ~4.2 M and ~9.3 M people for the Tokyo-Kawasaki-Yokohama-chiba, Osaka-Kobe and Mie-Aichii metropolitan regions respectively, this amounts to ~675,000, ~182,000 and ~400,000 vehicles respectively. If we assume each car has a 1 kg monolithic catalyst, this amounts to 3 to 105, 1.5 to 54 and 0.2 to 8.4 pg Os/m^2/yr respectively.

This is comparable to previous Os emission estimates for New York City of 3 to 126 pg Os /m^2/yr (Poirier and Gariépy, 2005). This suggests that Os emission from catalytic convertors are significant in urban areas when compared to natural Os inputs of ~810 pg Os/m^2/yr (Poirier and Gariépy, 2005) from continental erosion and atmospheric dust inputs of 1 pg Os /m^2/yr (Williams and Turekian, 2002). However, point source Os emissions, such as MSWIs (16 to 38 ng Os/m^2/yr), can become far more significant then vehicle emissions in densely populated regions (Funari et al., 2016).

3.4.4.3 Impact of anthropogenic osmium on surface waters

Contemporary surface seawater has a lower ^{187}Os/^{188}Os composition (~0.95) than deep waters, which has been attributed to human activities (Chen et al., 2009; Levasseur et al., 1999b). If we assume that surface waters at the mouth of a bay (M) represents the mixing between an anthropogenic source of Os (A) coming from the bay and a natural source of Os coming from seawater (SW), we can describe the isotopic composition and concentration at the mouth using the following equation:

$$^{187}\mathrm{Os}/^{188}\mathrm{Os}_{\mathrm{M}}\ ([\mathrm{Os}]_{\mathrm{SW}}+[\mathrm{Os}]_{\mathrm{A}}) = {}^{187}\mathrm{Os}/^{188}\mathrm{Os}_{\mathrm{SW}}[\mathrm{Os}]_{\mathrm{SW}} + {}^{187}\mathrm{Os}/^{188}\mathrm{Os}_{\mathrm{A}}[\mathrm{Os}]_{\mathrm{A}}$$

We can then rearrange the above equation to determine the concentration of anthropogenic osmium:

$$[\mathrm{Os}]_{\mathrm{A}} = \frac{[\mathrm{Os}]_{\mathrm{SW}}(^{187}\mathrm{Os}/^{188}\mathrm{Os}_{\mathrm{SW}} - {}^{187}\mathrm{Os}/^{188}\mathrm{Os}_{\mathrm{M}})}{^{187}\mathrm{Os}/^{188}\mathrm{Os}_{\mathrm{M}} - {}^{187}\mathrm{Os}/^{188}\mathrm{Os}_{\mathrm{A}}}$$

If we assume that the isotopic composition of macroalgae from the mouth of the bay represents ^{187}Os/^{188}Os$_{\mathrm{M}}$ (^{187}Os/^{188}Os$_{\mathrm{TokyoBay}}$ = 0.86; ^{187}Os/^{188}Os$_{\mathrm{OsakaBay}}$ = 0.47; ^{187}Os/^{188}Os$_{\mathrm{IseBay}}$ = 0.6), and given a ^{187}Os/^{188}Os$_{\mathrm{SW}}$ and [Os]$_{\mathrm{SW}}$ for the Pacific Ocean (^{187}Os/^{188}Os$_{\mathrm{Pacific}}$ = 1.04; [Os]$_{\mathrm{Pacific}}$ = 8 ppq) and an ^{187}Os/^{188}Os$_{\mathrm{A}}$ representative of PGE ores (0.15) we estimate the concentration of anthropogenic Os in surface waters at the mouth of Tokyo, Osaka and Ise Bays to be 2 ppq, 14 ppq and 8 ppq respectively. Given a flow rate of 8 x 10^9 m^3/yr, 8 x 10^9 m^3/yr and 37 x 10^9 m^3/yr for surface waters leaving Tokyo, Osaka and Ise Bay respectively (Smith and Yanagi, 1997), we estimate a total of approximately 4.2 kg Os/yr of anthropogenic Os is delivered to the Pacific Ocean from these three bays.

Using an average value of 1.4 kg Os/yr delivered by each Japanese megacity and considering there are currently 16 megacities globally situated in coastal regions, this equates to 22.6 kg Os/ yr delivered from global coastal cities. However, coastal megacities only represent 242 million people or ~8.2% of people living within the coastal region (Pelling and Blackburn, 2014). Therefore, a potential 276 kg of anthropogenic Os could be delivered via surface waters to the world's oceans every year if we extrapolate to the entire global coastal population. Chen et al. (2009) calculated 2,391 kg/yr are required to drive the Os isotopic composition of ocean's surface waters (depth = 200m) from 1.05 to 0.95. They suggested that the majority of this anthropogenic Os is delivered to the atmosphere during the refining of PGE ores. However, this study suggests ~12% of anthropogenic Os in surface waters can be attributed mainly to the use of PGEs in catalytic convertors, and confirms human activity is impacting the global Os budget.

3.5 Implications and future outlook

The Re-Os data presented here suggests macroalgae can successfully trace the impact of environmental and human activity on the global osmium budget. It particular, the $^{187}Os/^{188}Os$ composition of macroalgae has traced fluctuations in natural Os from the weathering of volcanics and sedimentary material, and its mixing with seawater from the Pacific Ocean and the Sea of Japan in brackish waters around Hokkaido, northern Honshu, the Izu Peninsula and Noto Peninsula. Moreover, the $^{187}Os/^{188}Os$ composition of macroalgae has also successfully traced the impact of anthropogenic Os emissions from the use of catalytic convertors, MSWIs, hospitals and refineries on waters in Tokyo Bay, Osaka Bay and Ise/Mikawa Bay near densely populated regions of Japan. This supports previous work that indicates Os isotopes can act as a powerful tracer of earth surface processes such as basaltic weathering in Iceland (Chapter 2) and continental weathering in Greenland (Rooney et al., 2016).

The widespread use of catalytic convertors has led to the removal of a range of pollutants from the environment. Ironically, this has led to global Os pollution at the Earth's surface from the production of platinum for use in catalytic convertors. Unlike previous studies, we suggest that the refinery of PGEs does not have a significant influence on the Japanese marine Os budget. Instead, the widespread use of Os in medical research and the lack of treatment in sewage and municipal waste has led to significant contamination in regions directly adjacent to hospitals, MSWIs and sewage treatment plants. In densely populated regions, Os emissions from catalytic convertors dominate regional Os budgets, and represent a significant source of Os to the atmosphere. Transfer of anthropogenic Os from these sources, via surface waters, to the world's oceans represents ~12% of anthropogenic Os input to the surface ocean, which acts to drive the ^{187}Os/^{188}Os composition of seawater from 1.05 to 0.95. This study echoes Chen et al. (2009) who suggested that 'Os isotopes could be a valuable tracer for the hydrological cycle, similar to Pb from leaded gasoline usage before 1978 or tritium from atmospheric atomic bomb testing in the early 1960s.'

Further work is needed to understand the specific uptake rate of Os from seawater by macroalgae in a similar manner to Racionero-Gómez et al. (2017). Such data for Japanese macroalgae species will provide a better estimate of the Os abundance in Japanese coastal waters. This will help yield a better understanding of the global Os cycle and oceanic residence times. It would be wise to utilise other isotope systems in conjunction with the Os isotope system to distinguish between the sources of anthropogenic Os from populated regions. For instance, Al and organic C have used in conjunction with osmium isotopes to trace the flow of anthropogenic Os related to sewage outflow. This will allow the possibility to distinguish Os attributed to catalytic convertors from other sources in complex regions such as Tokyo.

3.6 References

Alves, S., Schiano, P., Allègre, C.J., 1999. Rhenium–osmium isotopic investigation of Java subduction zone lavas. Earth and Planetary Science Letters 168, 65-77.

Alves, S., Schiano, P., Capmas, F., Allègre, C.J., 2002. Osmium isotope binary mixing arrays in arc volcanism. Earth and Planetary Science Letters 198, 355-369.

Birck, J.L., Barman, M.R., Capmas, F., 1997. Re ‐ Os isotopic measurements at the femtomole level in natural samples. Geostandards newsletter 21, 19-27.

Chandler, A.J., Eighmy, T., Hjelmar, O., Kosson, D., Sawell, S., Vehlow, J., Van der Sloot, H., Hartlén, J., 1997. Municipal solid waste incinerator residues. Elsevier.

Chen, C., Sedwick, P.N., Sharma, M., 2009. Anthropogenic osmium in rain and snow reveals global-scale atmospheric contamination. Proceedings of the National Academy of Sciences of the United States of America 106, 7724-7728.

Chen, C., Sharma, M., 2009. High precision and high sensitivity measurements of osmium in seawater. Analytical chemistry 81, 5400-5406.

Chen, C., Sharma, M., Bostick, B.C., 2006. Lithologic controls on osmium isotopes in the Rio Orinoco. Earth and Planetary Science Letters 252, 138-151.

Cohen, A.S., Waters, F.G., 1996. Separation of osmium from geological materials by solvent extraction for analysis by thermal ionisation mass spectrometry. Analytica Chimica Acta 332, 269-275.

Creaser, R.A., Papanastassiou, D.A., Wasserburg, G.J., 1991. Negative thermal ion mass spectrometry of osmium, rhenium and iridium. Geochimica et Cosmochimica Acta 55, 397-401.

Cumming, V.M., Poulton, S.W., Rooney, A.D., Selby, D., 2013. Anoxia in the terrestrial environment during the late Mesoproterozoic. Geology 41, 583-586.

Dalai, T.K., Suzuki, K., Minagawa, M., Nozaki, Y., 2005. Variations in seawater osmium isotope composition since the last glacial maximum: A case study from the Japan Sea. Chemical Geology 220, 303-314.

Earth, G., 2016. Google Earth 7.1.2.2041. *Hospital, sewage treatment plant, steel mill and oil refienery locations.* Google, SK telecom and Zenrin data providers. In: https://www.google.com/earth/index.html (assessed 30th May 2017).

Ehrenbrink, B.P., Ravizza, G., 1996. Continental runoff of osmium into the Baltic Sea. Geology 24, 327-330.

ESRI, 2014. ArcGIS Desktop: Release 10.3. Redlands, CA: Environmental Systems Research Institute.

Esser, B.K., Turekian, K.K., 1993. Anthropogenic osmium in coastal deposits. Environmental science & technology 27, 2719-2724.

Finlay, A.J., Selby, D., Osborne, M.J., 2011. Re-Os geochronology and fingerprinting of United Kingdom Atlantic margin oil: Temporal implications for regional petroleum systems. Geology 39, 475-478.

Funari, V., Meisel, T., Braga, R., 2016. The potential impact of municipal solid waste incinerators ashes on the anthropogenic osmium budget. The Science of the total environment 541, 1549-1555.

Gannoun, A., Burton, K., 2014. High precision osmium elemental and isotope measurements of North Atlantic seawater. JAAS.

Gannoun, A., Burton, K.W., Thomas, L.E., Parkinson, I.J., van Calsteren, P., Schiano, P., 2004. Osmium isotope heterogeneity in the constituent phases of mid-ocean ridge basalts. Science 303, 70-72.

Gannoun, A., Burton, K.W., Vigier, N., Gíslason, S.R., Rogers, N., Mokadem, F., Sigfússon, B., 2006. The influence of weathering process on riverine osmium isotopes in a basaltic terrain. Earth and Planetary Science Letters 243, 732-748.

Gogot, J., Poirier, A., Boullemant, A., 2015. Osmium isotopic tracing of atmospheric emissions from an aluminum smelter. Comptes Rendus Geoscience 347, 277-283.

Hart, G.L., Johnson, C.M., Hildreth, W., Shirey, S.B., 2003. New osmium isotope evidence for intracrustal recycling of crustal domains with discrete ages. Geology 31, 427-430.

Hart, G.L., Johnson, C.M., Shirey, S.B., Clynne, M.A., 2002. Osmium isotope constraints on lower crustal recycling and pluton preservation at Lassen Volcanic Center, CA. Earth and Planetary Science Letters 199, 269-285.

Hashimoto, M., 1991. Geology of Japan. Springer Science & Business Media.

Helz, G.R., Adelson, J.M., Miller, C.V., Cornwell, J.C., Hill, J.M., Horan, M., Walker, R.J., 2000. Osmium isotopes demonstrate distal transport of contaminated sediments in Chesapeake Bay. Environmental science & technology 34, 2528-2534.

Huh, Y., Birck, J.-L., Allègre, C.J., 2004. Osmium isotope geochemistry in the Mackenzie River basin. Earth and Planetary Science Letters 222, 115-129.

Ishihara, S., Wu, C., 2001. Genesis of Late Cretaceous-Paleogene Granitioids with Contrasting Chemical Trends in the Chubu District, Central Japan. BULLETIN-GEOLOGICAL SURVEY JAPAN 52, 471-491.

Japan, G.S.o., 1992. Geological Map of Japan, 1:1,000,000. 3rd ed. Geological Survey of Japan, Tsukuba.

Johnson, C.M., Shirey, S.B., Barovich, K.M., 1996. New approaches to crustal evolution studies and the origin of granitic rocks: what can the Lu–Hf and Re–Os isotope systems tell us? Geological Society of America Special Papers 315, 339-352.

Jones, R., 1999. Platinum smelting in South Africa. South African J Sci 95, 525–534.

Kannari, A., Tonooka, Y., Baba, T., Murano, K., 2007. Development of multiple-species< span>< img height=. Atmospheric Environment 41, 3428-3439.

Koyama, M., Umino, S., 1991. Why Does the Higashi-Izu Monogenetic Volcano Group Exist in the Izu Peninsula? Journal of Physics of the Earth 39, 391-420.

Lambert, D., Foster, J., Frick, L., Hoatson, D., Purvis, A., 1998. Application of the Re ‑ Os isotopic system to the study of Precambrian magmatic sulfide deposits of Western Australia. Australian Journal of Earth Sciences 45, 265-284.

Levasseur, S., Birck, J.-L., Allegre, C., 1999a. The osmium riverine flux and the oceanic mass balance of osmium. Earth and Planetary Science Letters 174, 7-23.

Levasseur, S., Birck, J.-L., Allègre, C.J., 1998. Direct measurement of femtomoles of osmium and the 187Os/186Os ratio in seawater. Science 282, 272-274.

Levasseur, S., Birck, J.-L., Allègre, C.J., 1999b. Osmium isotopic composition of corals: Evidences for multiple sources. Geochimica et cosmochimica acta 63, 1335-1343.

Mas, J., Tagami, K., Uchida, S., 2005. Rhenium measurements on North Atlantic seaweed samples by ID-ICP-MS: an observation on the Re concentration factors. Journal of Radioanalytical and Nuclear Chemistry 265, 361-365.

McCandless, T., Ruiz, J., 1991. Osmium isotopes and crustal sources for platinum-group mineralization in the Bushveld Complex, South Africa. Geology 19, 1225-1228.

Morgan, J.W., Walker, R.J., Horan, M.F., Beary, E.S., Naldrett, A.J., 2002. 190 Pt-186 Os and 187 Re-187 Os systematics of the Sudbury igneous complex, Ontario. Geochimica et Cosmochimica Acta 66, 273-290.

Nakajima, T., 1994. The Ryoke plutonometamorphic belt: crustal section of the Cretaceous Eurasian continental margin. Lithos 33, 51-66.

Nowell, G., Luguet, A., Pearson, D., Horstwood, M., 2008. Precise and accurate 186 Os/188 Os and 187 Os/188 Os measurements by multi-collector plasma ionisation mass spectrometry (MC-ICP-MS) part I: Solution analyses. Chemical Geology 248, 363-393.

Ohta, A., Imai, N., Terashima, S., Tachibana, Y., 2005. Application of multi-element statistical analysis for regional geochemical mapping in Central Japan. Applied Geochemistry 20, 1017-1037.

Ohta, A., Imai, N., Terashima, S., Tachibana, Y., 2011. Regional geochemical mapping in eastern Japan including the nation's capital, Tokyo. Geochemistry: Exploration, Environment, Analysis 11, 211-223.

Ohta, A., Imai, N., Terashima, S., Tachibana, Y., Ikehara, K., Nakajima, T., 2004. Geochemical mapping in Hokuriku, Japan: influence of surface geology, mineral occurrences and mass movement from terrestrial to marine environments. Applied Geochemistry 19, 1453-1469.

Ohta, A., Imai, N., Terashima, S., Tachibana, Y., Ikehara, K., Okai, T., Ujiie-Mikoshiba, M., Kubota, R., 2007. Elemental distribution of coastal sea and stream sediments in the island-arc region of Japan and mass transfer processes from terrestrial to marine environments. Applied Geochemistry 22, 2872-2891.

Paul, M., Reisberg, L., Vigier, N., 2009. A new method for analysis of osmium isotopes and concentrations in surface and subsurface water samples. Chemical Geology 258, 136-144.

Pelling, M., Blackburn, S., 2014. Megacities and the coast: risk, resilience and transformation. Routledge.

Peucker-Ehrenbrink, B., Ravizza, G., 2000. The marine osmium isotope record. Terra Nova 12, 205-219.

Peucker-Ehrenbrink, B., Ravizza, G., 2012. Osmium Isotope Stratigraphy. 145-166.

Peucker‐Ehrenbrink, B., Jahn, B.m., 2001. Rhenium‐osmium isotope systematics and platinum group element concentrations: Loess and the upper continental crust. Geochemistry, Geophysics, Geosystems 2.

Peucker‐Ehrenbrink, B., Sharma, M., Reisberg, L., 2013. Recommendations for analysis of dissolved osmium in seawater. Eos, Transactions American Geophysical Union 94, 73-73.

Poirier, A., Gariépy, C., 2005. Isotopic signature and impact of car catalysts on the anthropogenic osmium budget. Environmental science & technology 39, 4431-4434.

Prouty, N.G., Roark, E.B., Koenig, A.E., Demopoulos, A.W., Batista, F.C., Kocar, B.D., Selby, D., McCarthy, M.D., Mienis, F., Ross, S.W., 2014. Deep‐sea coral record of human impact on watershed quality in the Mississippi River Basin. Global Biogeochemical Cycles 28, 29-43.

Racionero-Gómez, B., Sproson, A., Selby, D., Gröcke, D., Redden, H., Greenwell, H., 2016. Rhenium uptake and distribution in phaeophyceae macroalgae, Fucus vesiculosus. Royal Society Open Science 3, 160161.

Racionero-Gómez, B., Sproson, A.D., Selby, D., Gannoun, A., Gröcke, D.R., Greenwell, H.C., Burton, K.W., 2017. Osmium uptake, distribution, and 187Os/188Os and 187Re/188Os compositions in Phaeophyceae macroalgae, Fucus vesiculosus: Implications for determining the 187Os/188Os composition of seawater. Geochimica et Cosmochimica Acta 199, 48-57.

Rauch, S., Hemond, H.F., Peucker-Ehrenbrink, B., 2004. Recent changes in platinum group element concentrations and osmium isotopic composition in sediments from an urban lake. Environmental science & technology 38, 396-402.

Rauch, S., Hemond, H.F., Peucker-Ehrenbrink, B., Ek, K.H., Morrison, G.M., 2005. Platinum group element concentrations and osmium isotopic composition in urban airborne particles from Boston, Massachusetts. Environmental science & technology 39, 9464-9470.

Ravizza, G., Bothner, M.H., 1996. Osmium isotopes and silver as tracers of anthropogenic metals in sediments from Massachusetts and Cape Cod bays. Geochimica et Cosmochimica Acta 60, 2753-2763.

Rodushkin, I., Engstrom, E., Sorlin, D., Ponter, C., Baxter, D.C., 2007a. Osmium in environmental samples from Northeast Sweden. Part I. Evaluation of background status. The Science of the total environment 386, 145-158.

Rodushkin, I., Engstrom, E., Sorlin, D., Ponter, C., Baxter, D.C., 2007b. Osmium in environmental samples from Northeast Sweden. Part II. Identification of anthropogenic sources. The Science of the total environment 386, 159-168.

Rooney, A.D., Selby, D., Lloyd, J.M., Roberts, D.H., Lückge, A., Sageman, B.B., Prouty, N.G., 2016. Tracking millennial-scale Holocene glacial advance and retreat using osmium isotopes: Insights from the Greenland ice sheet. Quaternary Science Reviews 138, 49-61.

Selby, D., Creaser, R.A., 2005. Direct radiometric dating of hydrocarbon deposits using rhenium-osmium isotopes. Science 308, 1293-1295.

Selby, D., Creaser, R.A., Fowler, M.G., 2007. Re–Os elemental and isotopic systematics in crude oils. Geochimica et Cosmochimica Acta 71, 378-386.

Smith, I., 1974. Osmium: An appraisal of environmental exposure. Environ Health Perspect 8, 201–213.

Smith, S., Yanagi, T., 1997. NP budgets for three Japanese Bays. LOICZ-Biogeochemical Modelling Node.

Turekian, K.K., Sharma, M., Gordon, G.W., 2007. The behavior of natural and anthropogenic osmium in the Hudson River–Long Island Sound estuarine system. Geochimica et Cosmochimica Acta 71, 4135-4140.

Völkening, J., Walczyk, T., Heumann, K.G., 1991. Osmium isotope ratio determinations by negative thermal ionization mass spectrometry. International Journal of Mass Spectrometry and Ion Processes 105, 147-159.

Walker, R., Morgan, J., Horan, M., Czamanske, G., Krogstad, E., Fedorenko, V., Kunilov, V., 1994. Re-Os isotopic evidence for an enriched-mantle source for the Noril'sk-type, ore-bearing intrusions, Siberia. Geochimica et Cosmochimica Acta 58, 4179-4197.

Walker, R.J., Prichard, H.M., Ishiwatari, A., Pimentel, M., 2002. The osmium isotopic composition of convecting upper mantle deduced from ophiolite chromites. Geochimica et Cosmochimica Acta 66, 329-345.

Williams, G., Marcantonio, F., Turekian, K.K., 1997. The behavior of natural and anthropogenic osmium in Long Island Sound, an urban estuary in the eastern US. Earth and planetary science letters 148, 341-347.

Williams, G.A., Turekian, K.K., 2002. Atmospheric supply of osmium to the oceans. Geochimica et cosmochimica acta 66, 3789-3791.

Woodhouse, O., Ravizza, G., Falkner, K.K., Statham, P., Peucker-Ehrenbrink, B., 1999. Osmium in seawater: vertical profiles of concentration and isotopic composition in the eastern Pacific Ocean. Earth and Planetary Science Letters 173, 223-233.

Yang, J.S., 1991. High rhenium enrichment in brown algae: a biological sink of rhenium in the sea? Hydrobiologia 211, 165-170.

Yuhara, M., Kagami, H., Nagao, K., 2000. Geochronological characterization and petrogenesis of granitoids in the Ryoke belt, Southwest Japan Arc: constraints from K – Ar, Rb – Sr and Sm - Nd systematics. Island Arc 9, 64-80.

Zheng, G., Suzuki, K., Kuno, A., Mastuo, M., Takano, B., Shimizu, H., 2014. Osmium geochemistry of modern estuarine sediments from the Tama and Yasaka rivers in Japan. Applied Geochemistry 40, 82-88.

Chapter 4

Osmium and lithium isotope evidence for fluctuating oxidative and silicate weathering during periodic Silurian glaciations*

*A version of this chapter will be submitted to Nature, co-authored with Philip Pogge von Strandmann, Timothy M. Lenton, David Selby, Emilia Jarochowska, Jiri Fryda, Jindrich Hladil, David Loydell, Ladislav Slavik, Mikael Calner and Axel Munnecke

The Silurian (419.2 to 443.8 Ma) was one of the most climatically unstable periods of the Phanerozoic, punctuated by four large positive carbon isotope ($\delta^{13}C$) excursions, associated with rapid turnover in marine biota. Despite over two decades of research, the cause of these climatic fluctuations is still unclear. Here we use osmium ($^{187}Os/^{188}Os$) and lithium ($\delta^{7}Li$) isotope measurements of shales and carbonates spanning four of the most prominent Silurian $\delta^{13}C$ excursions, to assess the role of continental weathering during this time. We find two peaks of radiogenic $^{187}Os/^{188}Os$ compositions either side of the lightest $\delta^{7}Li$ values during each $\delta^{13}C$ excursion. Geochemical modelling attributes this to periodic continental glaciations, which act to enhance the oxidative weathering of organic- and sulphide-rich lithologies, whilst suppressing global silicate weathering. The production of atmospheric CO_2 from oxidative weathering, coupled to a reduction in silicate weathering – and therefore atmospheric CO_2 removal – acted to reverse the long-term decline in atmospheric CO_2 and global temperatures driven by orogenesis, land plant diversification, reduced volcanic arc degassing and/or changes in paleogeography during the Silurian.

4.1 Introduction

Over the past two decades it has become apparent that the Silurian is the most climatically unstable period of the Phanerozoic, punctuated by four large amplitude (>5‰) positive carbon isotope ($\delta^{13}C$) excursions (Fig. 1) associated with fluctuations in the carbon cycle, seawater temperatures and faunal extinction rates (Calner, 2008; Lehnert et al., 2010; Melchin et al., 2012; Munnecke et al., 2010; Noble et al., 2005). Traditional explanations for these events have invoked a shift between two stable oceanic-climate states, driven by changes in the location of deep-water formation from high to low latitudes (Jeppsson, 1990), or global precipitation rates and continental runoff (Bickert et al., 1997). However, these early attempts to explain Silurian climatic events have received much criticism (Johnson, 2006; Kaljo et al., 2003; Loydell, 1998).

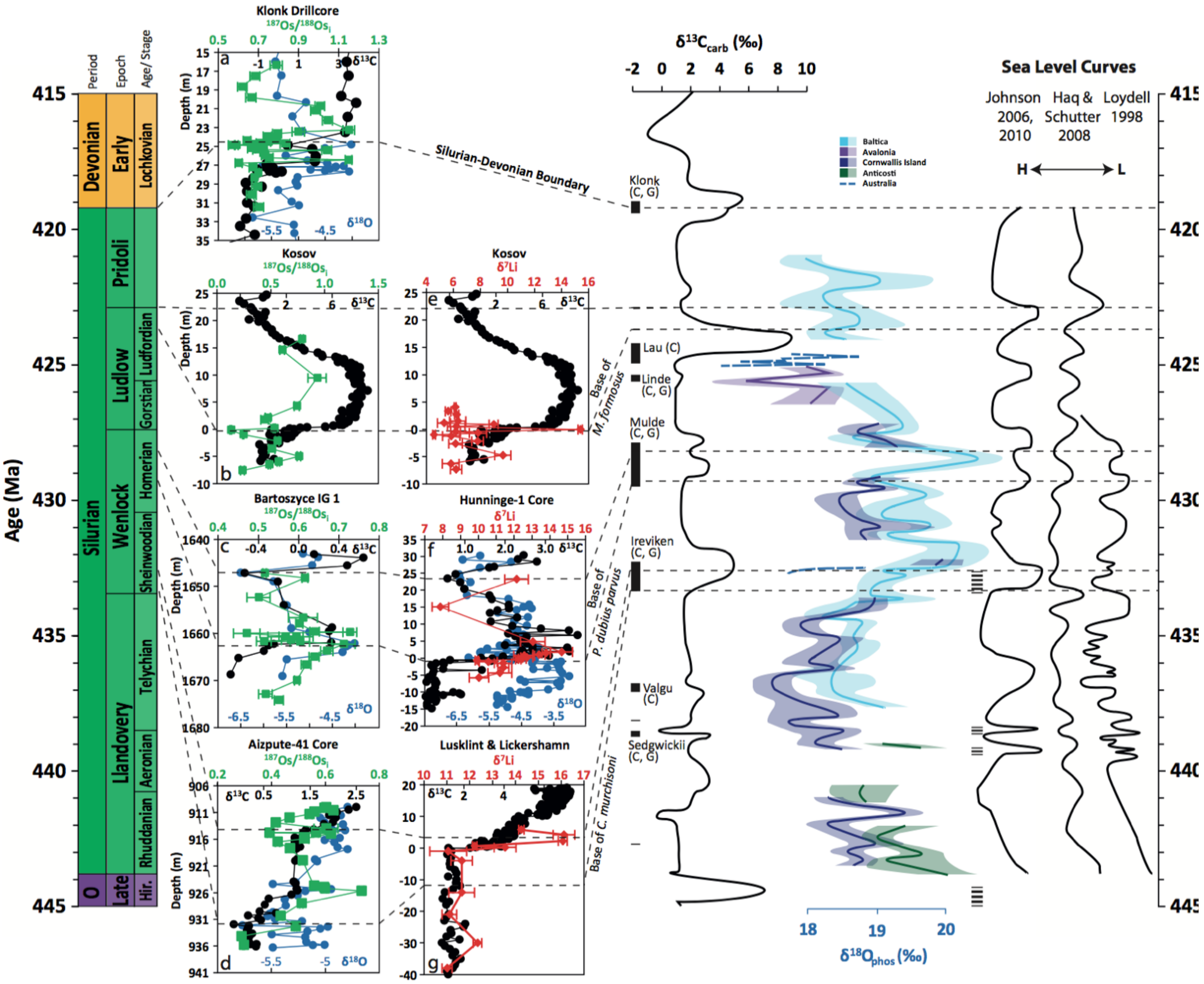

Figure 1. Osmium ($^{187}Os/^{188}Os$, green squares), lithium (δ^7Li, red diamonds), oxygen ($\delta^{18}O$, blue circles) and carbon ($\delta^{13}C$, black circles) isotope ratios for shale and carbonate sections measured. **a**, Klonk, **b**, Kosov (Os), **c**, Bartoszyce IG-1, **d**, Aizpute-41, **e**, Kosov (Li), **f**, Hunninge and **g**, Lusklint & Lickershamn. Data from this study is compared to the global conodont (C) and graptolite (G) bio-events (Melchin et al., 2012), $\delta^{13}C$ (Saltzman and Thomas, 2012; Cramer et al., 2011a), $\delta^{18}O$ (See Trotter et al., 2016), glacial tillites (thick dashed black line) (Caputo, 1998; Díaz-Martínez and Grahn, 2007; Grahn and Caputo, 1992) and sea-level reconstructions (Haq and Schutter, 2008; Johnson, 2006, 2010; Loydell, 1998).

More recently it has been postulated that Silurian climatic change could have been driven by glacial expansion over Gondwana, inferred in part from positive oxygen isotope ($\delta^{18}O$) shifts (Fig. 1) (Azmy et al., 1998; Brand et al., 2006; Eriksson and Calner, 2007; Kaljo et al., 2003; Lehnert et al., 2010; Trotter et al., 2016; Žigaitė et al., 2010) coupled to significant eustatic sea-level change (Haq and Schutter, 2008; Johnson, 2006, 2010; Loydell, 1998), much like the Late Ordovician that preceded it (Algeo et al., 2016; Harper et al., 2014). However, the lack of glacial sediments in the stratigraphic record for much of the Silurian (post-Wenlock) has hampered this notion (Caputo, 1998; Díaz-Martínez and Grahn, 2007; Grahn and Caputo, 1992).

In the absence of stratigraphic evidence for glacial sediments, seawater chemistry can become a powerful archive for reconstructing earth system responses to climatic or tectonic change, and several isotope systems have been utilised to reconstruct continental weathering and erosion. Traditionally, the rubidium-strontium (^{87}Rb-^{86}Sr) radiogenic isotope system has become the most widely used, and variations in marine $^{87}Sr/^{86}Sr$ are seen to reflect fluctuations in continental inputs caused by orogenesis (Raymo et al., 1988) and glaciation (Armstrong, 1971). However, the long residence time of strontium in the oceans (2 - 4 Myr) and multiple continental sources from both carbonate and silicate weathering (Jacobson et al., 2002; Palmer and Edmond, 1992) means that short-periodic fluctuations in unambiguous inputs are hard to detect (Hodell et al., 1990; Richter and Turekian, 1993). Unlike strontium, Os and Li isotope systems can overcome some of these difficulties.

The osmium isotopic composition ($^{187}Os/^{188}Os$) of seawater reflects a balance between the weathering of radiogenic Os-rich sedimentary rocks or silicate minerals and unradiogenic mantle and extraterrestrial derived sources (Georg et al., 2013; Peucker-Ehrenbrink and Ravizza, 2000). Likewise, the lithium isotopic composition ($\delta^{7}Li$) of seawater reflects the balance between chemical weathering of continental silicate minerals, high temperature weathering of oceanic silicate minerals at mid-ocean ridge spreading centres (Chan et al., 1993; Elderfield and Schultz, 1996; Huh et al., 1998), and incorporation into altered oceanic crust and authigenic clays (Chan et al., 1992; Chan et al., 2006; James et al., 1999; Mackenzie and Garrels, 1966; Misra and Froelich, 2012; Seyfried et al., 1998; Verney-Carron et al., 2011; Vigier et al., 2008). When combined with relatively short residence times in seawater (~1 - 50 kyr for Os and ~1 - 1.5 myr for Li) (Huh et al., 1998; Oxburgh, 2001; Rooney et al., 2016; Stoffynegli and Mackenzie, 1984), these isotope systems have permitted the ability to unlock vital information about a series of Earth system processes such as flood basalt volcanism (Cohen and Coe, 2002; Du Vivier et al., 2014; Ravizza and Peucker-Ehrenbrink, 2003; Turgeon and Creaser, 2008), paleoweathering (Hathorne and James, 2006; Lechler et al., 2015; Misra and Froelich, 2012; Pogge von Strandmann et al., 2013; Ravizza et al., 2001; Schmitz et al., 2004), basin connectivity (Poirier and Hillaire-Marcel, 2009), bolide impacts (Paquay et al., 2008) and mantle and peridotite formation (Pogge von Strandmann et al., 2011). In tandem, these systems have recently been utilised to determine how silicate weathering has been influenced by continental ice volume, atmospheric CO_2 and global temperatures during the Late Ordovician Hirnantian mass extinction (Finlay et al., 2010; Pogge von Strandmann et al., in review).

Here, shales were measured for osmium isotopes ($^{187}Os/^{188}Os$), and bulk carbonates were measured for lithium isotopes (δ^7Li) and trace metals, in stratigraphic sections that span the late Telychian-early Sheinwoodian, mid-Homerian, mid-Ludfordian and late Pridoli-early Lochkovian positive carbon isotope excursions (See Fig. 1). This study represents the first application of Os and Li isotopes to stratigraphic sections from the Silurian. The results demonstrate the ability of Os and Li isotopes to trace global fluctuations in Earth system processes, and when combined with dynamic isotope models, elucidate potential causes, such as fluctuations in ocean circulation, flood basalt volcanism, global temperature, hydrothermal activity and/or continental ice volume. Finally, this study looks at geological and climatic trends in atmospheric CO_2 during the Silurian, and relates them to negative feedback mechanisms that help maintain a habitable planet.

4.2 Materials and methods

4.2.1 Geological setting

In this study, four shale sections were analysed for osmium isotopes and four bulk carbonate sections were analysed for lithium isotopes (See Fig. 3 to 9). Combined, these sections covered four periods of Silurian time: the late Telychian to Early Sheinwoodian; mid Homerian; late Ludfordian; and the Silurian-Devonian boundary. Shales from the Aizpute-41 core (Latvia) and carbonates from the Lusklint & Lickershamn sections (Gotland, Sweden) cover the latest Telychian to earliest Silurian. Shales from the Bartoszyce core (Poland) and bulk carbonates from the Hunninge-1 core (Sweden) cover the mid Homerian. Shales and bulk carbonates from the Kosov (Czech Republic) section cover the Late Ludfordian. Shales from the Klonk core (Czech Republic) cover the Silurian-Devonian Boundary. The location of these sections can be found in Figure 2. Sections were chosen because they have all had extensive carbon isotope and biological stratigraphy carried out. Meanwhile they represent the most distal coastal environemnts away from restricted basins, and therefore are the most likely sections to record ocean signatures. The following will detail the geology, sampling strategy and paleoenvironment of each section studied.

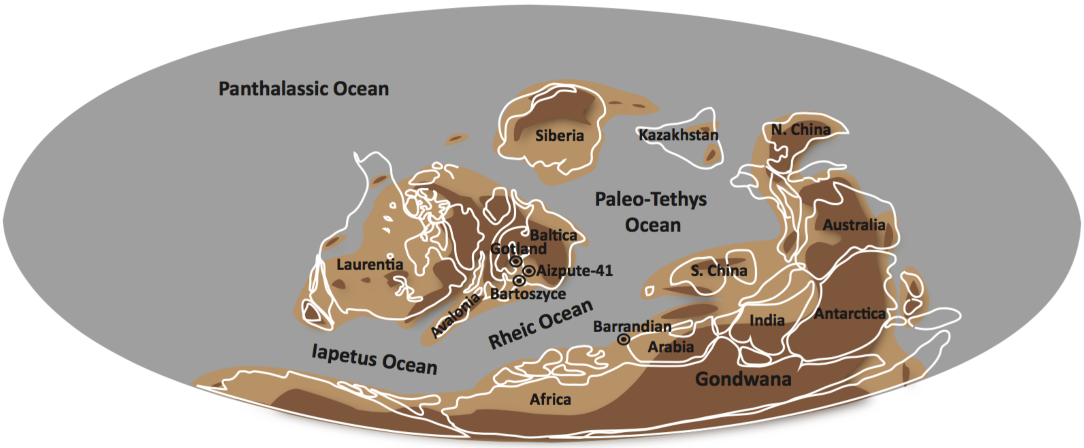

Figure 2. Silurian (425 Ma) paleogeographic map (adapted from Melchin et al., 2012). Sample locations from Gotland (Hunninge-1), Aizpute-41, Bartoszyce and the Barrandian (Kosov and Klonk) are highlighted. Dark and light brown represent the position of continents and continental shelves respectively, during the Silurian. White lines represent the configuration of modern continents.

4.2.1.1 Aizpute core

The late Telychian-early Sheinwoodian Aizpute-41 core is located in the town of Aizpute, situated in western Latvia, in the deeper shelf part of the Eastern Baltoscandian Basin. The latest Llandovery beds consist of greenish and brownish grey marlstones, while the earliest Wenlock consists of green, grey and brown marlstones with calcareous marlstones (Loydell et al., 2003). Sampling strategy of graptolite-rich, relatively high total organic carbon (TOC) shales was followed according to Loydell et al. (2003). The $\delta^{13}C_{carb}$ data for the drill core material can be found in Cramer et al. (2010).

4.2.1.2 Lusklint & Lickershamn

The late Telychian-early Sheinwoodian Lower Visby formation and the earliest Sheinwoodian Upper Visby formation can be found outcropping at Lusklint and Lickershamn along the north-western coast of Gotland, Sweden. The Lower Visby formation consists of up to 12 m of regular alternations of 2-5 cm thick, wavy bedded to nodular argillaceous limestones and approximately 10 cm thick marls which were deposited in a distal shelf environment, below storm wave base and the photic zone (Maier, 2010; Calner et al., 2004). However, the bedding in the Upper Visby formation is not as regular, with the ratio of marl to limestone increasing in the uppermost part of the formation where detritic limestones become more dominant (Maier, 2010). Samples from the Lower Visby formation were sampled from Lusklint while samples from the Upper Visby formation were sampled from Lusklint. The $\delta^{13}C_{carb}$ data for the samples can be found in Maier (2010).

4.2.1.3 Bartoszyce

The mid-Homerian Bartoszyce IG 1 borehole is located in the eastern part of the Peribaltic Syneclize of the Polish part of the East European platform. The core consists of sparsely bioturbated, light-grey laminated and calcareous mudstones (Porębska et al., 2004). Sampling strategy of relatively high TOC shales, $\delta^{13}C_{carb}$ and $\delta^{18}O_{carb}$ data can be found in Porębska et al. (2004).

4.2.1.4 Hunninge core

The mid-Homerian hunninge-1 core is located in the Hunninge quarry of western Gotland, Sweden. The Gannarve member consists of alternating beds of brownish, argillaceous, fine dolostone with silty dolomarlstone and alum shales (Calner et al., 2006). The overlying bara oolite member and brick clay member consist of coated grains and argillaceous, nodular limestone alternating with shale respectively (Calner et al., 2006). Sampling strategy for carbonates and $\delta^{13}C_{carb}$ data can be found in Calner et al. (2006).

4.2.1.5 Kosov

The mid-Ludfordian Kosov section is located in the Barrandian region of the Czech Republic. The *kozlowskii* biozone consists of alternating beds of grey finely laminated shale and light-grey packstones and grainstones, while the overlying *Pristiograptus dubius postfrequens* biozone consists of alternating beds of light-grey packstones/grainstones and mudstones or grey coarsely laminated calcareous shales. Sampling strategy of carbonates and relatively high TOC shales and $\delta^{13}C_{carb}$ data can be found in Frýda and Manda (2013).

4.2.1.6 Klonk core

The Pridoli-Lochkovian (Silurian-Devonian) GSSP is located in the Czech Republic 35km southwest of Prague. The latest Pridolian and earliest Lochkovian beds consist of grayish-black, platy, mostly fine-grained bituminous limestones alternating with calcareous shale interbeds with occasional stringers of crinoidal limestones (Becker et al., 2012). Sampling strategy of relatively high total organic carbon (TOC) drill core material was followed according to Crick et al. (2001). $\delta^{13}C_{carb}$ and $\delta^{18}O_{carb}$ data for the drill core material can be found in Buggisch and Mann (2004).

4.2.2 Sample preparation

Prior to crushing, 20 - 80 g of shale sample was polished to eliminate contamination from cutting and drilling marks and samples with any signs of veining or weathering were avoided. The shale samples were then dried at 60 °C for ~12 h before being broken into chips with no metal contact. Bulk carbonates and shales were crushed to a fine powder (~30 µm) in a Zirconia ceramic dish using a shatterbox. Bulk carbonates were leached using a sequential extraction method (Pogge von Strandmann et al., 2013; Tessier et al., 1979), whereby ~0.1 g of carbonate was leached for 5 h at room temperature using Na acetate buffered to pH 5 by acetic acid. Leaching of interstitial silicates was monitored using elemental ratios such as Al/Ca and Mn/Ca. The Al/Ca ratio must be greater than >0.8 mmol/mol before silicate-derived Li will perturb the $\delta^{7}Li$ measured in carbonates (Pogge von Strandmann et al., 2013). The sample preparation and Re-Os isotope and trace metal analysis was carried out at the Durham Geochemistry Centre (Laboratory for Sulfide and

Source Rock Geochronology and Geochemistry) at Durham University. The Li isotope analysis was carried out at the stable isotope lab the University of Oxford.

4.2.3 Osmium isotope analysis of shales

Rhenium and osmium abundances and isotopic compositions were determined using isotope dilution negative thermal ionisation mass spectrometry using Cr^{VI}–H_2SO_4 digestion and solvent extraction ($CHCl_3$), micro-distillation and anion chromatography methods (Creaser et al., 1991; Cumming et al., 2013; Selby and Creaser, 2003). The Cr^{VI}–H_2SO_4 digestion employed here principally dissolves the organic fraction of a shale, thus liberating the hydrogenous Re-Os load of the sediment, and therefore avoiding detrital contamination (Kendall et al., 2004; Selby and Creaser, 2003).

For all shale samples between 0.5 and 1 g of powder was added to a carius-tube with a known amount of ^{185}Re-^{190}Os tracer solution and 8 ml of 0.25 g/g $Cr^{VI}O_3$-4 N H_2SO_4 at 220 °C for 48 h. Osmium was isolated from the acid medium using $CHCl_3$ solvent extraction, with back extraction in HBr, and then further purified using a micro-distillation technique. Rhenium was isolated using NaOH-C_3H_6O solvent extraction and purified using anion chromatography. The isolated Re and Os fractions were loaded onto Ni and Pt filaments respectively, and their isotopic composition was determined using a ThermoScientific TRITON mass spectrometer using Faraday collectors and the secondary electron multiplier, respectively.

Total procedural blanks for Re and Os are 1.1 and 0.1 pg respectively, with an average ^{187}Os/^{188}Os of 1.3 (n=6). Raw Re and Os oxide values were corrected for oxygen contribution and mass fractionation. Calculated uncertainties include those associated with mass spectrometer measurements, blank abundance and isotopic composition, spike calibration, and sample and spike weights. In-house standard solutions of Re and Os (DROsS) yield an average $^{185}Re/^{187}Re$ value of 0.59872 ± 0.00135 (1SD, n = 24), and $^{187}Os/^{188}Os$ of 0.16101 ± 0.000401 (1SD, n = 41), respectively, which is identical, within uncertainty to the previously published values (Nowell et al., 2008).

Initial $^{187}Os/^{188}Os$ ($^{187}Os/^{188}Os_i$) values in this study were determined from Re-Os data and the ^{187}Re decay constant ($1.666e^{-11}$ a^{-1}) (Smoliar et al., 1996) and interpolated graptolite biozone ages (Melchin et al., 2012). Analytical uncertainty for individual calculated Os_i is < 0.05. The reproducibility of calculated $^{187}Os/^{188}Os_i$ was based on 15 analyses of the USGS rock reference material SBC-1 (Bush Creek Shale) and has a value of ~0.65 ± 0.1 (2 SD). This uncertainty was used to account for the maximum uncertainty in the sample set. Calculated $^{187}Os/^{188}Os_i$ ratios assume closed system behavior after deposition with respect to both rhenium and osmium and that the $^{187}Os/^{188}Os$ ratios reflect the isotope composition of the local seawater at the time of sediment deposition, and are unaffected by mineral detritus.

4.2.4 Lithium isotope analysis of bulk carbonates

A split of each sample solution was retained for cation analysis using an Elan Quadrupole inductively coupled plasma mass spectrometer. Samples were matrix matched to 10 µg/g Ca and calibrated against a set of synthetic standards made up from single element solutions. The Al/Ca ratio in carbonates was monitored to detect the influence of Li leached from silicate clays. Previous work suggests carbonates must be >0.8 mmol/mol before carbonate Li isotope ratios become measurably perturbed by Li leached from clays (See Pogge von Strandmann et al., 2013). Accuracy and precision were assessed by repeated analyses of seawater, the international reference material JLs-1 and, in order to assess reproducibility of both analyses and carbonate leaching, repeated dissolutions and analysis of a sample of the Plenus Marl from Eastbourne were undertaken. Sample reproducibility of Li/Ca and Al/Ca was ~7% (2 SD, n = 6).

The larger part of each sample (typically containing 5 – 10 ng Li) was purified by passing it through a two-stage cation-exchange procedure (Pogge von Strandmann et al., 2011). Given that Li isotopes fractionate during cation chromatography, it is critical to have column yields close to 100% (Tomascak, 2004). To assess the efficacy of this process, splits of the solution were collected before and after the collected bracket for Li, and were analysed for Li content. Results showed that <0.1% of Li was present in these splits.

The total procedural blank for Li isotope analysis is ~0.02 ng Li, which is insignificant compared to the mass of sample used. Analyses were performed on a Nu Plasma HR multi-collector ICP-MS, using a sample-standard bracketing system relative to the LSVEC standard (Flesch et al., 1973). Each sample was measured three separate times during an analytical session, repeat measurements being separated by several hours, but during the same analytical session. Each individual measurement consisted of 10 ratios (10 s total integration time), giving a total integration time of 300 s/sample. At an uptake rate of 75 µl/min, the sensitivity for a 20 ng/ml solution is ~18 pA of 7Li. Background instrumental Li intensity, typically ~0.01 pA, was subtracted from each measurement. Accuracy and external reproducibility, as assessed from seawater, is 31.1 ± 0.6 ‰ (2 SD, n = 16, chemistry = 16). Precision was also assessed from repeated analyses (including leaching and chemistry) of an in-house marl standard, which also gives a reproducibility of ± 0.6 ‰ (n = 7).

4.2.5 Isotope modeling

Dynamic box models for seawater Os and Li cycles have been utilised to explore causes of the variations seen in the data. The models were adapted from those presented in Pogge von Strandmann et al. (2013).

4.2.5.1 Osmium isotope modeling

The Os model was constructed from the following mass balance equation:

$$\frac{dN_{Os}}{dt} = F_{sil} + F_{ORLW} + F_{lth} + F_{\mathrm{hth}} + F_{\mathrm{dust}} - F_{\mathrm{out}} \qquad \text{Eq. 1}$$

where N is the seawater Os reservoir, and F_x represents the input and output fluxes: sil = river input related to silicate weathering; ORLW = river input related to the weathering of organic-sulphide-rich lithologies; lht = low-temperature hydrothermal; hth = high-temperature hydrothermal; and dust = aeolian dust. The isotope balance equation is then given by:

$$N_{Os}\frac{dR_{sw}}{dt} = F_{sil}(R_{sil} - R_{SW}) + F_{ORLW}(R_{ORLW} - R_{SW}) + F_{lht}(R_{lth} - R_{SW}) +$$

$$F_{hth}(R_{hth} - R_{SW}) + F_{dust}(R_{dust} - R_{SW}) - F_{out}(R_{out} - R_{SW})$$

Eq. 2

where R_x is the isotope ratio of the various fluxes. Finally, the calculation of the sink of Os from seawater is based on the assumption that partitioning into the sink is due to a constant partition coefficient k, where:

$$F_{\mathrm{out}} = k \times N \qquad \text{Eq. 3}$$

These equations differ from the original model (Pogge von Strandmann et al., 2013) as the riverine input has been partitioned into two components derived from silicate weathering and organic-sulphide-rich lithology weathering (ORLW) (See Georg et al., 2013). During the Cenozoic, riverine Os fluxes are largely controlled by the oxidative weathering of

ORL and represents 70% of riverine Os budget, with silicate weathering representing the other 30% (Georg et al., 2013; Li et al., 2009). However, during the Silurian, the absence of extensive terrestrial vegetation will lower the availability of organic-rich sediments for weathering, and silicate weathering will therefore represent a more dominant control on the riverine Os budget (60%). Cosmic dust is not included in the model as it is unlikely its flux changed during this time.

4.2.5.2 Lithium isotope modeling

The Li model was constructed from the following mass balance equation:

$$\frac{dN_{Li}}{dt} = F_{riv} + F_{\mathrm{hth}} - F_{\mathrm{sed}} \qquad \text{Eq. 4}$$

where N is the seawater Li reservoir, and F_x represents the input and output fluxes: riv = river; hth = hydrothermal; and sed = sediment (combined uptake into marine sediments, and alteration of the oceanic crust). The isotope balance equation is then given by:

$$N_{Li}\frac{dR_{SW}}{dt} = F_{riv}(R_{riv} - R_{SW}) + F_{hth}(R_{hth} - R_{SW}) - F_{sed}(R_{sed} - R_{SW}) \qquad \text{Eq. 5}$$

where R_x is the isotope ratio of the various fluxes where SW = seawater. R_{sink} is given by $\Delta_{sink} = R_{sink}-R_{sw}$, where Δ^7Li_{sink} = 15-16‰ (Chan et al., 1993; Huh et al., 1998; Misra and Froelich, 2012). Finally, the calculation of the sink of Li from seawater is based on the assumption that partitioning into the sink is due to a constant partition coefficient k, where:

$$F_{\mathrm{out}} = k \times N \quad \text{Eq. 6}$$

The fractionation of Li uptake into carbonates is accounted for by the model. Assuming a modern oceanic sink (Hazen et al., 2013) and hydrothermal δ^7Li, an unfractionated riverine δ^7Li (~0‰) similar to continental crust (Sauzéat et al., 2015) is required to produce the δ^7Li of seawater recorded for the Hirnantian (Pogge von Strandmann et al., in review). Such an isotopically light riverine flux was most likely due to the domination of illites, which cause little fractionation (Millot and Girard, 2007), prior to the advent of terrestrial plants (Pogge von Strandmann et al., in review). Li was modelled over 10 kyr steps, while Os was modeled over 5 kyr steps. Table 1 lists the values used in the models for each system.

Table 1

Model input parameters. Starting parameters are based on Pogge von Strandmann et al., 2013 and Pogge von Strandmann et al., 2017. However, Os riverine flux has been modified to represent contributions from the weathering of both silicates and ORL. See text for details on model perturbations.

	Starting Parameters		
	Li		Os
F river (Gmol/yr)	20	Silicate (mol/yr)	600
		ORLW (mol/yr)	400
F hydro (Gmol/yr)	9.3	low-T hydro (mol/yr)	95.4
		high-T hydro (mol/yr)	366
F dust (mol/yr)			150
R river	0	Silicate	0.6
		ORLW	1.34
R hydro	7	low-T hydro	0.878
		high-T hydro	0.115
R dust			1.05

4.3 Results

4.3.1 Rhenium-osmium isotope data

Rhenium and osmium isotope compositions and abundance data for the Aizpute-41 (Latvia), Bartoszyce (Poland), Kosov (Czech Republic) and Klonk (Czech Republic) samples are presented in Table 2.

Table 2

Rhenium and osmium abundance and isotope data for the Aizpute-41, Bartoszyce, Kosov and Klonk shale samples. Initial $^{187}Os/^{188}Os$ ($^{187}Os/^{188}Os_i$) were calculated using graptolite biozone ages from (Melchin et al. (2012).

Depth (m)	Re (ppb)	2 s.e.	Os (ppt)	2 s.e.	$^{187}Re/^{188}Os$	2 s.e.	$^{187}Os/^{188}Os$	2 s.e.	$^{187}Os/^{188}Os_i$	2 s.e.
Aizpute-41 Core, Latvia										
910.06	2.22	0.01	65.0	0.7	206.9	2.9	2.10	0.04	0.602	0.015
910.19	2.31	0.01	67.2	0.7	208.8	3.0	2.11	0.04	0.595	0.014
910.60	2.42	0.01	74.0	0.8	196.9	2.8	2.06	0.04	0.629	0.015
910.90	2.91	0.05	73.8	0.6	244.6	4.9	2.33	0.03	0.558	0.013
911.33	3.23	0.03	87.2	0.7	226.6	3.0	2.18	0.03	0.540	0.010
912.00	2.79	0.05	77.3	0.6	217.4	4.3	2.04	0.03	0.466	0.011
912.90	2.17	0.04	98.9	0.5	121.7	2.3	1.30	0.01	0.414	0.008
914.01	2.02	0.15	84.9	0.5	136.6	10.1	1.59	0.01	0.602	0.045
914.74	5.60	0.01	130.7	1.1	271.3	2.5	2.53	0.03	0.564	0.009
914.80	5.53	0.02	135.4	1.1	250.0	2.3	2.20	0.03	0.391	0.006
914.95	3.26	0.01	115.1	0.7	166.7	1.2	1.83	0.02	0.620	0.007
915.90	7.88	0.25	128.0	0.9	433.6	14.0	3.66	0.03	0.521	0.017
916.50	10.52	0.19	152.8	1.0	502.4	9.2	4.06	0.03	0.422	0.008
917.70	10.20	0.33	144.1	1.1	525.5	17.0	4.28	0.03	0.468	0.016
919.96	9.59	0.17	144.5	1.1	481.5	8.9	4.00	0.03	0.515	0.010
924.70	1.88	0.01	81.2	0.5	131.7	1.1	1.51	0.01	0.557	0.007
924.98	1.52	0.01	78.6	0.5	108.2	0.8	1.38	0.01	0.593	0.007
925.21	3.77	0.04	98.3	0.5	237.6	2.6	2.32	0.01	0.597	0.007
925.65	9.64	0.03	152.7	1.3	460.6	3.5	4.07	0.04	0.733	0.009
928.01	16.74	0.04	207.6	1.8	644.7	4.5	5.18	0.05	0.511	0.006
930.38	17.95	0.32	230.0	1.8	606.8	11.2	4.83	0.04	0.433	0.009
932.35	27.46	0.07	274.0	2.2	929.8	5.2	7.23	0.05	0.489	0.004
934.20	15.86	0.04	249.7	1.9	439.6	2.9	3.47	0.03	0.287	0.003
935.82	5.98	0.02	143.5	0.9	253.5	1.7	2.13	0.02	0.296	0.003

Bartoszyce Core, Poland										
1674.20	12.46	0.22	162.3	1.3	597.0	11.1	4.83	0.04	0.551	0.011
1672.90	12.55	0.40	196.3	1.5	454.8	14.8	3.78	0.03	0.517	0.017
1670.00	8.71	0.02	131.5	1.0	482.9	3.0	4.06	0.03	0.595	0.006
1666.65	9.46	0.17	147.8	1.0	461.5	8.5	3.93	0.03	0.618	0.012
1665.00	14.96	0.27	238.4	1.6	449.5	8.3	3.86	0.03	0.638	0.013
1663.75	3.01	0.05	69.8	0.6	275.5	5.5	2.65	0.03	0.670	0.016
1662.30	1.71	0.06	42.7	0.5	253.2	8.9	2.53	0.05	0.711	0.029
1661.80	1.10	0.02	27.9	0.4	244.2	6.7	2.35	0.07	0.603	0.024
1661.70	1.29	0.01	30.0	0.4	268.5	5.7	2.44	0.07	0.513	0.018
1661.40	1.17	0.02	34.6	0.5	203.6	5.6	2.04	0.06	0.580	0.023
1660.72	0.74	0.02	26.2	0.6	166.2	8.7	1.76	0.10	0.567	0.044
1660.70	0.51	0.01	34.2	0.7	81.1	3.4	1.18	0.07	0.594	0.042
1660.00	4.09	0.04	87.4	2.1	298.5	12.4	2.61	0.15	0.471	0.033
1659.75	3.80	0.07	106.3	0.9	221.5	4.4	2.32	0.03	0.727	0.017
1659.65	0.53	0.01	39.8	0.2	72.9	1.1	1.16	0.01	0.639	0.012
1657.95	3.81	0.01	126.9	1.0	177.5	1.5	1.87	0.02	0.601	0.009
1656.72	4.38	0.25	126.4	0.9	210.1	12.1	2.12	0.02	0.611	0.036
1652.36	8.61	0.49	192.2	1.2	283.8	16.3	2.54	0.02	0.500	0.029
1648.20	7.93	0.02	184.6	1.3	272.9	2.0	2.57	0.02	0.615	0.007
1647.20	9.32	0.02	204.1	1.2	290.9	1.5	2.60	0.02	0.515	0.004
Kosov, Czech Republic										
-7.60	5.60	0.39	79.7	1.0	499.9	35.7	3.78	0.07	0.235	0.017
-6.5	3.28	0.01	55.9	0.6	401.1	4.9	3.33	0.05	0.486	0.010
-6	4.26	0.01	60.9	0.7	518.7	6.1	4.25	0.07	0.570	0.011
-5.00	4.45	0.08	100.9	0.8	285.9	5.8	2.79	0.03	0.761	0.017
-3.65	9.34	0.53	134.0	1.0	511.4	29.4	4.13	0.03	0.509	0.029
-2.20	2.07	0.04	22.3	0.3	802.9	19.5	6.25	0.13	0.559	0.018
-1.00	8.35	0.16	102.7	1.1	623.6	12.8	4.66	0.06	0.243	0.006
-0.15	15.28	0.87	145.7	1.4	949.4	54.7	6.86	0.06	0.129	0.008
0.15	1.65	0.01	25.1	0.2	473.3	5.9	3.89	0.05	0.533	0.009
1.75	0.33	0.03	12.9	0.1	146.1	11.7	1.48	0.03	0.443	0.036
2.10	0.84	0.02	30.0	0.5	160.7	5.4	1.61	0.06	0.472	0.024
4.25	0.22	0.00	10.4	0.1	124.8	3.1	1.63	0.04	0.740	0.024
9.45	0.64	0.04	27.0	0.6	140.7	10.0	1.93	0.11	0.930	0.085
14.60	1.16	0.00	21.9	0.3	355.3	7.6	3.12	0.09	0.605	0.022
16.60	3.02	0.01	35.4	0.4	721.7	7.2	5.90	0.08	0.788	0.013
Klonk Core, Czech Republic										
16.37	1.93	0.07	66.3	0.5	175.0	6.4	2.02	0.03	0.789	0.031
17.53	2.77	0.01	81.6	1.1	206.7	4.3	2.13	0.06	0.682	0.024
18.67	7.30	0.26	176.3	1.5	259.9	9.5	2.44	0.03	0.619	0.024
19.82	4.45	0.16	152.2	1.2	172.9	6.3	1.87	0.02	0.662	0.026
20.73	2.60	0.01	137.6	1.4	110.7	1.6	1.78	0.03	1.006	0.024
21.22	1.98	0.01	104.8	1.1	110.6	1.6	1.76	0.03	0.984	0.024
22.25	2.37	0.01	111.1	1.1	126.8	1.8	1.93	0.04	1.044	0.025

23.27	1.81	0.01	64.0	0.7	176.5	2.7	2.39	0.05	1.149	0.029
23.45	3.50	0.01	76.4	1.1	304.0	5.8	3.03	0.08	0.898	0.030
23.65	6.46	0.02	148.2	1.9	282.7	4.7	2.77	0.06	0.792	0.022
23.95	2.35	0.01	59.6	0.7	248.2	4.3	2.48	0.06	0.745	0.021
24.25	4.61	0.02	142.2	1.7	198.0	3.3	2.17	0.05	0.787	0.022
24.4	6.00	0.02	158.1	1.9	234.3	4.0	2.29	0.05	0.643	0.019
24.54	8.84	0.03	182.4	1.6	321.0	3.2	3.00	0.04	0.750	0.012
24.65	3.52	0.02	124.9	1.5	167.0	3.0	1.88	0.04	0.710	0.021
24.72	3.76	0.02	125.2	1.5	181.9	3.2	2.11	0.05	0.832	0.024
24.77	4.07	0.02	161.2	1.8	146.6	2.5	1.70	0.04	0.671	0.019
24.87	5.77	0.02	150.2	1.8	235.5	4.1	2.22	0.05	0.567	0.016
24.87	6.04	0.02	159.7	1.3	232.2	2.1	2.22	0.03	0.590	0.009
25.01	3.12	0.02	84.5	1.1	229.3	4.4	2.33	0.06	0.721	0.022
25.21	5.06	0.02	123.4	1.6	258.1	4.6	2.47	0.06	0.665	0.020
25.35	6.71	0.02	136.2	1.8	325.3	5.7	2.97	0.07	0.691	0.020
25.42	2.54	0.01	111.1	1.2	137.3	2.0	2.00	0.04	1.039	0.025
25.60	6.34	0.02	116.8	1.4	370.3	5.3	3.32	0.07	0.725	0.018
25.98	3.75	0.01	118.8	1.3	190.5	2.7	2.07	0.04	0.732	0.018
26.22	2.13	0.01	99.4	1.0	123.5	1.8	1.62	0.03	0.754	0.018
26.45	5.13	0.02	152.4	1.3	215.9	2.0	2.66	0.03	1.148	0.017
26.78	10.42	0.04	175.5	2.4	411.3	6.9	3.48	0.08	0.602	0.017
27.25	6.47	0.02	208.0	2.4	186.2	3.1	1.98	0.04	0.673	0.019
27.8	17.46	0.06	200.9	1.4	729.0	3.9	5.81	0.03	0.697	0.005
28.34	4.55	0.02	105.6	0.9	274.3	2.6	2.60	0.03	0.678	0.010
29.28	6.86	0.24	185.3	1.0	229.0	8.2	2.30	0.01	0.690	0.025
30.15	9.95	0.35	224.8	1.3	283.7	10.1	2.65	0.02	0.665	0.024
31.45	6.94	0.25	206.0	1.1	204.8	7.3	2.14	0.01	0.701	0.025

4.3.1.1 Aizpute-41 Core

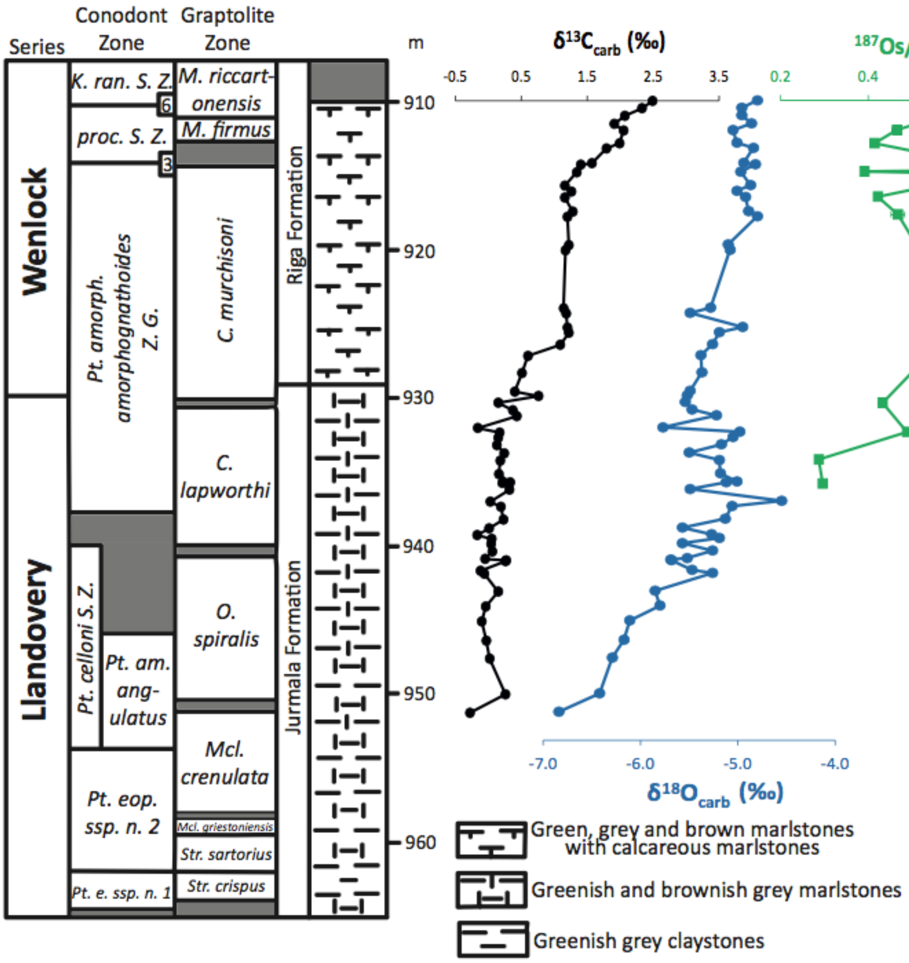

Figure 3. Osmium ($^{187}Os/^{188}Os$, green squares), oxygen ($\delta^{18}O_{carb}$, blue circles) and carbon ($\delta^{13}C_{carb}$, black circles) isotope ratios for shales and carbonates from the Llandovery-Wenlock Aizpute core. Biozone, lithology and carbon and oxygen data have been adapted from Cramer et al. 2010. See text for details.

The Re and Os abundances and $^{187}Re/^{188}Os$ and $^{187}Os/^{188}Os$ ratios are variable throughout the Aizpute-41 section ([Re] = 1.52 to 27.46 ppb; [Os] = 65 to 274 ppt; $^{187}Re/^{188}Os$ = 108 to 930; $^{187}Os/^{188}Os$ = 1.3 to 7.2; Table 2; Fig. 3). Initial $^{187}Os/^{188}Os$ values range from 0.29 to 0.73 (Table 2d; Fig. 2). From 934.82 to 965.28 m, within the latest *lapworthi* and earliest *murchisoni* biozones, $^{187}Os/^{188}Os_i$ increases from ~0.29 to ~0.73. From 925.65 to 916.5 m, $^{187}Os/^{188}Os_i$ decreases from ~0.73 to ~0.42. The $^{187}Os/^{188}Os_i$ then fluctuates between ~0.39 and ~0.62 during the latter part of the *murchisoni* biozone. From 912.9 to 910.6m, spanning the *firmus* biozone, the $^{187}Os/^{188}Os_i$ increases from 0.41 to 0.63. A hiatus in the *riccartonensis* biozone prevents further analysis into the Wenlock.

4.3.1.2 Bartoszyce Core

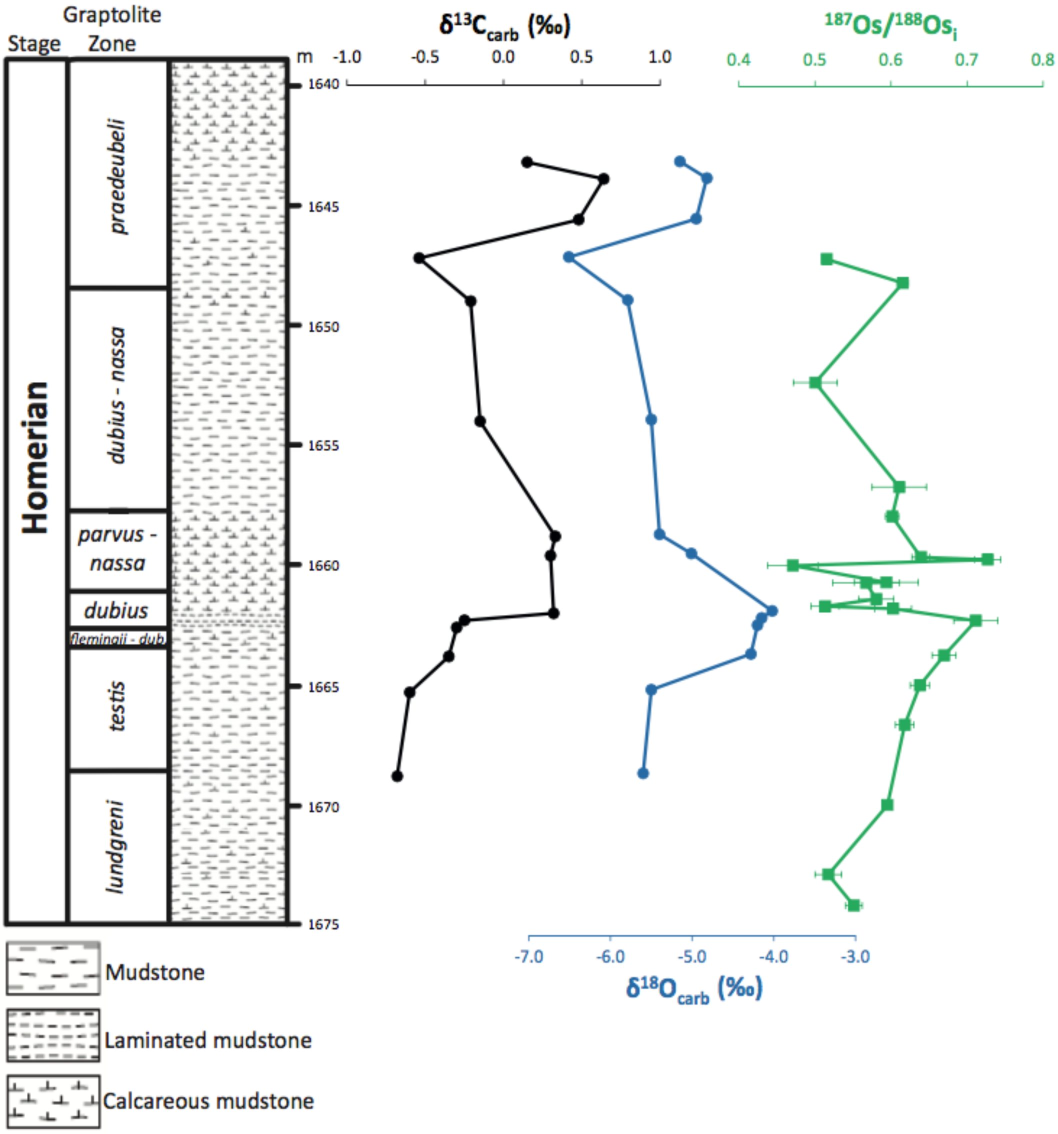

Figure 4. Osmium ($^{187}Os/^{188}Os$, green squares), oxygen ($\delta^{18}O_{carb}$, blue circles) and carbon ($\delta^{13}C_{carb}$, black circles) isotope ratios for shales and carbonates from the mid-Homerian Bartoszyce section. Biozone, lithology and carbon and oxygen data have been adapted from Porębska et al. (2004). See text for details.

The Re and Os abundances and $^{187}Re/^{188}Os$ and $^{187}Os/^{188}Os$ ratios are variable throughout the Bartoszyce IG-1 core ([Re] = 0.5 to 15 ppb; [Os] = 26.2 to 238.4 ppt; $^{187}Re/^{188}Os$ = 73 to

597; ^{187}Os/^{188}Os = 1.2 to 4.8; Table 2; Fig. 4). Initial ^{187}Os/^{188}Os values range from 0.47 to 0.73 (Table 2; Fig. 2c). From 1672.9 to 1662.3 m, from the latest *lundgreni* to the base of the *nassa* biozone, the ^{187}Os/^{188}Os$_i$ increases from ~0.52 to ~0.71. Immediately afterwards, the ^{187}Os/^{188}Os$_i$ decreases from ~0.71 to ~0.51 where it remains relatively low (~0.5) between 1661.7 to 1660 m. From 1660 to 1659.7 m, the ^{187}Os/^{188}Os$_i$ sharply increases from ~0.47 to ~0.73. The ^{187}Os/^{188}Os$_i$ then proceeds to decrease throughout the rest of the *nassa* biozone.

4.3.1.3 Kosov section

The Re and Os abundances and ^{187}Re/^{188}Os and ^{187}Os/^{188}Os ratios are variable throughout the Kosov section ([Re] = 0.2 to 15.3 ppb; [Os] = 10.4 to 145.7 ppt; ^{187}Re/^{188}Os = 124.8 to 949.4; ^{187}Os/^{188}Os = 1.5 to 6.9; Table 2; Fig. 5). Initial ^{187}Os/^{188}Os values range from 0.13 to 0.93 (Table 2; Fig. 2b). From 7.6 to 5 m, the ^{187}Os/^{188}Os$_i$ increases from ~0.23 to ~0.76. Prior to the base of the *dubius postfrequens* biozone, the ^{187}Os/^{188}Os$_i$ decreases from ~0.76 to ~0.13 between 5 and 0.13 m. The ^{187}Os/^{188}Os$_i$ then increases from ~0.13 to ~0.93 between 0.13 and -9.45 m before decreasing again towards the end of the *dubius postfrequens* biozone

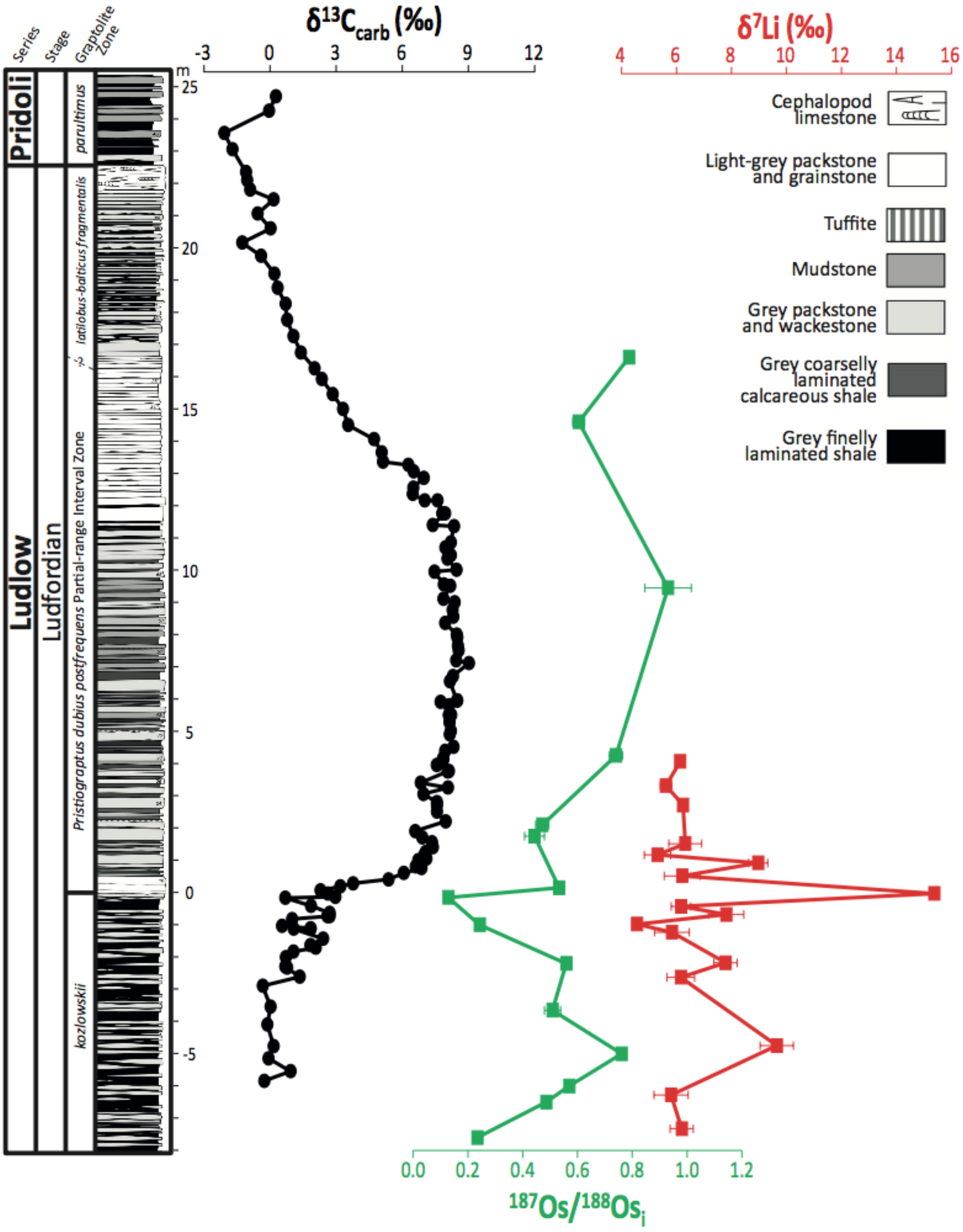

.

Figure 5. Osmium (^{187}Os/^{188}Os, green squares), Lithium (δ^{7}Li, red squares), oxygen (δ^{18}O$_{carb}$, blue circles) and carbon (δ^{13}C$_{carb}$, black circles) isotope ratios for carbonates and shales from the Ludfordian Kosov section. Biozone, lithology and carbon and oxygen data have been adapted from Frýda and Manda (2013). See text for details.

4.3.1.4 Klonk Core

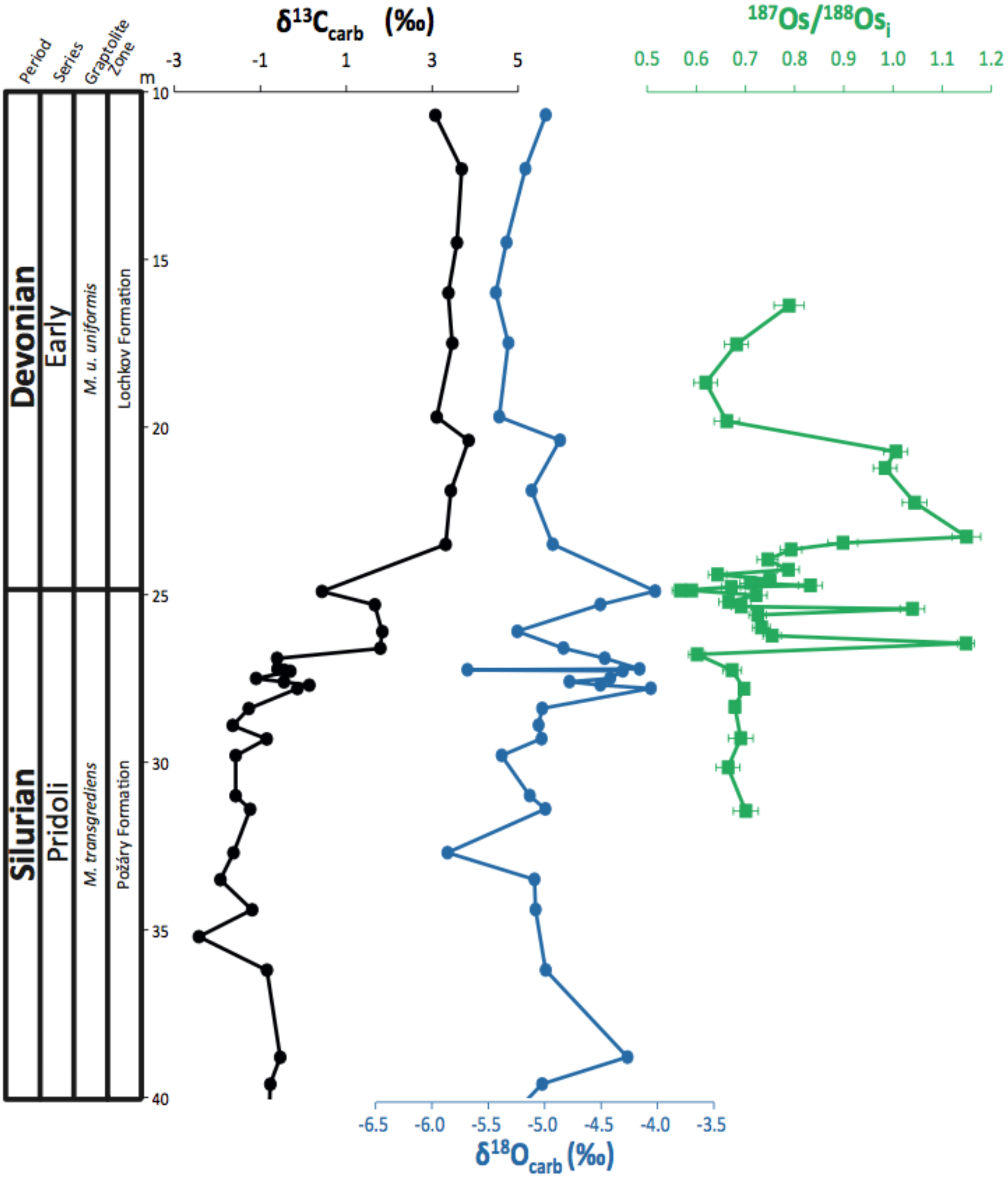

Figure 6. Osmium (^{187}Os/^{188}Os, green squares), oxygen ($\delta^{18}O_{carb}$, blue circles) and carbon ($\delta^{13}C_{carb}$, black circles) isotope ratios for carbonates and shales from the Silurian-Devonian GSSP at Klonk. Biozone information adapted from Crick et al. (2001). Carbon and oxygen isotope data have been adapted from Buggisch and Mann (2004). See text for details.

The Re and Os abundances and ^{187}Re/^{188}Os and ^{187}Os/^{188}Os ratios are variable throughout the Klonk core ([Re] = 1.8 to 17.4 ppb; [Os] = 59.6 to 224.8 ppt; ^{187}Re/^{188}Os = 110 to 729; ^{187}Os/^{188}Os = 1.6 to 5.8; Table 2; Fig. 6). Initial ^{187}Os/^{188}Os values range from 0.57 to 1.15

(Table 2; Fig. 2a). From 31.45 to 26.78 m, the $^{187}Os/^{188}Os_i$ are moderately radiogenic, ranging from ~0.6 to ~0.7. Between 26.78 and 25.35 m, the $^{187}Os/^{188}Os_i$ fluctuates between ~0.6 and ~1.15. Across the Silurian-Devonian boundary, the $^{187}Os/^{188}Os_i$ is also moderately radiogenic, with values between ~0.57 and ~0.83 (25.35 - 23.95 m). From 23.95 to 23.27 m, the $^{187}Os/^{188}Os_i$ increases from 0.74 to 1.15 before subsequently decreasing from 1.15 to 0.62 during the earliest Devonian.

4.3.2 Lithium isotope and trace metal data

Lithium isotope measurements and trace metal data for the Hunninge-1 (Sweden) and Kosov (Czech Republic) samples are presented in Table 3.

Table 3

Lithium isotope and trace metal data for the Hunninge-1 and Kosov carbonate samples.

Depth (m)	δ^7Li (‰)	2 s.d.	Mg/Ca (µmol/mol)	Al/Ca (µmol/mol)	Mn/Ca (µmol/mol)	Sr/Ca (µmol/mol)
Lusklint & Lickerdhamn, Sweden						
38	11.0	0.2	6.50	0.27	0.51	0.17
30	12.3	0.2	4.81	0.17	0.49	0.09
21	11.1	0.3	5.11	0.15	0.45	0.10
14	11.6	0.6	4.39	0.12	0.38	0.12
4	11.6	0.5	5.53	0.18	0.50	0.18
1	11.1	0.8	4.45	0.17	0.47	0.09
-0.19	13.5	0.5	4.00	0.15	0.41	0.09
-0.66	12.2	0.1	6.63	0.22	0.38	0.20
-2.25	16.1	0.2	5.36	0.14	0.29	0.22
-3.27	17.6	0.5	4.18	0.21	0.22	0.15
-4.2	16.1	0.5	4.15	0.08	0.26	0.12
-5.8	14.3	0.1	5.15	0.20	0.32	0.17
Hunninge-1 Drillcore, Sweden						
-4.4	11.2	0.7	39.32	0.536	2.74	0.75
-2.8	11.4	0.3	28.51	0.290	3.64	0.74
-1.5	11.4	0.5	40.49	1.006	2.46	0.66
-1.1	10.6	0.5	32.11	0.521	1.76	0.29
-0.7	9.9	0.1	20.51	0.123	1.97	0.39
-0.4	12.2	0.2	41.29	0.827	1.89	0.60
-0.2	12.5	0.2	40.12	0.536	1.47	0.68
0.2	12.7	0.3	48.25	1.002	1.07	0.96

0.7	12.6	0.6	24.21	0.108	0.67	0.83
1	13.4	0.3	15.61	0.007	0.50	0.70
1.5	13.8	0.2	19.00	0.007	0.53	0.63
1.8	14.7	0.6	24.94	0.114	0.49	1.27
4.8	13.0	0.7	22.07	-0.005	0.61	1.35
Kosov, Czech Republic						
-4.77	9.6	0.6	13.64	-0.018	1.23	0.56
-2.65	6.2	0.5	12.69	0.066	0.78	0.55
-2.2	7.8	0.4	14.60	0.014	0.74	0.51
-1.25	5.8	0.6	14.48	0.108	0.85	0.44
-1	4.6	0.1	12.34	0.200	0.85	0.79
-0.7	7.8	0.6				
-0.45	6.2	0.4				
-0.05	15.4	0.2	10.93	0.052	0.47	0.97
0.5	6.2	0.7				
0.9	9.0	0.3	13.24	0.129	0.35	0.95
1.15	5.3	0.5				
1.5	6.3	0.6				
2.7	6.2	0.2				
3.3	5.6	0.2				
4.05	6.1	0.1	13.67	0.072	0.41	0.99
5.28	12.8	0.6	13.29	0.065	0.31	0.98

4.3.2.1 Lusklint section

The Mg/Ca, Al/Ca, Mn/Ca and Sr/Ca ratios are variable throughout the Hunninge-1 drillcore (Mg/Ca = 4.38 to 6.5 µmol/mol; Al/Ca = 0.12 to 0.27 µmol/mol; Mn/Ca = 0.38 to 0.51 µmol/mol; Sr/Ca = 0.09 to 0.18 µmol/mol; Table 3; Fig. 7). The Al/Ca ratios remain below the ~0.8 mmol/mol threshold, suggesting little influence from Li leached from clays. The δ^7Li values range from 11 to 12.3 ‰ (Table 3; Fig. 7). The δ^7Li values remain relatively constant throughout the *bicornis* and *procerus* biozones.

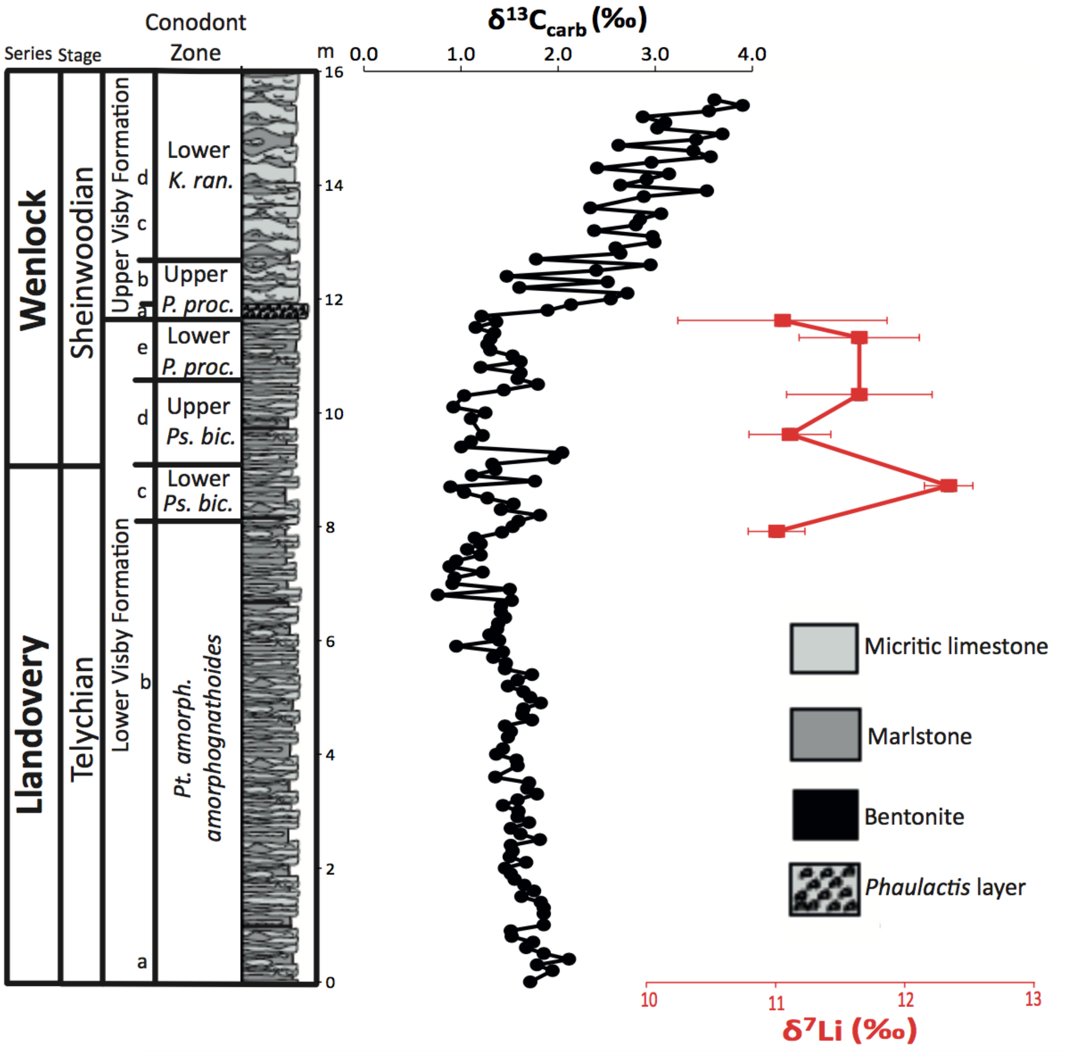

Figure 7. Lithium (δ^7Li, red squares) and carbon ($\delta^{13}C_{carb}$, black circles) isotope ratios for carbonates from the Llandovery-Wenlock Lusklint section. Biozone, lithology and carbon data have been adapted from Maier (2010). See text for details.

4.3.2.2 Lickershamn section

The Mg/Ca, Al/Ca, Mn/Ca and Sr/Ca ratios are variable throughout the Hunninge-1 drillcore (Mg/Ca = 4 to 6.63 µmol/mol; Al/Ca = 0.08 to 0.22 µmol/mol; Mn/Ca = 0.22 to 0.41 µmol/mol; Sr/Ca = 0.09 to 0.22 µmol/mol; Table 3; Fig. 7). The Al/Ca ratios remain below the ~0.8 mmol/mol threshold, suggesting little influence from Li leached from clays. The δ^7Li values range from 12.2 to 17.6 ‰ (Table 3; Fig. 8). The δ^7Li values relatively low (~13 ‰) at the base of the upper *procerus* biozones before rising to 17.6 ‰ by the end of the upper biozone, decreasing again to ~ 14.3 ‰ during the lower *ranuliformis* zone.

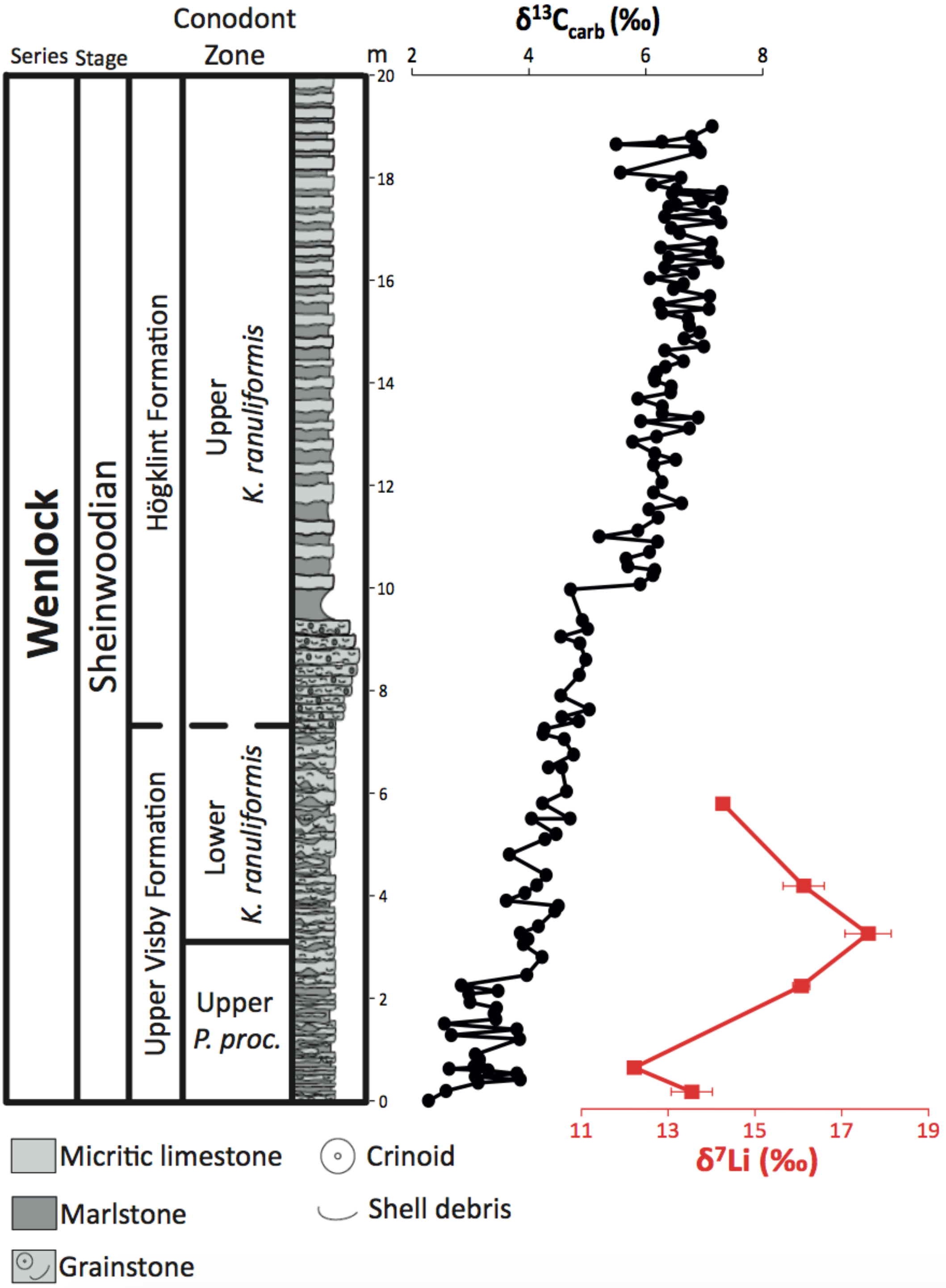

Figure 8. Lithium (δ^7Li, red squares) and carbon ($\delta^{13}C_{carb}$, black circles) isotope ratios for carbonates from the Llandovery-Wenlock Lickershamn section. Biozone, lithology and carbon data have been adapted from Maier (2010). See text for details.

4.3.2.3 Hunninge-1 drillcore

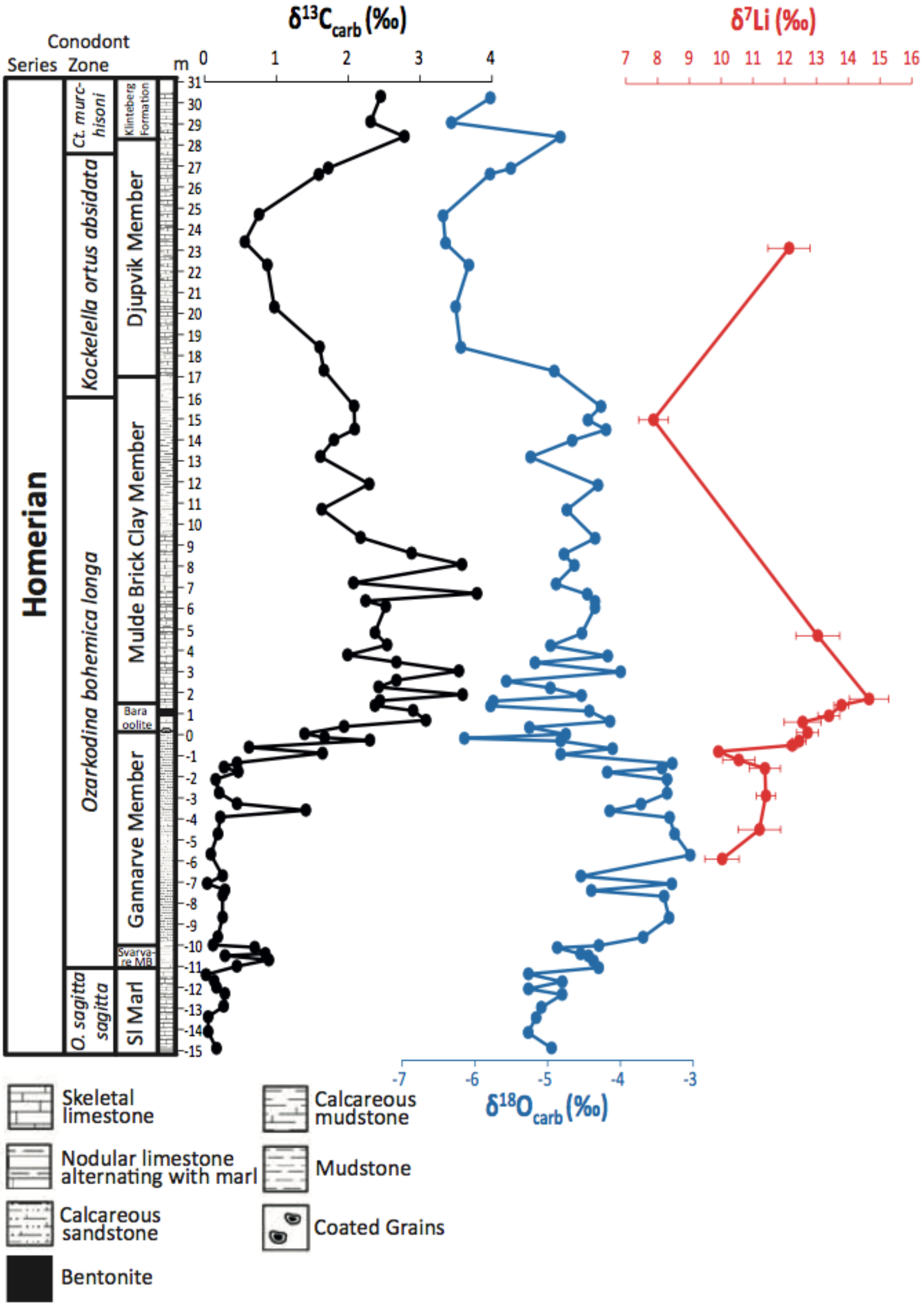

Figure 9. Lithium (δ^7Li, red squares), oxygen ($\delta^{18}O_{carb}$, blue circles) and carbon ($\delta^{13}C_{carb}$, black circles) isotope ratios for carbonates from the mid-Homerian Hunninge core. Biozone, lithology and carbon and oxygen data have been adapted from Calner et al. (2006). See text for details.

The Mg/Ca, Al/Ca, Mn/Ca and Sr/Ca ratios are variable throughout the Hunninge-1 drillcore (Mg/Ca = 15.6 to 48.3 µmol/mol; Al/Ca = -0.005 to 1.006 µmol/mol; Mn/Ca = 0.49 to 3.64 µmol/mol; Sr/Ca = 0.29 to 1.35 µmol/mol; Table 3). The majority of Al/Ca ratios remain below the ~0.8 mmol/mol threshold, suggesting little influence from Li leached from clays. However, samples from a depth of -1.5 and 0.2 m have an Al/Ca of ~1 suggesting possible influence from Li leached from clays. The δ^7Li values range from 9.9 to 14.7 ‰ (Table 3; Fig. 9). From 4.4 to 1.5 m, just prior to the base of the *nassa* biozone, δ^7Li remains relatively constant (~11.3 ‰). Just after the base of the *nassa* biozone, δ^7Li drops to 9.9 ‰ before rapidly increasing to 14.7 ‰ between 0.7 and -1.8 m. The δ^7Li then decreases to 13 ‰.

4.3.2.4 Kosov section

The Mg/Ca, Al/Ca, Mn/Ca and Sr/Ca ratios are variable throughout the Kosov section (Mg/Ca = 10.93 to 14.6 µmol/mol; Al/Ca = -0.02 to 0.2 µmol/mol; Mn/Ca = 0.31 to 1.23 µmol/mol; Sr/Ca = 0.44 to 0.99 µmol/mol; Table 3). Al/Ca remains below the 0.8 mmol/mol threshold, suggesting little influence from Li leached from clays. The δ^7Li values range from 4.6 to 15.4 ‰ (Table 3; Fig. 2e). From 4.77 to 1 m, prior to the base of the *dubius postfrequens* biozone, δ^7Li decreases from 9.6 to 4.6 ‰. Between 1 and 0.05 m, the δ^7Li increases from 4.6 to 15.4 ‰ before decreasing again to 5.3 ‰ by -1.15 m. The δ^7Li values remain relatively constant at ~6 ‰ before subsequently increasing to 12.8 ‰ between -4.05 and -5.28 m.

4.4 Discussion

The Os and Li isotope records (Fig. 1 and Figs. 3 to 9) show similar profiles for each time period studied, but with differing magnitudes of change. Prior to the δ^{13}C excursion there is change of 0.19 to 0.56 in the $^{187}Os/^{188}Os$ composition to more radiogenic values. This change in the $^{187}Os/^{188}Os$ composition is often associated with an increase in $\delta^{18}O$ of between 0.55 and 1.74 ‰ (Fig. 1 and Figs. 3 to 9). This is followed by a decline in the $^{187}Os/^{188}Os$ composition to previous values. This interval continues to be characterized by high $\delta^{18}O$ values. During the $\delta^{13}C$ excursion of between 0.9 and 8.29 ‰, the $^{187}Os/^{188}Os$ composition generally remains low (unradiogenic). In contrast, the $\delta^{7}Li$ increases by 4.8 to 9.2 ‰. During the relatively plateaued $\delta^{13}C$ interval, the $\delta^{18}O$ and $\delta^{7}Li$ values begin to return to pre-excursion values. During this decline, the $^{187}Os/^{188}Os$ values increase by 0.26 to 0.8 before returning to the more unradiogenic pre-excursion values either in time with the descending limb of the $\delta^{13}C$ record or prior to it, with exception of the Telychian-Sheinwoodian boundary, which has a hiatus after the ascending limb of the $\delta^{13}C$ excursion.

Processes that could cause these variations include contamination during sample processing, diagenesis, or a primary seawater signal driven by local or global changes in Earth system processes. Contamination of Re and Os from the detrital fraction of analysed shales was avoided using by the CrO_3–H_2SO_4 digestion method, while cation exchange or leaching of clays, which could impart an isotopically light $\delta^{7}Li$ signal, was monitored by analysing cation/Ca ratios of the carbonate samples (See section 4.2). Diagenesis can be discounted because similar trends and absolute values are repeated in sections from temporally separated sections (This study; Finlay et al., 2010; Pogge von Strandmann et al., in review). Furthermore, carbon and oxygen isotopes in studied profiles show similar values to other correlated sections that span the same intervals (Fig. 1; Saltzman and Thomas, 2012; Trotter et al., 2016, Cramer et al., 2011). It is therefore suggested that the isotopic shifts in the carbonate and shale sections must represent primary seawater signatures.

In the following section we will discuss how changes in a variety of Earth system processes can influence both the $^{187}Os/^{188}Os$ and $\delta^{7}Li$ of seawater, and determine if these processes could have caused the variations in isotope data seen in this study using dynamic Os and Li cycle models. Initially we will explore traditional ocean circulation models (Bickert et al., 1997; Jeppsson, 1990) used to explain lithological and carbon and oxygen isotope variations during the Silurian. We will then discuss the potential of rapid climatic cooling (e.g. Lechler et al., 2015; Pogge von Strandmann et al., 2013; Ravizza et al., 2001), flood basalt volcanism (e.g. Du Vivier et al., 2014; Lechler et al., 2015; Pogge von Strandmann et al., 2013) and hydrothermal activity as possible explanations. Finally we will discuss Silurian glacial expansions over Gondwana as a driver of global environmental change (Azmy et al., 1998; Brand et al., 2006; Kaljo et al., 2003; Trotter et al., 2016).

4.4.1 Isotopic constraints on Silurian seawater chemistry

4.4.1.1 Climatically induced changes in ocean circulation

Several ocean-climate models were developed during the 1990s to try and explain the observed changes in faunal turnover, lithology and carbon and oxygen isotopes. The first model was established by Jeppsson (1990) to explain observed changes in the lithology and conodont faunas of Gotland. The model proposes that major bio-events occurred during the transition between two stable oceanic states, known as Primo and Secundo Episodes, driven by a change in the latitudinal position of deep-water formation. Primo episodes were characterised by low atmospheric CO_2 concentration, cooler climates and relatively low global sea level. Downwelling of cold-dense high latitude surface waters ventilated the deep ocean, causing upwelling of oxic, nutrient-rich waters at low latitudes, which drove an increase in primary productivity and shelf fauna diversity. Low latitude climate was humid, and high rainfall would have intensified continental weathering, delivering abundant clay and nutrients to shelf seas. The Secundo episodes were characterised by higher atmospheric CO_2, warmer climates and therefore thermal expansion of the ocean. Cold-dense waters no longer formed at high latitudes, and salinity driven deep-water formation occurred at intermediate latitudes instead. This created a stratified ocean with lower primary productivity and shelf fauna diversity. The low latitude climate was dry, leading to lower run-off and a decline in continental weathering intensity. The Ireviken, Mulde and Lau events all supposedly culminated from a switch between these two oceanic states (Jeppsson, 1998).

As previously explained, the switch between Primo and Secundo episodes would have had a profound influence on low latitude continental weathering intensity and therefore the riverine flux and isotopic composition of osmium and lithium delivery to the ocean. During the Primo episodes, warmer temperatures, a humid climate and higher precipitation rates would be associated with enhanced chemical weathering rates of radiogenic continental crust resulting in an increase in the $^{187}Os/^{188}Os$ composition of seawater (Peucker-Ehrenbrink and Ravizza, 2000; Peucker-Ehrenbrink and Ravizza, 2012; Ravizza et al., 2001). High intensity weathering and extensive clay formation, as proposed by the Jeppsson (1990) model, would lead ^{7}Li-depleted clays and other secondary minerals to remain in the weathering zone for a long time, leading to dissolution of these phases and relatively low δ^{7}Li in river water and therefore a decrease in the δ^{7}Li of seawater (Bouchez et al., 2013; Dellinger et al., 2015). During the Secundo episodes, lower temperatures, a more arid climate and lower precipitation rates would be associated with reduced chemical weathering rates and therefore result in a lowering the $^{187}Os/^{188}Os$ composition of seawater (Peucker-Ehrenbrink and Ravizza, 2000; Peucker-Ehrenbrink and Ravizza, 2012). A lower weathering intensity and reduced clay formation would cause ^{6}Li to be retained in precipitated secondary minerals, leading to isotope fractionation and relatively high δ^{7}Li in the dissolved load of rivers and an increase in the δ^{7}Li of seawater (Bouchez et al., 2013; Dellinger et al., 2015).

According to the above scenarios, a switch between these two (Primo-Secundo) states during the Ireviken, Mulde and Lau events would be associated with permanent change from relatively radiogenic $^{187}Os/^{188}Os$ and low δ^7Li to relatively unradiogenic $^{187}Os/^{188}Os$ and high δ^7Li. However, the observed variations in $^{187}Os/^{188}Os$ and δ^7Li, associated with continental inputs, from this study (Fig. 1) do not follow this trend. Therefore, our data does not support a switch between Primo and Secundo episodes as a driver of Silurian climate perturbations, at least in terms of continental precipitation changes.

The model by Jeppsson (1990) was later further developed by Bickert et al. (1997) using geochemical data. They noticed that the Ireviken, Mulde and Lau events were all associated with anomalies in the $\delta^{13}C$ and $\delta^{18}O$ record from Gotland. Bickert et al. (1997) argued that the positive shifts in $\delta^{18}O$ during these events were driven by salinity fluctuations associated with changes in global evaporation-precipitation rates and continental run-off. As a result the ocean circulation model of Jeppsson (1990) was adapted accordingly to the stable isotope fluctuations into shifts between humid periods (H-periods) with high continental input and upwelling in coastal waters, and arid periods (A-periods) with little continental runoff and downwelling in coastal waters.

Generally, the model suggests that the Silurian climate is in a humid state punctuated by short arid episodes. A full humid-arid cycle (A-H modes) during the Ireviken, Mulde and Lau events would be associated with a decline in low-latitude continental weathering intensity during A-periods. To test the A-H modes a series of dynamic models were run to constrain the influence of a gradual decrease in global continental weathering rates by ~50 %, over 250 kyr, on the Os and Li isotope systems (Fig. 10). During a switch from an H- to A-period, a decline in riverine fluxes related to silicate and/or organic- and sulphide-rich lithology weathering (Fig. 10b) causes a shift to less radiogenic $^{187}Os/^{188}Os$

values (Fig. 10a), due to a reduction in the flux of radiogenic Os into the ocean. The $^{187}Os/^{188}Os$ values proceed to plateau at relatively unradiogenic values for ~750 kyr (Fig. 10a), before rising to more radiogenic values as the riverine input of more radiogenic Os resumes as the climate returns to a humid mode (Fig. 10b). For Li, the δ^7Li gradually increases to more positive values, peaking towards the end of the arid period (Fig. 10c). During the switch back to an H-period, the flux of continental derived Li increases (Fig. 10d), driving the δ^7Li back to previous values over the next 5 Myr (Fig. 10d).

Figure 10. Dynamic model of Os (**a**) and Li (**c**) isotopes for changes in continental precipitation rates according to Bickert et al. (1997). The model shown was generated by assuming a 50% drop in continental weathering and therefore riverine flux (**b**, **d**) during a switch from a humid-period (H) to an arid-period (A). In the case of Li, the weathering congruency is modelled by varying the isotope ratio of the riverine end member (**d**). See text for details.

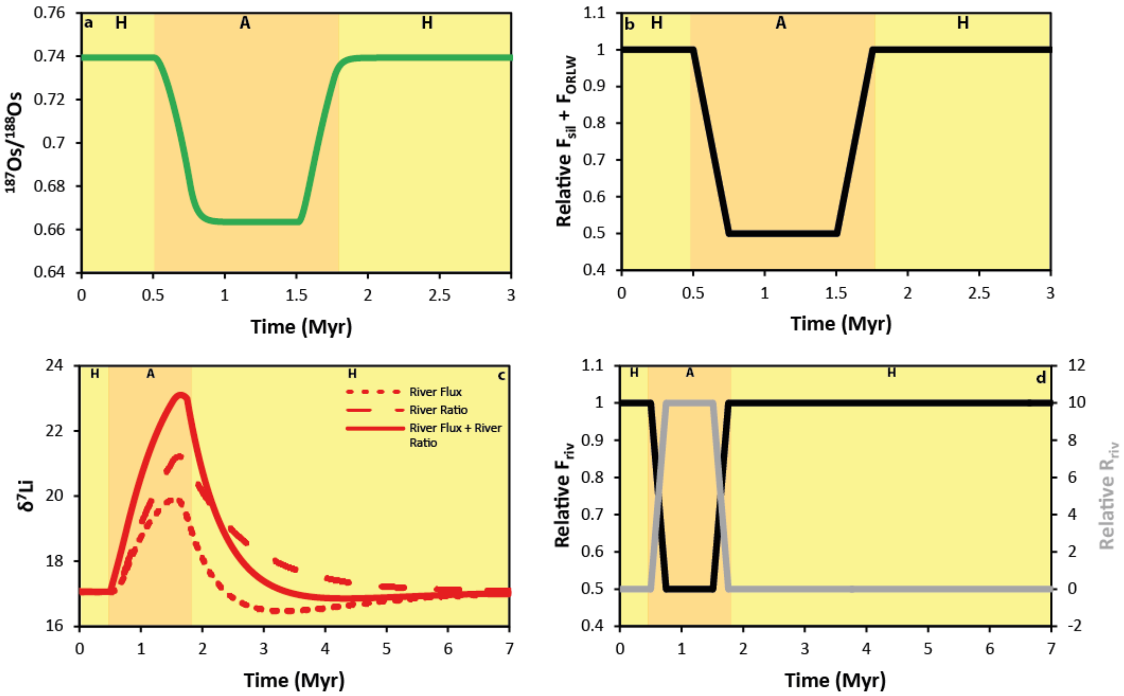

This is supported by the data from this study (Fig. 1), which shows less radiogenic $^{187}Os/^{188}Os$ compositions at the same time as the peak in δ^7Li values of similar magnitudes to the model (Fig. 10) during the A-periods associated with the Mulde and Lau events. We also see less radiogenic $^{187}Os/^{188}Os$ compositions during the Ireviken and Klonk events (Fig. 1). However, we would expect the corresponding H-periods to be associated with relatively radiogenic $^{187}Os/^{188}Os$ compositions (Fig. 10a), which would persist for much of the Silurian. In contrast, short-lived peaks characterized by radiogenic $^{187}Os/^{188}Os$ compositions are observed, with background levels during predicted H-periods similar to the duration of the A-period (Fig. 1). In addition, the ascending limb towards radiogenic $^{187}Os/^{188}Os$ compositions is associated with an increase in $\delta^{18}O$ in most instances (Fig. 1). According to the Bickert et al. (1997) model, this should be the converse, with a decline to unradiogenic $^{187}Os/^{188}Os$ compositions during an increase in $\delta^{18}O$ as a lower continental flux is associated with more saline coastal waters. This is compounded by previous criticisms that argue the concept of globally increasing aridity or humidity is not supported by modelling or existing data, and is therefore difficult to argue as a cause for global events (Johnson, 2006; Kaljo et al., 2003; Loydell, 1998; Munnecke et al., 2010).

4.4.1.2 Flood Basalt Volcanism

Periods of intense submarine or continental volcanism and the emplacement of large igneous provinces (LIPs) have a profound influence on global climate and are penecontemporaneous with the onset of ocean anoxic events (OAE). Additionally, newly formed basaltic terrains can have a large impact on secular variations in the osmium (Bottini et al., 2012; Cohen and Coe, 2002; Du Vivier et al., 2014; Ravizza and Peucker-Ehrenbrink, 2003; Turgeon and Creaser, 2008) and lithium (Lechler et al., 2015; Pogge von Strandmann et al., 2013) isotope records. Submarine fumarole and hydrothermal alteration / weathering of juvenile basalts delivers a flux of unradiogenic Os to the oceans, driving the $^{187}Os/^{188}Os$ composition of seawater towards mantle values. Further, during OAEs, abrupt global warming associated with rising atmospheric CO_2 caused enhanced weathering of mafic silicate material which delivered low δ^7Li (high [Li]) inputs to the ocean, driving the δ^7Li of seawater to lower values. Therefore, any igneous activity during the Silurian intervals studied here would be met by a rapid decrease in both the ^{187}Os/^{188}Os and δ^7Li of seawater, which is not observed (Fig. 1). Furthermore, this is compounded by the lack of evidence for LIPs during the Silurian.

4.4.1.3 Temperature-weathering feedbacks

Over geological timescales (Myr) temperature has partly been controlled by interactions between atmospheric CO_2 and continental weathering (Berner et al., 1983; Walker et al., 1981). Rising temperatures stimulate increased chemical weathering of silicate rocks drawing down CO_2 from the atmosphere, leading to a decline in temperature and vice versa (Berner et al., 1983; Walker et al., 1981). Rapid temperature fluctuations in the geological past could influence continental weathering and therefore secular variations in both Os and Li isotope records. This is supported by Os and Li isotope data from the Paleocene-Eocene Thermal Maximum (PETM) and OAEs respectively, which are interpreted to reflect abrupt release of greenhouse gases which resulted in an increase in global temperatures, stimulating continental silicate weathering and delivering radiogenic Os and isotopically heavy Li to the ocean (Lechler et al., 2015; Pogge von Strandmann et al., 2013; Ravizza et al., 2001).

Silurian oxygen isotope records of phosphates (Fig. 1) (Trotter et al., 2016) show globally recognised positive excursions, indicative of cooling during the Ireviken, Mulde and Lau events. Likewise, oxygen isotope data from sections studied here show an increase in δ^{18}O in time with, or slightly preceding, the Os and Li isotope excursions (Fig. 1). According to the above theory, a rapid cooling would be associated with a decline in global continental silicate weathering and therefore decrease the flux of the radiogenic Os and isotopically heavy Li to the ocean, driving the $^{187}Os/^{188}Os$ and δ^7Li composition of seawater to lower and higher values respectively. However, this study shows an increase in the $^{187}Os/^{188}Os$ composition of the hydrogenous component of the organic-rich sedimentary units, and thus by inference that of the contemporaneous seawater during, or slightly preceding the increase in the $\delta^{18}O$ values; with the excursion to more positive δ^7Li values occuring sometime after the initial rise in the $\delta^{18}O$ values (Fig. 1). This suggests that temperature change alone is not the driver of Os and Li isotope variations seen in this study.

4.4.1.4 Hydrothermal activity

In the modern oceans, hydrothermal activity at mid-ocean ridges accounts for a significant input of Os and Li to the ocean, with a $^{187}Os/^{188}Os$ composition and δ^7Li value of ~0.12 and ~8‰ respectively (Hathorne and James, 2006; Misra and Froelich, 2012; Peucker-Ehrenbrink and Ravizza, 2000). The isotopic composition of these fluxes is seen to be relatively consistent through time, however a change in their flux could cause variations in the isotopic composition of seawater. Although hard to constrain, a reduction in pluton emplacement (Hardie, 1996) and an increase in the Mg/Ca ratio of seawater (Stanley and Hardie, 1998) suggests a reduction in sea-floor spreading during the late-Wenlock to early-Ludlow (Cramer et al., 2011b). However, the low resolution of available data prevents an estimation of variations of hydrothermal activity over the relatively short timescales studied here.

Several dynamic models were run to constrain the influence of short periodic fluctuation in the flux of high temperature hydrothermal activity on the Os and Li isotope systems (Fig. 11). Two scenarios were modelled: 1. A pulsed decrease in the hydrothermal flux by ~50% (Fig. 11b); and, 2. A single, extended period of reduced (~50%) hydrothermal flux (Fig. 11d). During the pulsed scenario we see a simultaneous increase to more radiogenic ^{187}Os/^{188}Os compositions and more positive δ^{7}Li values with each decrease in hydrothermal flux (Fig. 11a). Although the ^{187}Os/^{188}Os compositions become more unradiogenic in time with an increase in hydrothermal flux, the δ^{7}Li values show a delayed response, declining over the proceeding 250 kyr (Fig. 11a). This compares well with the ^{187}Os/^{188}Os data from this study (Fig. 1), which show two uniform peaks in radiogenic ^{187}Os/^{188}Os compositions. However, the magnitude of change predicted by the model (0.07) is much smaller than measured isotope ratios. Likewise, the δ^{7}Li values measured here (Fig. 1) show one singular peak in δ^{7}Li towards the second peak in ^{187}Os/^{188}Os compositions, which is not seen in the model (Fig. 11a).

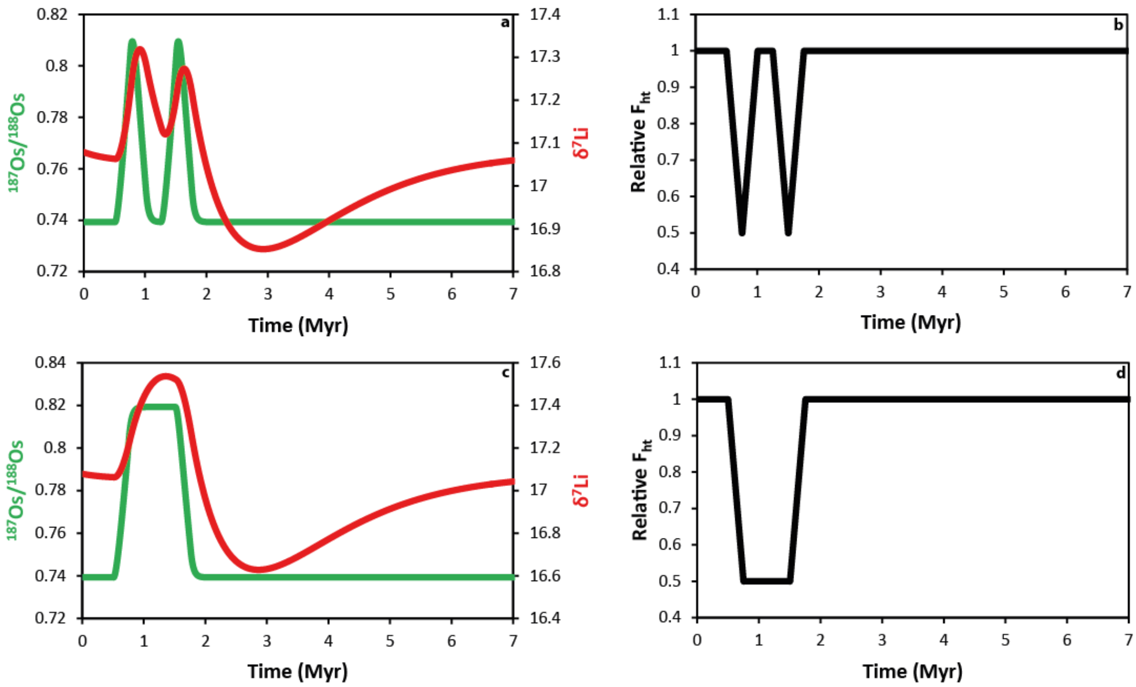

Figure 11. Dynamic model of Os and Li isotopes for a pulsed reduction in hydrothermal flux (**a**) and an extended period of reduced hydrothermal flux (**c**). The model shown was

generated by assuming a 50% drop in hydrothermal flux over two relatively short 250 kyr periods (**b**) or over a single, more extended 750 kyr period (**d**). See text for details.

During an extended period of reduced hydrothermal flux (Fig. 11d), the ^{187}Os/^{188}Os compositions and δ^{7}Li values increase over a similar period of time (Fig. 11c). This compares well with Li isotope data from this study (Fig. 1), which shows a singular peak in δ^{7}Li. However, the magnitude of change predicted by the model (<0.5 ‰) is far too small when compared to the excursion observed (>4 ‰). Likewise, the ^{187}Os/^{188}Os composition determined here (Fig. 1) show two peaks in radiogenic ^{187}Os/^{188}Os values, which is not seen in the model (Fig. 11c). In both model outputs (Fig. 11a and c) the δ^{7}Li decreases by >0.3‰ below background levels after the excursion due to a dependence of the partition coefficient on seawater concentration, which remains low even after the input has increased. These modelling studies (Fig. 11) suggest that fluctuations in the hydrothermal flux cannot cause the variations in Os and Li isotope data seen here (Fig. 1).

4.4.1.5 Glaciation

Osmium and Li isotope variations found in this study bear a striking resemblance to those measured for the Hirnantian glaciation (Finlay et al., 2010; Pogge von Strandmann et al., in review), some 12 Myrs earlier than the Telychian-Sheinwoodian boundary (Fig. 1). Authors postulated these variations were driven by fluctuations in chemical weathering rates related to enhanced continental ice volume over Gondwana. Due to the similarities in Os and Li isotope trends determined here, combined with reoccurring global trends in oxygen isotopes (Azmy et al., 1998; Calner, 2008; Lehnert et al., 2010; Munnecke et al., 2010; Noble et al., 2005; Trotter et al., 2016), carbon isotopes (Cramer et al., 2011a; Cramer et al., 2010; Munnecke et al., 2010; Saltzman and Thomas, 2012), sea-level reconstructions (Haq and Schutter, 2008; Johnson, 2006, 2010; Loydell, 1998), marine faunal turnover

(Calner, 2008; Cooper et al., 2013; Melchin et al., 2012), and in the case of the early Sheinwoodian, the presence of glacial sediments (Díaz-Martínez and Grahn, 2007), we suggest changes in continental weathering caused by glaciation events could have occurred during each of the four Silurian time intervals studied.

During glacial advance, physical erosion of the underlying bedrock provides abundant freshly comminuted rock flour to ice-sheet margins and the proglacial zone (Tranter, 1982). Subglacial and proglacial conditions promote sulphide oxidation and the chemical weathering of carbonates in these newly formed reactive mineral surfaces regardless of underlying lithology (Anderson et al., 2000; Cooper et al., 2002; Fairchild et al., 1999; Tranter et al., 2002) whilst stimulating the microbially mediated oxidation of ancient organic matter supplied by comminuted shales (Petsch et al., 2001a; Wadham et al., 2004). Sedimentary sulphides and organic matter are often associated with high Os concentrations and highly radiogenic ^{187}Os/^{188}Os compositions (Jaffe et al., 2002; Peucker-Ehrenbrink and Hannigan, 2000; Peucker-Ehrenbrink and Ravizza, 2000; Pierson-Wickmann et al., 2002; Ravizza and Turekian, 1989), and their erosion and subsequent oxidation by advancing ice-sheets would impact on the global riverine Os end-member, driving seawater to more radiogenic values. The initial peak in ^{187}Os/^{188}Os values seen in this study (Fig. 1) and during the Hirnantian glaciation (Finlay et al., 2010) can therefore be attributed to glacial advance.

However, low temperatures in newly glaciated regions would act to suppress chemical silicate weathering to lower rates than previously non-glaciated regions (Anderson, 2005, 2007; Anderson et al., 2000; Anderson et al., 1997; Gislason et al., 2009; Maher and Chamberlain, 2014). If physical erosion rates increase, while silicate chemical weathering remains constant or decreases, weathering intensity will decline and therefore increase the dissolved δ^7Li values of rivers (Bouchez et al., 2013; Dellinger et al., 2015; Li and West, 2014; Pogge von Strandmann et al., 2017). Likewise, regions of low chemical weathering intensity will drive the δ^7Li of glacial rivers to more positive values, as ^{6}Li is retained by secondary minerals (Pogge von Strandmann et al., 2006), and the formation of Fe-oxyhydroxides during sulphide oxidation under ice-sheets will also preferentially uptake ^{6}Li onto mineral surfaces, contributing to the rise in the δ^7Li of glacial waters (Wimpenny et al., 2010). An increase in the δ^7Li values of the riverine flux combined with a decrease in the overall global riverine flux of Li, due to the gradual covering of Gondwana by continental ice-sheets preventing weathering of the underlying silicate minerals (Kump and Alley, 1994; Pogge von Strandmann et al., in review), will drive the δ^7Li value of seawater to more positive values (Fig. 1).

As glacial expansion began to slow and glacial maximum was established, the previously high denudation rates would have diminished along with the oxidation of proglacial and subglacial sulphides and organic matter, reducing the input of Os with a radiogenic ^{187}Os/^{188}Os composition to the oceans. When diminutive denudation is coupled with enhanced low latitude continental cover by ice sheets and generally colder, drier conditions, overall global chemical weathering rates would have remained low under glacial maximum (Kump and Alley, 1994), maintaining high δ^7Li values and low ^{187}Os/^{188}Os compositions in seawater (Fig.1) (Finlay et al., 2010; Pogge von Strandmann et al., in review). For the Hirnantian glaciation, authors have suggested that this transient decline in silicate weathering, and therefore a decline in one of the Earth's major atmospheric CO_2 withdrawal mechanisms, would have caused an increase in atmospheric CO_2 that ultimately terminated the glaciation (Kump et al., 1999; Pogge von Strandmann et al., in review). The similarity between Li isotope records for the Hirnantian (Pogge von Strandmann et al., in review) and this study (Fig. 1) suggest a similar mechanism for deglaciation could have occurred throughout the Silurian.

Whatever the cause of deglaciation, the extensive availability of fresh material, increased melt water and generally wetter conditions during the demise of continental ice sheets would enhance the oxidation and/or weathering of sulphides, shales and silicates left behind (Bluth and Kump, 1994; Drever and Zobrist, 1992; Gaillardet et al., 1999; Huh and Edmond, 1999; Meybeck, 1987; Petsch et al., 2001b; Vance et al., 2009; Wildman et al., 2004). This would cause a shift in the global riverine Os end-member, and therefore seawater, to more radiogenic values (Finlay et al., 2010; Peucker-Ehrenbrink and Blum, 1998) creating the second peak in the ^{187}Os/^{188}Os composition record (Fig. 1). Greater weathering intensity of silicates will decrease Li isotope fractionation between the dissolved and suspended loads of glacial rivers, as less ^{6}Li is retained in secondary minerals, driving δ^{7}Li to lower values (Huh et al., 1998; Pogge von Strandmann et al., 2006). As these newly formed river systems become more mature, continued weathering of suspended material will increase the saturation state of the dissolved load with respect to secondary minerals, lowering δ^{7}Li values further (Dellinger et al., 2015; Pogge von Strandmann et al., 2006). A decrease in the δ^{7}Li value and Li concentration of riverine end-members would lead to a decrease in δ^{7}Li value of seawater, eventually restoring the system to pre-excursion values (Fig. 1).

Several dynamic models were run to constrain the influence of glacial processes on the Os and Li isotope systems (Fig. 12). Biozone boundary ages (Melchin et al., 2012) were used to constrain the timings of glaciation (~250 kyr; light blue box denoted by G in Fig. 12), glacial maximum (~500 kyr; dark blue box denoted by GM in Fig. 12) and deglaciation (~250 kyr; light blue box denoted by D in Fig. 12). During glaciation, the relative continental flux related to silicate weathering (Fig. 12b and 12e) gradually decreases by 50%, while the weathering of organic-sulphide-rich lithologies increases by ~80% (Fig. 12c). In the case of the Os isotope system, this causes a switch from a riverine budget dominated by silicate weathering (60% of total F_{riv}), to a riverine budget dominated by ORLW (70% of total F_{riv}). The highly radiogenic nature of ORL ($^{187}Os/^{188}Os$ = 1.34; Table 1) when compared to silicate minerals ($^{187}Os/^{188}Os$ = 0.6; Table 1) causes total R_{riv} to become more radiogenic, whilst F_{riv} remains constant, driving the $^{187}Os/^{188}Os$ composition of seawater to more radiogenic values (Fig. 12a). Meanwhile, a reduction in riverine inputs related to silicate weathering (Fig. 12e) drives δ^7Li to more positive values (Fig. 12d).

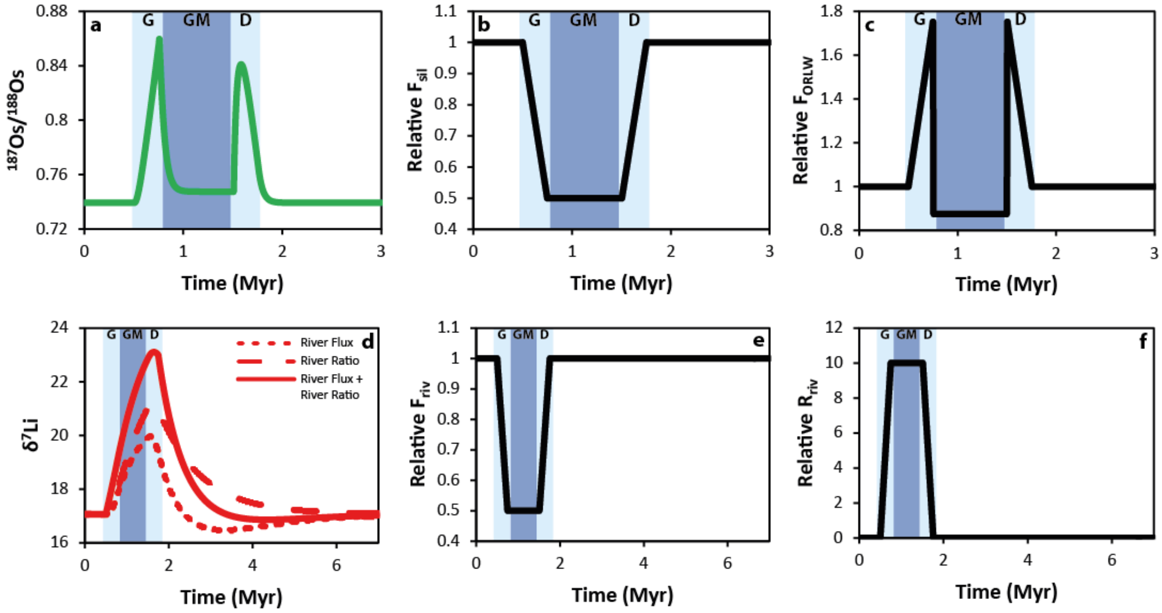

Figure 12. Dynamic model of Os (**a**) and Li (**d**) isotopes during a change in high-latitude continental ice volume. The model shown was generated by assuming a 50% decrease in continental silicate weathering (**b**, **e**) during glaciation (G), which remains low during glacial maximum (GM), before increasing during deglaciation (D). In the case of Os, two periods of enhanced ORLW during glaciation and deglaciation are generated by assuming a 70% increase in the riverine flux related to ORLW (**c**). In the case of Li, the weathering congruency is modelled by varying the isotope ratio of the riverine end member (**f**). See text for details.

During glacial maximum, ice sheet movement stops, causing the immediate cessation of enhanced ORLW and the relative flux of F_{ORLW} drops to below pre-excursion values (Fig. 12c). This causes a decrease in the $^{187}Os/^{188}Os$ composition of seawater as the input of radiogenic Os to seawater is removed (Fig. 12a). The δ^7Li of seawater continues to increase, reaching peak values towards the end of the glacial maximum (Fig. 12d). During deglaciation, the riverine flux related to silicate weathering gradually increases back to pre-excursion levels (Fig. 12b and 12e), while the riverine input related to ORLW shows a second instantaneous increase before gradually declining to pre-excursion levels (Fig. 12c). This causes an increase in the ^{187}Os/^{188}Os composition of seawater before the ^{187}Os/^{188}Os composition decreases to pre-excursion values (Fig. 12a). The δ^7Li value of seawater gradually decreases to pre-excursion values over the next ~2 Myr (Fig. 12d).

This compares well to Os isotope data for the Ireviken, Mulde, Lau and Klonk events (Fig. 1), which all show a similar two-peak profile to model outputs (Fig. 12a). However, the magnitude of change from model outputs (~0.12) is lower than described in the data (0.19-0.8). Possible causes of these discrepancies could be: a misrepresentation of model input parameters; or, a stronger influence from local continental sources of Os in coastal shelf sampling localities, which will drive larger variations in recorded ^{187}Os/^{188}Os when compared to a well-mixed ocean. Lithium isotope records (Fig. 1) show a similar singular peak in δ^7Li values to the model outputs (Fig. 12d). A scenario in which river flux alone varied throughout the glaciation event causes a δ^7Li excursion of ~3 ‰ (Fig. 12d), which compares well to recorded data for the Mulde and Lau events (<4.4 ‰; Fig. 1). Peak δ^7Li values occur during deglaciation and the second peak of radiogenic ^{187}Os/^{188}Os values (Fig. 12a and d), consistent with data for the Mulde event (Fig. 1). A scenario in which the river flux decreased, while riverine δ^7Li ratios increased caused a variation in δ^7Li (~6 ‰) greater than observed in the data, suggesting weathering congruency remained constant throughout the glaciation.

The failure of Silurian ocean circulation models (See section 4.1.1), flood basalt volcanism (See section 4.1.2), rapid cooling (See section 4.1.3) and variations in hydrothermal activity (See section 4.1.4) in describing variations in Os and Li isotopes found here (Fig. 2), leads us to the conclusion that periodic glaciations are the most likely cause of

Silurian climate events, based on the current understanding of the Os and Li isotope systems. The data and models are consistent with glaciation events during the late Telychian to early Sheinwoodian, mid-Homerian, mid-Ludfordian and the Silurian-Devonian boundary. During glaciation, expanding continental ice sheets enhance physical erosion whilst stimulating chemical weathering of organic and sulphide rich rocks as evidenced by an increase in the $^{187}Os/^{188}Os$ composition to more radiogenic values (Fig. 1; Fig. 12a). Meanwhile, glacial cover, subglacial processes and declining global temperatures reduce silicate weathering, decreasing the riverine flux of Li to the ocean, leading to an increase in the $\delta^{7}Li$ value of seawater (Fig. 1; Fig. 12e). Declining temperatures coupled to enhanced continental ice volume drive the $\delta^{18}O$ of seawater to more positive values (Azmy et al., 1998; Calner, 2008; Lehnert et al., 2010; Munnecke et al., 2010; Noble et al., 2005; Trotter et al., 2016). A drop in eustatic sea-level (Haq and Schutter, 2008; Johnson, 2006, 2010; Loydell, 1998) exposes carbonate shelves to weathering, driving the $\delta^{13}C$ of seawater to more positive values (Cramer et al., 2011a; Kump et al., 1999; Saltzman and Thomas, 2012). As the glacial maximum is reached, ice sheet expansion abruptly terminates, reducing the availability of freshly comminuted rock for the oxidation of ancient organic matter and sulphide rich lithologies and therefore reducing the flux of Os to the ocean bearing a radiogenic $^{187}Os/^{188}Os$ composition (Fig. 1; Fig. 12a). Extensive stable continental ice-sheets maintain low levels of silicate weathering (Fig. 1; Fig. 12e) and sea-level (Johnson 2006, 2010; Haq and Schutter, 2008; Loydell, 1998) whilst maintaining a higher $\delta^{18}O$ value of seawater (Trotter et al., 2016). During deglaciation, rising temperatures and the increased availability of melt water and freshly comminuted and/or scoured bedrock, enhances chemical silicate weathering and the oxidation of organic and sulphide rich rocks, driving an increase in the $^{187}Os/^{188}Os$ composition of seawater, and a decrease in the $\delta^{7}Li$ value of seawater (Fig. 1; Fig. 12a and 12e). An increase in global temperatures and a reduction in continental ice-volume, drives a decrease in the $\delta^{18}O$ value of seawater (Trotter et al.,

2016) and an increase in global eustatic sea-level (Haq and Schutter, 2008; Johnson, 2006, 2010; Loydell, 1998).

A coupled drop in eustatic sea level and global temperatures would have had a profound influence on marine biota. The Ireviken, Mulde, Lau and Klonk bio-events are defined by global extinctions of conodonts, graptolites, acritarchs, and other benthos (Aldridge et al., 1993; Calner, 2008; Cooper et al., 2013; Jeppsson, 1990, 1997; Jeppsson, 1998; Jeppsson and Aldridge, 2000; Loydell, 2007; Melchin et al., 1998; Štorch, 1995). Cooper et al. (2013) utilised graptoloid evolutionary rates to track global climatic change. Relatively calm Ordovician extinction and origination rates gave way to highly volatile rates during the late Katian through to the Early Devonian, with sharp extinction episodes triggered by environmental crisis (Cooper et al., 2013). This supports the idea presented in this study, in which a switch from relatively stable greenhouse conditions during the Early and Middle Ordovician, to relatively unstable icehouse conditions during the Hirnantian and Silurian, created highly volatile conditions for marine biota. Abrupt glaciations presented here coincide with high graptloid extinction rates during the early Sheinwoodian, mid Homerian, late Ludfordian and latest Pridolian, with subsequent high levels of originations during recovery phases (Cooper et al., 2013).

4.4.2 Scenarios for triggering Silurian Glaciations

Several mechanisms, usually involving a drop below threshold atmospheric CO_2 levels (~6 PAL; Pohl et al., 2014), have been put forth as triggers for the Hirnantian glaciation, and include changes in: orogeny (Kump et al., 1999); land plant diversification (Lenton et al., 2012; Porada et al., 2016); volcanic arc degassing (McKenzie et al., 2016; Pogge von Strandmann et al., in review); and, paleogeography (Nardin et al., 2011). Like the Ordovician that preceded it, many of these processes were active during the Silurian, providing several possible candidates for the mechanism that triggered the glaciations proposed in this study.

4.4.2.1 Orogeny

It has been argued that enhanced weatherability of silicate rocks during the Taconic orogeny, led to a long-term decline in atmospheric CO_2 which eventually dropped below the threshold levels that would allow continental ice to expand (Kump et al., 1999). During the Silurian, Avalonia and Baltica collided, with subsequent collision of these combined landmasses with Laurentia to form the Scandian orogeny (Cocks and Torsvik, 2002; Torsvik and Cocks, 2013). The rapid rise to more radiogenic $^{87}Sr/^{86}Sr$ isotope ratios during the Silurian has been attributed to enhanced weathering of old sialic crust exposed during the aforementioned formation of the Caledonian-Appalachian orogenic belt (Cramer et al., 2011b). Moreover, steep inflection points in the Sr isotope record occur prior to and/or during the late-Telychian, mid-Homerian, mid-Ludfordian and the Silurian-Devonian boundary (Cramer et al., 2011b; Frýda et al., 2002). These repeating periods of enhanced weatherability of exposed sialic crust would have led to the long-term decline in atmospheric CO_2 and global temperatures which, if dropped below threshold levels (Kump et al., 1999), would initiate the formation of continental ice sheets.

4.4.2.2 Land plant diversification

It has been hypothesized (Lenton et al., 2012) that the expansion of non-vascular land-plants during the Ordovician accelerated global chemical weathering by up to three times modern weathering fluxes (Porada et al., 2016), leading to the drawdown of enough atmospheric CO_2 (< 6 PAL) to trigger the growth of ice sheets. Moreover, the development of vascular land plants during the Devonian is thought to have caused a dramatic drawdown in atmospheric CO_2 that led to global cooling and polar glaciations during the Late Devonian, ultimately leading to Carboniferous icehouse conditions (Algeo and Scheckler, 2010; Algeo and Scheckler, 1998; Berner, 1997). During the Silurian, non-vascular and vascular land plants expanded geographically to inhabit new continents and land masses (Steemans et al., 2009). Meanwhile, the development of evolutionary traits in vascular land-plants, such as more extensive rooting structures and 'the seed habit', originally assigned to the Devonian (Algeo and Scheckler, 2010; Algeo et al., 1995; Algeo and Scheckler, 1998), are now thought to have developed earlier, during the Silurian (Edwards et al., 2014; Gensel, 2008; Kenrick et al., 2012). Geographical expansion and/or the development of more extensive root systems would act to enhance the weathering rates of silicates, leading to a reduction in atmospheric CO_2, global cooling and periodic glaciations.

4.4.2.3 Volcanic arc degassing

Recently, variations in volcanic arc activity have been shown to have a direct relationship with climatic shifts between icehouse and greenhouse conditions (McKenzie et al., 2016). Continental collisions during the assembly of Gondwana led to a reduction in continental arc volcanism, and therefore atmospheric CO_2 emissions, culminating in global cooling and the Hirnantian glaciation (McKenzie et al., 2016; Pogge von Strandmann et al., in review). In the Mid-Late Silurian, the Iapetus Ocean closed during the formation of Laurussia. This newly formed continent rapidly travelled southward, eventually colliding with Gondwana, causing the closure of the Rheic Ocean by the Carboniferous (Cocks and torsvik, 2002). This would have led to a reduction in continental arc volcanism, as evidenced by cumulative age distributions of Silurian Zircons (McKenzie et al., 2016), leading to global cooling and intermittent Silurian glaciations.

4.4.2.4 Paleogeography

Another explanation for the upper Ordovician through to late Llandovery glacial period involves changes in paleogeography that caused the movement of freshly exposed volcanic rocks (Lefebvre et al., 2010; Young et al., 2009) through the intertropical convergence zone (ITCZ), stimulating continental weathering and a decline in atmospheric CO_2 below a threshold that would allow continental glaciations to occur (Nardin et al., 2011). In particular, the progressive amalgamation of Baltica, Avalonia and Laurentia at tropical latitudes led to high runoff and therefore weathering, maintaining the low atmospheric CO_2 required to initiate the early Silurian glaciations (Nardin et al., 2011). Although this model could explain the mechanism by which a glaciation just after the Telychian-Sheinwoodian boundary (Fig. 1), it precludes the existence of late Silurian glaciations due to decreases in continental runoff as continental landmasses move out of the ITCZ (Nardin et al., 2011). However, this may be due to the low temporal resolution of the model.

4.4.2.5 Orbital forcing

Although there have been many Paleozoic-centric mechanisms put forth as drivers for Paleozoic glaciations (See section 4.4.2.1 to 4.4.2.4) it has recently become apparent that a more ‘Cenozoic-style’ scenario may have caused the end-Ordovician glaciations (Ghienne et al., 2014). The Hirnantian glaciation is generally viewed as a singular event, with marine extinctions tied to glaciation and deglaciation. However, high resolution stratigraphic records have led to the discovery of several high-order glacial cycles, suggesting a multi-order climate signal similar to the Cenozoic (Sutcliffe et al., 2000; Ghienne et al., 2014). Both two (Sutcliffe et al., 2000) and three (Ghienne et al., 2014) glacial cycles of ice-sheet growth have been recorded for the end-Ordovician, controlled by a 0.1 Myr eccentricity periodicity (Sutcliffe et al., 2000) or 1.2 Myr obliquity modulation (Ghienne et al., 2014) respectively.

Much like previous views for the Ordovician, the Silurian climatic events are generally seen to have a singular peak, lacking in high order glacial cycles. However, the Silurian is severely lacking in high resolution stratigraphic and isotopic records, precluding the discovery of orbitally forced 'Cenozoic-style' glacial cycles. Moreover, Os and Li isotopic records from this study (See Fig. 1) are of such low-resolution that they prevent recognition of such events. However, Silurian oxygen isotope (Trotter et al., 2016) and sea-level ((Haq and Schutter, 2008; Johnson, 2006, 2010; Loydell, 1998) records show high-order fluctuations possible related to glacial eustasy on glacial-interglacial timescales (See Fig.1). Furthermore, the Hirnantian, Sedgwicki, Ireviken, Mulde, Lau and Klonk events appear to be spaced over 4 to 5 Myr intervals (See Fig. 1) suggesting a pacing to Silurian glaciations which could be set by the interaction between eccentricity, obliquity and precession cycles, ultimately controlled through changes in insolation. More work will need to be generate high-resolution stratigraphic and isotopic records for Silurian climatic events in a similar manner to the end-Ordovician (See Sutcliffe et al., 2000 and Ghienne et al., 2014).

4.4.2.6 Why did we not see 'Snowball Earth' conditions during the Silurian?

Large glaciations encompassing the entire globe, otherwise known as 'Snowball Earths', are believed to have occurred during the Neoproterozoic (1000 – 542 Ma), as evidenced from the existence of low-latitude glacial deposits at sea-level (See Hoffman & Schrag, 2002 and references therein). These events could have potentially been triggered by high obliquity caused by the lunar-forming impact (See Williams, 2008) or positive ice-albedo feedbacks which led to glacials that lasted tens of millions of years before the slow accumulation of atmospheric CO_2 due to volcanic degassing brought them to an end (See Hoffman & Schrag, 2002). However, unlike the Neoproterozoic snowball Earths, Paleozoic glaciations such as those found in the Cambrian, Late Ordovician, Silurian, Late Devonian and Carboniferous are generally not met by low-latitude glacial deposits and deglacial cap-carbonates and negative $\delta^{13}C$ excursions (>10 ‰). This suggests there was either more/less feedback mechanisms active during the Neoproterozoic when compared to the Paleozoic, that allowed for runaway icehouse conditions to occur.

Phanerozoic paleogeography reconstructions (Cocks and Torsvik, 2002; Torsvik and Cocks, 2013) often situates continental masses at high-latitudes over one or both of the poles, either as a supercontinent e.g. Pangea or a smaller continent e.g. Antarctica. However, unlike the Phanerozoic, Neoproterozoic snowball Earths are dominated by a severe lack of high-latitude continental masses. This would have created an absence of continental ice-weathering feedbacks proposed in this study for the Silurian (See section 4.4.1.5). Therefore, once polar glaciation is initiated, sea-ice formation would proceed to low latitudes via positive ice-albedo feedback without the subsequent reduction in silicate weathering and enhancement of oxidative weathering associated with continental ice, which would otherwise act to increase atmospheric CO_2 leading to global warming. This suggests weathering feedbacks help regulate atmospheric CO_2, preventing runaway icehouse conditions and snowball Earths (See section 4.4.3).

4.4.3 Weathering feedbacks help regulate atmospheric CO_2

Weathering regulates atmospheric CO_2 over multimillion year timescales and can be summarised by several chemical reactions (Berner and Berner, 2012; Berner, 2006; Berner et al., 1983; Torres et al., 2014; Walker et al., 1981). The dissolution of Mg- and Ca- bearing silicate minerals by carbonic acid, and the subsequent transport of solutes to the ocean where inorganic carbon is buried as marine carbonates, sequesters atmospheric CO_2:

$$CO_2 + (Ca, Mg)SiO_3 \rightarrow (Ca, Mg)CO_3 + SiO_2 \qquad \text{Eq.7}$$

On the other hand, the oxidative weathering of ancient sedimentary organic matter releases CO_2 back to the atmosphere:

$CH_2O + O_2 \rightarrow CO_2 + H_2O$ Eq. 8

Other sources of atmospheric CO_2 include the oxidative dissolution of pyrite and the subsequent dissolution of carbonates by sulfuric acid:

$15O_2 + 4FeS_2 + 14H_2O \rightarrow 4Fe(OH)_3 + 8H_2SO_4$ Eq.9

$CaCO_3 + H_2SO_4 \rightarrow CO_2 + H_2O + Ca^{2+} + SO_4^{2-}$ Eq.10

and

$2CaCO_3 + H_2SO_4 \rightarrow 2Ca^{2+} + 2HCO_3^{-} + SO_4^{2-} \leftrightarrow CaCO_3 + CO_2 + SO_4^{2-} + Ca^{2+}$

Eq.11

Reactions 7 to 11 show a strong dependence on climatic parameters such as temperature, runoff and/or physical weathering (Georg et al., 2013; Torres et al., 2014). During the Cenozoic, concurrent increases in the $^{87}Sr/^{86}Sr$, $^{187}Os/^{188}Os$ and δ^7Li records (Klemm et al., 2005; McArthur et al., 2001; Misra and Froelich, 2012) suggest enhanced physical and chemical denudation during extensive uplift of mountain ranges may have stimulated CO_2 consumption via silicate weathering (Raymo et al., 1988). However, in the absence of enhanced CO_2 production from other sources, this would have stripped the atmosphere of all its CO_2 within a few million years (Berner and Caldeira, 1997). This decline in atmospheric CO_2 may have been offset by a release of CO_2 from a simultaneous increases in oxidative weathering of ancient organic carbon (Li et al., 2009) and/or carbonate–sulfuric acid weathering (Torres et al., 2014).

During Quaternary glacial-interglacial cycles, enhanced physical weathering left behind fine-grained material for chemical weathering at glacial terminals (Bell and Laine, 1985; Goodbred and Kuehl, 2000; Hinderer, 2001; Thomas and Thorp, 1995). This caused deglacial pulses in silicate weathering that could have theoretically lowered atmospheric CO_2 by 10 - 20 ppm (Vance et al., 2009). However, ice cores record a rise in CO_2 during deglaciations (Petit et al., 1999) due to a concurrent release of CO_2 from the enhanced weathering of organic- and sulphide-rich sedimentary rocks, which exceeded CO_2 consumption by silicate weathering (Georg et al., 2013).

Here, we propose similar processes occurred during the Silurian. The long-term decline in atmospheric CO_2 caused by orogeny, land-plant diversification, volcanic degassing and/or paleogeographic changes, induced global cooling. Eventually atmospheric CO_2 dropped below threshold levels (~6 PAL) triggering an expansion of southern hemisphere ice sheets over Gondwana, which proceeded to expand via positive ice-albedo feedback. During glaciation, enhanced physical weathering and glacial processes acted to increase the oxidation of ancient organic carbon and sedimentary sulphides, which subsequently dissolved carbonates, releasing atmospheric CO_2 to the atmosphere. Meanwhile, silicate weathering declined, partially suppressing one of the Earth's major CO_2 removal mechanisms. The combined influence of these two effects began to reverse the global cooling trend. During glacial maximum, relatively low silicate weathering rates allowed CO_2 to build up in the atmosphere via other processes e.g. volcanism, leading to rapid warming and eventually deglaciation. This deglaciation exposed scoured bedrock to the atmosphere and generated freshly comminuted glacial till, acting as a fertile substrate for meltwater to chemically attack. A decline in atmospheric CO_2 due to enhanced silicate weathering at glacial terminals would have been largely offset by enhanced oxidation of organic- and sulphide- rich sedimentary rocks. This work lends itself to the idea of the Earth having a self-regulating climate that allows life to remain within habitable conditions (Berner and Caldeira, 1997; Berner et al., 1983; Garrels et al., 1976; Walker et al., 1981).

4.5 Implications and future outlook

Osmium and Li isotope data presented here are interpreted to trace fluctuations in continental weathering through Silurian climatic perturbations. During the Silurian, orogeny, the diversification and global expansion of land plants, changes in paleogeography and/or a reduction in volcanic arc degassing, led to a long-term decline in atmospheric CO_2 and global cooling. During the late Telychian-early Sheinwoodian, mid-Homerian, mid-Ludfordian and across the Silurian-Devonian boundary, atmospheric CO_2 dropped below the threshold levels (~6 PAL) that would have allowed continental ice over Gondwana to expand through ice-albedo feedbacks. Once triggered, the expansion of continental ice enhanced the denudation of underlying bedrock and the production of fine-grained material for chemical attack. Subglacial and proglacial processes favour the oxidation of ancient organic carbon and sulphides, whilst suppressing silicate weathering, causing a net release of CO_2 to the atmosphere. Under glacial maximum, the production of fine-grained material ceased, and oxidative weathering rates diminished. A reduction in silicate weathering, and therefore one of the Earth's major CO_2 removal mechanisms, allowed CO_2 to build up in the atmosphere via other processes, leading to global warming and rapid deglaciation. During deglaciation, retreating ice-sheets would have enhanced chemical weathering through the provision of fresh material, increased melt water and generally wetter conditions. The oxidative weathering of organic and sulphide-rich lithologies would have largely offset the reduction in atmospheric CO_2 from enhanced silicate weathering during deglaciation.

Fluctuations in the Silurian $\delta^{18}O$ record were driven by changes in continental ice volume and global temperatures, with more positive $\delta^{18}O$ values during glacial periods. The associated drop in eustatic sea level, exposed carbonate shelves to weathering and drove positive shifts in the $\delta^{13}C$ record, attaining the highest $\delta^{13}C$ values during glacial maximum. A coupled drop in eustatic sea level and global temperatures would have had a profound influence on marine biota. The Ireviken, Mulde, Lau and Klonk bio-events are defined by global extinctions of conodonts, graptolites, acritarchs, and other benthos, with high levels of originations during post-glacial recovery.

In contrast to previous views of the Silurian as a greenhouse world punctuated by large carbon cycle perturbations associated with changes in ocean circulation and precipitation rates, this study presents a new outlook on the Silurian. We suggest the Silurian is an icehouse world like the late Ordovician that preceded it, punctuated by glaciations associated with abrupt climatic and biological change. The long-term decline in atmospheric CO_2 during the Silurian was periodically reversed by negative feedback mechanisms associated with said glaciations, and prevented a 'runaway' icehouse, helping to maintain a habitable planet. Future work will need to focus on generating similar osmium and lithium isotope curves for different paleogeographic locations to validate a global signal and help ascertain the timings of glaciation, glacial maximum and deglaciation. More work is necessary to help determine between orogeny, land plant diversification, paleogeographic changes or volcanic arc degassing as the driver of atmospheric CO_2 decline and global cooling.

Much like the Cenozoic, generating Os and Li isotope curves for the entire Silurian could help track the timing and extent of orogenic events. More detailed spore and macrofossil records for Silurian land-plants could help track evolutionary and geographical changes and help ascertain their potential influence on global weathering and atmospheric evolution through computer modelling. Modelling could also help predict the influence of enhanced volcanic weathering on atmospheric CO_2 during Laurussia's passage through the ITCZ. Finally, the hunt for glacial sediments in South America and Africa should be resumed to provide unequivocal evidence for Silurian glaciations and their timing.

4.6 References

Aldridge, R., Jeppsson, L., Dorning, K., 1993. Early Silurian oceanic episodes and events. Journal of the Geological Society 150, 501-513.

Algeo, T., Scheckler, S., 2010. Land plant evolution and weathering rate changes in the Devonian. J. Earth Sci. 21, 75-78.

Algeo, T.J., Berner, R.A., Maynard, J.B., Scheckler, S.E., 1995. Late Devonian oceanic anoxic events and biotic crises:"rooted" in the evolution of vascular land plants. GSA today 5, 45.

Algeo, T.J., Marenco, P.J., Saltzman, M.R., 2016. Co-evolution of oceans, climate, and the biosphere during the 'Ordovician Revolution': A review. Palaeogeography, Palaeoclimatology, Palaeoecology 458, 1-11.

Algeo, T.J., Scheckler, S.E., 1998. Terrestrial-marine teleconnections in the Devonian: links between the evolution of land plants, weathering processes, and marine anoxic events. Philosophical Transactions of the Royal Society B: Biological Sciences 353, 113-130.

Anderson, S.P., 2005. Glaciers show direct linkage between erosion rate and chemical weathering fluxes. Geomorphology 67, 147-157.

Anderson, S.P., 2007. Biogeochemistry of Glacial Landscape Systems. Annual Review of Earth and Planetary Sciences 35, 375-399.

Anderson, S.P., Drever, J.I., Frost, C.D., Holden, P., 2000. Chemical weathering in the foreland of a retreating glacier. Geochimica et Cosmochimica Acta 64, 1173-1189.

Anderson, S.P., Drever, J.I., Humphrey, N.F., 1997. Chemical weathering in glacial environments. Geology 25, 399-402.

Armstrong, R.L., 1971. Glacial erosion and the variable isotopic composition of strontium in sea water. Nature 230, 132-133.

Azmy, K., Veizer, J., Bassett, M.G., Copper, P., 1998. Oxygen and carbon isotopic composition of Silurian brachiopods: implications for coeval seawater and glaciations. Geological Society of America Bulletin 110, 1499-1512.

Becker, R.T., Gradstein, F.M., Hammer, O., 2012. Chapter 22 - The Devonian Period, in: Gradstein, F.M., Ogg, J.G., Schmitz, M.D., Ogg, G.M. (Eds.), The Geologic Time Scale. Elsevier, Boston, pp. 559-601.

Bell, M., Laine, E., 1985. Erosion of the Laurentide region of North America by glacial and glaciofluvial processes. Quaternary Research 23, 154-174.

Berner, E.K., Berner, R.A., 2012. Global environment: water, air, and geochemical cycles. Princeton University Press.

Berner, R.A., 1997. The rise of plants and their effect on weathering and atmospheric CO2. Science 276, 544-546.

Berner, R.A., 2006. GEOCARBSULF: A combined model for Phanerozoic atmospheric O2 and CO2. Geochimica et Cosmochimica Acta 70, 5653-5664.

Berner, R.A., Caldeira, K., 1997. The need for mass balance and feedback in the geochemical carbon cycle. Geology 25, 955-956.

Berner, R.A., Lasaga, A.C., Garrels, R.M., 1983. The carbonate-silicate geochemical cycle and its effect on atmospheric carbon dioxide over the past 100 million years. Am J Sci 283, 641-683.

Bickert, T., Pätzold, J., Samtleben, C., Munnecke, A., 1997. Paleoenvironmental changes in the Silurian indicated by stable isotopes in brachiopod shells from Gotland, Sweden. Geochimica et Cosmochimica Acta 61, 2717-2730.

Bluth, G.J., Kump, L.R., 1994. Lithologic and climatologic controls of river chemistry. Geochimica et Cosmochimica Acta 58, 2341-2359.

Bottini, C., Cohen, A.S., Erba, E., Jenkyns, H.C., Coe, A.L., 2012. Osmium-isotope evidence for volcanism, weathering, and ocean mixing during the early Aptian OAE 1a. Geology 40, 583-586.

Bouchez, J., von Blanckenburg, F., Schuessler, J.A., 2013. Modeling novel stable isotope ratios in the weathering zone. American Journal of Science 313, 267-308.

Brand, U., Azmy, K., Veizer, J., 2006. Evaluation of the Salinic I tectonic, Cancañiri glacial and Ireviken biotic events: Biochemostratigraphy of the Lower Siluriansuccession in the Niagara Gorge area, Canada and U.S.A. Palaeogeography, Palaeoclimatology, Palaeoecology 241, 192-213.

Buggisch, W., Mann, U., 2004. Carbon isotope stratigraphy of Lochkovian to Eifelian limestones from the Devonian of central and southern Europe. International Journal of Earth Sciences 93, 521-541.

Calner, M., 2008. Silurian global events – at the tipping point of climate change, Mass Extinction. Springer Berlin Heidelberg, pp. 21-57.

Calner, M., Kozłowska, A., Masiak, M., Schmitz, B., 2006. A shoreline to deep basin correlation chart for the middle Silurian coupled extinction-stable isotopic event. GFF 128, 79-84.

Caputo, M.V., 1998. Ordovician–Silurian glaciations and global sea-level changes. Silurian cycles, 15-25.

Chan, L.-H., Edmond, J.M., Thompson, G., 1993. A lithium isotope study of hot springs and metabasalts from Mid-Ocean Ridge Hydrothermal Systems. Journal of Geophysical Research 98, 9653.

Chan, L., Edmond, J., Thompson, G., Gillis, K., 1992. Lithium isotopic composition of submarine basalts: implications for the lithium cycle in the oceans. Earth and Planetary Science Letters 108, 151-160.

Chan, L.H., Leeman, W.P., Plank, T., 2006. Lithium isotopic composition of marine sediments. Geochemistry, Geophysics, Geosystems 7.

Cocks, L., Torsvik, T., 2002. Earth geography from 500 to 400 million years ago: a faunal and palaeomagnetic review. Journal of the Geological Society 159, 631-644.

Cohen, A.S., Coe, A.L., 2002. New geochemical evidence for the onset of volcanism in the Central Atlantic magmatic province and environmental change at the Triassic-Jurassic boundary. Geology 30, 267.

Cooper, R., Wadham, J., Tranter, M., Hodgkins, R., Peters, N., 2002. Groundwater hydrochemistry in the active layer of the proglacial zone, Finsterwalderbreen, Svalbard. Journal of Hydrology 269, 208-223.

Cooper, R.A., Sadler, P.M., Munnecke, A., Crampton, J.S., 2013. Graptoloid evolutionary rates track Ordovician–Silurian global climate change. Geological Magazine 151, 349-364.

Cramer, B.D., Brett, C.E., Melchin, M.J., Maennik, P., Kleffner, M.A., McLaughlin, P.I., Loydell, D.K., Munnecke, A., Jeppsson, L., Corradini, C., 2011a. Revised correlation of Silurian Provincial Series of North America with global and regional chronostratigraphic units and δ13Ccarb chemostratigraphy. Lethaia 44, 185-202.

Cramer, B.D., Loydell, D.K., Samtleben, C., Munnecke, A., Kaljo, D., Mannik, P., Martma, T., Jeppsson, L., Kleffner, M.A., Barrick, J.E., Johnson, C.A., Emsbo, P., Joachimski, M.M., Bickert, T., Saltzman, M.R., 2010. Testing the limits of Paleozoic chronostratigraphic correlation via high-resolution (<500 k.y.) integrated conodont, graptolite, and carbon isotope (13Ccarb) biochemostratigraphy across the Llandovery-Wenlock (Silurian) boundary: Is a unified Phanerozoic time scale achievable? Geological Society of America Bulletin 122, 1700-1716.

Cramer, B.D., Munnecke, A., Schofield, D.I., Haase, K.M., Haase-Schramm, A., 2011b. A Revised87Sr/86Sr Curve for the Silurian: Implications for Global Ocean Chemistry and the Silurian Timescale. The Journal of Geology 119, 335-349.

Creaser, R.A., Papanastassiou, D.A., Wasserburg, G.J., 1991. Negative thermal ion mass spectrometry of osmium, rhenium and iridium. Geochimica et Cosmochimica Acta 55, 397-401.

Crick, R., Ellwood, B., Hladil, J., El Hassani, A., Hrouda, F., Chlupac, I., 2001. Magnetostratigraphy susceptibility of the Přídolian–Lochkovian (Silurian–Devonian) GSSP (Klonk, Czech Republic) and a coeval sequence in Anti-Atlas Morocco. Palaeogeography, Palaeoclimatology, Palaeoecology 167, 73-100.

Cumming, V.M., Poulton, S.W., Rooney, A.D., Selby, D., 2013. Anoxia in the terrestrial environment during the late Mesoproterozoic. Geology 41, 583-586.

Dellinger, M., Gaillardet, J., Bouchez, J., Calmels, D., Louvat, P., Dosseto, A., Gorge, C., Alanoca, L., Maurice, L., 2015. Riverine Li isotope fractionation in the Amazon River basin controlled by the weathering regimes. Geochimica et Cosmochimica Acta 164, 71-93.

Díaz-Martínez, E., Grahn, Y., 2007. Early Silurian glaciation along the western margin of Gondwana (Peru, Bolivia and northern Argentina): Palaeogeographic and geodynamic setting. Palaeogeography, Palaeoclimatology, Palaeoecology 245, 62-81.

Drever, J.I., Zobrist, J., 1992. Chemical weathering of silicate rocks as a function of elevation in the southern Swiss Alps. Geochimica et Cosmochimica Acta 56, 3209-3216.

Du Vivier, A.D.C., Selby, D., Sageman, B.B., Jarvis, I., Gröcke, D.R., Voigt, S., 2014. Marine 187Os/188Os isotope stratigraphy reveals the interaction of volcanism and ocean circulation during Oceanic Anoxic Event 2. Earth and Planetary Science Letters 389, 23-33.

Edwards, D., Morris, J.L., Richardson, J.B., Kenrick, P., 2014. Cryptospores and cryptophytes reveal hidden diversity in early land floras. New phytologist 202, 50-78.

Elderfield, H., Schultz, A., 1996. Mid-ocean ridge hydrothermal fluxes and the chemical composition of the ocean. Annual Review of Earth and Planetary Sciences 24, 191-224.

Eriksson, M.J., Calner, M., 2007. A sequence stratigraphical model for the Late Ludfordian (Silurian) of Gotland, Sweden: implications for timing between changes in sea level, palaeoecology, and the global carbon cycle. Facies 54, 253-276.

Fairchild, I.J., Killawee, J.A., Sharp, M.J., Spiro, B., Hubbard, B., Lorrain, R.D., Tison, J.L., 1999. Solute generation and transfer from a chemically reactive alpine glacial–proglacial system. Earth Surface Processes and Landforms 24, 1189-1211.

Finlay, A.J., Selby, D., Gröcke, D.R., 2010. Tracking the Hirnantian glaciation using Os isotopes. Earth and Planetary Science Letters 293, 339-348.

Flesch, G., Anderson, A., Svec, H., 1973. A secondary isotopic standard for 6Li/7Li determinations. International Journal of Mass Spectrometry and Ion Physics 12, 265-272.

Frýda, J., Hladil, J., Vokurka, K., 2002. Seawater strontium isotope curve at the Silurian/Devonian boundary: a study of the global Silurian/Devonian boundary stratotype. Geobios 35, 21-28.

Frýda, J., Manda, Š., 2013. A long-lasting steady period of isotopically heavy carbon in the late Silurian ocean: evolution of the δ 13 C record and its significance for an integrated δ 13 C, graptolite and conodont stratigraphy. Bulletin of Geosciences 88.

Gaillardet, J., Dupré, B., Louvat, P., Allegre, C., 1999. Global silicate weathering and CO 2 consumption rates deduced from the chemistry of large rivers. Chemical geology 159, 3-30.

Garrels, R.M., Lerman, A., Mackenzie, F.T., 1976. Controls of atmospheric O 2 and CO 2: past, present, and future: geochemical models of the earth's surface environment, focusing on O 2 and CO 2 cycles, suggest that a dynamic steady-state system exists, maintained over time by effective feedback mechanisms. American Scientist, 306-315.

Gensel, P.G., 2008. The Earliest Land Plants. Annual Review of Ecology, Evolution, and Systematics 39, 459-477.

Georg, R.B., West, A.J., Vance, D., Newman, K., Halliday, A.N., 2013. Is the marine osmium isotope record a probe for CO2 release from sedimentary rocks? Earth and Planetary Science Letters 367, 28-38.

Ghienne, J-F., et al., 2014. A Cenozoic style scenario for the end-Ordovician glaciation. Nature communications, 5:4485.

Gislason, S.R., Oelkers, E.H., Eiriksdottir, E.S., Kardjilov, M.I., Gisladottir, G., Sigfusson, B., Snorrason, A., Elefsen, S., Hardardottir, J., Torssander, P., Oskarsson, N., 2009. Direct evidence of the feedback between climate and weathering. Earth and Planetary Science Letters 277, 213-222.

Goodbred, S., Kuehl, S.A., 2000. The significance of large sediment supply, active tectonism, and eustasy on margin sequence development: Late Quaternary stratigraphy and evolution of the Ganges–Brahmaputra delta. Sedimentary Geology 133, 227-248.

Grahn, Y., Caputo, M.V., 1992. Early Silurian glaciations in Brazil. Palaeogeography, Palaeoclimatology, Palaeoecology 99, 9-15.

Haq, B.U., Schutter, S.R., 2008. A chronology of Paleozoic sea-level changes. Science 322, 64-68.

Hardie, L.A., 1996. Secular variation in seawater chemistry: An explanation for the coupled secular variation in the mineralogies of marine limestones and potash evaporites over the past 600 my. Geology 24, 279-283.

Harper, D.A.T., Hammarlund, E.U., Rasmussen, C.M.Ø., 2014. End Ordovician extinctions: A coincidence of causes. Gondwana Research 25, 1294-1307.

Hathorne, E.C., James, R.H., 2006. Temporal record of lithium in seawater: A tracer for silicate weathering? Earth and Planetary Science Letters 246, 393-406.

Hazen, R.M., Sverjensky, D.A., Azzolini, D., Bish, D.L., Elmore, S.C., Hinnov, L., Milliken, R.E., 2013. Clay mineral evolution. American Mineralogist 98, 2007-2029.

Hinderer, M., 2001. Late Quaternary denudation of the Alps, valley and lake fillings and modern river loads. Geodinamica Acta 14, 231-263.

Hodell, D.A., Mead, G.A., Mueller, P.A., 1990. Variation in the strontium isotopic composition of seawater (8 Ma to present): Implications for chemical weathering rates and dissolved fluxes to the oceans. Chemical Geology: Isotope Geoscience section 80, 291-307.

Hoffman, P.F. & Schrag D.P. 2002.The snowball Earth hypothesis: testing the limits of global change. Terra Nova 14, 129-155.

Huh, Y., Chan, L.-H., Zhang, L., Edmond, J.M., 1998. Lithium and its isotopes in major world rivers: implications for weathering and the oceanic budget. Geochimica et Cosmochimica Acta 62, 2039-2051.

Huh, Y., Edmond, J.M., 1999. The fluvial geochemistry of the rivers of Eastern Siberia: III. Tributaries of the Lena and Anabar draining the basement terrain of the Siberian Craton and the Trans-Baikal Highlands. Geochimica et Cosmochimica Acta 63, 967-987.

Jacobson, A.D., Blum, J.D., Chamberlain, C.P., Poage, M.A., Sloan, V.F., 2002. Ca/Sr and Sr isotope systematics of a Himalayan glacial chronosequence: carbonate versus silicate weathering rates as a function of landscape surface age. Geochimica et Cosmochimica Acta 66, 13-27.

Jaffe, L.A., Peucker-Ehrenbrink, B., Petsch, S.T., 2002. Mobility of rhenium, platinum group elements and organic carbon during black shale weathering. Earth and Planetary Science Letters 198, 339-353.

James, R.H., Rudnicki, M.D., Palmer, M.R., 1999. The alkali element and boron geochemistry of the Escanaba Trough sediment-hosted hydrothermal system. Earth and Planetary Science Letters 171, 157-169.

Jeppsson, L., 1990. An oceanic model for lithological and faunal changes tested on the Silurian record. Journal of the Geological Society 147, 663-674.

Jeppsson, L., 1997. The anatomy of the mid-early Silurian Ireviken Event and a scenario for PS events. Paleontological events: stratigraphic, ecological, and evolutionary implications, 451-492.

Jeppsson, L., 1998. Silurian oceanic events: summary of general characteristics. Silurian cycles: Linkages of dynamic stratigraphy with atmospheric, oceanic and tectonic changes, 239-257.

Jeppsson, L., Aldridge, R.J., 2000. Ludlow (late Silurian) oceanic episodes and events. Journal of the Geological Society 157, 1137-1148.

Johnson, M.E., 2006. Relationship of Silurian sea-level fluctuations to oceanic episodes and events. GFF 128, 115-121.

Johnson, M.E., 2010. Tracking Silurian eustasy: Alignment of empirical evidence or pursuit of deductive reasoning? Palaeogeography, Palaeoclimatology, Palaeoecology 296, 276-284.

Kaljo, D., Martma, T., Männik, P., Viira, V., 2003. Implications of Gondwana glaciations in the Baltic late Ordovician and Silurian and a carbon isotopic test of environmental cyclicity. Bulletin de la Société géologique de France 174, 59-66.

Kendall, B.S., Creaser, R.A., Ross, G.M., Selby, D., 2004. Constraints on the timing of Marinoan “Snowball Earth” glaciation by 187Re–187Os dating of a Neoproterozoic, post-glacial black shale in Western Canada. Earth and Planetary Science Letters 222, 729-740.

Kenrick, P., Wellman, C.H., Schneider, H., Edgecombe, G.D., 2012. A timeline for terrestrialization: consequences for the carbon cycle in the Palaeozoic. Phil. Trans. R. Soc. B 367, 519-536.

Klemm, V., Levasseur, S., Frank, M., Hein, J.R., Halliday, A.N., 2005. Osmium isotope stratigraphy of a marine ferromanganese crust. Earth and Planetary Science Letters 238, 42-48.

Kump, L., Alley, R.B., 1994. Global chemical weathering on glacial time scales. Material Fluxes on the Surface of the Earth, 46-60.

Kump, L., Arthur, M., Patzkowsky, M., Gibbs, M., Pinkus, D., Sheehan, P., 1999. A weathering hypothesis for glaciation at high atmospheric pCO 2 during the Late Ordovician. Palaeogeography, Palaeoclimatology, Palaeoecology 152, 173-187.

Lechler, M., Pogge von Strandmann, P.A.E., Jenkyns, H.C., Prosser, G., Parente, M., 2015. Lithium-isotope evidence for enhanced silicate weathering during OAE 1a (Early Aptian Selli event). Earth and Planetary Science Letters 432, 210-222.

Lefebvre, V., Servais, T., François, L., Averbuch, O., 2010. Did a Katian large igneous province trigger the Late Ordovician glaciation?: A hypothesis tested with a carbon cycle model. Palaeogeography, Palaeoclimatology, Palaeoecology 296, 310-319.

Lehnert, O., Männik, P., Joachimski, M.M., Calner, M., Frýda, J., 2010. Palaeoclimate perturbations before the Sheinwoodian glaciation: A trigger for extinctions during the 'Ireviken Event'. Palaeogeography, Palaeoclimatology, Palaeoecology 296, 320-331.

Lenton, T.M., Crouch, M., Johnson, M., Pires, N., Dolan, L., 2012. First plants cooled the Ordovician. Nature Geoscience 5, 86-89.

Li, G., Ji, J., Chen, J., Kemp, D.B., 2009. Evolution of the Cenozoic carbon cycle: The roles of tectonics and CO2 fertilization. Global Biogeochemical Cycles 23, n/a-n/a.

Li, G., West, A.J., 2014. Evolution of Cenozoic seawater lithium isotopes: Coupling of global denudation regime and shifting seawater sinks. Earth and Planetary Science Letters 401, 284-293.

Loydell, D., Männik, P., Nestor, V., 2003. Integrated biostratigraphy of the lower Silurian of the Aizpute-41 core, Latvia. Geological Magazine 140, 205-229.

Loydell, D.K., 1998. Early Silurian sea-level changes. Geological Magazine 135, 447-471.

Loydell, D.K., 2007. Early Silurian positive δ13C excursions and their relationship to glaciations, sea-level changes and extinction events. Geological Journal 42, 531-546.

Mackenzie, F.T., Garrels, R.M., 1966. Chemical mass balance between rivers and oceans. American Journal of Science 264, 507-525.

Maher, K., Chamberlain, C., 2014. Hydrologic regulation of chemical weathering and the geologic carbon cycle. Science 343, 1502-1504.

Maier, G. 2010. Development of δ13Ccarb and δ13Corg isotope values from the Lower Silurian of Gotland (Sweden). Diploma thesis, GeoZentrum Nordbayern.

McArthur, J., Howarth, R., Bailey, T., 2001. Strontium isotope stratigraphy: LOWESS version 3: best fit to the marine Sr-isotope curve for 0–509 Ma and accompanying look-up table for deriving numerical age. The Journal of Geology 109, 155-170.

McKenzie, N.R., Horton, B.K., Loomis, S.E., Stockli, D.F., Planavsky, N.J., Lee, C.-T.A., 2016. Continental arc volcanism as the principal driver of icehouse-greenhouse variability. Science 352, 444-447.

Melchin, M., Koren, T., Štorch, P., 1998. Global diversity and survivorship patterns of Silurian graptoloids. New York State Museum Bulletin 491, 165-182.

Melchin, M.J., Sadler, P.M., Cramer, B.D., Cooper, R.A., Gradstein, F.M., Hammer, O., 2012. Chapter 21 - The Silurian Period, in: Gradstein, F.M., Ogg, J.G., Schmitz, M.D., Ogg, G.M. (Eds.), The Geologic Time Scale. Elsevier, Boston, pp. 525-558.

Meybeck, M., 1987. Global chemical weathering of surficial rocks estimated from river dissolved loads. American journal of science 287, 401-428.

Millot, R., Girard, J., 2007. Lithium isotope fractionation during adsorption onto mineral surfaces, International Meeting on Clays in Natural & Engineered Barriers for Radioactive Waste Confinement, Lille, France.

Misra, S., Froelich, P.N., 2012. Lithium isotope history of Cenozoic seawater: changes in silicate weathering and reverse weathering. Science 335, 818-823.

Munnecke, A., Calner, M., Harper, D.A.T., Servais, T., 2010. Ordovician and Silurian sea–water chemistry, sea level, and climate: A synopsis. Palaeogeography, Palaeoclimatology, Palaeoecology 296, 389-413.

Nardin, E., Godderis, Y., Donnadieu, Y., Hir, G.L., Blakey, R.C., Puceat, E., Aretz, M., 2011. Modeling the early Paleozoic long-term climatic trend. Geological Society of America Bulletin 123, 1181-1192.

Noble, P.J., Zimmerman, M.K., Holmden, C., Lenz, A.C., 2005. Early Silurian (Wenlockian) δ13C profiles from the Cape Phillips Formation, Arctic Canada and their relation to biotic events. Canadian Journal of Earth Sciences 42, 1419-1430.

Nowell, G., Luguet, A., Pearson, D., Horstwood, M., 2008. Precise and accurate 186 Os/188 Os and 187 Os/188 Os measurements by multi-collector plasma ionisation mass spectrometry (MC-ICP-MS) part I: Solution analyses. Chemical Geology 248, 363-393.

Oxburgh, R., 2001. Residence time of osmium in the oceans. Geochemistry, Geophysics, Geosystems 2, 1018.

Palmer, M., Edmond, J., 1992. Controls over the strontium isotope composition of river water. Geochimica et Cosmochimica Acta 56, 2099-2111.

Paquay, F.S., Ravizza, G.E., Dalai, T.K., Peucker-Ehrenbrink, B., 2008. Determining chondritic impactor size from the marine osmium isotope record. Science 320, 214-218.

Petit, J.-R., Jouzel, J., Raynaud, D., Barkov, N.I., Barnola, J.-M., Basile, I., Bender, M., Chappellaz, J., Davis, M., Delaygue, G., 1999. Climate and atmospheric history of the past 420,000 years from the Vostok ice core, Antarctica. Nature 399, 429-436.

Petsch, S., Eglinton, T., Edwards, K., 2001a. 14C-dead living biomass: evidence for microbial assimilation of ancient organic carbon during shale weathering. Science 292, 1127-1131.

Petsch, S.T., Smernik, R., Eglinton, T., Oades, J., 2001b. A solid state 13 C-NMR study of kerogen degradation during black shale weathering. Geochimica et Cosmochimica Acta 65, 1867-1882.

Peucker-Ehrenbrink, B., Blum, J.D., 1998. Re-Os isotope systematics and weathering of Precambrian crustal rocks: Implications for the marine osmium isotope record. Geochimica et Cosmochimica Acta 62, 3193-3203.

Peucker-Ehrenbrink, B., Hannigan, R.E., 2000. Effects of black shale weathering on the mobility of rhenium and platinum group elements. Geology 28, 475-478.

Peucker-Ehrenbrink, B., Ravizza, G., 2000. The marine osmium isotope record. Terra Nova 12, 205-219.

Peucker-Ehrenbrink, B., Ravizza, G., 2012. Osmium isotope stratigraphy. The Geologic Time Scale 2012, 145-166.

Pierson-Wickmann, A.-C., Reisberg, L., France-Lanord, C., 2002. Behavior of Re and Os during low-temperature alteration: results from Himalayan soils and altered black shales. Geochimica et Cosmochimica Acta 66, 1539-1548.

Pogge von Strandmann, P.A.E., Burton, K.W., James, R.H., van Calsteren, P., Gíslason, S.R., Mokadem, F., 2006. Riverine behaviour of uranium and lithium isotopes in an actively glaciated basaltic terrain. Earth and Planetary Science Letters 251, 134-147.

Pogge von Strandmann, P.A.E., Desrochers, A., Murphy, M.J., Finlay, A.J., Selby, D., Lenton, T.M., in review. Global climate stabilisation by chemical weathering during the Hirnantian glaciation. Geochemical Perspectives Letters.

Pogge von Strandmann, P.A.E., Elliott, T., Marschall, H.R., Coath, C., Lai, Y.-J., Jeffcoate, A.B., Ionov, D.A., 2011. Variations of Li and Mg isotope ratios in bulk chondrites and mantle xenoliths. Geochimica et Cosmochimica Acta 75, 5247-5268.

Pogge von Strandmann, P.A.E., Frings, P.J., Murphy, M.J., 2017. Lithium isotope behaviour during weathering in the Ganges Alluvial Plain. Geochimica et Cosmochimica Acta 198, 17-31.

Pogge von Strandmann, P.A.E., Jenkyns, H.C., Woodfine, R.G., 2013. Lithium isotope evidence for enhanced weathering during Oceanic Anoxic Event 2. Nature Geoscience 6, 668-672.

Pohl, A., Donnadieu, Y., Le Hir, G., Buoncristiani, J.F., Vennin, E., 2014. Effect of the Ordovician paleogeography on the (in)stability of the climate. Clim Past 10, 2053-2066.

Poirier, A., Hillaire-Marcel, C., 2009. Os-isotope insights into major environmental changes of the Arctic Ocean during the Cenozoic. Geophysical Research Letters 36.

Porada, P., Lenton, T.M., Pohl, A., Weber, B., Mander, L., Donnadieu, Y., Beer, C., Poschl, U., Kleidon, A., 2016. High potential for weathering and climate effects of non-vascular vegetation in the Late Ordovician. Nature communications 7, 12113.

Porębska, E., Kozłowska-Dawidziuk, A., Masiak, M., 2004. The lundgreni event in the Silurian of the East European Platform, Poland. Palaeogeography, Palaeoclimatology, Palaeoecology 213, 271-294.

Ravizza, G., Norris, R.N., Blusztajn, J., Aubry, M.P., 2001. An osmium isotope excursion associated with the Late Paleocene thermal maximum: Evidence of intensified chemical weathering. Paleoceanography 16, 155-163.

Ravizza, G., Peucker-Ehrenbrink, B., 2003. Chemostratigraphic evidence of Deccan volcanism from the marine osmium isotope record. Science 302, 1392-1395.

Ravizza, G., Turekian, K.K., 1989. Application of the 187Re-187Os system to black shale geochronometry. Geochimica et Cosmochimica Acta 53, 3257-3262.

Raymo, M.E., Ruddiman, W.F., Froelich, P.N., 1988. Influence of late Cenozoic mountain building on ocean geochemical cycles. Geology 16, 649-653.

Richter, F.M., Turekian, K.K., 1993. Simple models for the geochemical response of the ocean to climatic and tectonic forcing. Earth and Planetary Science Letters 119, 121-131.

Rooney, A.D., Selby, D., Lloyd, J.M., Roberts, D.H., Lückge, A., Sageman, B.B., Prouty, N.G., 2016. Tracking millennial-scale Holocene glacial advance and retreat using osmium isotopes: Insights from the Greenland ice sheet. Quaternary Science Reviews 138, 49-61.

Saltzman, M.R., Thomas, E., 2012. Chapter 11 - Carbon Isotope Stratigraphy, The Geologic Time Scale. Elsevier, Boston, pp. 207-232.

Sauzéat, L., Rudnick, R.L., Chauvel, C., Garçon, M., Tang, M., 2015. New perspectives on the Li isotopic composition of the upper continental crust and its weathering signature. Earth and Planetary Science Letters 428, 181-192.

Schmitz, B., Peucker-Ehrenbrink, B., Heilmann-Clausen, C., Åberg, G., Asaro, F., Lee, C.-T.A., 2004. Basaltic explosive volcanism, but no comet impact, at the Paleocene–Eocene boundary: high-resolution chemical and isotopic records from Egypt, Spain and Denmark. Earth and Planetary Science Letters 225, 1-17.

Selby, D., Creaser, R.A., 2003. Re–Os geochronology of organic rich sediments: an evaluation of organic matter analysis methods. Chemical Geology 200, 225-240.

Seyfried, W., Chen, X., Chan, L.-H., 1998. Trace element mobility and lithium isotope exchange during hydrothermal alteration of seafloor weathered basalt: an experimental study at 350 C, 500 bars. Geochimica et Cosmochimica Acta 62, 949-960.

Smoliar, M.I., Walker, R.J., Morgan, J.W., 1996. Re-Os Ages of Group IIA, IIIA, IVA, and IVB Iron Meteorites. Science 271, 1099-1102.

Stanley, S.M., Hardie, L.A., 1998. Secular oscillations in the carbonate mineralogy of reef-building and sediment-producing organisms driven by tectonically forced shifts in seawater chemistry. Palaeogeography, Palaeoclimatology, Palaeoecology 144, 3-19.

Steemans, P., Herisse, A.L., Melvin, J., Miller, M.A., Paris, F., Verniers, J., Wellman, C.H., 2009. Origin and radiation of the earliest vascular land plants. Science 324, 353.

Stoffynegli, P., Mackenzie, F.T., 1984. Mass balance of dissolved lithium in the oceans. Geochimica et Cosmochimica Acta 48, 859-872.

Štorch, P., 1995. Biotic crises and post-crisis recoveries recorded by Silurian planktonic graptolite faunas of the Barrandian area (Czech Republic). Geolines 3, 59-70.

Sutcliffe, O.E., 2000. Calibrating the Late Ordovician glaciation and mass extinction by the eccentricity cycles of Earth's orbit. Geology 28 (11), 967-970.

Tessier, A., Campbell, P.G., Bisson, M., 1979. Sequential extraction procedure for the speciation of particulate trace metals. Analytical chemistry 51, 844-851.

Thomas, M.F., Thorp, M.B., 1995. Geomorphic response to rapid climatic and hydrologic change during the late Pleistocene and early Holocene in the humid and sub-humid tropics. Quaternary Science Reviews 14, 193-207.

Tomascak, P.B., 2004. Developments in the understanding and application of lithium isotopes in the earth and planetary sciences. Reviews in Mineralogy and Geochemistry 55, 153-195.

Torres, M.A., West, A.J., Li, G., 2014. Sulphide oxidation and carbonate dissolution as a source of CO2 over geological timescales. Nature 507, 346-349.

Torsvik, T.H., Cocks, L.R.M., 2013. New global palaeogeographical reconstructions for the Early Palaeozoic and their generation. Geological Society, London, Memoirs 38, 5-24.

Tranter, M., 1982. Controls on the chemical composition of alpine glacial meltwaters. University of East Anglia.

Tranter, M., Sharp, M.J., Lamb, H.R., Brown, G.H., Hubbard, B.P., Willis, I.C., 2002. Geochemical weathering at the bed of Haut Glacier d'Arolla, Switzerland?a new model. Hydrological Processes 16, 959-993.

Trotter, J.A., Williams, I.S., Barnes, C.R., Männik, P., Simpson, A., 2016. New conodont δ18O records of Silurian climate change: Implications for environmental and biological events. Palaeogeography, Palaeoclimatology, Palaeoecology 443, 34-48.

Turgeon, S.C., Creaser, R.A., 2008. Cretaceous oceanic anoxic event 2 triggered by a massive magmatic episode. Nature 454, 323-326.

Vance, D., Teagle, D.A., Foster, G.L., 2009. Variable Quaternary chemical weathering fluxes and imbalances in marine geochemical budgets. Nature 458, 493-496.

Verney-Carron, A., Vigier, N., Millot, R., 2011. Experimental determination of the role of diffusion on Li isotope fractionation during basaltic glass weathering. Geochimica et Cosmochimica Acta 75, 3452-3468.

Vigier, N., Decarreau, A., Millot, R., Carignan, J., Petit, S., France-Lanord, C., 2008. Quantifying Li isotope fractionation during smectite formation and implications for the Li cycle. Geochimica et Cosmochimica Acta 72, 780-792.

Wadham, J.L., Bottrell, S., Tranter, M., Raiswell, R., 2004. Stable isotope evidence for microbial sulphate reduction at the bed of a polythermal high Arctic glacier. Earth and Planetary Science Letters 219, 341-355.

Walker, J.C.G., Hays, P.B., Kasting, J.F., 1981. A negative feedback mechanism for the long-term stabilization of Earth's surface temperature. Journal of Geophysical Research 86, 9776.

Wildman, R.A., Berner, R.A., Petsch, S.T., Bolton, E.W., Eckert, J.O., Mok, U., Evans, J.B., 2004. The weathering of sedimentary organic matter as a control on atmospheric O2: I. Analysis of a black shale. American Journal of Science 304, 234-249.

Wimpenny, J., James, R.H., Burton, K.W., Gannoun, A., Mokadem, F., Gíslason, S.R., 2010. Glacial effects on weathering processes: New insights from the elemental and lithium isotopic composition of West Greenland rivers. Earth and Planetary Science Letters 290, 427-437.

Young, S.A., Saltzman, M.R., Foland, K.A., Linder, J.S., Kump, L.R., 2009. A major drop in seawater 87Sr/86Sr during the Middle Ordovician (Darriwilian): Links to volcanism and climate? Geology 37, 951-954.

Žigaitė, Ž., Joachimski, M.M., Lehnert, O., Brazauskas, A., 2010. δ18O composition of conodont apatite indicates climatic cooling during the Middle Pridoli. Palaeogeography, Palaeoclimatology, Palaeoecology 294, 242-247.

Chapter 5

Conclusion

This body of work has determined the osmium isotopic composition seawater for past and present oceans by applying Re-Os isotope measurements to organic-rich shales and macroalgae respectively. This has led to a better understanding of basaltic weathering in Iceland, mankind's influence on the Os isotope cycle and the discovery of several Silurian glaciations. This final chapter briefly draws together key aspects of each chapter and then suggests possible directions for future work.

5.1 Re-Os isotope uptake and distribution in macroalgae

Research conducted by B. Racionero-Gómez at the University of Durham, in part under supervision by myself, looked at Re and Os uptake and distribution in the common macroalgae species, *Fucus vesiculosus* (Racionero-Gómez et al., 2016; Racionero-Gómez et al., 2017). These studies demonstrated Re and Os varies within the macroalgae and that Re and Os are not located within one specific structure. Rhenium, and therefore most likely Os, is not held within the chloroplasts or cytoplasmic proteins. Rhenium and Os abundance in cultured macroalgae increased with increasing culture media abundance. Moreover, cultured macroalgae doped in seawater with a known Os isotopic composition, took on the isotopic signature of the fluid, with no signs of fractionation (Racionero-Gómez et al., 2017). Rhenium did not accumulate in dead macroalgae, suggesting syn-life bioadsorption/bioaccumulation (Racionero-Gómez et al., 2016).

This work suggested Re and Os in macroalgae are taken up directly from the water column in which they live, where they accumulate to far higher concentrations than seawater. Meanwhile, the uptake of Os by macroalgae does not fractionate Os isotopes and macroalgae retains the isotopic composition of seawater. This overcomes several problems associated with direct Os isotope analysis in seawater, such as ultra-low concentrations and multiple oxidation states (Peucker-Ehrenbrink et al., 2013). It is therefore possible for Os isotopes in macroalgae to become a proxy for the Os isotopic composition of seawater, a powerful tracer of Earth system processes. More work will need to be done to understand the uptake mechanism and storage location for Re and Os within the macroalgae.

5.2 Re-Os isotopes in macroalgae as a tracer of Earth system processes

Chapter 2 utilised Re and Os abundance and isotope data from Icelandic macroalgae, dissolved load and bedload. This work established that Re and Os abundance and isotopic composition reflected that of the brackish, estuarine habitats in which they live. In the instance of Iceland, estuarine conditions represent the mixing between rivers draining either younger basaltic catchments that have undergone congruent weathering, or, older basaltic catchments that have undergone incongruent weathering of primary basaltic minerals with North Atlantic seawater. However, although the $^{187}Os/^{188}Os$ composition of macroalgae is controlled by that of seawater, the $^{187}Re/^{188}Os$ composition of seawater is far higher than Icelandic geochemical reservoirs. This suggests the preferential uptake of Re over Os at high ambient seawater Re concentrations, a notion supported by further data presented in Chapter 3.

This study built on previous work (See section 5.1) by confirming the use of Os isotopes in macroalgae as a proxy for the $^{187}Os/^{188}Os$ composition of seawater in a real-world setting. However, it also became apparent that macroalgae could not be used to trace fluctuation in the Os abundance and $^{187}Re/^{188}Os$ composition of seawater. More work will need to be done to understand Os uptake rates in a range of common macroalgae species. This will allow for more accurate estimates of the Os abundance of seawater, which in turn can be utilised alongside $^{187}Re/^{188}Os$ ratios to help constrain the residence time of Os in the ocean. Finally, macroalgae is not a substantial sink of Re and Os and global macroalgae biomass does not play a significant role in the marine Os and Re cycle, both today and in Earth's geological past.

5.3 Re-Os isotopes in macroalgae as a tracer of anthropogenic processes

Chapter 3 utilised Re and Os abundance and isotope data in Japanese macroalgae to trace not only natural processes, but also anthropogenic contamination associated with human activity in densely populated regions of Japan. The ^{187}Os/^{188}Os of macroalgae reflects mixing between seawater and: rivers draining Miocene-Holocene continental rocks; and/or, anthropogenic sources. In particular, the use of PGE ores in catalytic convertors has led to the widespread release of appreciable unradiogenic Os to the atmosphere and marine environment surrounding major Japanese cities. This is compounded by further point source release of PGE derived Os associated with medical research and municipal solid waste processing.

This study built on previous work (See section 5.1 and 5.2) by confirming that the ^{187}Os/^{188}Os of macroalgae could trace environmental fluctuations in anthropogenic Os related to the widespread use of PGE ores. Osmium isotopes in macroalgae can therefore become powerful tracers of pollution. However, more work will need to be done to find ways to distinguish between the various anthropogenic sources of Os. One way could be to develop the use of other isotope and elemental systems with specific association to vehicle use, municipal solid waste or relevant medical research sources. As an example, Al and organic carbon concentrations in sediments have been used in conjunction with Os isotopes to trace anthropogenic Os associated with sewage. Finally, Chapter 3 suggested coastal cities are a significant source of anthropogenic Os to the ocean, and the use of PGE ores in catalytic convertors has led to lower ^{187}Os/^{188}Os ratios in global oceanic surface waters.

5.4 The Os and Li isotopic composition of Silurian seawater

In Chapter 4, Re-Os and Li isotope systematics were measured in organic-rich shales and carbonates, from sections that spanned the Silurian Ireviken, Mulde, Lau and Klonk bioevents. Osmium and Li isotope profiles were similar to those previously recorded for the Hirnantian glaciation (Finlay et al., 2010; Pogge von Strandmann et al., in review) and are associated with fluctuation in the weathering of organic-sulphide-rich shales and silicates respectively. This suggests that much like the Ordovician, the Silurian is punctuated by several glaciation events associated with enhanced continental ice volume over Gondwana, and is supported by carbon and oxygen isotope data and sea-level reconstructions.

As continental ice expands subglacial and proglacial processes act to enhance the weathering of organic and sulphide rich shales, delivering an increased flux of radiogenic Os to the oceans. Meanwhile, subglacial processes act to suppress silicate weathering causing a reduction in the delivery of isotopically light Li to the ocean. Under glacial maximum the supply of freshly comminuted shales ceases along with weathering and the supply of radiogenic Os to the ocean. However, the enhanced ice cover maintains relatively low levels of silicate weathering. During deglaciation, subglacial and proglacial processes enhance the weathering of organic and sulphide rich shales and silicates, delivering radiogenic Os and isotopically light Li to the ocean.

This study has several major implications:

1. The Silurian was traditionally thought of as a greenhouse like the Devonian that proceeds it. However, this work suggests the Silurian is an icehouse much like the Ordovician that preceded it.

2. The Silurian is punctuated by several glaciations associated with minor marine extinctions and a reduction in global temperatures and sea-level.
3. Osmium and Li isotopes can be used in tandem to reconstruct fluctuation in continental oxidative and silicate weathering respectively. If used properly, these proxies could help us understand how weathering influences atmospheric CO_2 through geological time.
4. Subglacial and proglacial processes lead to enhanced oxidative weathering whilst suppressing silicate weathering during glaciations. This acts to reverse global cooling by releasing net carbon dioxide to the atmosphere.
5. A long-term decline in atmospheric CO_2 associated with orogeny, land-plant diversification, reduced volcanic arc degassing and/or paleogeography, is ultimately reversed by weathering processes associated with enhanced continental ice volume, preventing runaway icehouse conditions.
6. This study supports the idea of the Earth having a self-regulating climate that maintains a habitable planet.

5.6 Future outlook

Osmium isotopes in macroalgae as a proxy for the $^{187}Os/^{188}Os$ composition of seawater remains in its infancy despite the great strides made in this body of work. One major limitation is the inability to determine the Os abundance in seawater using macroalgae. More work will need to be done to determine Os uptake relationships in a similar manner to previous work (Racionero-Gómez et al., 2017) but at natural Os levels. This will then have to be repeated for the most common globally distributed macroalgae species. This study has shown the $^{187}Os/^{188}Os$ of macroalgae represents that of the seawater in which it lives, and if it could be combined with a reconstruction of [Os], would allow the determination of continental inputs of Os to the ocean. This would allow for better constraints on the marine Os cycle and Oceanic residence times.

This work has shown the $^{187}Os/^{188}Os$ of macroalgae can trace anthropogenic sources of Os. However, it is difficult to distinguish between the various sources due to the similar nature of isotopic signatures. Other isotope or elemental systems with a specific affinity for one of these sources will need to be developed in macroalgae to distinguish between these sources. This could help macroalgae become a powerful tracer of human activity and a useful environmental indicator. In particular, it can be used to trace the influence of widespread catalytic convertor use, 'similar to Pb from leaded gasoline usage before 1978 or tritium from atmospheric atomic bomb testing in the early 1960s' (Chen et al., 2009).

This body of work provided further geochemical evidence for periodic Silurian glaciations by using Os and Li isotopes. However, physical evidence for mid-late Silurian glaciations still remains elusive. More work will need to be done to find glacial sediments for the time periods studied. This will provide unequivocal evidence for a Silurian icehouse world. Chapter 4 suggested that Os and Li isotope profiles represent changes in oxidative and silicate respectively. However, like most isotopes systems, these signals remain ambiguous. Data collected in this study could reflect changes in weathering of variable continental rocks (not just oxidative weathering) or a change in weathering congruency. More weathering proxies need to be utilised to separate out these signals. Moreover, samples were only analysed in one regional location. In order to determine a global signal samples from globally distributes sites need to be measured.

Finally, the cause of Silurian glaciations remains elusive. Most proposed mechanisms in this study suggest a long-term decline in atmospheric CO_2 and global temperatures resulting from changes in orogeny, land-plant diversification, volcanic-arc degassing or paleogeography. More work will need to be done to determine between these drivers of climatic change. In particular, complex carbon cycle modelling for the Silurian may provide unparalleled information.

5.7 References

Chen, C., Sedwick, P.N., Sharma, M., 2009. Anthropogenic osmium in rain and snow reveals global-scale atmospheric contamination. Proceedings of the National Academy of Sciences of the United States of America 106, 7724-7728.

Finlay, A.J., Selby, D., Gröcke, D.R., 2010. Tracking the Hirnantian glaciation using Os isotopes. Earth and Planetary Science Letters 293, 339-348.

Peucker-Ehrenbrink, B., Sharma, M., Reisberg, L., 2013. Recommendations for analysis of dissolved osmium in seawater. Eos, Transactions American Geophysical Union 94, 73-73.

Pogge von Strandmann, P.A.E., Desrochers, A., Murphy, M.J., Finlay, A.J., Selby, D., Lenton, T.M., in review. Global climate stabilisation by chemical weathering during the Hirnantian glaciation. Geochemical Perspectives Letters.

Racionero-Gómez, B., Sproson, A., Selby, D., Gröcke, D., Redden, H., Greenwell, H., 2016. Rhenium uptake and distribution in phaeophyceae macroalgae, Fucus vesiculosus. Royal Society Open Science 3, 160161.

Racionero-Gómez, B., Sproson, A.D., Selby, D., Gannoun, A., Gröcke, D.R., Greenwell, H.C., Burton, K.W., 2017. Osmium uptake, distribution, and 187Os/188Os and 187Re/188Os compositions in Phaeophyceae macroalgae, Fucus vesiculosus: Implications for determining the 187Os/188Os composition of seawater. Geochimica et Cosmochimica Acta 199, 48-57.